

General Disclaimer

One or more of the Following Statements may affect this Document

- This document has been reproduced from the best copy furnished by the organizational source. It is being released in the interest of making available as much information as possible.
- This document may contain data, which exceeds the sheet parameters. It was furnished in this condition by the organizational source and is the best copy available.
- This document may contain tone-on-tone or color graphs, charts and/or pictures, which have been reproduced in black and white.
- This document is paginated as submitted by the original source.
- Portions of this document are not fully legible due to the historical nature of some of the material. However, it is the best reproduction available from the original submission.



CONTRACT NAS 9-14243
DRL T-1032
LINE ITEM 4
AESC REPORT 5231

NASA CR-

147430

**PRELIMINARY DESIGN STUDY
SHUTTLE MODULAR SCANNING
SPECTRORADIOMETER**

FINAL REPORT

DECEMBER 1975

Prepared For

**NASA LYNDON B. JOHNSON SPACE CENTER
HOUSTON, TEXAS 77058**

***AEROJET
ELECTROSYSTEMS
COMPANY***

AZUSA, CALIFORNIA



(NASA-CR-147430) PRELIMINARY DESIGN STUDY.
SHUTTLE MODULAR SCANNING SPECTRORADIOMETER
Final Report, 20 Jun. 1974 - 30 Nov. 1975
(Aerojet ElectroSystems Co.) 247 p HC \$8.00

N76-16163

Unclas
CSCI 14B G3/19 09985

ABSTRACT

Fundamental concepts on which to base a detailed design for a Shuttle Modular Scanning Spectroradiometer were developed, and a preliminary design is presented.

The recommended design features modularity and flexibility. It includes a 75-cm f/1.7-telescope assembly in an all-reflective Schmidt configuration, a solid-state-scan system ("pushbroom") with high resolution over a 15° field of view, and ten detector channels covering the spectral range from 0.45 to 12.5 μm . It uses charge-transfer-device techniques to accommodate a large number of detector elements for earth-observation measurements.

Methods for in-flight radiometric calibration, for image-motion compensation, and for data processing are described. Recommendations for ground support equipment are included, and interfaces with the Shuttle Orbiter vehicle are illustrated.



FOREWORD

This final technical report covers the results of a study to define and provide a preliminary design for a Shuttle Modular Scanning Spectroradiometer (SMSS). It was prepared by the Research Department of Aerojet ElectroSystems Company (AESC) in accordance with Line Item 4 of the Data Requirements List under National Aeronautics and Space Administration Contract NAS 9-14243. The work was performed from 20 June 1974 to 30 November 1975 and was administered under the direction of the Sensor Systems Development Branch, Lyndon B. Johnson Space Center, Houston, Texas.



TABLE OF CONTENTS

Section		Page
1	INTRODUCTION AND SUMMARY	1-1
1.1	PURPOSE	1-1
1.2	DESIGN OBJECTIVES	1-1
1.3	KEY FEATURES OF SMSS CONCEPT	1-2
2	RESULTS, CONCLUSIONS, AND RECOMMENDATIONS	2-1
3	SMSS REQUIREMENTS/POTENTIAL APPLICATIONS	3-1
4	SYSTEM CONSIDERATIONS	4-1
4.1	OPTIMIZATION OF SMSS AVAILABILITY	4-1
4.2	SYSTEM SENSITIVITY	4-2
4.2.1	Measures of Sensitivity	4-2
4.2.2	Cooled Optics	4-9
4.3	SCANNING, DATA RATE, AND RELATED CONSIDERATIONS	4-11
4.4	MODULATION TRANSFER FUNCTION	4-23
4.4.1	Optical MTF	4-25
4.4.2	Array MTF	4-27
4.4.3	Charge-Coupled-Device MTF	4-32
4.5	POINTING AND IMAGE-MOTION COMPENSATION	4-32
4.6	CALIBRATION	4-36
4.7	SENSOR CONTAMINATION	4-40
5	OPTICAL SYSTEM	5-1
5.1	GENERAL CONSIDERATIONS	5-1
5.2	RECOMMENDED TELESCOPE CONFIGURATION	5-5
6	DETECTOR/CTD TECHNOLOGY AND FOCAL-PLANE DESIGN	6-1
6.1	DETECTOR MATERIALS AND TYPES	6-2
6.2	CTD SATURATION EFFECTS	6-8



TABLE OF CONTENTS (CONT.)

Section		Page
6.3	NONUNIFORMITIES IN RESPONSE OF DETECTOR ELEMENTS	6-13
6.4	FOCAL-PLANE DESIGN CONCEPT USING PRESENTLY AVAILABLE CTDs	6-19
7	FOCAL-PLANE/GIMBAL-MODULE CONSIDERATIONS AND DESIGN	7-1
7.1	FOCAL-PLANE COOLING AND CONFIGURATION	7-1
7.2	ACTIVE FOCUSING	7-10
7.3	GIMBAL MODULE	7-11
8	DATA PROCESSING AND DATA COMPRESSION	8-1
8.1	DATA-HANDLING CONCEPTS	8-1
8.2	DATA COMPRESSION	8-8
9	REAL-TIME CALIBRATION	9-1
10	GROUND SUPPORT EQUIPMENT	10-1
10.1	TARGET SIMULATOR	10-1
10.2	ELECTRONIC CHECKOUT MODULE AND AUXILIARY EQUIPMENT	10-7
Appendix A	CONSIDERATIONS RELATED TO EARTH-OBSERVATION MISSIONS	A-1
Appendix B	BACKGROUND AND CONSIDERATIONS FOR OPTICAL-DESIGN SELECTION	B-1
	REFERENCES	C-1



FIGURES

Figure No.		Page
Frontis	ARTIST'S CONCEPTION OF ORBITER-MOUNTED SMSS SYSTEM	xii
2-1	SMSS TELESCOPE-ASSEMBLY CONCEPT	2-2
3-1	SUMMARY OF SENSITIVITY REQUIREMENTS	3-3
3-2	SURFACE-RESOLUTION REQUIREMENTS	3-4
3-3	SPECTRAL-RESOLUTION REQUIREMENTS	3-5
3-4	RANGE OF EARTH RADIANCE (DESERT)	3-7
3-5	RANGE OF EARTH RADIANCE (OCEAN)	3-8
3-6	RANGE OF EARTH RADIANCE (ANTARCTIC)	3-9
3-7	CLOUD-RADIANCE LEVELS	3-10
3-8	TERRAIN-RADIANCE LEVELS	3-11
3-9	OCEAN-RADIANCE LEVELS	3-12
4-1	VARIATION OF NEAT WITH SCENE TEMPERATURE	4-5
4-2	INFLUENCE OF BACKGROUND PHOTON FLUX ON INSTRUMENT SENSITIVITY (10.5 TO 12.5 μm), SHOWING TYPICAL COOLING REQUIREMENTS	4-12
4-3	BASIC SCENE-GENERATION SYSTEMS	4-13
4-4	OSCILLATING MIRROR SCANNERS	4-14
4-5	ROTATING OBJECT-PLANE SCANNERS	4-15
4-6	ROTATING IMAGE-PLANE SCANNERS	4-16
4-7	DATA RATE VS ALTITUDE AND SURFACE RESOLUTION	4-22
4-8	THEORETICAL OPTICAL-TRANSFER FUNCTIONS	4-26
4-9	OPTICAL-TRANSFER FUNCTION, GAUSSIAN IMAGE	4-28
4-10	LINEAR-ARRAY MTF	4-31
4-11	TYPICAL LONG-WAVELENGTH CHANNEL	4-39
5-1	ALL-REFLECTIVE SCHMIDT, OPTICAL SCHEMATIC	5-2
5-2	IR DIFFRACTION-LIMITED RESOLUTION FOR 1-METER APERTURE	5-4
5-3	SMSS TELESCOPE ASSEMBLY	5-6



FIGURES (CONT.)

Figure No.		Page
5-4	ALL-BERYLLIUM PRIMARY-MIRROR MODULE	5-7
5-5	ALL-BERYLLIUM CORRECTOR-MIRROR MODULE	5-8
5-6	TELESCOPE-STRUCTURE SKELETON	5-10
5-7	TYPICAL TELESCOPE-BARREL SECTION	5-11
6-1	INFRARED-DETECTIVITY REQUIREMENTS FOR CHANNELS 8, 9, AND 10	6-9
6-2	REQUIRED D^* VS AVAILABLE D^*	6-11
6-3	ONE-DIMENSIONAL CTD SYSTEM WITH PARALLEL PROCESSING, SCHEMATIC	6-15
6-4	ELECTRONIC NONUNIFORMITY COMPENSATION	6-16
6-5	CLOCKING SEQUENCE FOR SUMMING SIGNALS FROM TWO RESOLUTION ELEMENTS	6-20
6-6	AREA-ARRAY DATA FORMAT	6-22
6-7	SHORT-WAVELENGTH FOCAL-PLANE CONCEPT	6-23/24
6-8	IRCTD HYBRID ARRAY CONCEPT	6-26
7-1	FOCAL-PLANE/GIMBAL-MODULE ASSEMBLY, COOLING AND SUPPORT DETAILS	7-5
7-2	SMSS FOCAL-PLANE/DEWAR ASSEMBLY	7-9
7-3	SMSS ACTIVE FOCUS, SCHEMATIC	7-12
7-4	PRELIMINARY LAYOUT, GIMBAL MODULE WITH "SPIDER" SUPPORT	7-14
7-5	ACTUAL-POSITION LIMIT CYCLE (WORST CASE) AND IDEALIZED IMC COMMAND AND RESPONSE	7-21
7-6	FOCAL-PLANE MOTION-COMPENSATION SERVOS (EACH AXIS), BLOCK DIAGRAM	7-22
8-1	PROCESSING ELECTRONICS, BLOCK DIAGRAM	8-2
8-2	DIGITAL SYSTEM FOR REMOVAL OF HIGH-BACKGROUND BIAS	8-4
8-3	ANALOG MODIFICATION FOR REMOVAL OF HIGH-BACKGROUND BIAS	8-5
8-4	TIMING DIAGRAM	8-6



FIGURES (CONT.)

Figure No.		Page
9-1	ONBOARD CALIBRATION, BLOCK DIAGRAM	9-2
10-1	GROUND SUPPORT SYSTEM, SMSS SIGNAL PROCESSING	10-2
10-2	INFRARED TARGET SIMULATOR, ISOMETRIC VIEW	10-3
A-1	TYPICAL SPECTRAL RESPONSE OF VEGETATION	A-4
A-2	COMBINED SIGNATURES FOR FIVE CROPS	A-4
A-3	RANGE OF VISIBLE-SCENE RADIANCE	A-7
A-4	REQUIRED VISIBLE-REGION DYNAMIC RANGE	A-8
B-1	LINEAR DIAMETER OF DIFFRACTION IMAGE OF A CIRCULAR UNOBSTRUCTED OPTICAL SYSTEM AS A FUNCTION OF FOCAL RATIO AND WAVELENGTH	B-1
B-2	APERTURE VS FABRICATION TIME FOR $\lambda/40$ RMS SURFACE	B-2
B-3	MIRROR FABRICATION VS SIZE AND FOCAL RATIO	B-2
B-4	REPRESENTATIVE TRANSMISSION (INCLUDING REFLECTION LOSSES)	B-3
B-5	REPRESENTATIVE TRANSMISSION (INCLUDING SURFACE REFLECTION)	B-4
B-6	REPRESENTATIVE REFLECTANCE OF SELECTED MIRROR COATINGS	B-6
B-7	BASIC MIRROR SYSTEMS -- I	B-8
B-8	BASIC MIRROR SYSTEMS -- II	B-8
B-9	BASIC MIRROR SYSTEMS -- III	B-9
B-10	ANGULAR-BLUR DIAMETER FOR SPHERICAL MIRROR	B-10
B-11	PARABOLOID: STOP AT MIRROR	B-10
B-12	PARABOLOID: STOP AT FOCAL PLANE	B-11
B-13	APERTURE CONFIGURATIONS FOR VARIOUS OPTICAL SYSTEMS	B-14
B-14	ALL-REFLECTIVE SCHMIDT TELESCOPE, WITH STOP AT CORRECTOR	B-16
B-15	ALL-REFLECTIVE SCHMIDT TELESCOPE: TWO CORRECTORS WITH OBJECT-PLANE SCANNING	B-17



FIGURES (CONT.)

Figure No.		Page
B-16	OFF-AXIS ALL-REFLECTIVE SCHMIDT TELESCOPE WITH STOP AT CORRECTOR	B-19
B-17	SPHERICAL MIRROR, $f/5.5$ STOP AT CENTER OF CURVATURE	B-20
B-18	CASSEGRAIN TELESCOPE WITH SCANNING MIRROR, $f/2.5$ STOP AT PRIMARY MIRROR	B-22
B-19	OFF-AXIS CASSEGRAIN TELESCOPE WITH SCANNING MIRROR, $f/2.5$ STOP AT PRIMARY MIRROR	B-23
B-20	THREE-MIRROR OPTICAL SYSTEM	B-24
B-21	SPHERICAL MIRROR WITH IMAGE-PLANE SCANNER	B-25
B-22	OFF-AXIS CONFOCAL PARABOLOIDS WITH SMALL OBJECTIVES	B-26
B-23	INTERFACE-FEASIBILITY LAYOUT, SMSS MOUNTED IN ORBITER (CROSS-SECTIONAL VIEW)	B-29
B-24	INTERFACE-FEASIBILITY LAYOUT, SMSS MOUNTED IN ORBITER (SIDE VIEW)	B-30
B-25	COMPARISON OF SURFACE PROFILES FOR REFRACTIVE AND REFLECTIVE SCHMIDT CORRECTORS	B-33
B-26	CORRECTION TERMS FOR CORRECTOR MIRROR OF REFLECTIVE SCHMIDT	B-34
B-27	INITIAL OPTIMIZATION, ALL-REFLECTIVE SCHMIDT TELESCOPE	B-37
B-28	RESULTS OF INITIAL DESIGN STUDY FOR $f/1.5$ REFLECTIVE SCHMIDT	B-38
B-29	RESULTS OF INITIAL DESIGN STUDY FOR $f/1.7$ and $f/1.8$ REFLECTIVE SCHMIDT	B-39
B-30	REFLECTIVE-SCHMIDT COMPUTER OPTIMIZATION FOR WIDE FIELD	B-41
B-31	MIRROR SIZE (APERTURE AT CENTER OF CURVATURE)	B-42
B-32	DEPTH OF FOCUS	B-43
B-33	DIFFRACTION-LIMITED RESOLUTION FOR 75-cm APERTURE	B-46
B-34	TELESCOPE IN ORBITER, CROSS SECTION (TWO SIZES)	B-48
B-35	TELESCOPE, SIDE VIEW (TWO SIZES)	B-49
B-36	THERMAL PROPERTIES OF MIRROR MATERIALS	B-54
B-37	REFLECTANCE OF ALUMINUM-COATED BERYLLIUM AT $0.6 \mu\text{m}$	B-58
B-38	REFLECTANCE OF OPTICAL COATINGS AND MIRROR SUBSTRATES	B-59
B-39	SCATTER FUNCTION OF STATE-OF-ART MIRROR SURFACES, $\lambda = 10.6 \mu\text{m}$	B-61



TABLES

Table No.		Page
2-1	SYSTEM PARAMETERS	2-4
2-2	COMPARISON OF NASA EARTH-OBSERVATION SYSTEMS	2-5
2-3	SPECTRAL-CHANNEL CHARACTERISTICS	2-6
2-4	RECOMMENDED MINIMUM DETECTIVITIES	2-6
2-5	DYNAMIC-RANGE REQUIREMENTS, DESIGN GOALS	2-7
3-1	EARTH-RESOURCES FIELDS FOR REMOTE-SENSING APPLICATIONS	3-2
4-1	OBJECT-PLANE SCANNERS	4-18
4-2	IMAGE-PLANE SCANNERS	4-20
4-3	COMPARISON OF PUSHBROOM SENSOR WITH OBJECT-PLANE SCANNER	4-24
6-1	COMMERCIALLY AVAILABLE CTD ARRAYS	6-3
6-2	IRCTD CANDIDATES FOR SMSS	6-4
6-3	RECOMMENDED BASELINE SMSS MATERIALS AND DEVICES	6-10
6-4	MAXIMUM-RADIANCE, DYNAMIC-RANGE, AND PHOTON-FLUX DATA	6-12
6-5	IRCTD PARAMETERS FOR 10.4- TO 12.5- μ m BAND	6-14
7-1	COMPARISON OF FOCAL-PLANE COOLING SYSTEMS	7-4
8-1	APPLICABLE DATA-COMPRESSION TECHNIQUES	8-10
10-1	SIMULATION CAPABILITIES AND CHARACTERISTICS	10-5

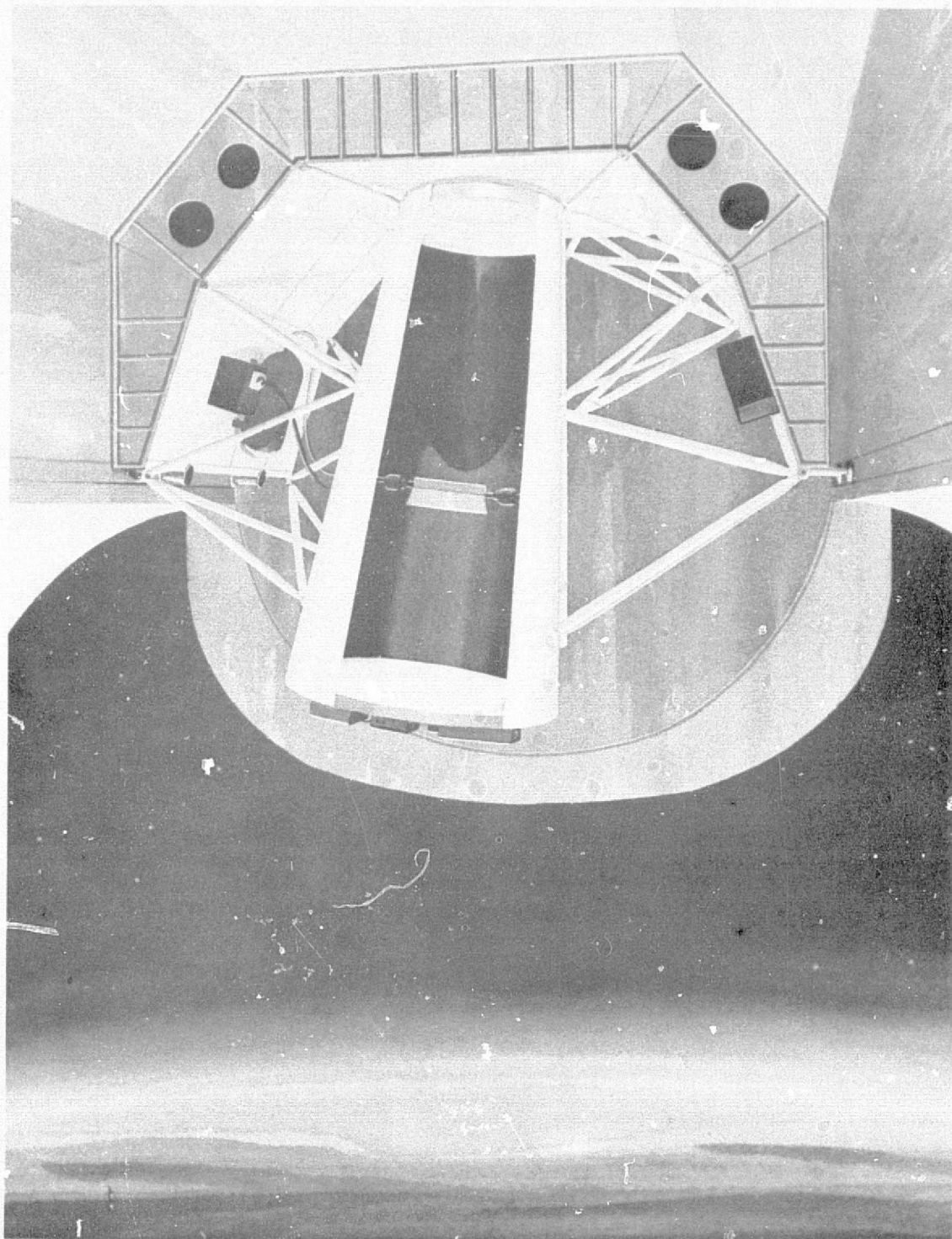


TABLES (CONT.)

Table No.		Page
A-1	CANDIDATE SPECTRAL BANDS FOR AGONOMY APPLICATIONS . . .	A-5
A-2	THEMATIC-MAPPER WAVELENGTH-BANDWIDTH COMMENTS	A-6
B-1	CHARACTERISTICS OF VARIOUS CANDIDATE OPTICAL SYSTEMS . .	B-15
B-2	APPROXIMATE WEIGHT AND SIZE OF MIRRORS	B-44
B-3	COMPARISON OF SMSS SYSTEM PARAMETERS WITH APERTURE REDUCTION	B-47
B-4	ROOM-TEMPERATURE PROPERTIES OF MIRROR-SUBSTRATE MATERIALS	B-53



CN575-011



ARTIST'S CONCEPTION OF ORBITER-MOUNTED SMSS SYSTEM



ORIGINAL PAGE IS
OF POOR QUALITY

SECTION 1

INTRODUCTION AND SUMMARY

1.1 PURPOSE

The overall purpose of the Shuttle Modular Scanning Spectroradiometer (SMSS) study has been to develop a test-bed-facility concept for earth-observation measurements. This facility is intended for use by National Aeronautics and Space Administration agencies in obtaining data for optimizing point designs (i.e., specific-purpose instruments and measurement systems), providing a quick-reaction capability for testing new concepts, obtaining basic information on new phenomena, and satisfying present and future earth-observation-data needs. The facing page shows an artist's conception of the SMSS mounted in the Space Shuttle System Orbiter vehicle.

The most important use envisioned for this test-bed facility will be in assessing the physical feasibility and utility of proposed earth-observation programs and systems--and to do so quickly and economically before considerable funds and resources are committed to the proposed programs.

Earth observations cover a large number and variety of measurements of potentially great value to industry, agriculture, government, and scientific disciplines. In many cases, however, capabilities for obtaining the desired quality and quantity of data and/or the usefulness of the data that can be obtained have not been proven or demonstrated. The SMSS test bed will allow proposed measurements, instruments, and programs to be evaluated so that resources can be allocated to missions of known value and feasibility.

1.2 DESIGN OBJECTIVES

Several basic design objectives were established to satisfy this broad test-bed purpose.



It was determined, as a fundamental consideration, that the facility should be able to take full advantage of the measurement opportunities that will be provided by the Space Shuttle System's Orbiter vehicle and should have minimum impact on the Orbiter and its resources--specifically, a facility requiring low power, little or no crew support, no heat-radiator surfaces, minimum prelaunch service and service time, and no ordnance, propellants, momentum devices, or high pressures.

Other key design objectives were

- A broad and flexible spectral coverage--i.e., a facility able to cover all the wavelength regions of interest in earth observations (from the ultraviolet out through the long-wavelength infrared) and with flexibility of choice for specific spectral operating regions within this wide band of wavelengths
- Sensitivity and spatial resolution equivalent to or better than those of existing or planned earth-observation systems.

1.3 KEY FEATURES OF SMSS CONCEPT

The foregoing objectives have been met by the design concept developed in the study. Descriptions and rationales for the choice of particular approaches, materials, devices, and designs are presented in the body of this report. Key points of the technical approach and of the resultant design are summarized below to provide an overview and prelude to the more detailed technical discussions that follow.

The choice of scanning method was the most important decision involved in the design approach. For a system to be operated from an orbital vehicle, the basic choice is between (a) a fixed array of detectors in a wide-field optical system scanning the earth by virtue of vehicle motion, as in a "pushbroom" scan, and (b) a smaller array of detectors in a narrower-field optical system scanning the earth by a combination of vehicle motion and any of a variety of mechanical-scan techniques.



The fixed-array pushbroom scan requires many detectors but can obtain greater sensitivity because of the longer scan or dwell time of a detector over a resolution element, and eliminates mechanical scanning and compensating momentum devices. The mechanical-scan approach, on the other hand, uses few detectors and minimizes the multiplexing and interconnection problems associated with large numbers of discrete detectors.

Until recently, mechanical scanning has always been preferable in applications of this type, but recent rapid advances in charge-transfer-device (CTD) technology have made large-number, high-density focal planes more feasible and practical. A pushbroom scan with a solid-state (detector/CTD) focal plane was therefore chosen for the SMSS and has been designed for flexible operation with interchangeable detector modules.

The system operates with up to ten modular arrays and with interchangeable filters on each array. The use of a large number of detectors in each array allows high sensitivity to be achieved with ordinary-quality detectors and detector materials--i.e., detectors that can be produced in high yields and at relatively low cost. Most importantly, the modular design of the focal plane makes it possible to utilize improvements and new developments from rapidly advancing detector/CTD technology with minimum system impact.

An all-beryllium reflective-Schmidt optical system was chosen for the collecting optics--reflective to permit wide spectral coverage, and all-beryllium for self-compensation of temperature effects. The optical system provides a wide field of view (15°), a high resolution ($66 \mu\text{r}$), a large collecting aperture (75 cm), and light weight [approximately 90 kg (≈ 200 lb) including mirror mounts and housing structure].

Additional features particularly pertinent to the purposes and design objectives of the SMSS facility include the following:



- An automatic optical-focus system
- A gimballed focal plane for compensation of perturbations in vehicle motions, and consequent minimization of ground data-processing requirements
- An open-cycle, cryogen-package cooling system that can easily be adapted to the cooling requirements of various types of detectors--i.e., a system that needs no electrical power or radiating surfaces
- A calibrating system that is an integral part of the focal plane, complete with secondary sources (light-emitting diodes) designed to allow sequential calibration of detector channels during measurement operations and for convenient test and checkout procedures
- Digital formatting and recording of data for efficient data reduction and analysis.

In summary, the SMSS program to date has yielded a facility concept with a wide and flexible range of measurement capabilities, designed for minimum impact on the Orbiter vehicle and to take maximum advantage of the measurement opportunities to be provided by the Shuttle program. The facility is intended as a test bed for NASA agencies--a tool that can contribute greatly in both scientific and economic evaluation and management of earth-observation measurement programs.



Section 2

RESULTS, CONCLUSIONS, AND RECOMMENDATIONS

The modular design generated during this study and recommended for further development provides for easy Shuttle Orbiter mounting, in-flight re-configuration, and adaptability for a variety of potential earth-observation measurement and data-acquisition missions involving the ultraviolet, visible, and infrared (IR) regions of the spectrum. The presently configured spectral range from 0.45 to 12.5 μm can readily be extended for operation of shorter and longer wavelengths.

An artist's conception of the mounted SMSS telescope assembly is shown in the frontispiece. Figure 2-1 presents a schematic diagram, and detailed requirements are provided in the preliminary specification (Ref. 2-1).

The system features reflective Schmidt optics and will normally operate at altitudes of 185 to 460 km (100 to 250 nmi). It incorporates the following subsystem modules: focal-plane/Dewar assembly, focal-plane-gimbal assembly, aperture closure, sun and albedo shade, primary mirror and mount, corrector mirror and mount, cryogen-storage unit, and electronic data-handling subsystem.

The modular, fixed, linear, detector arrays are designed to cover a swath width up to 15° from the Orbiter in a pushbroom type of scan that is accomplished by vehicle motion alone. Radiated energy is collected in ten visible and infrared channels of 4000 detector elements each. Analog signals proportional to this radiation are generated and shifted out for processing by charge-transfer devices. After analog-to-digital (A/D) conversion, the data from any six of the ten channels are recorded simultaneously on a space-borne high-density tape recorder for subsequent processing.





875-180°

ORIGINAL PAGE IS
OF POOR
QUALITY

2-2

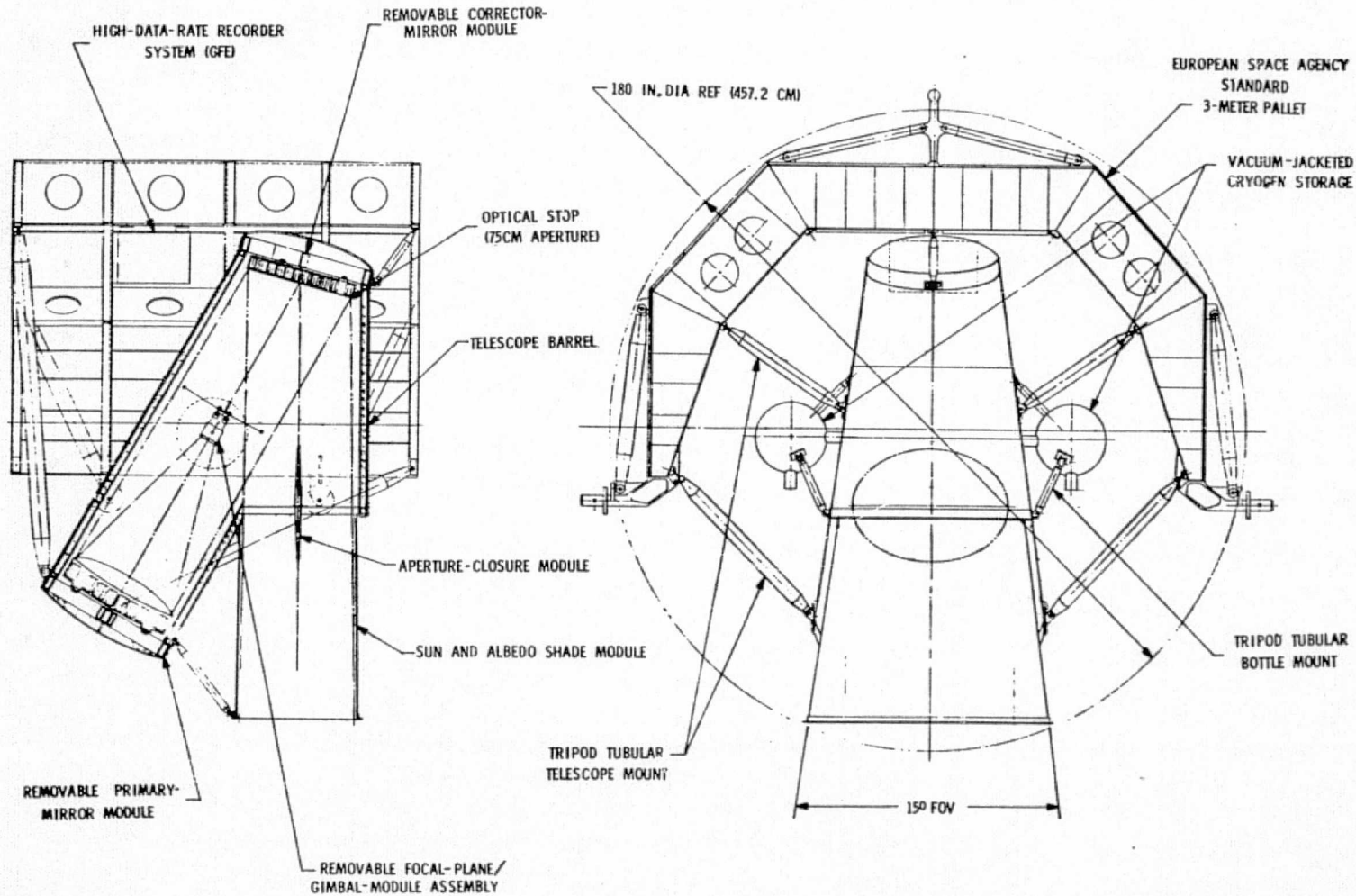


FIGURE 2-1 SMSS TELESCOPE-ASSEMBLY CONCEPT

The performance characteristics conceived for the SMSS are set forth in Table 2-1, and comparisons with other existing or planned NASA earth-observation systems are provided in Table 2-2.

As conceived, the SMSS reproduces information from each scan at a nominal resolution of 66 μ r for all ten spectral channels. The relative spectral-response characteristics of the ten channels are indicated in Table 2-3. They apply to the entire SMSS, including optics, filters, and detectors.

The required sensitivity for Channels 1 through 7 (visible light and near-infrared) is measured in terms of noise-equivalent reflectance difference (NE Δ p), which is defined as the change in scene reflectance (compared with a given average reflectance) that will cause a change in the peak signal amplitude equal to the root-mean-square (rms) noise. Because of atmospheric-noise effects (discussed in paragraph 4.2.1), NE Δ p values are limited to approximately 0.5%. As a design goal, changes in spectral radiance corresponding to this NE Δ p are not to exceed the worst-case values (i.e., when the solar elevation is 20 $^{\circ}$) specified in Table 2-4, and the detectivity (D*) values are to equal or exceed those given there. (These D* values are based on tentative SMSS parameters for aperture, angular resolution, focal ratio, dwell time, and electronic and optical efficiency).

The sensitivities of Channels 8 through 10 (infrared) are measured in terms of the noise-equivalent temperature difference (NEAT), which is defined as the change in scene temperature (about a given temperature) that will cause a change in the signal amplitude equal to the rms noise. As a design goal, the NEAT is not to exceed 0.1 $^{\circ}$ K in any of these channels for an extended scene temperature of 280 $^{\circ}$ K. The detectivities for this temperature are to equal or exceed those specified in Table 2-4.

The total dynamic range required for a sensor with an NE Δ p of 0.5% over a range of illumination conditions corresponding to solar-elevation angles of 20 to 75 $^{\circ}$ can be determined as extending between the change in



TABLE 2-1 SYSTEM PARAMETERS

Parameter	Value
Focal ratio, f/no.	f/1.7
Instantaneous field of view	66 μ r
Swath width	15 $^{\circ}$
Detector-element size	84 x 84 μ m (0.0033 x 0.0033 in.)
No. of detector elements per spectral channel	4000
No. of channels	10 (6 active)
Integration time at altitude of 185 km (100 nmi)	1.62 msec
Video encoding	8 bits
Mission data rate for one sample per dwell time (t_d) at 185-km altitude	118.5 Mbps
Optics	
Aperture	75 cm
Focal length	127.5 cm
Spectral range	0.45 to 12.5 μ m
Efficiency	\geq 50%
Noise-equivalent reflectance difference, NE $\Delta\rho$ (atmospheric-noise-limited)*	0.5%
Noise-equivalent temperature difference, NE ΔT	0.1 $^{\circ}$ K
Calibration	Two-level, offset removed, linearized
* See paragraph 4.2.1.	





TABLE 2-2 COMPARISON OF NASA EARTH-OBSERVATION SYSTEMS

Parameter	Skylab S-192	ERTS-MSS (No IR)	LANDSAT-D EOS-TM Concept	SMSS Concept
Number of spectral channels	13	4	7	10 (6 active)
Visible bandwidth, $\Delta\lambda$ (μm)	0.05	0.1	0.06	0.06
Angular resolution, θ (μr)	182	86	{ 42 visible 126 IR }	66
Swath width (degrees)	9	11.5	15	15
Type of scan	Conical	Oscillating mirror	Oscillating mirror	Pushbroom
No. of detectors/channel	1	6	{ 12 visible 4 IR }	4000
Scan efficiency (%)	30	44	85	99
Dwell time, t_d (μsec)	9.6	9	{ 5 visible 15 IR }	1620
Mission data rate (Mbps)	10.8 ?	15	80	118.5
Aperture, D (cm)	43	23	46	75
Focal ratio, f/no.	f/1.5	f/3.6	f/3	f/1.7
Relative system sensitivity, $(f/\text{no.})/\Delta\lambda D \theta\sqrt{t_d}$	8.7	43	{ 81 visible 16 IR }	1

2-5

TABLE 2-3 SPECTRAL-CHANNEL CHARACTERISTICS

Channel No.	Wavelength (μm)		Maximum Edge Slope (μm) [†]
	Cut-On	Cut-Off	
1	0.45 \pm 0.01	0.52 \pm 0.01	0.04
2	0.52 \pm 0.01	0.60 \pm 0.01	0.04
3	0.63 \pm 0.01	0.69 \pm 0.01	0.04
4 ^{††}	0.69 \pm 0.01	0.75 \pm 0.01	0.06
5 ^{††}	0.80 \pm 0.01	0.95 \pm 0.01	0.06
6	1.55 \pm 0.02	1.75 \pm 0.02	0.10
7	2.05 \pm 0.02	2.35 \pm 0.02	0.10
8	3.5 \pm 0.04	5.0 \pm 0.04	0.20
9	8.2 \pm 0.1	9.3 \pm 0.1	0.40
10	10.4 \pm 0.1	12.5 \pm 0.1	0.40

[†]Wavelength interval between 5% absolute transmittance and 70% peak transmittance.

^{††}The LANDSAT-D Thematic Mapper Technical Working Group in Ref. 2-2 suggests the use of 0.74 to 0.80 and 0.80 to 0.91 μm for channels in this spectral region to study vegetation in particular.

TABLE 2-4 RECOMMENDED MINIMUM DETECTIVITIES

Channel No.	Spectral Band (μm)	Spectral Radiance Change [†] ($\text{W}/\text{m}^2\text{-sr}$)	Required D* ($\text{cm-Hz}^{1/2}/\text{W}$)
Visible and Near-Infrared Spectrum			
1	0.45 - 0.52	0.010	1.9×10^{10}
2	0.52 - 0.60	0.022	8.7×10^9
3	0.63 - 0.69	0.024	8.0×10^9
4	0.69 - 0.75	0.025	7.7×10^9
5	0.80 - 0.95	0.06	3.2×10^9
6	1.55 - 1.75	0.014	1.4×10^{10}
7	2.05 - 2.35	0.004 ^{††}	4.8×10^{10}
Infrared Spectrum			
8	3.5 - 5.0	(0.85) ^{†††}	5.6×10^{10}
9	8.2 - 9.3	(7.25) ^{†††}	1.3×10^{10}
10	10.4 - 12.5	(14.5) ^{†††}	8.2×10^9

[†]Worst case, Channels 1-7: solar elevation = 20°, equivalent to NEAp of 0.5%, as set forth in Ref. 2-2.

^{††}Extrapolation of data in Ref. 2-2.

^{†††}Channels 8-10: radiance ($\text{W}/\text{m}^2\text{-sr}$) for 280°K.

scene radiance corresponding to a 0.5% NEAp for a 20° solar elevation and the maximum radiance viewed at maximum reflectance (60%) and a 75° solar elevation.

Table 2-5 specifies the maximum radiance, the minimum change in radiance, and the resulting dynamic range for the shorter wavelengths as well as the longer. In the latter case the dynamic range is between the change in scene radiance corresponding to a 0.1°K NEAT and the radiance of a nominal 320°K maximum scene temperature.

TABLE 2-5 DYNAMIC-RANGE REQUIREMENTS, DESIGN GOALS

Channel No.	Spectral Band (μm)	Radiance (W/m ² -sr)		Dynamic Range
		Maximum*	Minimum Change	
Visible and Near-Infrared Spectrum				
1	0.45 - 0.52	21	0.010	2100
2	0.52 - 0.60	24	0.022	1100
3	0.63 - 0.69	17	0.024	600
4	0.69 - 0.75	15	0.025	600
5	0.80 - 0.95	30	0.060	500
6	1.55 - 1.75	7	0.014	500
7	2.08 - 2.35	3	0.004	800
Infrared Spectrum				
8	3.5 - 5.0	3.8	0.00347	1100
9	8.2 - 9.3	21.0	0.0152	1380
10	10.4 - 12.5	25.8	0.0235	1100
* Channels 1-7: 75° solar-elevation, albedo = 0.6 from Ref. 2-2.				

The preliminary design provides internal sources for periodic system calibration at discrete input-radiance levels in order to maintain radiometric-measurement accuracy for the entire mission. The sources are linear arrays of light-emitting diodes (LEDs) mounted under the spectral filters and between the staggered CTD arrays. The calibration references will also be used to maintain a constant overall gain and reference level.



Image-motion compensation (IMC) is included in the SMSS to accommodate the pitch, yaw, and roll drift of the Orbiter. When all Orbiter RCS thrusters are operational, the drift rate in the three axes will be of the order of $0.01^\circ/\text{sec}$, which will result in a ground-scene drift of one resolution element or less in 0.29 sec. The IMC will be coupled to an Orbiter-furnished attitude signal to achieve SMSS pointing equal to or less than $6.6 \mu\text{r}$ (1.36 seconds of arc, or 0.1 IFOV).

The SMSS design permits interfacing with the standard 3-m Space-lab pallet as shown in Figure 2-1. The pallet carries SMSS electrical-power, monitoring, and control leads to the Orbiter, and distributes SMSS loads to the Orbiter longeron and the payload-bay keel. The mount must accommodate acceleration, random vibration, and acoustic loads without degradation of the required performance. The SMSS housing is to have an inner frame of beryllium, graphite-reinforced epoxy, or other suitable material whose thermal-expansion coefficient can be tailored to match that of the beryllium mirrors. Thus, telescope defocusing will not occur over the operating-temperature range.

The frame will be covered on the inner and outer surfaces with a beryllium (or equivalent) skin, and the space between the skins will be filled with insulating material having a low thermal-conduction coefficient.

The telescope housing and structure design permits removal and replacement of the focal-plane/gimbal module without removal of the telescope from the pallet. It will assure accurate positioning of the focal-plane/gimbal module and retention of system focus and alignment within the limits provided by the active focus mechanism.

Recent advances in optical-manufacturing techniques and in the multiplexing of large numbers of data channels permit this innovative SMSS design, which may well be considered the forerunner of a new group of earth-observation sensors with solid-state scan systems. The preliminary design covered in succeeding sections is responsive to presently envisioned earth-observation-data needs and provides capabilities for ready modification to meet future requirements at modest cost.



Section 3

SMSS REQUIREMENTS/POTENTIAL APPLICATIONS

The program efforts concerned with phenomenology, objectives, and definition of requirements showed that the SMSS can provide enhanced performance for a variety of earth-observation missions. Table 3-1 (based on Ref. 3-1) categorizes areas of interest for such missions.

When consideration was given to such mission requirements as spectral and spatial resolution, spectral bands, coverage/swath width, and field of view, it was found that a modular sensor can have interchangeable detector arrays, selected on each flight to satisfy different measurement needs. This approach is more cost-effective than deploying multiple sensors on different unmanned spacecraft. The SMSS is therefore ideally suited for use as a flexible research facility to determine the feasibility of performing desired measurement missions from a remote sensor in space, or for data-acquisition missions that require high spatial and spectral resolution measurements on an occasional basis.

An extensive analysis of potential SMSS earth-observation applications was not undertaken. It would have been beyond the scope of this program, as well as duplicating work underway elsewhere (e.g., the General Electric Company program reported in Ref. 3-1). The survey that was undertaken to provide a basis for the definition of SMSS requirements is summarized below in the representative areas of agronomy, atmospheric physics, atmospheric pollution, hydrology, and geology.



TABLE 3-1 EARTH-RESOURCES FIELDS FOR REMOTE-SENSING APPLICATIONS

General Field	Area of Interest
Earth Sciences	
Geology	Geochemistry Mineralogy Pedology Seismology Lithology Volcanology
Geography	Physiography Demography Cartography Geodesy
Hydrology	Limnology
Oceanography	Global and coastal zone (physical, chemical, biological) Coastal zone
Life Sciences	
Agronomy Forestry	Rangelands Grasslands
Ecology	
Environmental quality	Air pollution Water pollution Land pollution

Figures 3-1 through 3-3 (derived from Ref. 3-2) summarize the sensitivity, surface-resolution, and spectral-bandwidth ranges considered desirable for a remote-sensing system for earth observations in various broad categories. They illustrate the need for a facility that has high sensitivity as well as capabilities for (a) reconfiguration to permit exchange of spectral resolution for sensitivity, and (b) the selection of spectral bands for specific missions and observations. The SMSS facility that has been conceived and is described in this report can accommodate a large majority of the earth observations currently envisioned.

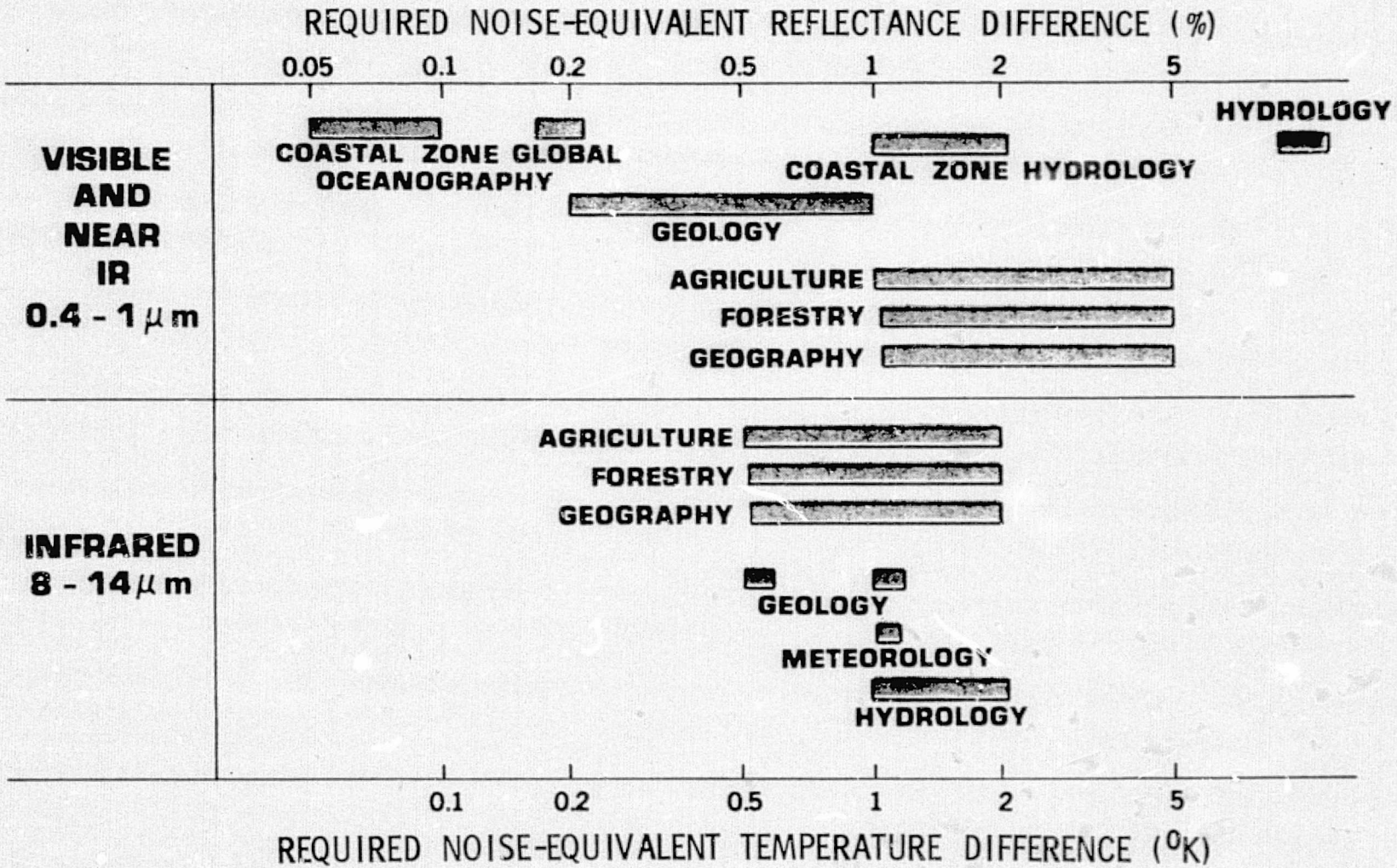
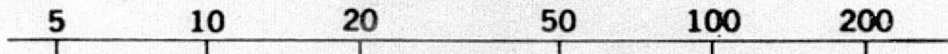


FIGURE 3-1 SUMMARY OF SENSITIVITY REQUIREMENTS



SURFACE RESOLUTION (METERS)



AGRICULTURE, FORESTRY, GEOGRAPHY



COASTAL ZONE



GEOLOGY



METEOROLOGY



**HYDROLOGY, COASTAL ZONE,
GEOGRAPHY, AGRICULTURE,
FORESTRY, GEOLOGY**



**HYDROLOGY, COASTAL ZONE,
GLOBAL OCEANOGRAPHY,
GEOGRAPHY, AGRICULTURE,
FORESTRY, GEOLOGY**



COASTAL ZONE



**GEOLOGY, METEOROLOGY
COASTAL ZONE,
GLOBAL
OCEANOGRAPHY,
GEOLOGY**

FIGURE 3-2 SURFACE-RESOLUTION REQUIREMENTS



SPECTRAL BANDWIDTH (μm)

0.01

0.1

1.0

VISIBLE

3-5

 **WATER POLLUTION, OCEANOGRAPHY, COASTAL ZONE**

 **FORESTRY, AGRICULTURE, GEOGRAPHY**

 **HYDROLOGY, GEOLOGY**

 **METEOROLOGY**

INFRARED

GEOLOGY, COASTAL ZONE, OCEANOGRAPHY 

FORESTRY, AGRICULTURE, GEOGRAPHY, 
METEOROLOGY

 **GEOLOGY**

FIGURE 3-3 SPECTRAL-RESOLUTION REQUIREMENTS

The extreme ranges of infrared radiance (desert, ocean, Antarctic) and of visible radiance (sunlit clouds, terrain, and ocean) are shown in Figures 3-4 through 3-9 (derived from Ref. 3-3).

Considerations related to earth-observation missions are detailed in Appendix A.





NIMBUS 4 IRIS DATA

3-7

RADIANCE
(10^{-3} watts/sr-m²-cm⁻¹)

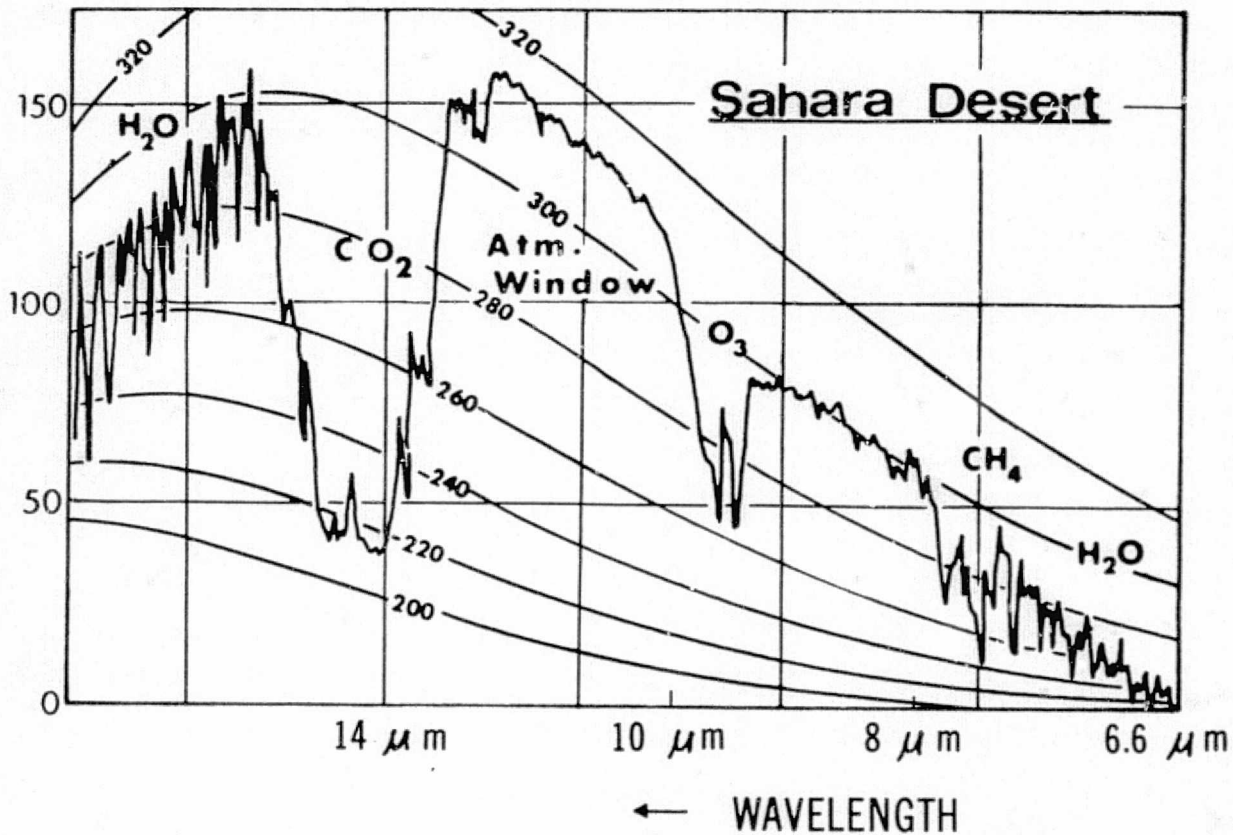


FIGURE 3-4 RANGE OF EARTH RADIANCE (DESERT)



275-1121

NIMBUS 4 IRIS DATA

3-8

RADIANCE
(10^{-3} watts/sr-m²-cm⁻¹)

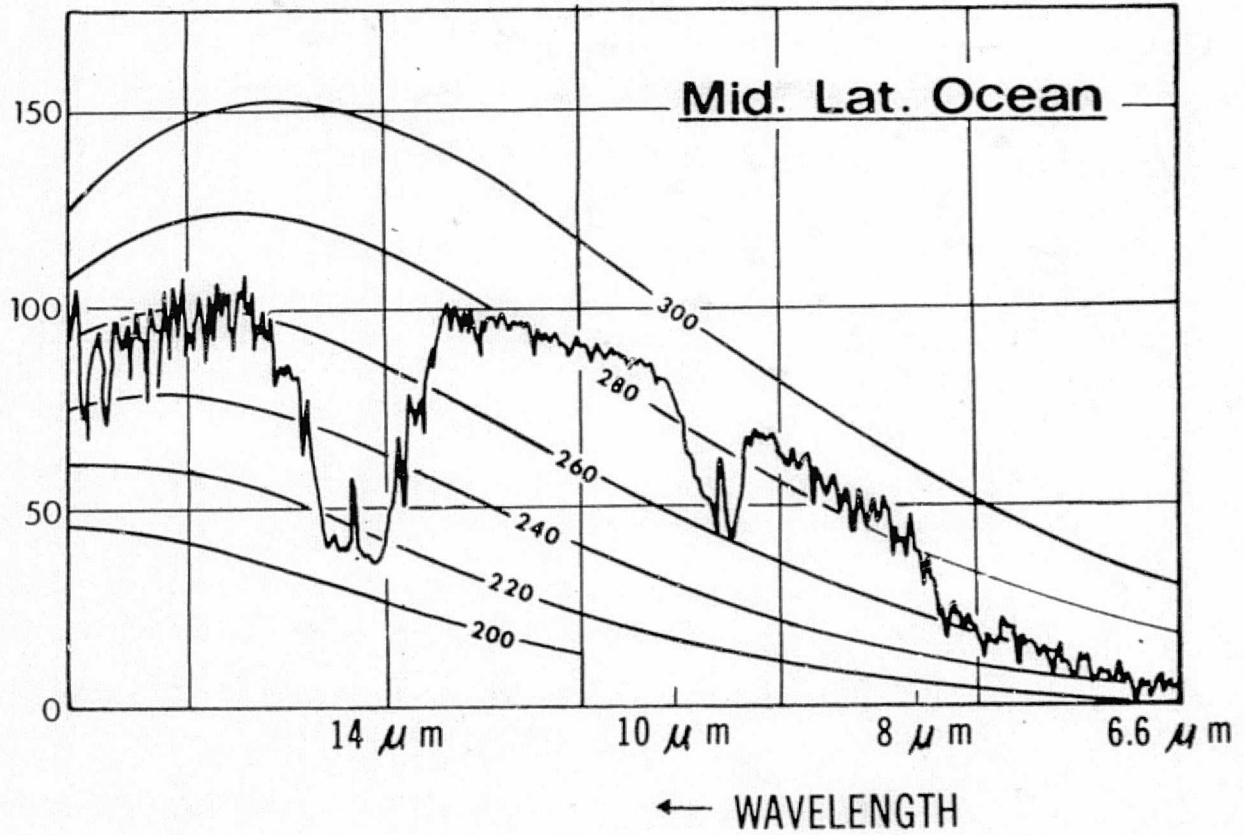


FIGURE 3-5 RANGE OF EARTH RADIANCE (OCEAN)

Report 5231



NIMBUS 4 IRIS DATA

3-9

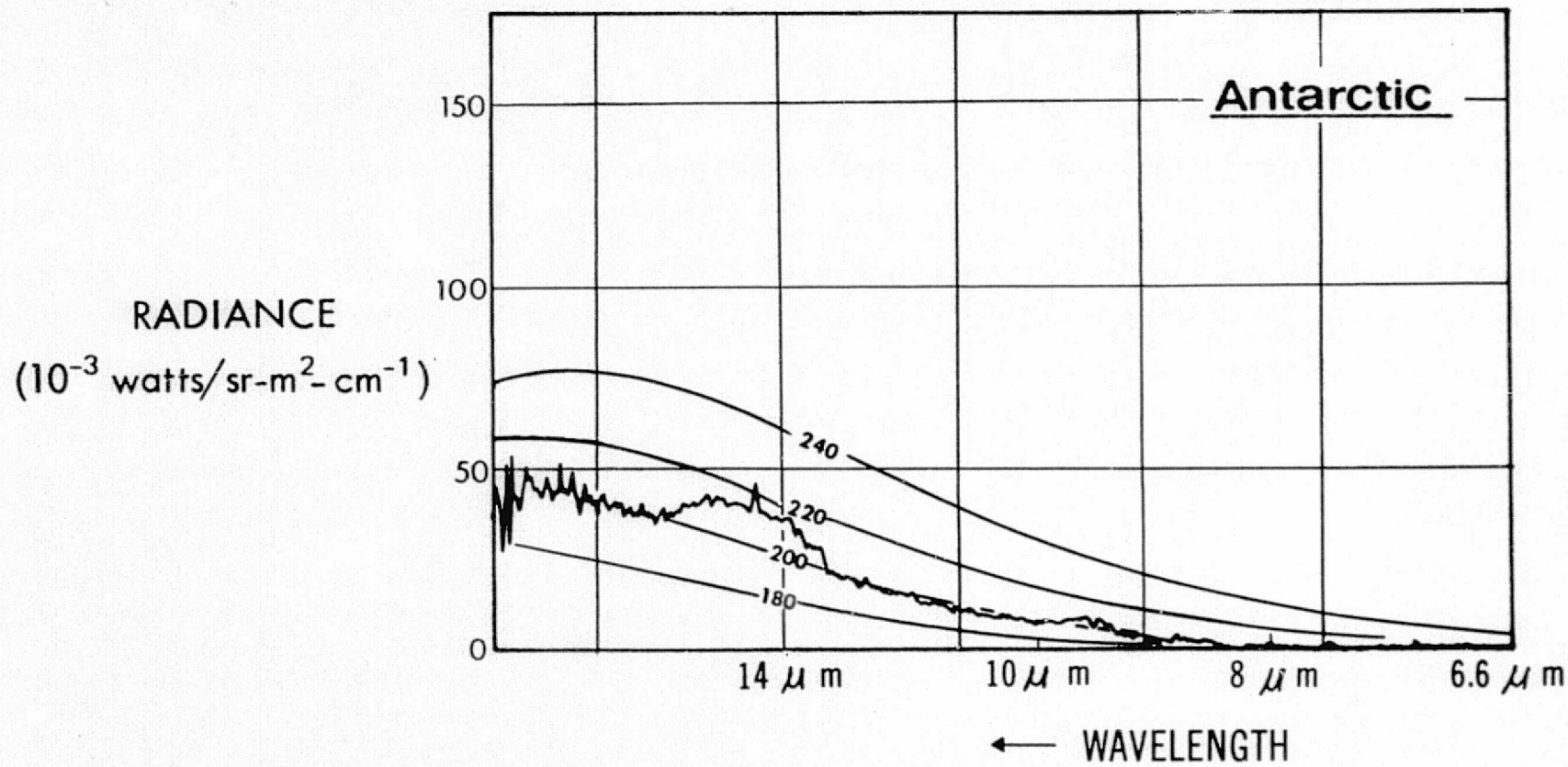


FIGURE 3-6 RANGE OF EARTH RADIANCE (ANTARCTIC)

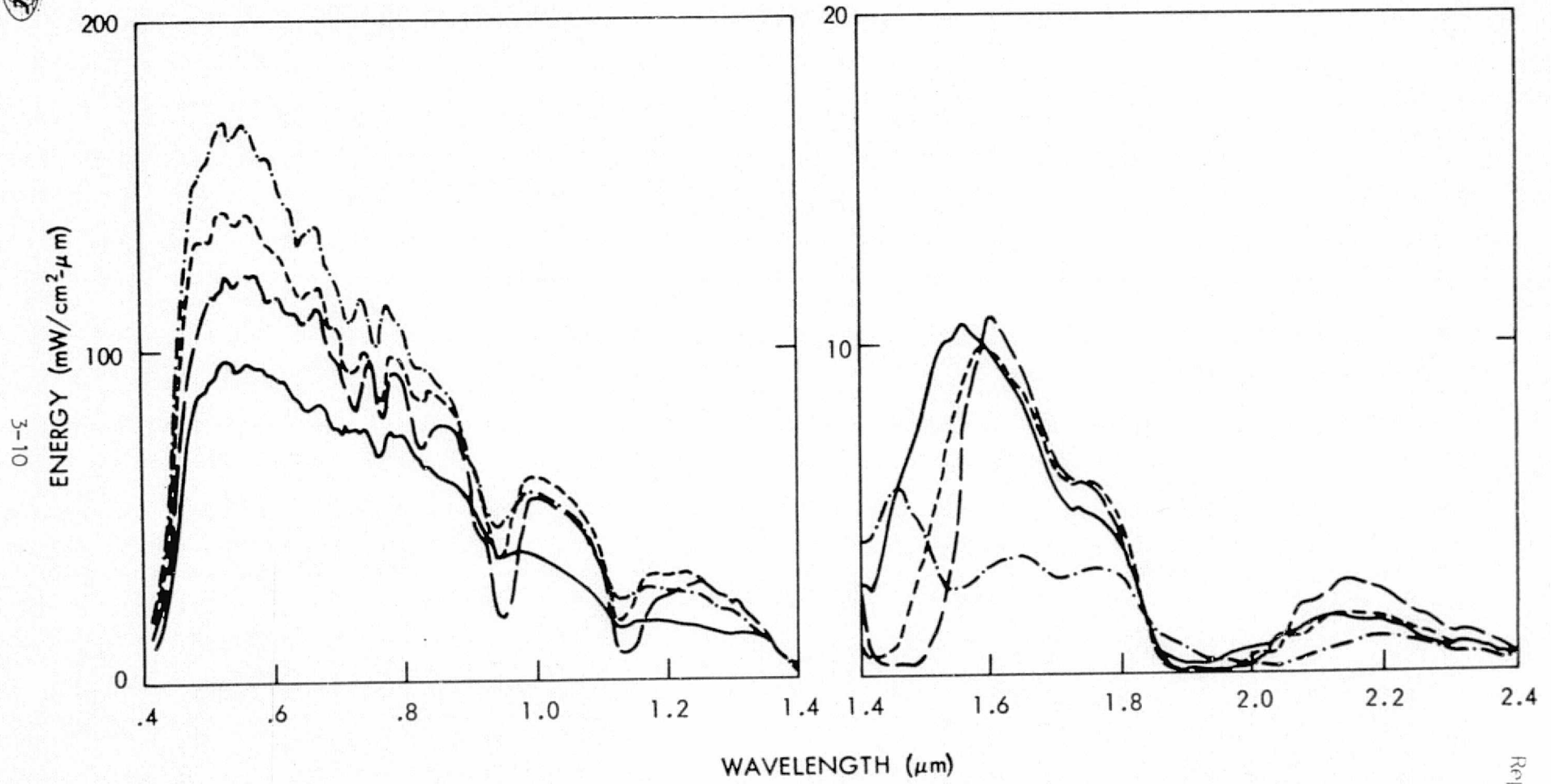


FIGURE 3-7 CLOUD-RADIANCE LEVELS

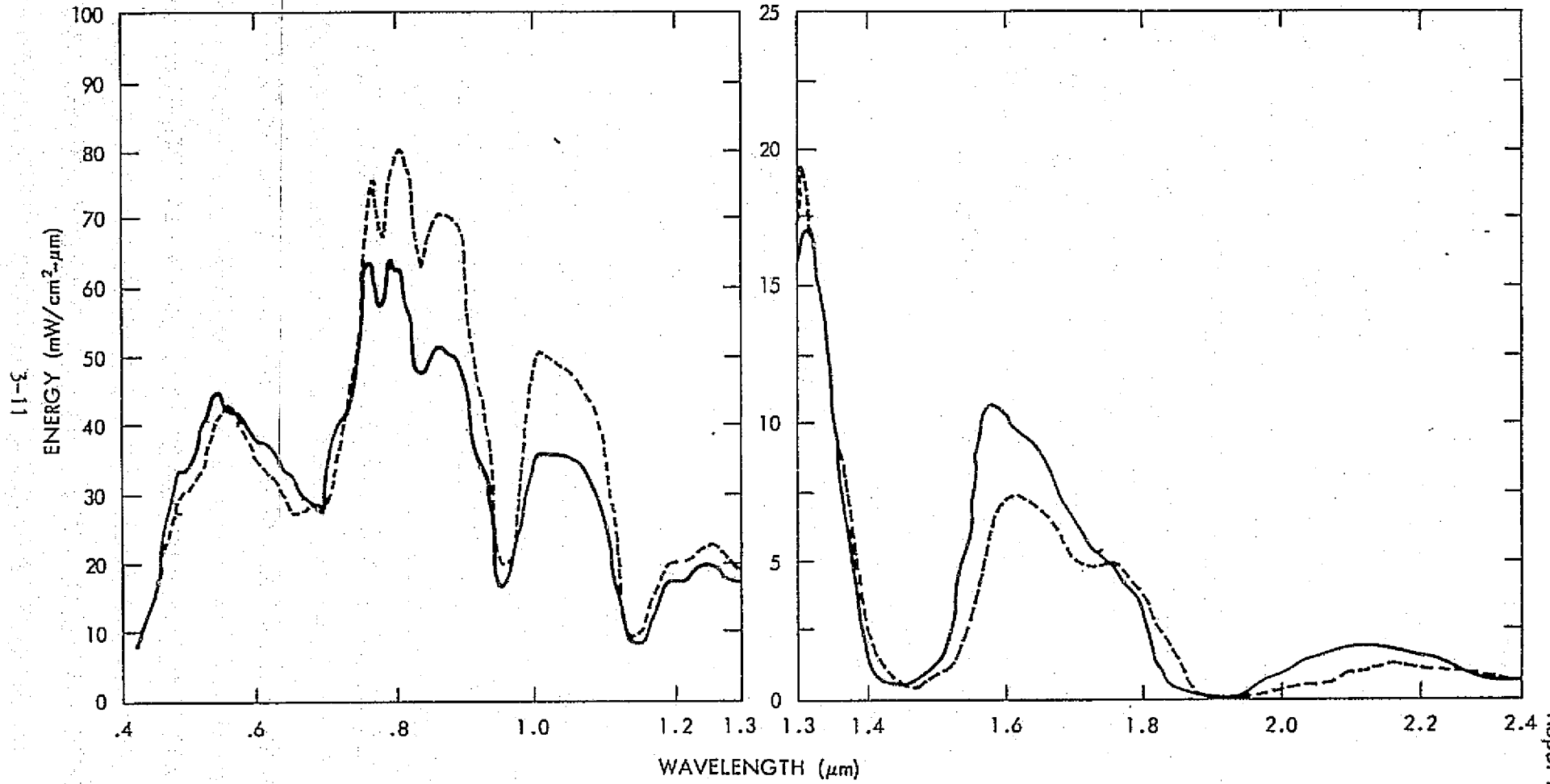


FIGURE 3-8 TERRAIN-RADIANCE LEVELS



275-1133

3-12

ENERGY
(mW/cm²-μm)

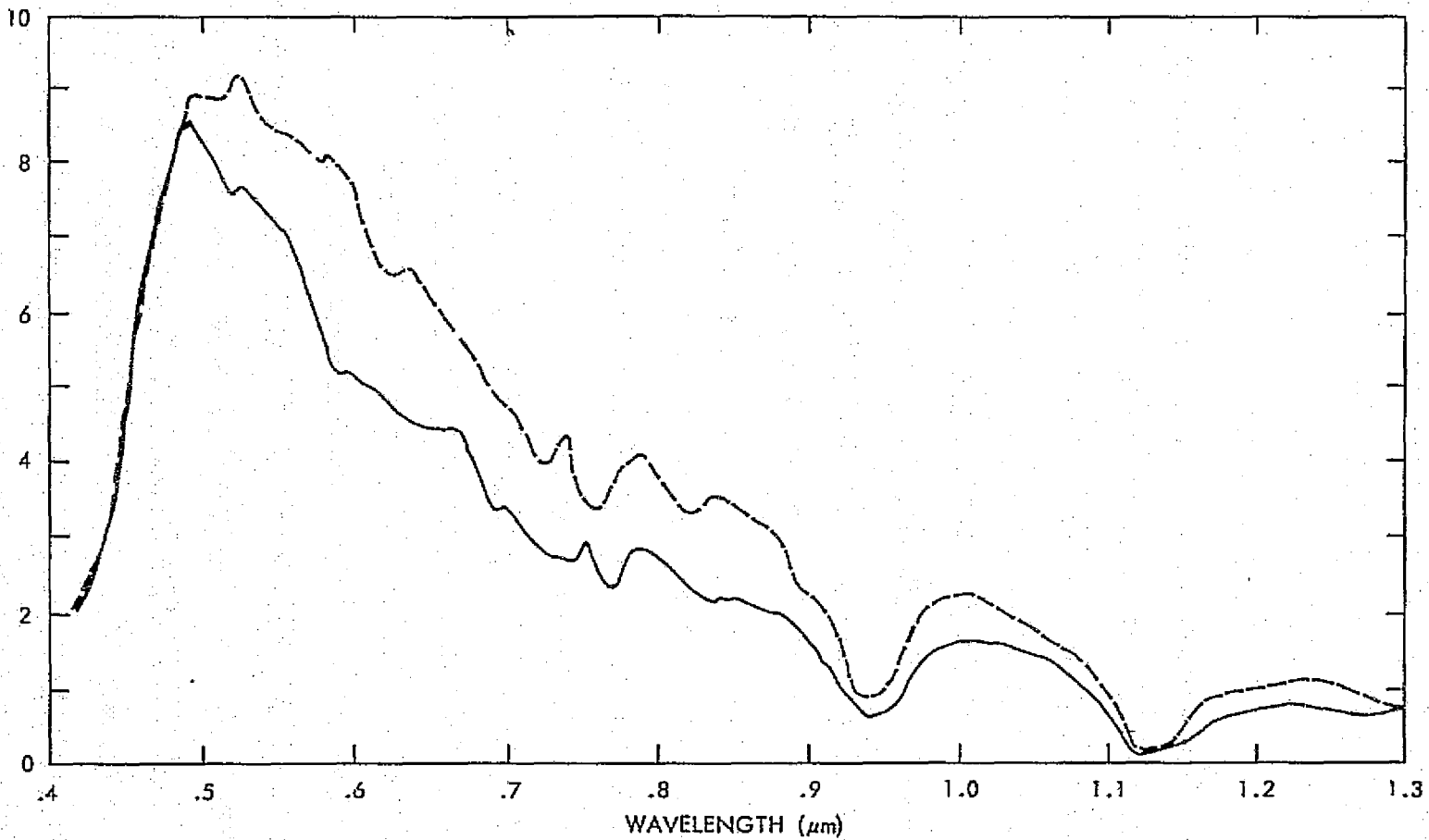


FIGURE 3-9 OCEAN-RADIANCE LEVELS

Section 4

SYSTEM CONSIDERATIONS

The key objectives of maximum availability, broad spectral coverage, and high spatial resolution are addressed below as they influence SMSS system design. Succeeding paragraphs discuss optimization of test-bed availability, factors affecting sensitivity requirements, and scanning techniques and the basis for selection of the pushbroom system. They also consider other requirements including detector size (instantaneous field of view), data-rate limitations, swath width, and modulation transfer function, as well as pointing and image-motion compensation. In addition, a method for in-flight radiometric calibration is presented, and potential system contamination is discussed.

4.1 OPTIMIZATION OF SMSS AVAILABILITY

A major factor driving development of a design concept for the SMSS was that of optimized availability to permit its use on a multiplicity of missions. This consideration made it apparent that the SMSS must be as nearly self-contained as possible and should require minimum support from the Orbiter or Spacelab crew. In addition, it should be as light as practical, occupy a minimum length of the payload bay, and be mounted directly to Orbiter retention points or to a standard Spacelab pallet.

Light weight and short length will permit SMSS installation at a variety of stations in the Orbiter's payload bay without significantly affecting the center of gravity. It might even prove desirable to use the SMSS for ballast or center-of-gravity adjustment.

A self-contained unit will require minimum support during launch and countdown operations. Ease of installation and lack of interference with other equipment will permit SMSS inclusion as a piggyback payload on a large percentage of flights.



The nominal overall landing-payload weight of 14,500 kg (32,000 lb) can impose a restriction on piggyback-type payloads, which must be retained in the Orbiter and landed. Maintaining the lightest system possible can significantly reduce the impact of that restriction.

The SMSS study goals therefore included a system that can be operated essentially independently of the Orbiter or Spacelab, will introduce no special operator-safety requirements (e.g., monitoring of momentum wheels or pressure vessels), will not contaminate the payload compartment with excessive gas venting, and will be protected from exhaust gases and effluents.

The tape-recording equipment should be capable of installation in the SMSS structure so that it is part of the self-contained unit. If the recorder must operate under essentially earth-ambient conditions, an isolation shroud (Spacelab igloo) should be considered. This feature will permit the SMSS to be carried on the Space Tug type of mission when the Spacelab is not carried or when the Spacelab experiment load does not permit SMSS-mission support.

Because zero-gravity space processing is contemplated for some Spacelab missions, the SMSS must be designed to reduce vibration to a very low level (10^{-4} g) if the SMSS experiment is to be run concurrently with space-processing experiments. Solid-state scanning is optimum with respect to this constraint.

4.2 SYSTEM SENSITIVITY

4.2.1 Measures of Sensitivity

Spectroradiometer sensitivity, another primary consideration in SMSS design, is most generally described in terms of noise-equivalent irradiance or flux density at the aperture (NEI or NEFD, respectively), expressed in watts per square centimeter in each spectral band. In earth-resources missions, however, it is often useful to apply the concepts of noise-equivalent temperature difference (NEAT) for infrared wavelengths, and

of noise-equivalent reflectance difference (NE $\Delta\rho$) for visible wavelengths. These measures of sensitivity and their application to predictions useful in conceptual design are discussed below.

The signal-to-noise level (S/N) of a spectroradiometer can be expressed as

$$\frac{S}{N} = \frac{P}{NEP} = \frac{\text{radiant power on detector}}{\text{noise-equivalent power}} = \frac{N_{\Delta\lambda} \theta^2 (\pi D^2/4) K_o}{d \sqrt{\Delta f/K_e} D_\lambda^*} \quad (4-1)$$

where

$N_{\Delta\lambda}$ = scene radiance in the $\Delta\lambda$ spectral band

θ = angular resolution (IFOV of one detector element)

$\pi D^2/4$ = collecting area of optics of diameter D

K_o = optical efficiency

d = detector size (assumed square) = $(f/\text{no.}) D\theta$

$f/\text{no.}$ = focal ratio

Δf = information bandwidth = $0.5 \times$ dwell time (t_d) of point source = $t_d/2$

K_e = electronic efficiency

D_λ^* = specific detectivity at wavelength of interest (λ)

Substituting and rearranging,

$$\frac{S}{N} = \frac{\pi N_{\Delta\lambda} \theta D K_o K_e D_\lambda^* \sqrt{2t_d}}{4 (f/\text{no.})} \quad (4-2)$$

The thermal resolution or system sensitivity in terms of NE ΔT can be estimated by taking S/N for the difference in target radiance from the background level, $\Delta N_{\Delta\lambda}$, which is approximately $\left(\frac{\partial N_{\Delta\lambda}}{\partial T}\right)_T \Delta T$ if $\Delta T \ll T$,

where T = temperature. By definition, NEAT is the value of ΔT when S/N is unity; it can be expressed as

$$\text{NEAT} = \frac{4 (f/\text{no.})}{\pi (dN_{\Delta\lambda}/dT) \theta D K_o K_e D_{\lambda}^* \sqrt{2t_d}} \quad (4-3)$$

The variation of NEAT with scene temperature and spectral region is shown in Figure 4-1.

As an alternative to NEAT, earth-survey systems can be compared by using the noise-equivalent radiance (NER) in a spectral band--i.e., the radiance providing a signal-to-noise ratio of unity. This radiance can be considered to be emitted by a blackbody at a noise-equivalent temperature designated as NET. The SMSS signal-to-noise ratio given in Equation (4-2) is unity for

$$\text{NER} = \frac{4 (f/\text{no.})}{\pi \theta D K_o K_e D_{\lambda}^* \sqrt{2t_d}} \quad (4-4)$$

For a pushbroom system of the type considered for the SMSS,

$$\theta = 66 \mu\text{r}$$

$$D = 75 \text{ cm}$$

$$K_o = 0.5$$

$$K_e = 0.8$$

$$D_{\lambda}^* = 8.2 \times 10^9 \text{ cm-Hz}^{1/2}/\text{W} \text{ for the longest-wavelength band (10.4 to 12.5 } \mu\text{m) when NEAT} = 0.1^{\circ}\text{K}$$

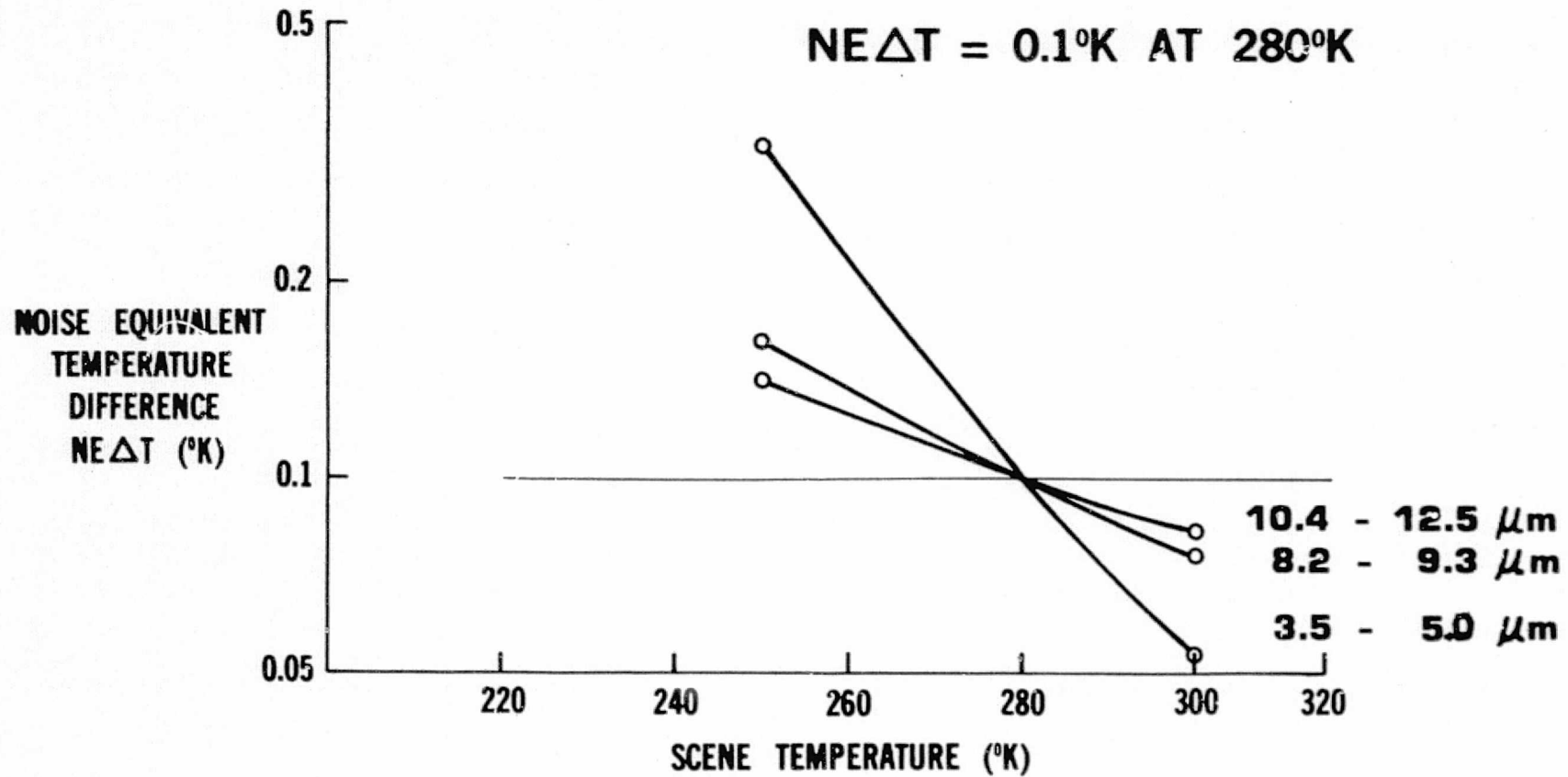
$$t_d = 1.62 \text{ msec}$$

$$f/\text{no.} = 1.7$$





4-5

FIGURE 4-1 VARIATION OF NE Δ T WITH SCENE TEMPERATURE

With these values,

$$\text{NER} \cong 2.34 \times 10^{-6} \text{ W/cm}^2\text{-sr}$$

Reference to a blackbody slide rule or tables reveals that the related NET is about 114°K. At this NET, the radiance of a blackbody in the 10.4- to 12.5- μm band can be computed as follows (where H represents blackbody emittance):

$$\frac{H}{\pi} \left(\frac{H_{0-12.5 \mu\text{m}}}{H} - \frac{H_{0-10.4 \mu\text{m}}}{H} \right) = \frac{9.6 \times 10^{-4} (0.0095 - 0.0020)}{\pi} = 2.29 \times 10^{-6} \text{ W/cm}^2\text{-sr}$$

An expression similar to that for NEAT is derivable for $\text{NE}\Delta\rho$, which can be used as a measure of system sensitivity in the visible spectrum. The signal-to-noise ratio for a sunlit scene can be expressed as

$$\frac{S}{N} = \frac{H_d}{H_o} = \frac{\text{detector irradiance}}{\text{noise-equivalent irradiance}} = \frac{\pi \rho H_s K_o K_e / [4(f/\text{no.})^2]}{\text{NEP}/d^2} \quad (4-5)$$

where ρ = reflectance

H_s = scene irradiance by the sun in the spectral band used

ρH_s = apparent scene radiance, N ($\text{W/cm}^2\text{-sr}$)

For comparison, using photometric units,

$$\frac{S}{N} = \frac{E_d}{E_o} = \frac{\text{detector illuminance}}{\text{noise-equivalent illuminance}} = \frac{\rho E_s K_o K_e / [4(f/\text{no.})^2]}{\text{NE}\phi/d^2} \quad (4-6)$$

where E_s = scene illuminance (lumens/m^2)

$\text{NE}\phi$ = noise-equivalent flux (lumens)

ρE_s = scene luminance or brightness ($\text{lumens/m}^2\text{-sr}$)



Using the radiometric relationships defined above,

$$\frac{S}{N} = \frac{\pi \rho H_s \theta D K_o K_e D_\lambda^* \sqrt{2E_d}}{4 (f/\text{no.})} \quad (4-7)$$

For a signal corresponding to a change in reflectance ($\Delta\rho$) when H_s is constant,

$$\Delta N = \Delta\rho H_s \quad (4-8)$$

and

$$NE\Delta\rho = \frac{4 (f/\text{no.})}{\pi H_s \theta D K_o K_e D_\lambda^* \sqrt{2t_d}} \quad (4-9)$$

which is similar to the expression for NEAT. As in the case of NEAT, NE $\Delta\rho$ can be made small (improved) by increasing values of θ , D , K_o , K_e , D_λ^* , and t_d . It is also small when H_s is large--e.g., when the sun is directly overhead.

Atmospheric noise due to small-scale variations in haze and humidity limits NE $\Delta\rho$. Because smaller surface-reflectance differences cannot be discriminated in the image data, atmospheric noise imposes a practical lower limit on NE $\Delta\rho$.

Although little information is available on the magnitude of such noise, Duggin (Ref. 4-1) measured the temporal variations of solar irradiance in four LANDSAT spectral bands over periods up to an hour. Assuming them equivalent to spatial variations, his results give a measure of atmospheric noise. The coefficient of irradiance variation ranged from a minimum of 1.39% to a maximum of 13.4%. The average ranged from 3.62% (between 0.5 and 0.6 μm) to 7.31% (between 0.8 and 1.05 μm).



The apparent scene-reflectance variance is the product of the above coefficient and the reflectance, which varies from a minimum of 2% to a maximum that increases from 25% (between 0.45 and 0.52 μm) to 90% (between 0.7 and 0.9 μm). The average apparent scene-reflectance variance therefore ranges from $(0.02 \times 3.6\%) = 0.072\%$ to $(0.90 \times 7.3\%) = 6.6\%$. A geometric mean of these, 0.7%, is typical of an agricultural scene in the region from 0.5 to 0.6 μm .

Scene reflectance including atmospheric effects can be expressed as

$$\rho = \frac{\pi(N_s - N_a)}{H k_b}$$

where

N_s = total radiance measured at the orbiting sensor

N_a = atmospheric-path radiance produced by back-scattering of solar radiation, sometimes called "air light"

H = total incident solar irradiance

k_b = fractional atmospheric transmittance or beam transmittance

These parameters are wavelength-dependent. They also depend on solar zenith angle and observation angle. The incident solar irradiance is given by

$$H = I_0 e^{-\tau \sec \theta} \cos \theta + S$$

where

θ = solar zenith angle

S = sky light

I_0 = solar constant (extraterrestrial irradiance)

τ = normal (zenith) optical depth of the atmosphere

and the atmospheric transmittance is given by

$$k_b = e^{-\tau \sec \phi}$$

where ϕ is the nadir angle of observation. Therefore,

$$\rho = \frac{\pi (N_s - N_a)}{(I_0 e^{-\tau \sec \theta} \cos \theta + S) e^{-\tau \sec \theta}}$$

The N_a and S terms are complex functions of atmospheric optical depth, solar zenith angle, and ground albedo, and are most significant at short, blue, wavelengths where molecular scattering dominates.

On the basis of these considerations, a 0.5% NE $\Delta\rho$ has been recommended for the LANDSAT-D thematic mapper by the technical working group assigned to that program (Ref. 4-2). The same practical considerations will probably limit SMSS sensitivity to approximately the 0.5% value.

The instrument itself, however, will be sensitive to the 0.1% originally specified, as long as detectivity values can be achieved that correspond to the spectral-radiance change at solar-elevation angles when data would be taken. For example, at a solar elevation of 75°, ΔN in Channel 3 (0.63 to 0.69 μm) would be 0.018 $\text{W}/\text{m}^2\text{-sr}$ for 0.1%, requiring a D^* of $1.07 \times 10^{10} \text{ cm-Hz}^{1/2}/\text{W}$. At a 20° solar elevation, ΔN_3 would be 0.0048 $\text{W}/\text{cm}^2\text{-sr}$ for 0.1%, requiring a D^* of 4×10^{10} .

4.2.2 Cooled Optics

The use of cooled optics was considered during the study and was deemed unnecessary because of the long dwell time inherent in the conceptual design and because the scene temperatures do not dictate a low-background system. The cooled-optics analysis is presented below.

The D^* value used in calculations of NEAT depends on the degree of cooling of optical filters and internal optics to reduce the level of background radiation falling on the IR-detector arrays. Multilayer interference filters for each array module will permit flexibility of focal-plane experiments that would not be possible with gratings. Filters of this type have been fabricated with a transmittance of about 80% in the band from 10.4 to 12.5 μm , and are coolable to the lowest expected focal-plane operating temperature.

The total photon flux (Q , photons/ cm^2 -second) at each detector element will consist of three parts: (a) that from a hemisphere at the filter temperature for wavelengths below the filter cut-on value, λ_1 , (b) that from the interior optical walls seen through the filter in its spectral passband, $\Delta\lambda$, and (c) that from the scene viewed through the small solid conical angle set by the focal ratio, also in the spectral passband. It is given by

$$Q = (Q_F)_{0-\lambda_1} + \left\{ \left[1 - \frac{1}{(2F)^2} \right] [0.8 Q_O + 0.2 Q_F] + \frac{0.8 Q_S + 0.2 Q_F}{(2F)^2} \right\} \Delta\lambda$$

where Q_F , Q_O , and Q_S are blackbody photon fluxes corresponding to the temperatures of the filter, optical walls, and scene, and F = focal ratio.

Both detector temperature and background flux affect detectivity for intrinsic photoconductors such as mercury-cadmium telluride and lead-tin telluride (HgCdTe and PbSnTe), which require less cooling for the same detectivity at 11 μm than extrinsic detectors such as doped germanium or silicon. If optically and thermally excited carrier densities are assumed equal, the limiting D^* for the intrinsic type is degraded by a factor of 2 from the ideal background-limited-photodetector (BLIP) D^* :

$$D^* = \frac{\lambda}{4 hc} \sqrt{\frac{\eta}{Q}} = 1.26 \times 10^{18} \lambda \sqrt{\frac{\eta}{Q}}$$

where η is the quantum efficiency, typically about 40%.



Figure 4-2 shows the influence of background-photon flux on instrument sensitivity in the 10.5- to 12.5- μm band in terms of typical cooling requirements. Without cooling, the D^* is about 10^{10} $\text{cm-Hz}^{1/2}/\text{W}$ and the NEAT is relatively high. If only the filter is cooled, the improvement is limited to a factor of 2. If the optical walls can be cooled ("cold-stopped") even to only 200 $^\circ\text{K}$, further improvement is possible. A total improvement factor of 10 is realized at a wall-cold-stop temperature of 100 $^\circ\text{K}$.

With a pushbroom sensor permitting a long dwell time, optical cooling should not be necessary. Mechanical-scanning approaches with short dwell times or pushbrooms with very narrow spectral bandwidths, however, would require optical cooling in order to achieve a 0.1 $^\circ$ NEAT.

4.3 SCANNING, DATA RATE, AND RELATED CONSIDERATIONS

Scanning systems may be categorized as "nonscanning", oscillating, and rotating, with many variations in each category. Variations of each are illustrated in Figures 4-3 through 4-6, and descriptions follow.

The nonscanning category includes (a) direct-staring systems (no additional sensor motion, with a nonlinear detector array), (b) the "pushbroom" approach with a linear detector array perpendicular to the direction of vehicle motion, and (c) a nodding telescope to provide the required scan motion. These types are feasible for a small field of view (FOV).

The pushbroom approach is attractive because scanning is provided by vehicle motion, with a narrow linear FOV in the direction of motion and no moving parts. The optical system, however, must have an FOV (perpendicular to the satellite motion) equal to the swath width. For the SMSS application, a swath width of 15 $^\circ$ is desired, which is difficult to obtain with conventional all-reflective optics. Consequently, the optical system for this method must be one of the more sophisticated designs, such as an all-reflective Schmidt or a confocal paraboloid configuration (discussed in Section 5).



TRANSMISSION OF INTERFERENCE FILTER = 80%
SCENE TEMPERATURE = 280°K

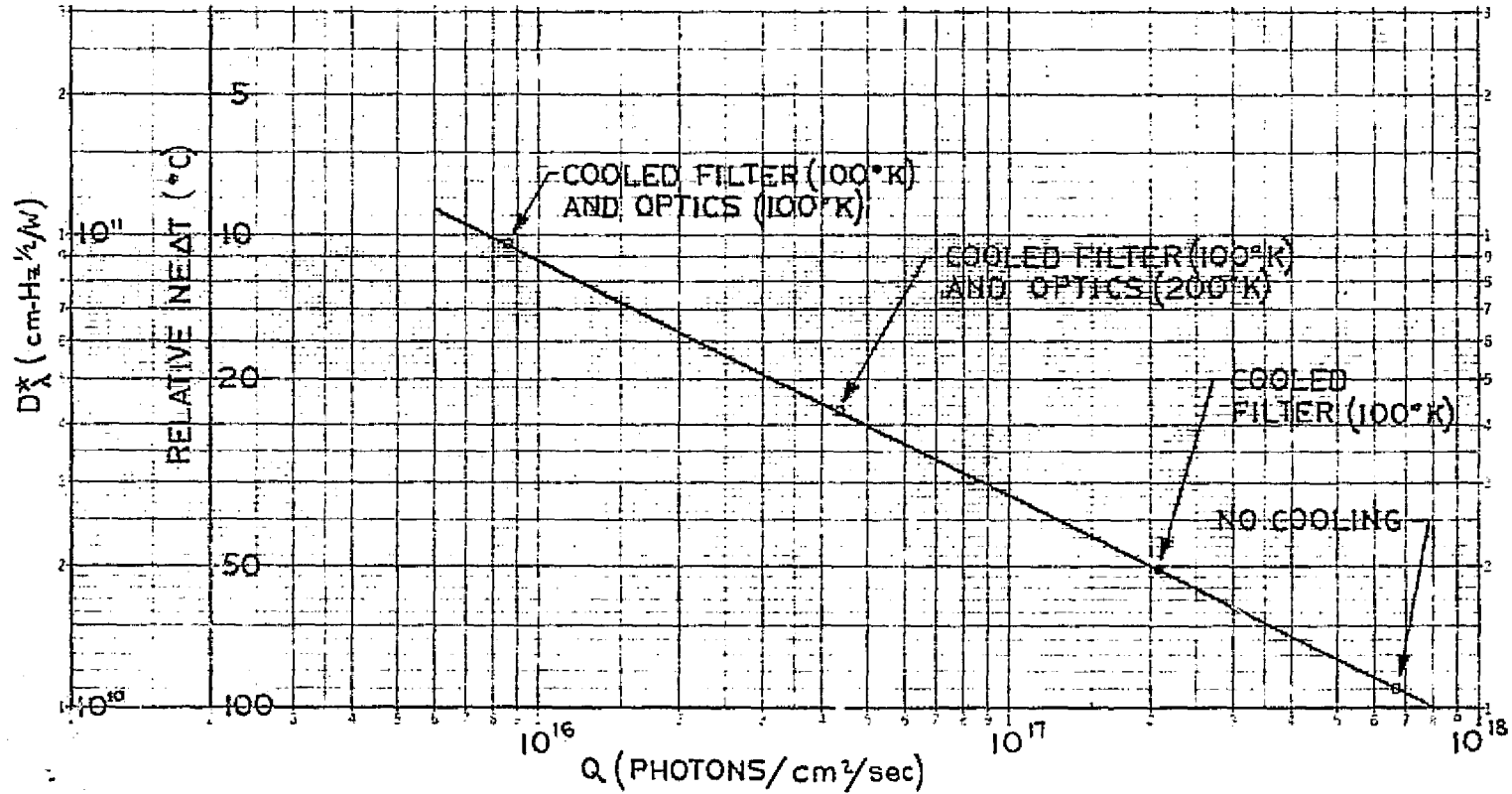
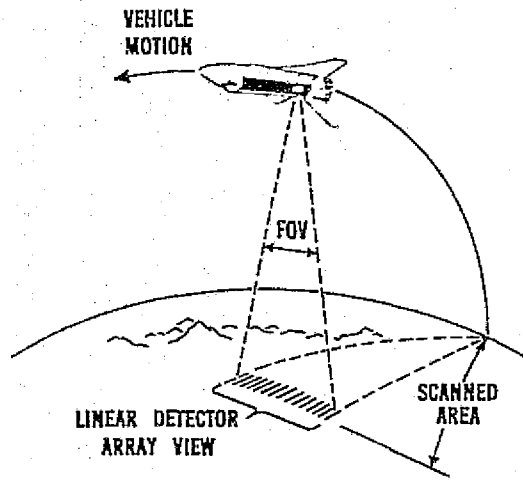


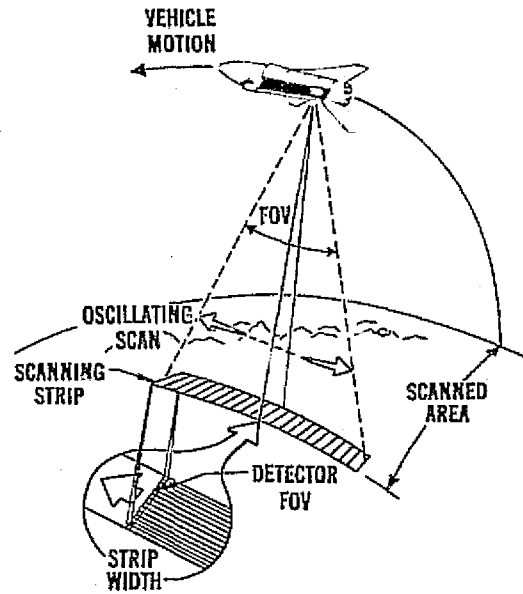
FIGURE 4-2 INFLUENCE OF BACKGROUND PHOTON FLUX ON INSTRUMENT SENSITIVITY (10.5 TO 12.5 μm), SHOWING TYPICAL COOLING REQUIREMENTS



• SOLID-STATE [Pushbroom] SCANNER



• MECHANICAL SCANNER



• CONICAL SCAN PATTERN

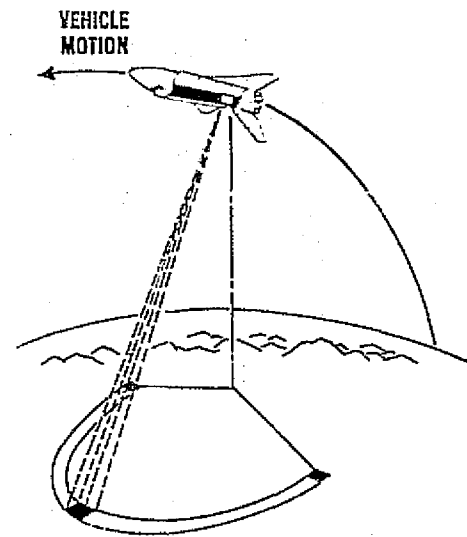
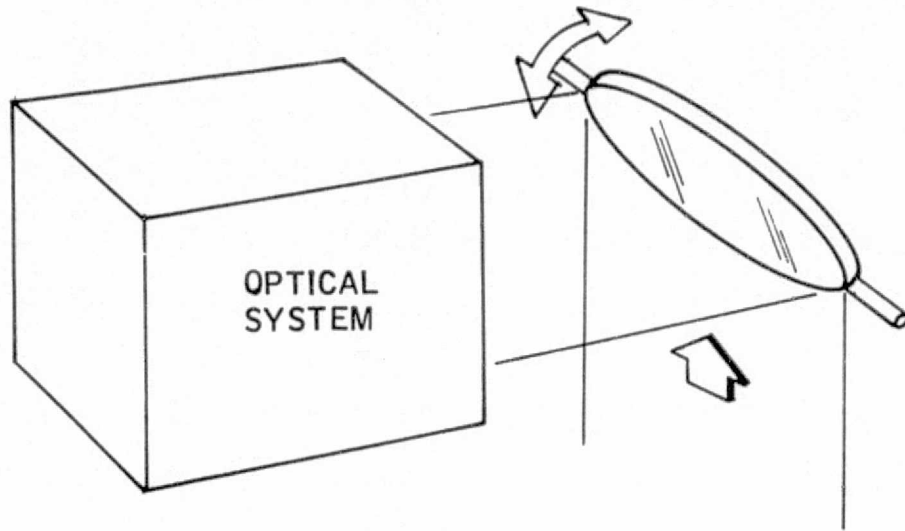
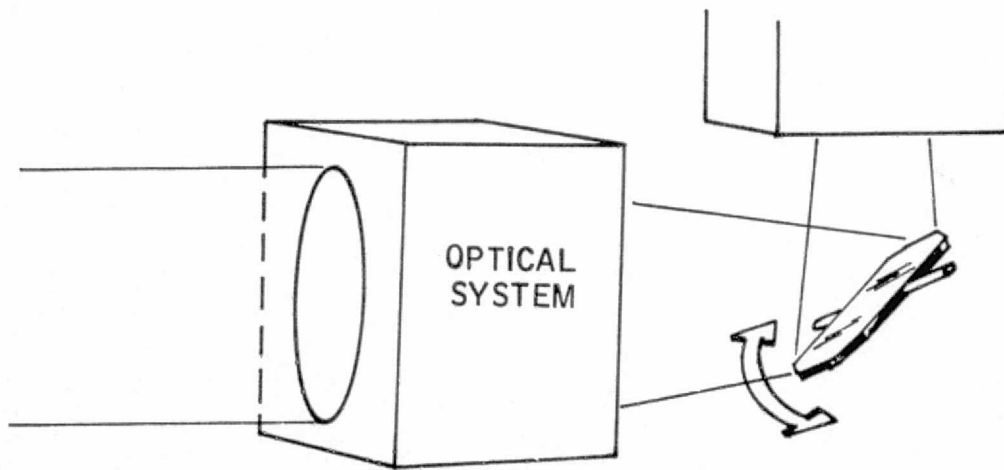


FIGURE 4-3 BASIC SCENE-GENERATION SYSTEMS



OSCILLATING PLANO OBJECT-PLANE SCANNER

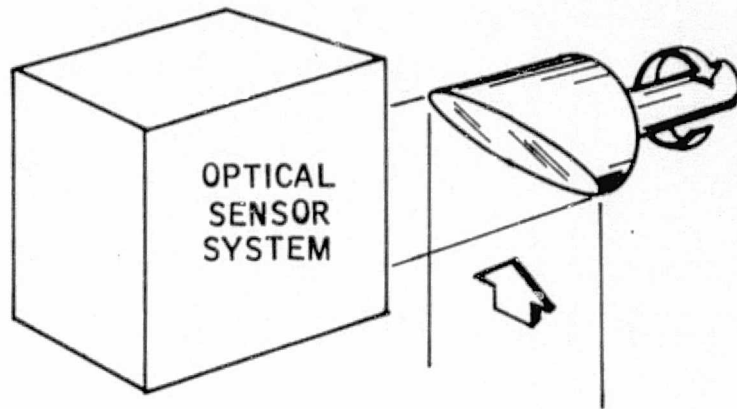


OSCILLATING PLANO IMAGE-PLANE SCANNER

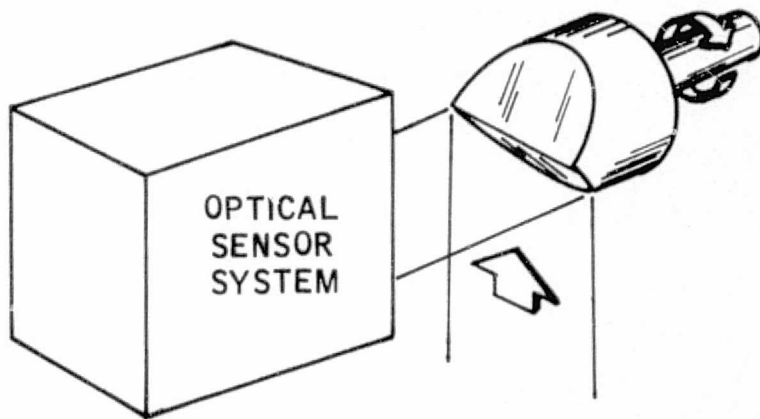
FIGURE 4-4 OSCILLATING MIRROR SCANNERS



ONE-MIRROR
ROTATING SCANNER



TWO-MIRROR
ROTATING SCANNER



FOUR-MIRROR
ROTATING SCANNER

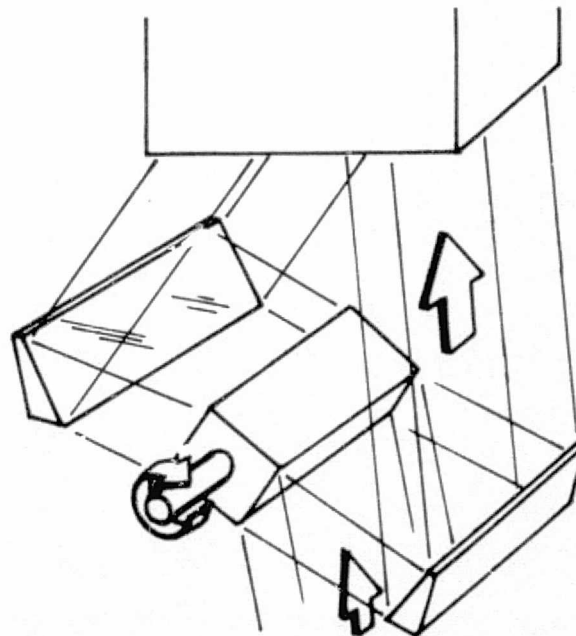
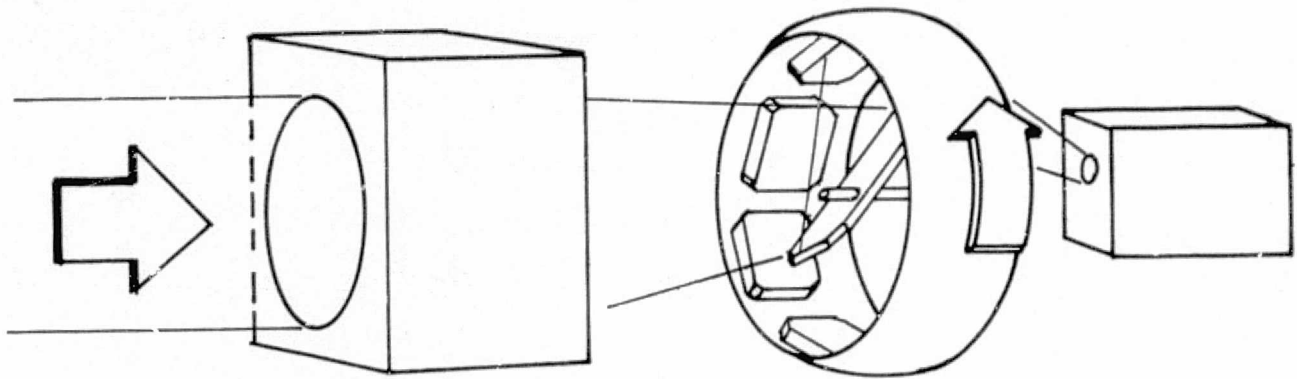
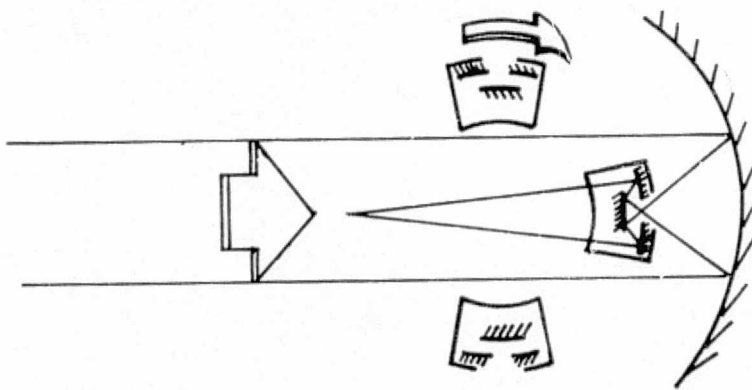


FIGURE 4-5 ROTATING OBJECT-PLANE SCANNERS

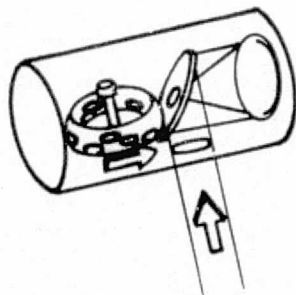




ROTATING PLANO-MIRROR IMAGE-PLANE SCANNER



ROTATING RELAY-MIRROR IMAGE-PLANE SCANNER



ROTATING DRUM WITH MULTIPLE RELAY MIRRORS

FIGURE 4-6 ROTATING IMAGE-PLANE SCANNERS

Oscillating scanners (Figure 4-4) include both object-plane (in the parallel beam) and image-plane (in the converging beam) devices. An oscillating flat mirror in front of the optics (an object-plane scanner) can be used to cover any size FOV, while an image-plane scanner (either plano or curved mirror) can provide scanning only for a small-FOV system. This approach is usually preferred for a moderate FOV. For the SMSS, therefore, a telescope with excellent image quality over only 1° or less would be needed. This would permit selection from a much larger number of candidate systems than is possible with the nonscanning approach. The rapid start-and-stop of an oscillating-mirror scanner, however, creates difficult design problems as the scan field, scan rate, and aperture size increase.

In addition, an oscillating-mirror object-plane scanner must be larger than the desired system aperture and yet maintain a precise optical surface during the rapid start-and-stop operation necessitated by the rapid scan rate. However, improvements in mirror materials, structural design, drive mechanisms, optical-fabrication techniques, and other areas have overcome these obstacles on several large-aperture systems during the past few years. The relative advantages of several object-plane scanners are summarized in Table 4-1.

Image-plane scanning exhibits properties exactly opposite to those of object-plane scanning. The scanners are usually small, being in the converging beam or small-diameter afocal region, but the optics must perform over the entire scanned field, just as with the staring and pushbroom systems. Image-plane scanners can take either an oscillating or a rotating configuration (Figures 4-4 and 4-6). An oscillating flat mirror, with its simplicity and size, offers a very attractive approach, especially when the mirror movement is small (i.e., for small scan fields).

The advantages of a rotating scanner become evident as the desired scan field increases (e.g., beyond about 20°). For example, the advantages of a rotating drum, with its small-aperture relay optics, begin to overcome its undesirable properties, such as size.

TABLE 4-1 OBJECT-PLANE SCANNERS

Description of Scanning Means	Comparative Advantages & Disadvantages				
	Efficiency		Resolution	Rotating-Element Size	Ease of Manufacture & Assembly
	Scanning	Optical			
Mirror rotating or oscillating about an axis parallel to faces and perpendicular to optical axis	Poor	Good	Good	Large	Moderate
Two prisms counterrotating about optical axis, with prism vertexes perpendicular thereto	Fair	Fair	Good	Large	Poor
Rotation of entire system about an axis perpendicular to optical axis	Poor	Good	Good	Very large	Moderate
Rotation of entire system about an axis parallel or nearly parallel to optical axis	Good	Good	Good	Large	Moderate
Rotation of a single prism about optical axis, with prism vertexes perpendicular thereto	Fair	Fair	Good	Large	Moderate
Mirror with face inclined at slight angle to an axis of rotation parallel to optical axis	Fair	Good	Good	Large	Moderate
Mirror with face inclined at 45° to an axis of rotation parallel to optical axis	Very poor	Fair	Good	Large	Moderate

The most frequently used types of rotating scanners employ one-, two-, or multiple-sided prisms in front of the optical system (Figure 4-5 shows typical examples). Many types of image-plane scanners using rotating plano or relay mirror systems have been devised (see Figure 4-6). Rotating systems generally provide large scan fields with high scan efficiencies. However, extreme care is needed during design because this type of device tends to require large and/or sophisticated mechanisms for proper scanning. The relative advantages of several image-plane scanners are summarized in Table 4-2.

Advancing charge-transfer-device technology will permit a large number of detectors to be interrogated sequentially and processed serially through a single amplifier. With this potential, the advantages of the push-broom-sensor approach in earth-resources applications become evident for swath widths of the order of 20° or less. This approach is therefore recommended for detailed SMSS development. It eliminates mechanical scanning by a large oscillating or rotating mirror or by multiple rotating probes; this in turn eliminates major areas of concern in reliability, alignment, and mirror flexure.

In addition, the increased sensitivity due to the longer detector-dwell time on each scene element permits the use of a smaller aperture or of more-relaxed optical-cooling specifications to attain a given threshold sensitivity than would be possible with a complex mechanical scanner. Furthermore, there is no sensitivity degradation caused by scan inefficiency. The prime disadvantage--a large number of detector elements--becomes less significant with the advent of low-cost solid-state imaging devices having serial readout that obviate the need for separate preamplifiers for each channel, as discussed below and detailed in Section 6.



TABLE 4-2 IMAGE-PLANE SCANNERS*

Description of Scanning Means	Comparative Advantages & Disadvantages				
	Efficiency		Resolution	Rotating-Element Size	Ease of Manufacture & Assembly
	Scanning	Optical			
Mirror rotating or oscillating about an axis parallel to faces and perpendicular to optical axis	Poor	Fair	Poor	Small	Fair
Two prisms counterrotating about optical axis, with prism vertices perpendicular thereto	Fair	Fair	Poor	Small	Poor
Rotation of single prism about optical axis, with prism vertices perpendicular thereto	Fair	Fair	Poor	Small	Fair
Mirror with face inclined at 45° to axis of rotation parallel to optical axis	Poor	Fair	Poor	Small	Fair
Four mirrors in convergent beam, rotating about an axis at an angle to optical axis, but passing through center of exit pupil	Good	Fair	Fair	Moderate	Poor

* Scanning devices introduced between an afocal telescope and a final objective lens are considered image-plane scanners, as are devices placed in a convergent beam. Unless otherwise noted, the afocal arrangement has been assumed.

If all spectral bands have 66- μ r resolution, 4000 detector elements per band are required to cover a 15 $^{\circ}$ pushbroom swath width. At the lowest orbital altitude of 185 km [giving the highest velocity/altitude value (v/h)], the dwell time per element has a minimum value and the required data rate is maximized because

$$\text{data rate} = f_s m N$$

where f_s = sample rate, which must be at least once per dwell time ($1/t_d$)
 m = analog-to-digital (A/D) quantization, usually 8 bits for precision earth-survey applications
 N = number of detectors

For a specific channel capacity of six spectral bands recorded simultaneously, the minimum data rate is

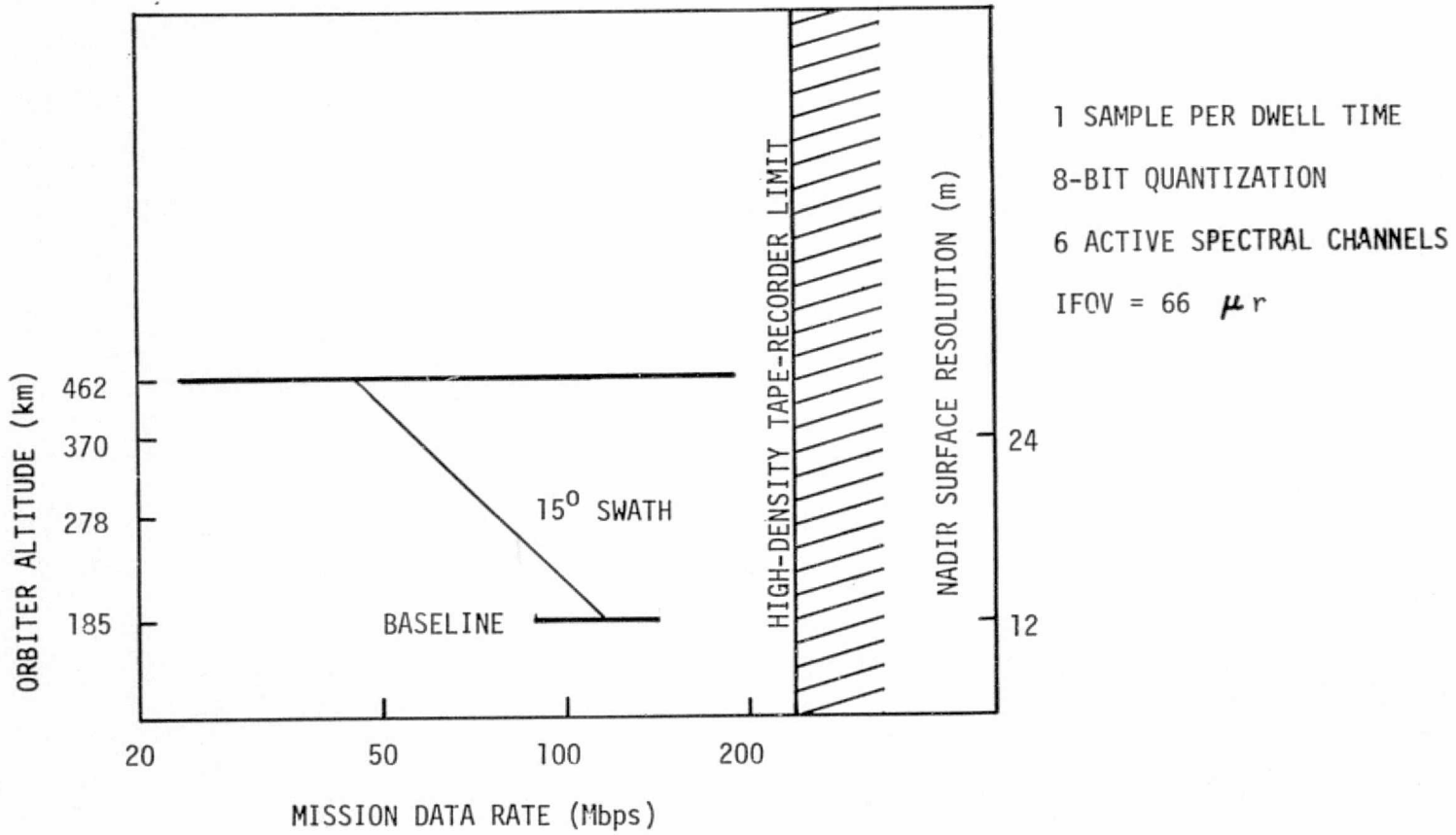
$$(1/1.62 \text{ msec})(8)(4000)(6) = 118.5 \text{ megabits/second (Mbps)}$$

This can be compared with the maximum-permissible data rate of 240 Mbps (based on design goals set forth for a high-data-rate recording system currently under development). That rate (see Figure 4-7) includes calibration and housekeeping data. For the 15 $^{\circ}$ nominal swath, the sampling rate could be increased or the resolution could be improved somewhat if optical constraints permitted.

The physical size of the detectors in the focal plane is an important consideration because of fabrication limits and, for solid-state detectors, the available sizes of mass-produced low-cost arrays. Typical examples are one- and two-dimensional CTDs, which can be read out serially to minimize the number of preamplifiers and simplify the data processing. Present CTDs for the visible and near-visible regions have elements spaced



1275-1152



4-22

FIGURE 4-7 DATA RATE VS ALTITUDE AND SURFACE RESOLUTION

on centers as close to each other as $13\ \mu\text{m}$ (0.0051 in.). A typical 500-element linear array has $30\text{-}\mu\text{m}$ spacing. A typical, 190×244 -element, two-dimensional mosaic has spacings of $18\ \mu\text{m}$ vertically and $30\ \mu\text{m}$ horizontally.

Infrared-detector-array elements have been made as small as $25\ \mu\text{m}$ (0.001 in.) for most spectral regions and at least as small as $50\ \mu\text{m}$ for all regions. Although infrared CTDs are not yet commercially available, experimental models have been produced for both hybrid devices (coupling IR arrays to separate silicon shift registers) and monolithic devices (in which the IR-array substrate acts as the shift register just as in visible-spectrum silicon CTDs).

Optical design for a wide field is much easier at larger focal ratios. As an example, the blur spot size for conventional refractive Schmidt optics can be expressed as $0.0417\ \theta^2/(f/\text{no.})^3$, where θ is the angle off axis. For $\theta = \pm 5^\circ$, the spot size is $317\ \mu\text{r}$ at $f/1$, $94\ \mu\text{r}$ at $f/1.5$, and $40\ \mu\text{r}$ at $f/2$. The reflective Schmidt system selected for the SMSS, as discussed in Section 5, provides comparable performance.

Table 4-3 compares a pushbroom sensor with one of the most attractive mechanical scanners, which employs an object-plane oscillating mirror. The shorter dwell time in the mechanical scanner, using one-tenth as many detectors and a lower scan efficiency, degrades the sensitivity by a factor of nearly 5 from that of the pushbroom.

4.4 MODULATION TRANSFER FUNCTION

The system MTF is a valuable parameter for use in the design of an electro-optical system and evaluation of its performance, although all the factors involved cannot be determined with precision. It describes the combined effects of the following factors on the image of a sinusoidal distribution of radiant intensity as the spatial frequency (cycles per unit length) of the scene is varied: atmospheric contrast reduction, diffraction by the aperture, optical aberrations and obscuration, image motion, the geometry of the detector array, degradation by charge-transfer inefficiencies and diffusion, electronic preamplifiers, filters, and sampling.



TABLE 4-3 COMPARISON OF PUSHBROOM SENSOR WITH OBJECT-PLANE SCANNER*

Parameter	Pushbroom	Object Plane (Oscillating Mirror)
Scan efficiency	100%	45%
Dwell time at 185 km	1620 μ sec	72.8 μ sec
Optics	Reflective Schmidt	Ritchey-Chrétien
Field of view	15°	1.5°
Resolution	66 μ r	66 μ r
Optical efficiency	50%	50%
Number of active detector elements (6 spectral bands)	24,000	2400
Mission-data rate (one sample per dwell time, 8-bit quantization)	118.5 Mbps	118.5 Mbps
Typical NEAT	0.1°K	0.47°K

* For 15° swath, 75-cm aperture at f/1.7.

The MTF is the ratio of the scene contrast at the output of the electro-optical system to the original ground-scene contrast for an object with sinusoidal brightness variation. It can be used to determine the limiting resolution of a system at any desired threshold of contrast. The ground scene can be assigned an MTF appropriate to its inherent contrast. As an example, for 2:1 contrast at all spatial frequencies,

$$\text{modulation} = \frac{I_{\max} - I_{\min}}{I_{\max} + I_{\min}} = \frac{2 - 1}{2 + 1} = 0.333$$

where I represents intensity. A system MTF of 0.015 at, for example, a spatial frequency of 12 cycles/mm (1 cycle per 84 μ m of detector width) would degrade this scene modulation to 0.005, or 0.5%.

4.4.1 Optical MTF

The MTF of the optics (or the OTF) is the two-dimensional Fourier transform of the point-spread function (PSF). It can be theoretically estimated as the value for a diffraction-limited optical system at 12 μm with a 12-13% central obscuration (SMSS parameters), third-order spherical aberrations, and an optical-path difference of $\lambda/4$. This is shown in three stages of degradation in Figure 4-8. The central obscuration actually improves the response to high-spatial-frequency information as compared with the low-frequency response. The MTF response at a spatial frequency matching the SMSS-detector-element dimension of 84 μm is about 0.46.

The ideal OTF of curve A for a diffraction-limited system with monochromatic radiation of wavelength λ is given by

$$\text{MTF}_A = \frac{2}{\pi} \left(\cos^{-1} z - z \sqrt{1 - z^2} \right)$$

where

$$z = \lambda (f/\text{no.}) \frac{\omega}{2\pi}$$

and ω is the spatial frequency in radians/radian. (Ref. 4-3 discusses the effect of a finite spectral bandwidth.) The "limiting resolution" is $\frac{1}{\lambda (f/\text{no.})}$, where $\text{MTF}_A = 0$. For $f/1.7$ and 12 μm (SMSS parameters), this is about 49 line pairs (lp) per millimeter.

The central obscuration of a circular optical system degrades MTF as shown in curve AB of Figure 4-8. The OTF is given by

$$\text{MTF}_{AB} = \frac{2}{1 - \alpha^2} \left(\cos^{-1} z - z \sqrt{1 - z^2} \right)$$

where α , the linear obscuration factor, is 35% for 12.5% area obscuration of the SMSS focal plane (i.e., $\sqrt{0.125} = 0.3535$).

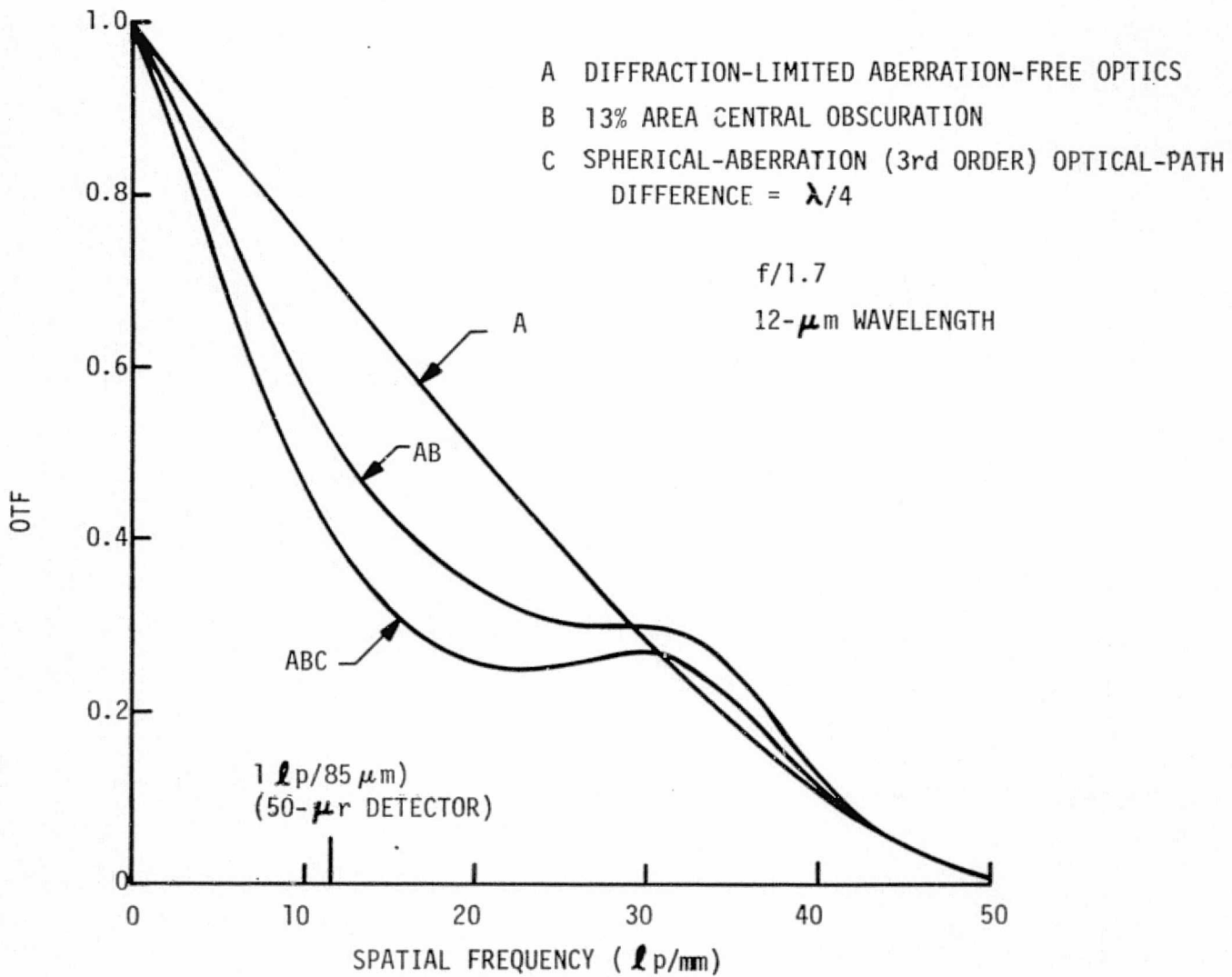


FIGURE 4-8 THEORETICAL OPTICAL-TRANSFER FUNCTIONS

Curve ABC represents the combined effects of the diffraction-limited system with the obscuration and spherical-aberration effects.

Alternatively, and probably more accurately for the SMSS case, the OTF can be approximated in terms of a Gaussian image for a circular aperture and wide spectral band as shown in Figure 4-9:

$$\text{MTF} = \exp(-\omega^2 \sigma^2 / 2)$$

where σ is the standard deviation of image size (84% of the energy is in a spot of radius 1.9σ).

The MTF response is about 0.35 at a spatial frequency matching the SMSS detector-element dimension (instantaneous field of view, IFOV, of $84 \mu\text{m}$). This Gaussian-image approximation has been found valid for a Schmidt-corrected optical system of the general type proposed for the SMSS.

4.4.2 Array MTF

The MTF of a pushbroom-system linear-detector array has been analyzed by Seyrafi (Ref. 4-4) in terms of array geometry and the sampling process. The spatial sampling is determined by the spacing or pitch of the elements. An electronic multiplexer such as a charge-coupled-device (CCD) shift register provides sampling in the direction of array motion across the scene. If individual detector elements are square and contiguous and if the sampling period is equal to the detector dwell time, the spatial filtering is the same in both directions.

The filtering effect on noise is different. If detector noise dominates, as is usually the case, the multiplexer sampling affects the noise through aliasing or folding around the limiting Nyquist frequency. The noise across the array, however, is independent of the multiplexing because each resolution element is sampled by a different detector. In order to minimize the aliasing effect of sampling on overall sensor noise, the rate is



375-1280

4-28

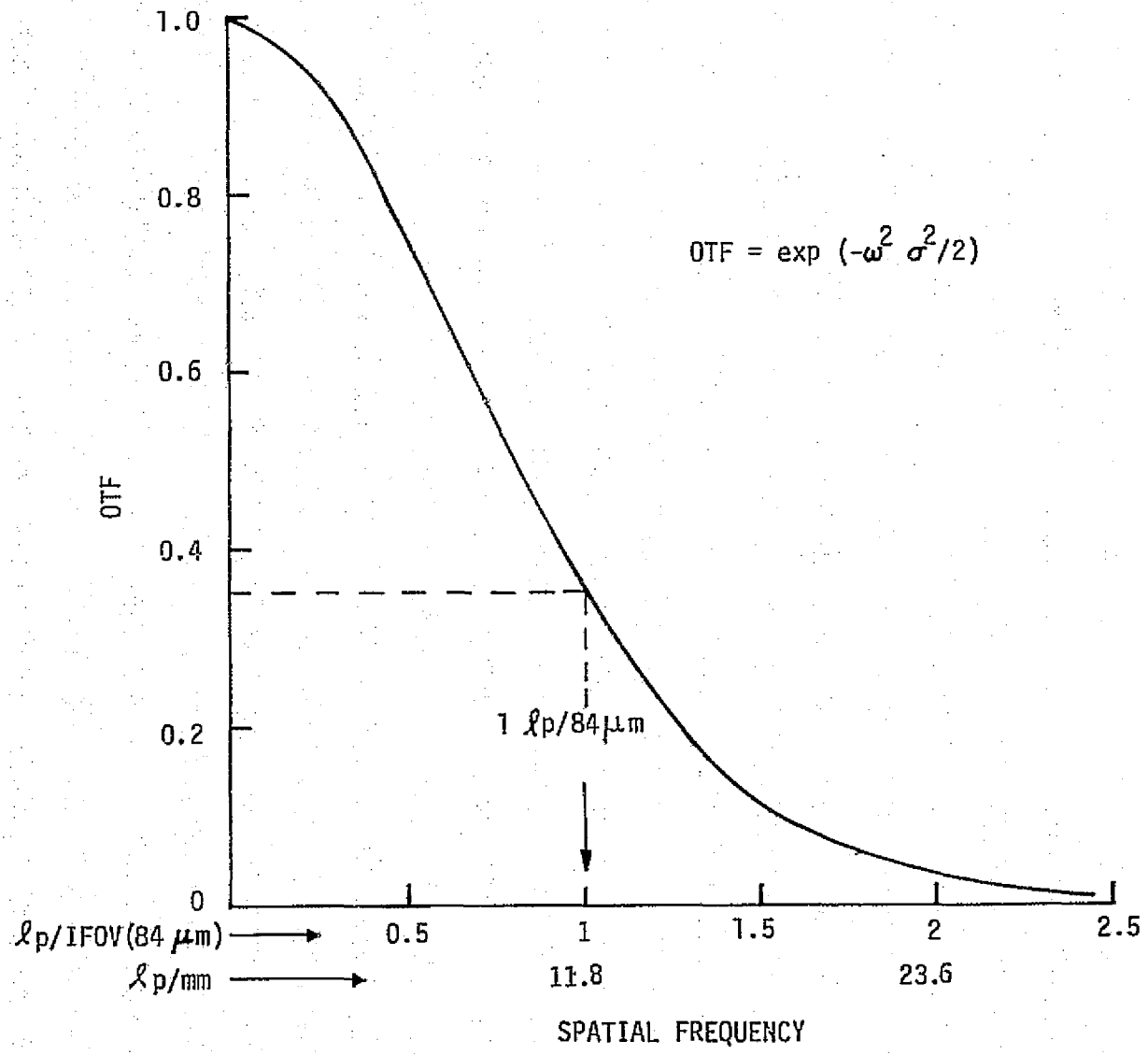


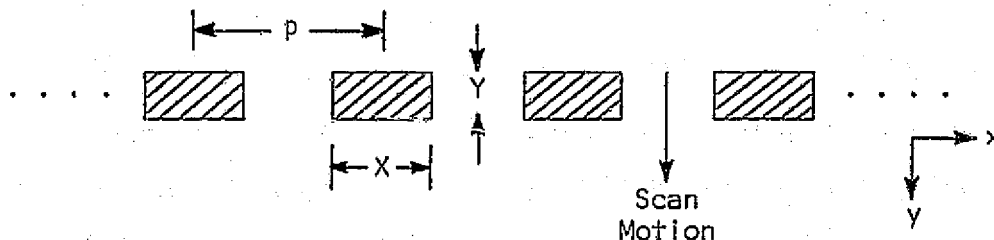
FIGURE 4-9 OPTICAL-TRANSFER FUNCTION, GAUSSIAN IMAGE

usually increased to 3 or 4 samples per dwell time. This, however, makes the spatial/temporal filtering nonuniform in the two directions. The higher sampling rate does not necessarily imply a higher data-recording rate because samples can be integrated before recording.

Long linear arrays of visible-spectrum silicon detectors are already available with CCD readout. As one example, a 1728-element device with a $13\text{-}\mu\text{m}$ (0.5-mil) pitch is being marketed (Ref. 4-5) that will cover the 0.45 to $0.95\text{-}\mu\text{m}$ spectral channels of the SMSS.

A technique has been described (Ref. 4-6) for computing the geometric design of the detectors in a linear array to yield the highest signal-to-noise ratio at the spatial-resolution limit. Arrays fabricated according to the criteria evolved in this reference should produce image data with maximum information content.

A linear array used in a pushbroom mode is sketched below with elements of size $X \cdot Y$:



The sampling theorem shows that the highest spatial frequency that can be reconstructed in the x direction of the image has a wavelength equal to twice the pitch, or $2p$. This high-frequency limit is the one at which the signal-to-noise ratio (S/N) is lowest and the information content is often highest. Maximizing performance at this limit is therefore desirable and can be accomplished by maximizing the MTF for this spatial frequency.

The MTF of the rectangular detectors shown above is given (in the x direction at the high-frequency limit) by

$$MTF = \frac{\sin [(\pi/2) (X/p)]}{(\pi/2) (X/p)}$$

The corresponding expression for MTF in the y direction has an additional term, because of image motion across the array during the integration time. When the image velocity is p divided by the sampling time, sample spacing is equal in the x and y directions:

$$MTF_y = \frac{\sin [(\pi/2) (Y/p)]}{(\pi/2) (Y/p)} \left[\frac{\sin (\pi/2)}{\pi/2} \right]$$

Because equal resolution is desired in the x and y directions for the SMSS, the limiting S/N will be made equal in both directions. The maximum performance for low-noise arrays, where S/N is proportional to the square root of the detector area, occurs for $x = 1.26 p$, $Y = 0.85 p$, and the MTF at the limiting spatial frequency is 0.46 (see Figure 4-10). The condition $X > p$ requires a staggered linear array, as shown in Figure 4-10 (with dimensions for a pitch of 84 μm).

The spacing between row centers should be a whole-number multiple of p if the image is to be reconstructed for viewing with equal spacing of samples on a Cartesian grid. The spacing should also be as small as possible, (a) to avoid a large-memory requirement prior to image reconstruction on a raster-scanning device, and (b) to avoid excessive misregistration arising from image-velocity errors in either x or y components.

Other considerations in focal-plane-array design, such as practical charge-transfer shift-register configurations, may preclude selection of the staggered-array format and dimensions discussed here. Alternative transfer to shift registers on each side of a detector array, however, is well established in linear-CCD technology.



375-1279

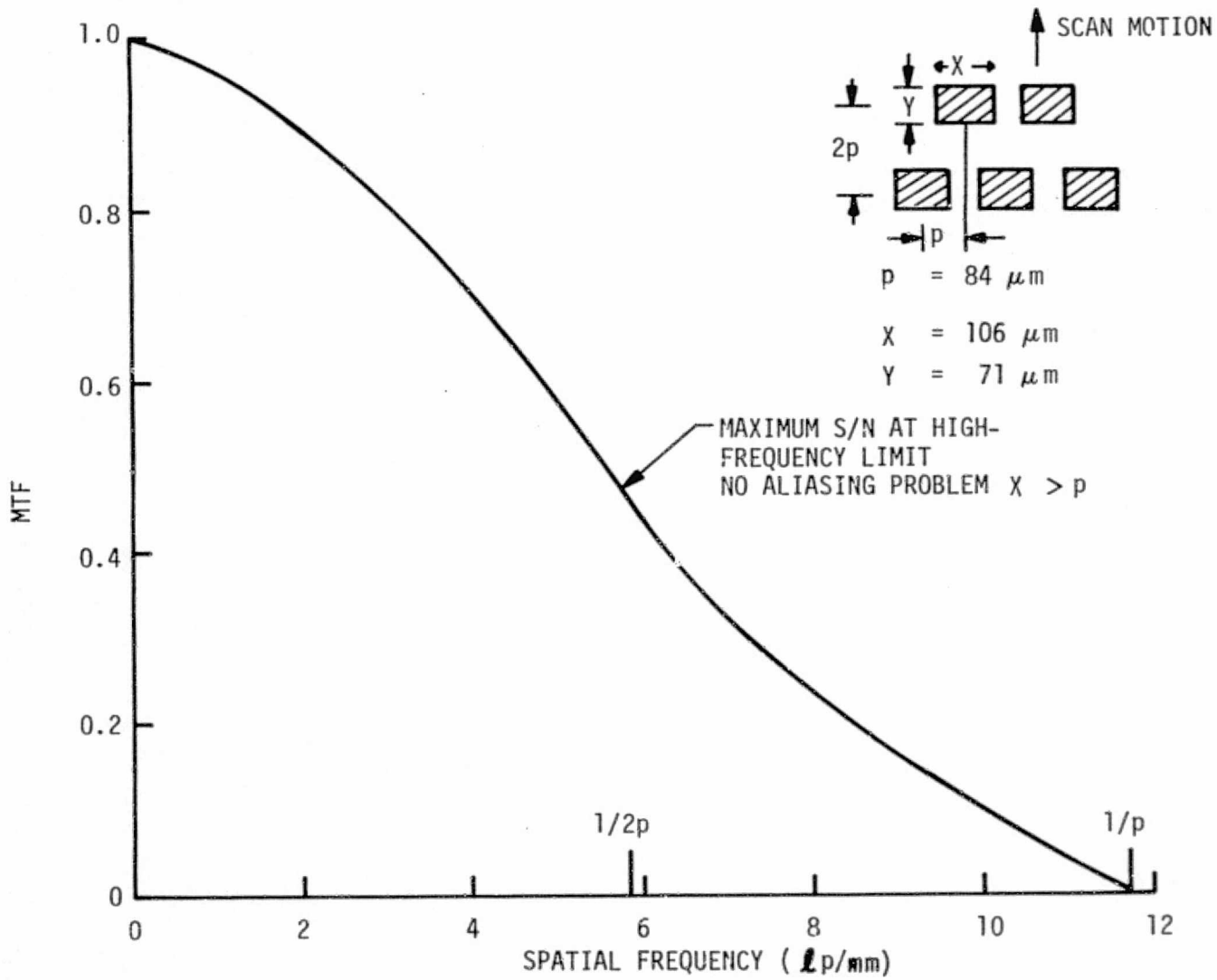


FIGURE 4-10 LINEAR-ARRAY MTF

4.4.3 Charge-Coupled-Device MTF

The response of charge-coupled imaging devices rolls off with increasing spatial frequency, not only because of the geometry of the array of integrating detector elements, but also because of transfer inefficiencies in the shift register and charge-diffusion losses (Ref. 4-7).

The transfer MTF is expressed as

$$MTF_{\dagger} = \exp \left\{ -n\epsilon [1 - \cos(\omega/2)] \right\}$$

when a fraction (ϵ) of the charge is lost from each sample at each of n transfers and ω is the normalized spatial frequency.

The diffusion MTF is given by

$$MTF_d = \frac{\cosh(d/L_o)}{\cosh(d/L)}$$

when photons are absorbed a distance d from the depletion regions, the diffusion length in the substrate used is L_o , and $L^{-2} = L_o^{-2} + \omega^2$.

4.5 POINTING AND IMAGE-MOTION COMPENSATION

The Orbiter will be able to achieve and maintain any desired attitude with respect to either its navigation base or a special sensor provided as part of its payload. The resulting accuracy as related to the SMSS will be limited by thermal influences on SMSS attitude and will also be a function of the payload-attitude sensor, vehicle flexure, type of control system, and signal-quantization errors of the digital autopilot.

If the SMSS is pointed by means of the Orbiter inertial measurement unit (IMU), an error greater than 2° can accrue because of Orbiter flexure, structural deformation, and mounting error with respect to the IMU navigation base (Ref. 4-8).



To achieve greater accuracy in pointing to an earth target, the Orbiter can accept signals from a more accurate sensor, provided by the payload, with the Improvements dependent upon sensor accuracy.

The capabilities of the Orbiter in attitude maintenance are as follows (from Table 3.2 of Ref. 4-9):

Orbiter Attitude/Position Reference	Attitude		Duration Between Alignments
	Accuracy (3-Sigma)	Degradation Rate (3-Sigma)	
Inertial	$\pm 0.5^\circ$	0.1 $^\circ$ /hour	1.5 orbits
Celestial	$\pm 0.35^\circ$	0	NA
Earth target	$\pm 0.5^\circ$	0.1 $^\circ$ /hour	1 orbit
Orbital object	TBD	TBD	TBD

Hence, Orbiter attitude can be maintained with the IMU to an accuracy of $\pm 0.5^\circ$ for up to 1.5 orbits before realignment is needed. Realignment may necessitate the interruption of attitude hold for up to 15 min, and the Orbiter may require maneuvering to acquire stellar references. The telescope-pointing uncertainty can thus be up to $\pm 0.5^\circ$. At an altitude of 185 km, this is equivalent to a ground-scene error of ± 1617 m, or 132 times the ground-scene footprint.

If star trackers are used to supply continuous celestial-attitude-reference signals, Ref. 4-9 indicates that the attitude accuracy can be increased to $\pm 0.35^\circ$ for an indefinitely long period and the attitude-error drift can be eliminated. However, the uncertainty due to vehicle flexures can still exist if the trackers are independent of the SMSS. Improved stabilization or gimbaling appears mandatory for the SMSS because of the high vehicle-drift rate, and because an error of as much as 2° could exist in alignment between a payload and the Orbiter navigation unit.

Regardless of the reference that is selected, the vehicle will slowly pitch, yaw, and roll throughout a deadband of $\pm 0.1^\circ$. When all RCS jets are operational, the angular rate of the Orbiter can be as high as $0.01^\circ/\text{sec}$ (1.74×10^{-4} rad/sec). This can result in a ground-scene drift of one resolution element in 0.38 sec and a misregistration of up to 26 resolution elements at the limits of the deadband.

In order to maintain a reasonable MTF for each data frame, stabilization errors should be controlled to at least one-sixth of the instantaneous field of view (IFOV) per exposure time, or for the SMSS, with a 75-cm aperture size:

$$\frac{66 \mu\text{r}}{(6)(1.62 \text{ msec})} = 6.79 \text{ mr/sec (or } 0.39^\circ/\text{sec)}$$

which is far in excess of the expected Orbiter drift rate of $0.01^\circ/\text{sec}$ and therefore presents no special problems.

The accuracy of the ephemeris data used to determine Orbiter position will be sufficiently high to position earth-sensor imagery in a cartographic reference system. In the absence of significant internal distortions in the display, excellent positioning may be achieved by using ground-control points.

Pointing errors in pitch and roll affect local verticality and distort the frame. Rotation about the local vertical (yaw error) affects cartographic positioning and increases the complexity of data processing in a digital system. Stabilization errors (short-term attitude variations, or jitter) affect line-to-line registration of the image produced by a scanning sensor. The present state of the art for LANDSAT is $\pm 0.015^\circ/\text{sec}$ (Ref. 4-10).



On the basis of the foregoing considerations, image-motion compensation (IMC) is necessary for the SMSS, and suitable methods for achieving it were sought, with emphasis on

- Modular design
- Registration accuracy to 10% of an IFOV
- Suitability for ground checkout, calibration, and testing under ambient pressure and gravity conditions.

The SMSS focal plane could be fixed and the telescope gimballed, or the telescope could be fixed and the focal-plane gimballed. Telescope gimbaling might be accomplished with a specially designed SMSS system or with the instrument pointing system (IPS) being developed by the European Spacelab consortium.

The latter would provide three-axis attitude control for experiments whose stabilization requirements exceed present Orbiter capabilities. The IPS has a design goal for pointing accuracy with respect to a given reference star and the sun of 1 second of arc (or $4.85 \mu\text{r}$) (1-sigma) in two axes and roll stability about an instrument line of sight of 30 seconds of arc (1-sigma). It is to have a hemispherical range of pointing control and to be capable of accommodating experiments up to (a) 2 m in diameter and 4 m in length, and (b) a mass of 2000 kg (4400 lb).

The SMSS could be designed to use the IPS. The IPS load capability, however, is considerably greater than that required for the 400-kg SMSS, and its off-nadir pointing capability is far greater than that of $\pm 5^\circ$ considered desirable for the SMSS.

It was found that the pointing and IMC requirements of the SMSS can be obtained more economically--with respect to weight, power, size, and cost--by gimbaling the focal plane rather than the entire telescope assembly. The approach is practical because of the wide-FOV optics of the SMSS, the very low Orbiter drift rates that require correction, and the relatively



small pointing excursions that are expected. The required gimbal module would occupy the space directly behind the focal plane, and the telescope obscuration would be the same as for a stationary focal plane. This method, described in detail in paragraph 7.3, is recommended for the SMSS.

4.6 CALIBRATION

A precise quantitative estimate of desirable data quality is difficult to make because users of remote-sensor data have widely varying requirements that are still being refined as experience is gained.

Relative and absolute accuracies in the range from 1 to 5%, for example, have been estimated as necessary in the visible and infrared spectra for agricultural and geological users (Ref. 4-10). Relative accuracy between spectral channels is of prime importance for signature analysis. The radiometric-calibration goal established for LANDSAT (ERTS-1) was an absolute accuracy of 5%. This can be considered as an upper limit for more advanced systems like the SMSS--a reasonable assumption because of the lack of facilities to verify compliance with more precise radiometric specifications and the lack of detailed specifications. Even the best radiometric standards for laboratory use have until recently been only 5% accurate.

Space radiometry has introduced new factors such as the long-term stability of visible sources, surfaces, and optical components when exposed to the high vacuum and ionizing particles of space. Systems with large fields of view like the SMSS are also difficult to calibrate.

The approaches in NASA programs such as the Earth Radiation Budget (ERB) experiment (Ref. 4-11) involved calibration of the spaceborne sensors (spectral response from 0.2 to 50 μm) using the sun, an enclosed 100-W tungsten-halogen lamp, and specially constructed blackbody units. The desired accuracy ranged from ± 0.5 to $\pm 3\%$ for each of 22 channels, with a desired precision or repeatability of ± 0.2 to $\pm 1\%$. In the ERB program, a primary transfer instrument similar to the flight units was maintained for transfer-calibration purposes before and after flight.



Calibration of the pushbroom-type SMSS unit presents special problems that are not encountered by mechanical and other scanners and are related to (a) a 100% duty cycle, (b) a wide viewing angle, and (c) the numerous detector elements. First, detector calibration must occur at the expense of viewing time. A mechanically scanning sensor (either image or object plane), however, can use inactive portions of the scan for viewing calibration sources and for zero restoration without losing scene data. The mechanical scanner also permits a variety of relatively large calibration sources to be mounted in the sensor structure without vignetting the focal plane. Second, the SMSS telescope will be viewing the earth constantly, and calibration against the sun or a deep-space zero reference would be difficult. These operations are less difficult in a dedicated spacecraft. Third, the pushbroom sensor requires that a large number of detectors be individually calibrated so that the pixel-to-pixel response is uniform.

If the earth scene is not masked out, calibration must be performed (a) for the visible channels, on the dark side of the earth, and (b) for the thermal channels, over a portion of the earth that is very cold or whose surface temperature and emissivity are known rather accurately. Because these restrictions could reduce SMSS utility, an alternative method is required. Relative detector response using two or more energy levels for all the calibration sources could be employed without earth-scene blocking, but absolute calibration is precluded by the fact that the earth scene is recorded simultaneously with the calibration signals.

Earth-scene interference can be countered by blocking during the calibration sequence. The signal channels can be blocked with a movable shutter during the period when the detectors are illuminated by the calibration sources. If the calibrator sources scan the focal plane in the cross-track direction on command while simultaneously blocking the earth scene, only portions of the scene would be lost at any given time. Furthermore, if the calibrator sources scan all ten channels simultaneously while the shutter is kept narrow, not all colors for a particular ground element would be lost at the same time. The reason is that the signals from nine of the ten channels

must be delayed before recording, in order that data from a particular ground element will be recorded concurrently for all the operating channels. This situation occurs because the channels are physically separated in the track direction.

As a result of the delay, the calibration signal would appear to plot a diagonal line across the scene for a particular channel. The other channels would plot similar parallel calibration lines. Consequently, scene information from some of the operating channels would always be present during calibration.

Implementation of the calibration system includes the application of linear light-emitting-diode (LED) arrays under spectral-channel filters to directly illuminate the detectors. Single-pass-band filters are used, and a shutter device is incorporated to block the earth scene during calibration. This method is illustrated schematically in Figure 4-11.

The focal plane will be calibrated with primary sources (blackbodies, lamps, etc.) during factory and prelaunch checkout. The data obtained at that time will be employed to establish the LED levels to be used for in-flight calibration. Two or more calibration-radiance levels can be established for each channel to approximate the scene range by merely pulsing the LEDs with a wave train of the desired number of voltage levels.

Aerojet and others have employed LEDs extensively to calibrate visible-spectrum and IR detectors. Their use is relatively simple, they are stable for long periods, and they can be pulsed electrically without resorting to the chopping devices required for blackbody calibrators.

The shutter/LED device can be developed without the application of new technology and should present no special problems. The proposed calibration system is described in Section 9.



675-1149

4-39

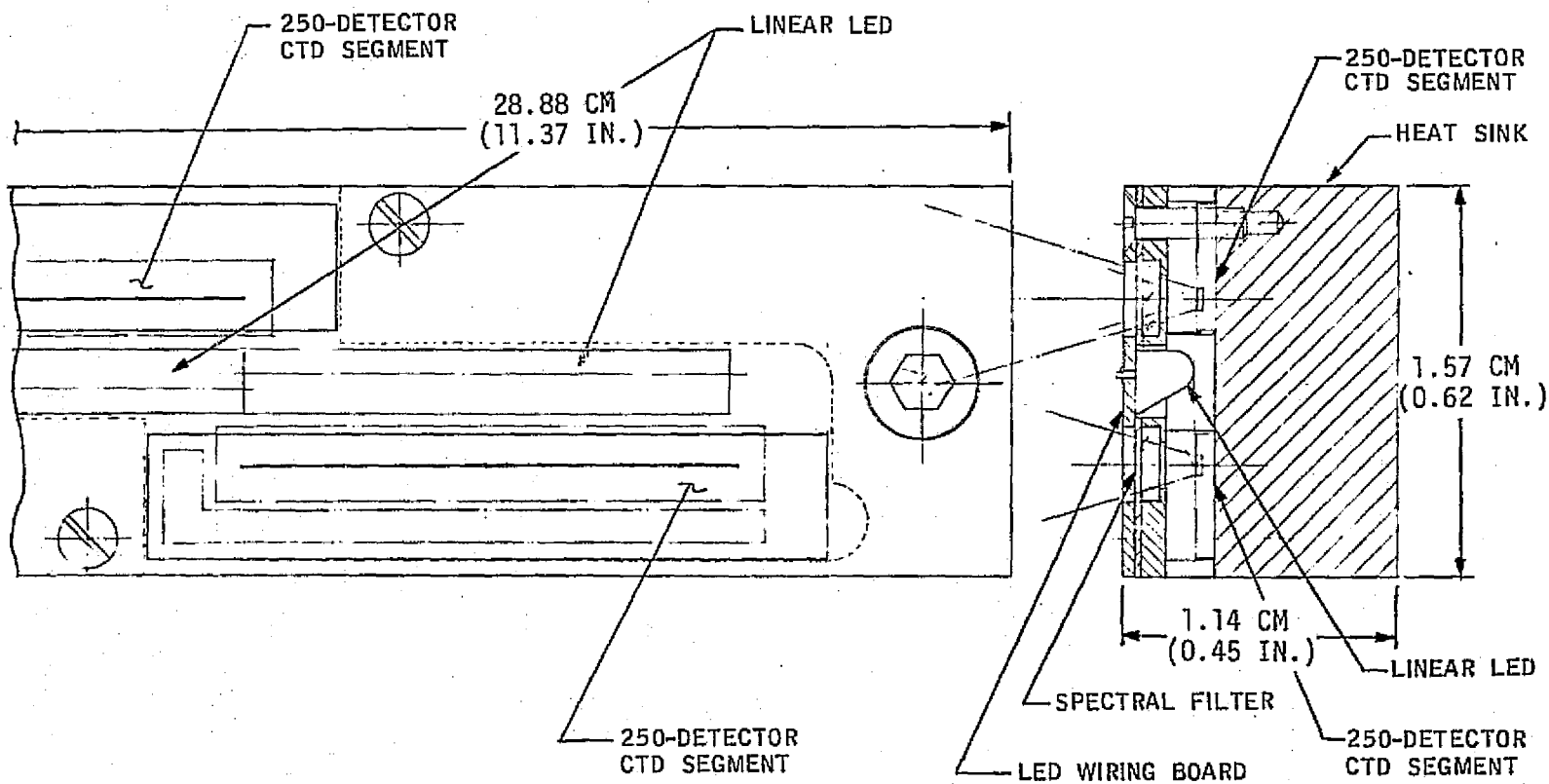


FIGURE 4-11 TYPICAL LONG-WAVELENGTH CHANNEL

4.7 SENSOR CONTAMINATION

The problem of sensor contamination in the Space Shuttle System environment has been recognized as an area of concern (Ref. 4-12). Multiple-payload mission sharing will be required, which increases the possibility of contamination. Preliminary information suggests it would be impractical to prohibit the venting of gaseous and particulate contaminants but that careful design and operational countermeasures can limit the effect on optical and radiant-cooling surfaces.

The SMSS will be mated in the Orbiter Processing Facility, on whose characteristics little information is now available. Unless a very high level of air cleanliness is maintained continuously, particulates can be deposited on surfaces within the Orbiter cargo bay. Conditioned-air purging is to be maintained after payload-bay closure up to 30 min before external-tank loading and to be continued with gaseous nitrogen until liftoff. If there is a requirement to open the bay doors at the launch pad, the operation will be conducted in an environmentally controlled payload-changeout room. The potential incompatibility between the GN₂-purged payload bay and the air-purged changeout room has not yet been established.

After launch, the Orbiter payload bay is vented and remains unpressurized until the reentry phase. As a design goal, overboard dumping of gases and liquids will be controlled to avoid contamination. Although the RCS-system exhaust will represent a major contamination source for the SMSS, its impact will be minimal because the combustion products are gaseous at the temperature of the SMSS structure and optics (~300°K).

It has been estimated (Ref. 4-12) that, over an extended period of operation, sensor performance could be degraded slightly by radiation absorption due to deposition on mirrors and, to a larger extent, by loss of resolution due to deposition-related scattering.

The recommended SMSS design will minimize sensor contamination by providing a closure in the telescope barrel to seal the entire system from the environment. In addition, the focal-plane assemblies will be housed in Dewar vessels with windows/filters to protect the detector arrays from contamination and to permit factory and prelaunch checkout without resorting to a space-simulation system. Protection of the detector arrays from contamination would be a secondary benefit.



Section 5

OPTICAL SYSTEM

5.1 GENERAL CONSIDERATIONS

This section describes some of the optical system parameters investigated for possible SMSS application and discusses their effect on the final recommended design. As a result of the study and consideration of these system parameters (detector dwell time, data rate, sensitivity requirements, resolution, etc.), an all-reflective Schmidt telescope, with the mirrors and structure manufactured from beryllium, is recommended for the SMSS. A schematic representation of the Schmidt system is shown in Figure 5-1.

After several iterations, it was determined that a nominal aperture of 75 cm with $f/1.7$ optics appears to be the most suitable. This system will size properly for the Orbiter payload bay and will provide $66\text{-}\mu\text{m}$ resolution, which corresponds to a scene resolution of approximately 12 m across a swath width of 15° . It will be compatible with the proposed recorder-data-rate limitations, and will permit achievement of a 0.1° NE Δ T and a 0.1% NE Δ p (disregarding atmospheric-transmission effects) using detectors with modest D^* performance. The detector yield during focal-plane fabrication will thus be relatively high.

The initial considerations in selection of suitable candidate optical systems depended in particular on (a) aperture diameter, (b) system focal ratio ($f/\text{no.}$), (c) field of view, both instantaneous and total for a system with scanning, (d) wavelength region of operation, and (e) image quality and target resolution. Other important parameters were (a) transmission, including any obscuration of vignetting, (b) scanning approach, and (c) mechanical, environmental, thermal, and other constraints. These parameters are interrelated and were considered iteratively, together with the



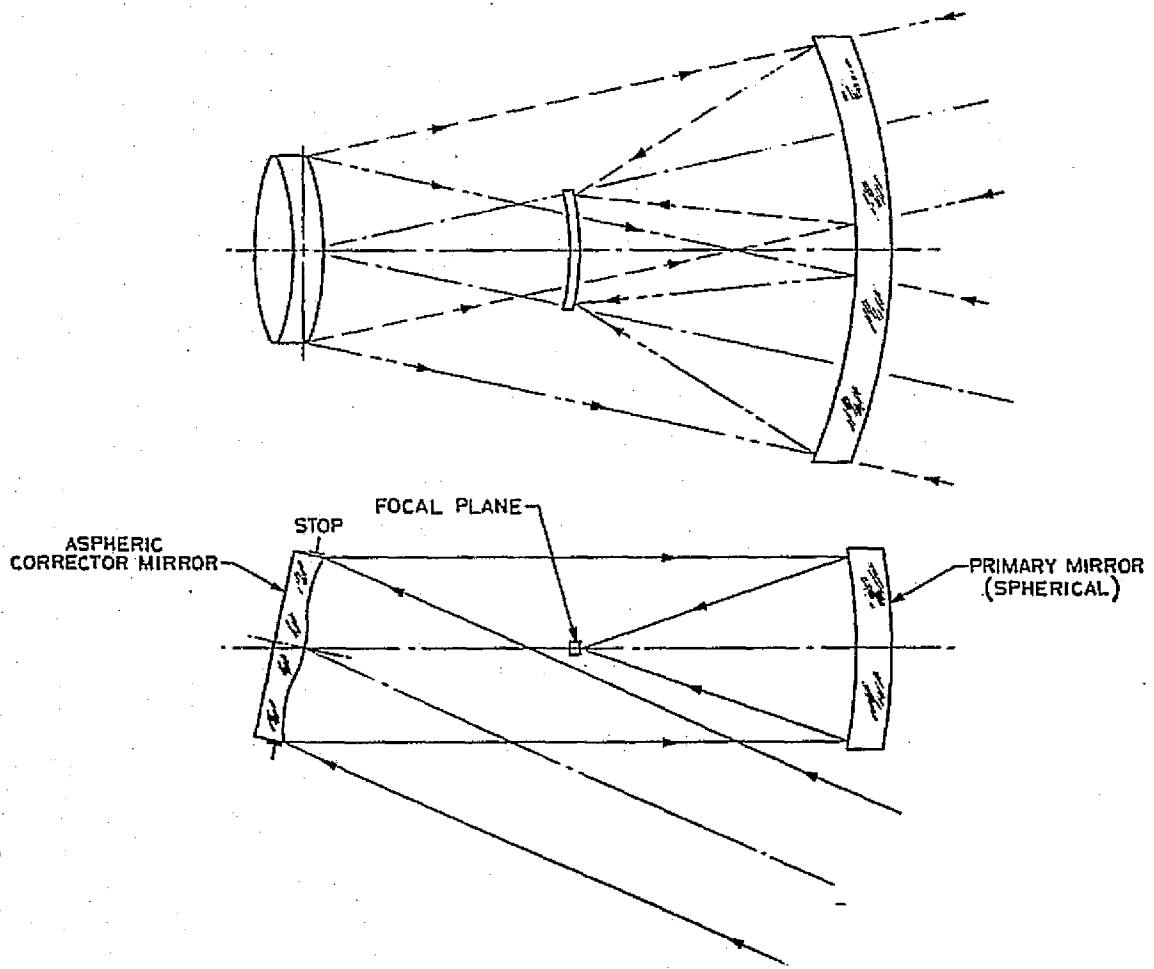


FIGURE 5-1 ALL-REFLECTIVE SCHMIDT, OPTICAL SCHEMATIC

desired use of the system. Appendix B covers the parameters considered and general optical background data.

The planned earth-resources orientation of the SMSS necessitates sensor operation from at least $0.45 \mu\text{m}$ in the visible spectrum to $12.5 \mu\text{m}$ in the long-wavelength infrared. Spectral channels outside this region may be proposed later in the development or even after the SMSS becomes operational. Because no refractive materials are presently available that transmit over this wide spectral range and also have suitable physical characteristics, it was considered necessary to limit the investigation to a study of all-reflective optics.

A scene or ground resolution of 10 m was arbitrarily selected as a first iteration baseline. This value was later changed to 12 m at an altitude of 185 km (100 nmi), based on system considerations of dwell time, sensitivity, and available detector sizes. Furthermore, the maximum aperture diameter considered practical for telescope installation in the Orbiter was initially considered to be approximately 1 m. Figure 5-2 shows the relation between scene resolution, Orbiter altitude, and wavelength for a 1-m aperture. Early investigations were based on that 1-m value. Again, the aperture was later reduced to 75 cm during the tradeoff portion of preliminary-design development.

Early in the study, an arbitrary criterion of 10 m was established for scene resolution with $10\text{-}\mu\text{m}$ radiation from a 185-km altitude. This criterion resulted in a required diffraction-limited aperture of approximately 45 cm, which was increased to 100 cm to account for geometric aberrations as a convenient size on which to base the various trade studies.*

* The operational limit of the optical system is determined by the diffraction of the observed radiation. The angular diameter of the first dark ring, or Airy disk, of the diffraction pattern for a circular, unobstructed aperture is given by $\beta = 0.244 \lambda/D$, where β is the angular diameter of the disk in milliradians, λ is the wavelength in micrometers, and D is the aperture diameter in centimeters.



5-5

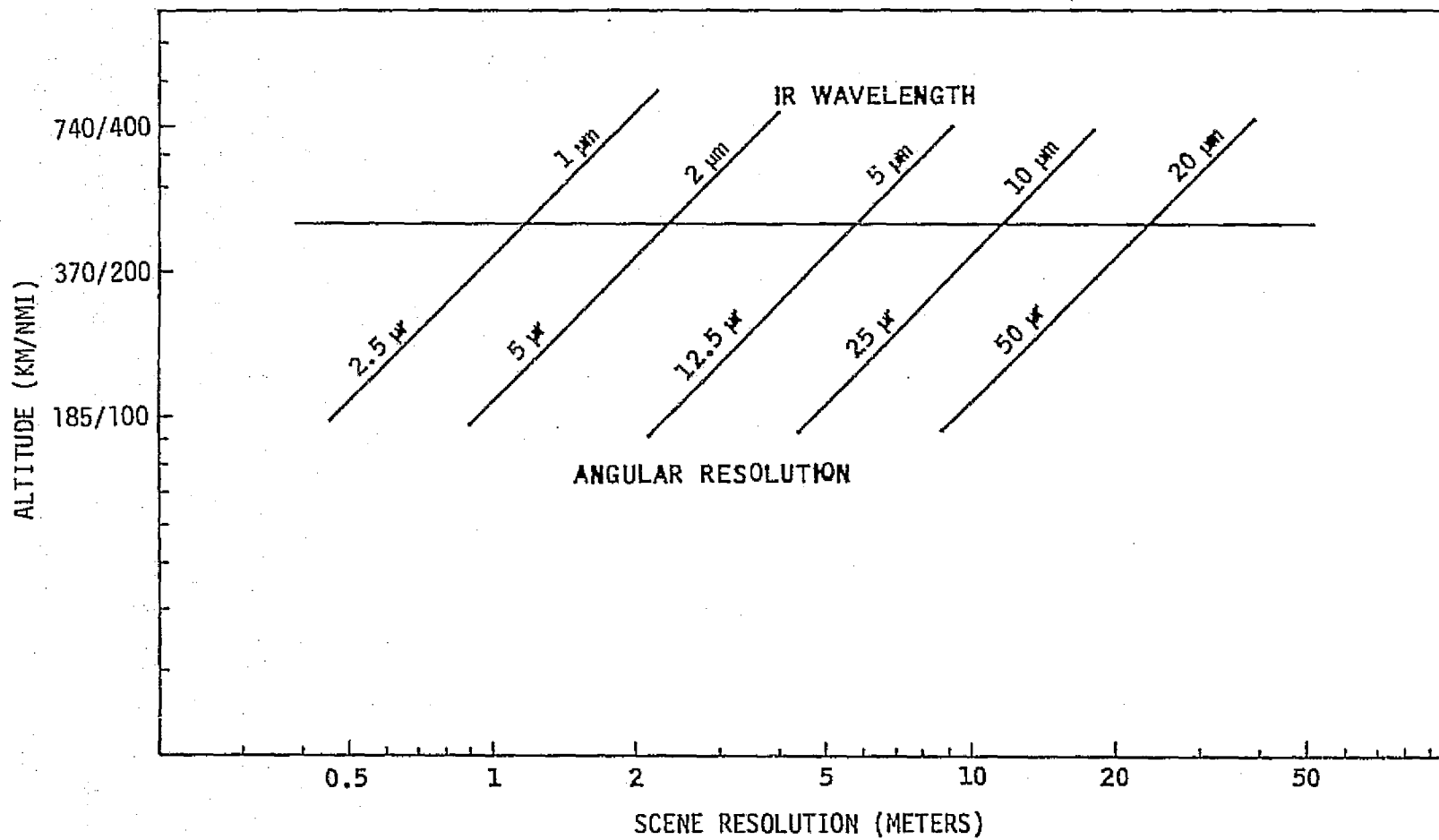


FIGURE 5-2 IR DIFFRACTION-LIMITED RESOLUTION FOR 1-METER APERTURE

5.2 RECOMMENDED TELESCOPE CONFIGURATION

Figure 5-3 depicts the SMSS telescope-assembly design that was evolved during this study. The assembly is shown as it would appear when mounted on the European Space Agency standard 3-m pallet. It features readily demountable subsystems that can be modified, repaired, substituted, or reconfigured as required for specific missions, and as new technologies permit improvement. They can also be removed as necessary for cleaning or refurbishment. The intent of the design has been to provide

- Maximum versatility through modularization
- Maximum utilization of the Orbiter by imposition of minimum interface requirements
- Minimum interference with Orbiter systems or with other Orbiter payloads.

The proposed SMSS system design includes the following subsystem modules: (a) primary mirror and mount, (b) corrector mirror and mount, (c) aperture closure, (d) sun and albedo shade, (e) focal-plane/Dewar assembly, (f) focal-plane gimbal, (g) cryogen-storage units, and (h) electronic-data-handling subsystem. The first four of these are covered below. The next three are described in Section 7, and the electronic-data-handling system is covered in Section 8.

The Schmidt primary and corrector modules are shown in Figures 5-4 and 5-5, respectively. The mirrors are on strong-back frames fabricated from rectangular beryllium tubing. Symmetrically located mounting pads provide support. A review of mounting methods for large beryllium optics indicated that the mirrors may be attached rigidly to the supporting frame. This method will provide satisfactory rigidity and will not introduce or permit the distortion of optical surfaces.

The back of the mirror has a honeycomb pattern of hexagonal cells machined in an undercut fashion from circular openings. The finished mirror resembles a sandwiched honeycomb. This approach has been used successfully



875-1804

ORIGINAL PAGE IS
OF POOR QUALITY
5-6

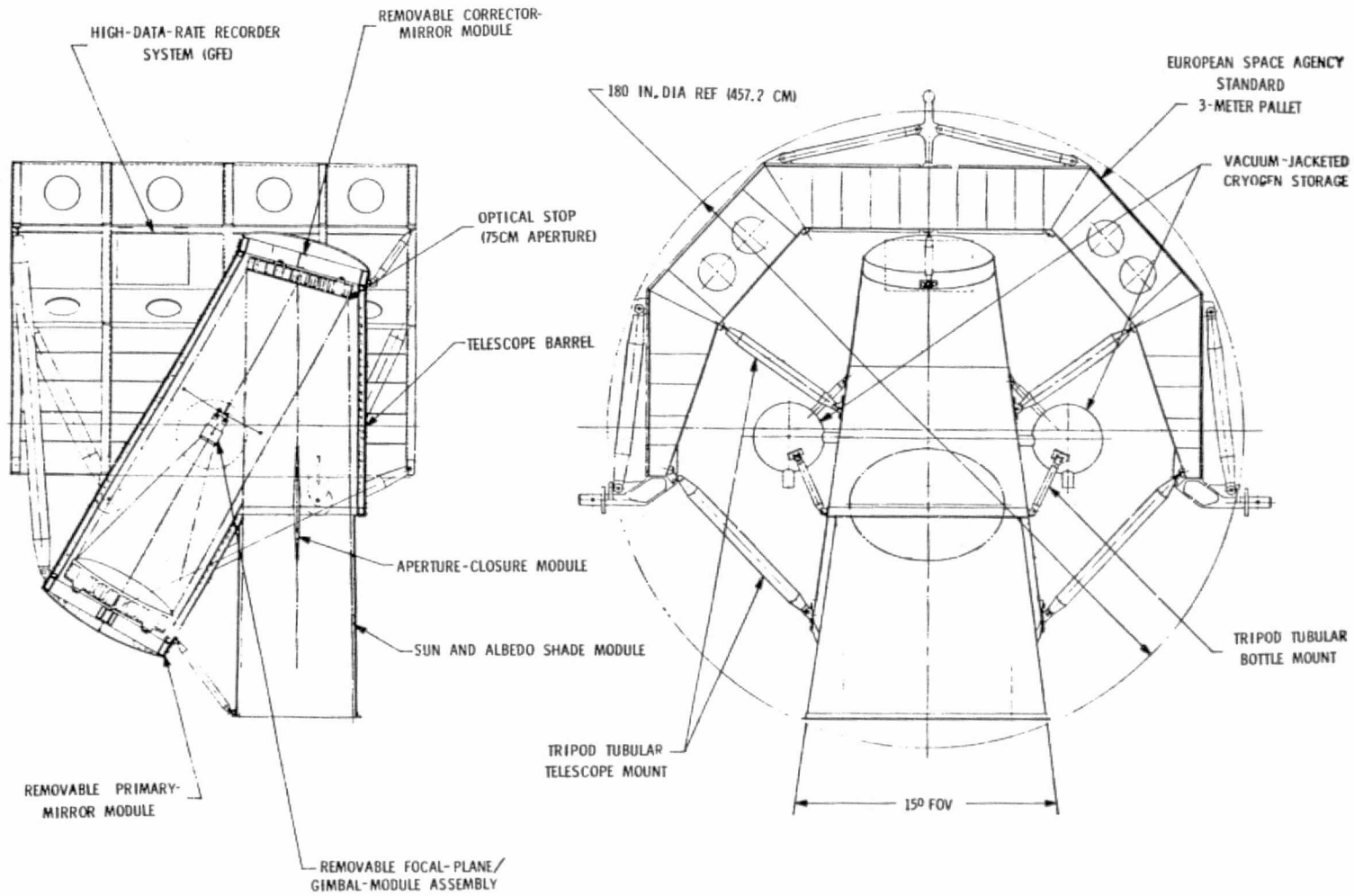


FIGURE 5-3 SMSS TELESCOPE ASSEMBLY

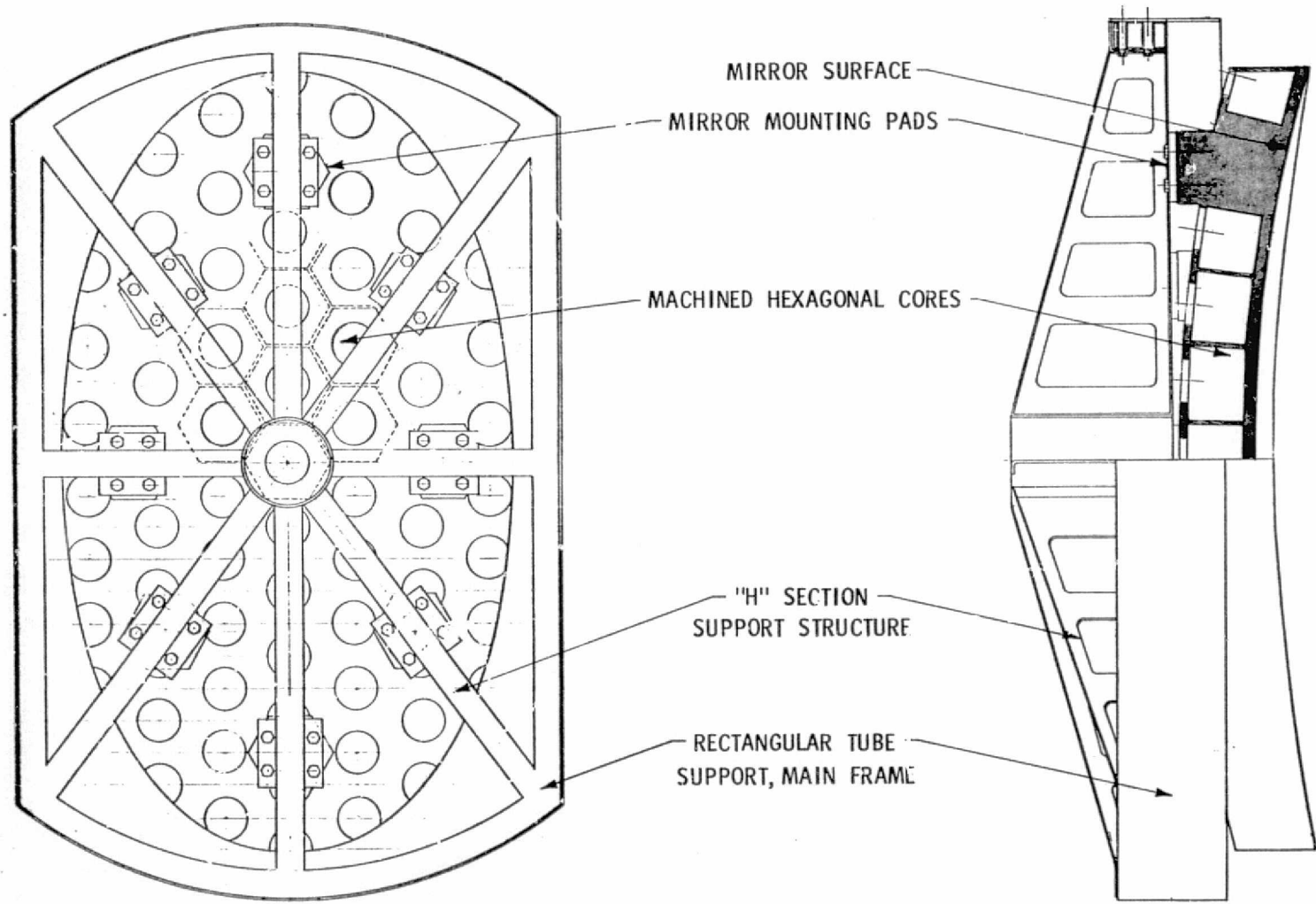


FIGURE 5-4 ALL-BERYLLIUM PRIMARY-MIRROR MODULE

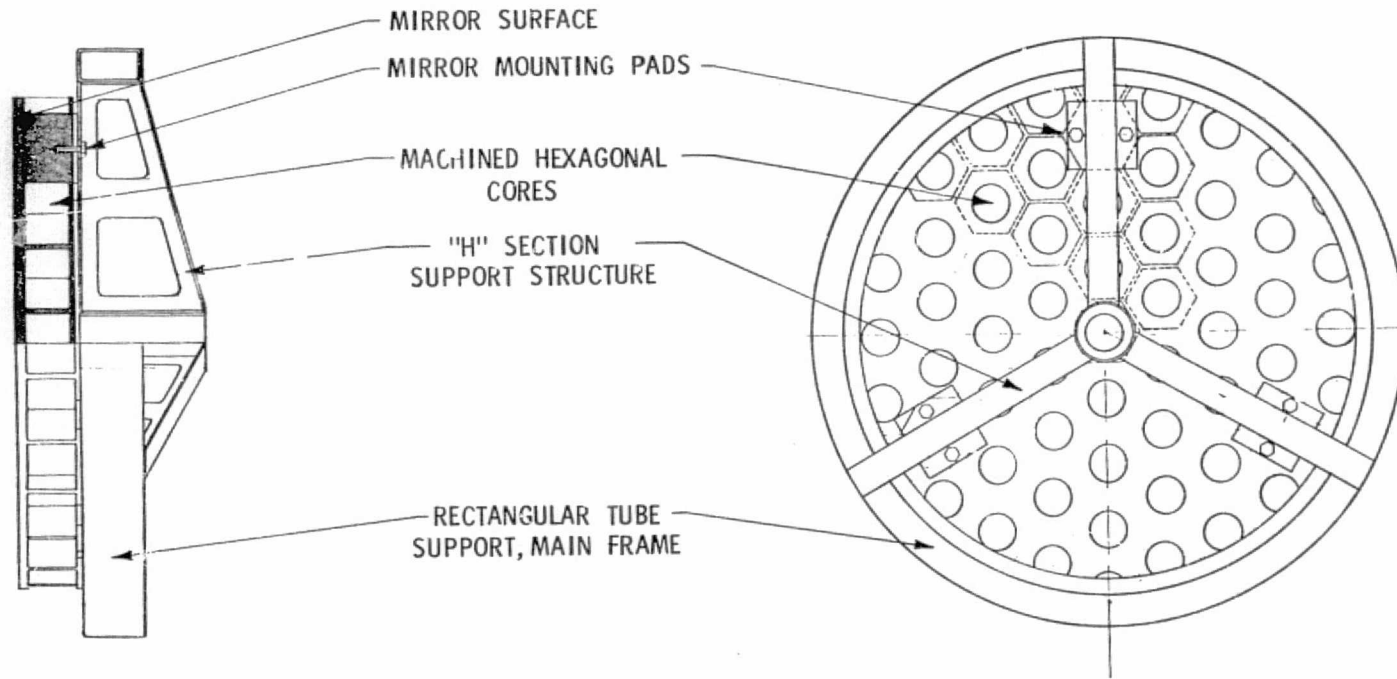


FIGURE 5-5 ALL-BERYLLIUM CORRECTOR-MIRROR MODULE

in fabricating beryllium optics, but computer-assisted analysis will be needed to establish the detailed SMSS design and dimensions.

It is planned that the module assemblies will be attached to the main telescope frame by means of fastener/lock assemblies to permit removal for cleaning, recoating, etc. with minimum impact on mission schedules. The detailed design will incorporate pins that establish the true mirror locations within acceptable optical-system tolerances, so that realignment after reassembly will not be necessary.

The aperture-closure and sun/albedo-shade modules are shown incorporated in the SMSS telescope assembly in Figure 5-3.

A possible telescope fabrication method is illustrated in Figures 5-6 and 5-7. The all-beryllium structure can be fabricated from welded and gusseted "Z" sections to provide an extremely strong, lightweight skeleton. An inner and an outer skin of beryllium sheet can then be bonded to the Z surfaces to provide a monocoque type of structure. The space between the skins will be filled with a superinsulation material attached to the inner skin with plastic standoffs. The entire structure will be light and strong and will provide focus maintenance through the expected temperature excursions because the all-beryllium system does not require compensation.

Details leading to selection of the all-reflective Schmidt system are provided in Appendix B.



ORIGINAL PAGE IS
OF POOR QUALITY

5-10

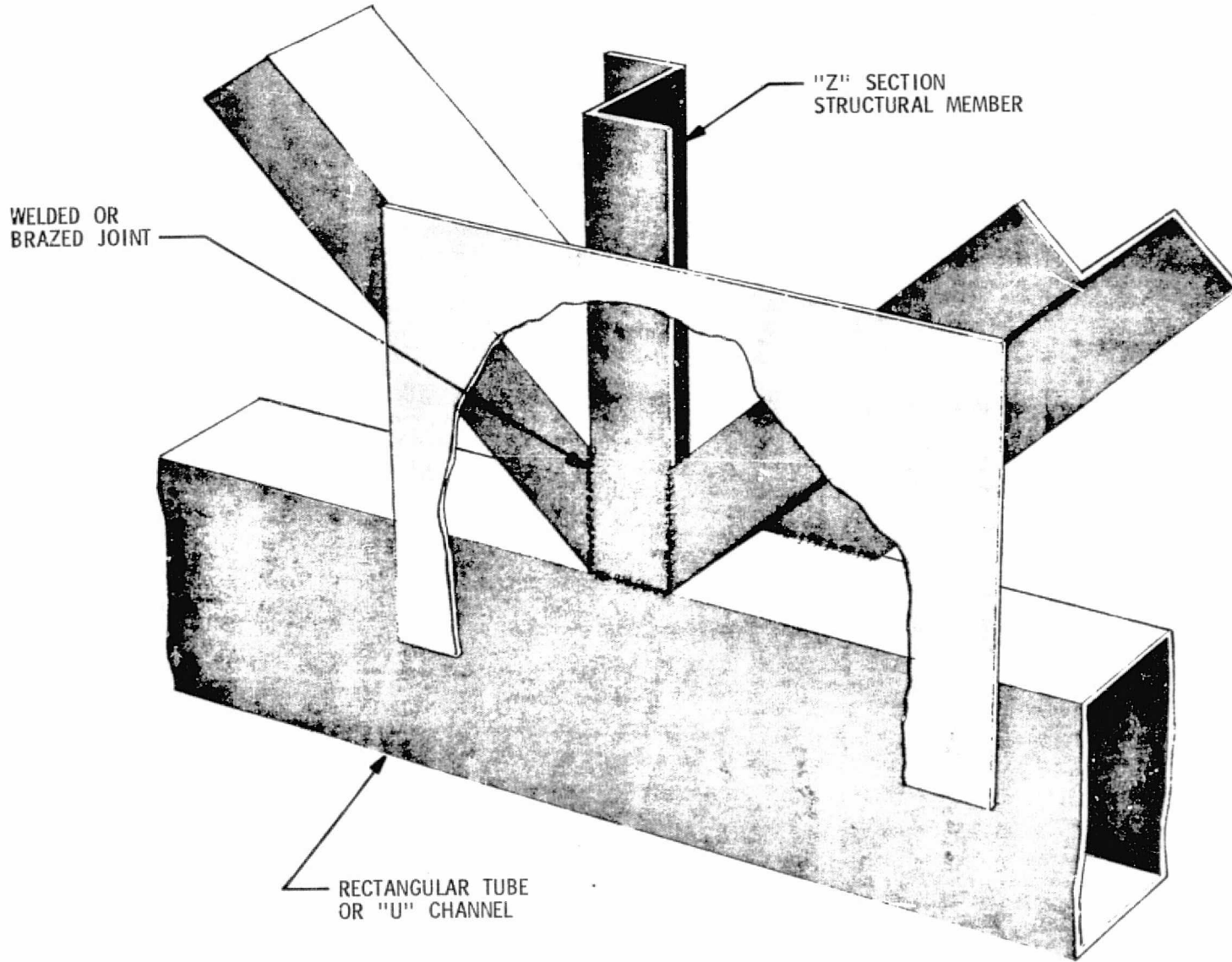


FIGURE 5-6 TELESCOPE-STRUCTURE SKELETON



1175-1356

5-11

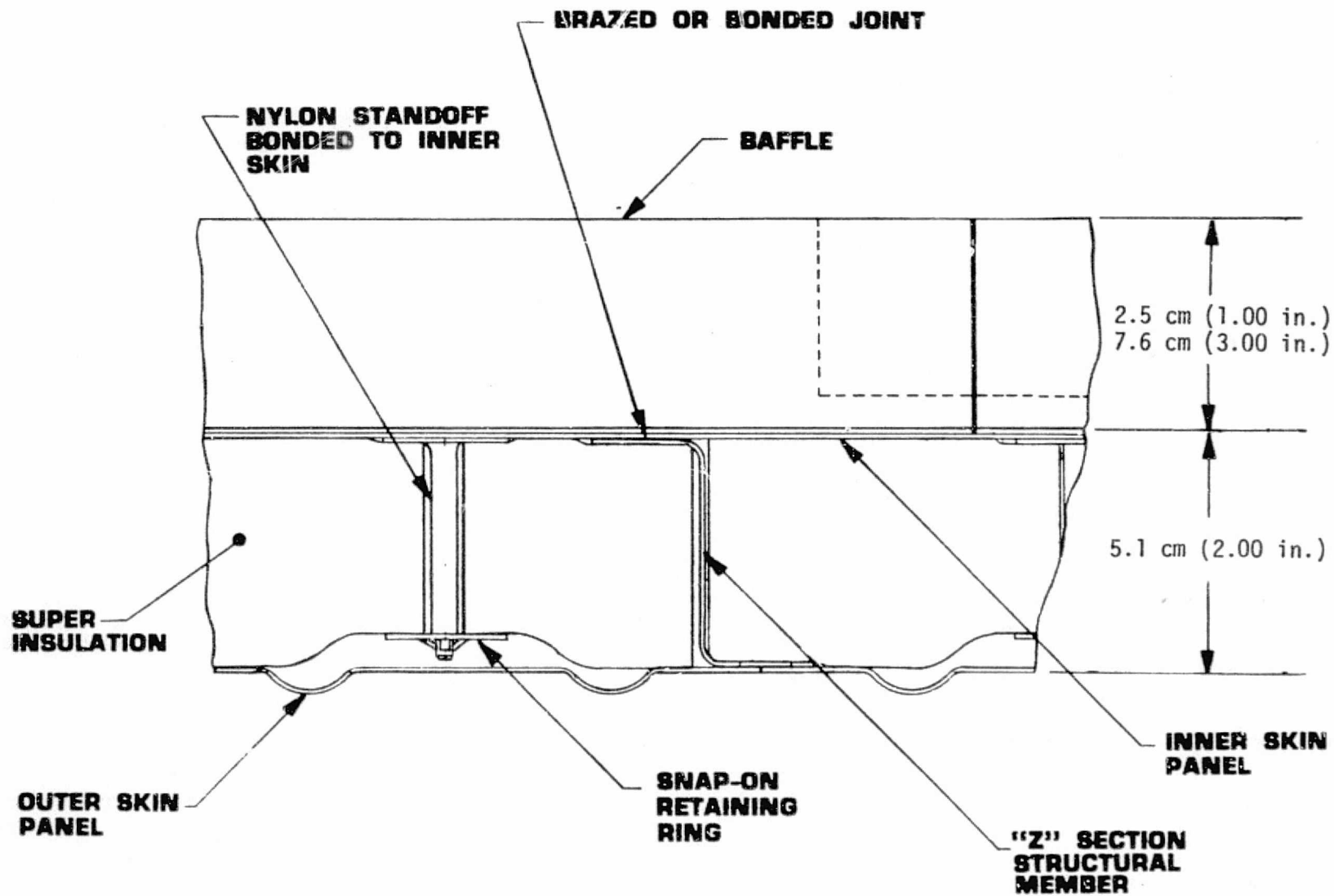


FIGURE 5-7 TYPICAL TELESCOPE-BARREL SECTION

Section 6

DETECTOR/CTD TECHNOLOGY AND FOCAL-PLANE DESIGN

The solid-state pushbroom-sensor concept appears viable because of rapid progress in CTD technology for commercial and Government use. Sequential readout of large arrays eliminates the need for individual pre-amplifiers for all detector elements and minimizes the complexity of the focal-plane electronic interface. Low-cost batch fabrication makes it practical to use several thousand picture elements (pixels) for each spectral band.

The CTD imaging devices have high reliability, high packing density, and low power requirements, and provide flexibility in module design. The quantum efficiency of silicon is high in the visible and near-infrared regions of the spectrum, and the dynamic range of silicon CTDs is broad. Hybrid combinations of infrared arrays with silicon CTD processing will permit extension of CTD technology to the long-wavelength spectral bands. These considerations are discussed below, and a focal-plane design concept using presently available CTDs is presented.

The bands designated as technical guidelines are as follows:

<u>Detector Channel No.</u>	<u>Bandwidth (μm)</u>
Short Wavelengths	
1	0.45 - 0.52
2	0.52 - 0.60
3	0.63 - 0.69
4	0.69 - 0.75
5	0.80 - 0.95
Long Wavelengths	
6	1.55 - 1.75
7	2.05 - 2.35
8	3.5 - 5.0
9	8.2 - 9.3
10	10.4 - 12.5



6.1 DETECTOR MATERIALS AND TYPES

Silicon devices can be used for detection in the first five of the foregoing bands. This material has been developed extensively for multiple-element arrays, including those with CTD serial readout. Although the spectral response of silicon falls off toward ultraviolet wavelengths, UV-enhanced Schottky-barrier photodiodes have been developed with a response that is down only 40% from the peak at 0.45 μm . Gallium arsenide (GaAs), with a spectral response similar to that of silicon, could also be used in these bands but has a lower sensitivity. Photomultipliers can have higher quantum efficiency at short wavelengths, but they are better suited for large single detectors than for arrays of small elements.

Silicon CTDs have been employed in commercial imaging applications (see Table 6-1) and have been incorporated into advanced deep-space instrumentation by the NASA Jet Propulsion Laboratory. Measured spectral sensitivities of General Electric Company charge-injection devices (CIDs) suggested for the visible and near-infrared SMSS channels indicate detectivities (D^*) in excess of 10^{10} $\text{cm}\cdot\text{Hz}^{1/2}/\text{W}$ for all channels for average room-temperature (25°C) dark current ($6 \text{ nA}/\text{cm}^2$) (incident radiant power density of $0.01 \mu\text{W}/\text{cm}^2$ at a $0.67\text{-}\mu\text{m}$ peak response). The visible-sensor portion of the focal plane may be maintained at some temperature slightly lower than 25°C in order to assure adequate sensitivity in all channels. The most severe requirement occurs for Channel 1 ($0.45\text{-}0.52 \mu\text{m}$), where the minimum spectral-radiance change is lowest (see Table 2-4, above) and the spectral response of silicon is also lowest.

A survey of infrared charge-transfer devices (IRCTDs) indicated that several categories of candidates should be available in the near future. Monolithic and hybrid IRCTD techniques that were investigated are shown in Table 6-2.





TABLE 6-1 COMMERCIALY AVAILABLE CTD ARRAYS

Manufacturer	No. of Pixels per Array		Minimum No. of Arrays for 5 Visible Channels at 4000 Pixels Each	Output Data Rate per Array (kHz)	Physical Size (mm)	
	As Designed	As Applied to SMSS			Chip	Raster
Linear Arrays (As Applied)						
Fairchild	1728x1	247x1 (requires lens)	83	156	23x1.5	22.5x0.013
Texas Instruments	160x5	40x1	495	25	-	3.7x0.115
Area Arrays						
Fairchild	190x244	63x48	64	200	6.3x6.1	5.7x4.4
Texas Instruments	400x400	100x100	40	309	-	9.2x9.2
RCA	320x256	106x85	38	334	12.7x19.0	9.9x7.8
General Electric	188x244	94x122	33	386	-	8.6x11.4
General Electric	100x100	100x100	40	309	7.2x8.8	6.4x8.4

6-3

Report 5231



TABLE 6-2 IRCTD CANDIDATES FOR SMSS*

Monolithic				Hybrid	
Inversion Mode	Accumulation Mode	Schottky Barrier	Charge Injection	Direct Injection	Indirect Injection
Intrinsic photo-voltaic: ** PbTe & InSb (3-5 μm), PbSnTe (8-12 μm) Extrinsic minor-ity carrier: Si:Ga (8-12 μm)	Extrinsic majority-carrier photoconductive: Si:As (8-12 μm), Si:Se & Si:In (3-6 μm)	Internal photoemission: Palladium on silicon (1-3 μm), PbSnTe (8-12 μm)	Direct-current-coupled minority carrier: InSb (1-5 μm)	Direct-current-coupled photovoltaic: InSb (3-5 μm), PbSnTe (8-12 μm)	Buffer-stage photoconductive: PbS (1-3 μm)
* Si:Ga, gallium-doped silicon. InSb, indium antimonide. Si:As, arsenic-doped silicon. Si:Se, selenium-doped silicon. Si:In, indium-doped silicon. PbS, lead sulfide. PbTe, lead telluride. PbSnTe, lead-tin telluride. ** Not yet verified experimentally.					

6-4

Intrinsic detectors have been used for inversion-mode monolithic devices with minority carriers. Extrinsic detectors have been used in accumulation-mode majority-carrier devices, but at least in one case have been found to provide a higher transfer efficiency in the inversion mode (Si:Ga, with long-IR-wavelength response, using p-type gallium substrate).

The Schottky-barrier device has a different structure than that of the usual monolithic MOS (metal-oxide semiconductor), and is based on internal photoemission from a metal-semiconductor barrier on a silicon substrate. The responsivity is more uniform than for most arrays (about 1%), and Schottky barriers may be good candidates for high-background applications in which the contrast is low, if the sensitivity can be made sufficiently high. Palladium silicide at 77°K has a response in the band from 1 to 2.5 μm .

Charge-injection devices have been made at IR wavelengths using only one material, InSb. The sensitivity is excellent throughout the 1- to 5- μm band (e.g., for Channels 6 through 8 of the SMSS), and is linear over a wide dynamic range (more than 10^5 in some cases).

Direct-injection hybrid devices are useful only with detectors operating at low direct currents, such as photovoltaic InSb and PbSnTe, which can be dc-coupled to the charge-transfer register, generally through a diode. They may have advantages over the indirect-injection types, which require a buffer stage between the photodetector and the shift register. However, photoconductive films that can be deposited on silicon dioxide without inducing interface problems may provide easily fabricated IRCTDs.

The monolithic candidates may eventually prove slightly superior, by combining the attractive features of high sensitivity, high uniformity, low cost, and low power dissipation. The hybrid candidates, however, should be available sooner for the first Shuttle Orbiter applications, and offer serial-readout capabilities without loss of sensitivity.



A significant advantage of a larger-aperture instrument such as the baseline SMSS is that the D^* can be well under the ultimate limit and still provide the desired system sensitivity (e.g., NEAT). In addition, the earth-background-radiation limit on D^* makes IR detectors operating near 80°K a more reasonable choice than extrinsic silicon detectors. The latter are ideal in applications that involve a space background and require cooling to much lower temperatures.

The principal 80°K detectors for 8- to 13- μ m radiation (SMSS Channels 9 and 10) are PbSnTe and mercury-cadmium telluride (HgCdTe). The present low-impedance HgCdTe detectors dissipate about 1 mW each and require preamplifiers. They are consequently not as attractive as PbSnTe photovoltaic detectors, which have higher impedance and can be directly coupled to CTD shift registers, minimizing the focal-plane power dissipation and cooling requirements.

At two recent meetings of the Infrared Information Symposia (IRIS) Specialty Group on Infrared Detectors (March 1974 and March 1975), 30 papers were presented on the performance of PbSnTe detectors. The presentations were made by the Army Night Vision Laboratory, Naval Electronics Laboratory Center, Aerojet ElectroSystems Company, Perkin-Elmer Corporation, Santa Barbara Research Center, Philco-Ford, Raytheon, Texas Instruments, Inc., and Rockwell International Science Center. A monolithic PbSnTe IRCTD metal-insulator-semiconductor (MIS) structure is a possible future development. This device, however, is not as promising as the shorter-wavelength PbTe MIS structure, unless significant improvements in materials markedly increase the minority-carrier lifetime, and therefore the possible number of transfers (Ref. 6-1).

Lead-tin telluride diode detectors have already been coupled to charge-coupled-device (CCD) shift registers (Ref. 6-2), by both direct-injection and buffer-amplifier/gate-modulation input methods. Detectivities above 10^{11} cm-Hz^{1/2}/W (approaching BLIP sensitivity) were achieved at backgrounds corresponding to SMSS earth-scene values and an 80°K operating

temperature. Devices with both types of injection were found to have excellent transfer efficiency at a clock frequency of 75 kHz. At low operating temperatures, when the detector conductance is much less than the CCD input transconductance, the transfer function of signal and noise current into the CCD approaches unity.

For Channels 6, 7, and 8, the choice of detector is not as clear cut. Indium antimonide operated at 80°K is a prime candidate, having been developed in two forms of CTD directly coupled to silicon shift registers--as a CID (Ref. 6-3) and as a hybrid photovoltaic device (Ref. 6-4). Linear arrays of 32 elements have been built in both approaches, as well as two-dimensional versions for at least the CID approach. The element size is appropriate for SMSS application: 50 to 100 μm (2 to 4 mils).

The InSb CID has achieved a D^* in excess of 10^{12} $\text{cm-Hz}^{1/2}/\text{W}$ with low backgrounds at a 4.5- μm wavelength; the dynamic range exceeded 10^5 . The quantum efficiency is nearly constant from 1 to 5 μm . (The relative spectral responses are 50% of peak for Channel 6, 60% of peak for Channel 7, and 90% of peak for Channel 8.) With a 300°K background and a 30° field of view, the blackbody D^* (500°K, 500 Hz, 1 Hz) is 5×10^{10} $\text{cm-Hz}^{1/2}/\text{W}$, which can be equated to a 4.5- μm D_{peak}^* of about 3×10^{11} . This seems adequate for the SMSS application. The photovoltaic InSb coupled to a CCD has also achieved nearly background-limited detectivity (D_{BLIP}^*).

Another good candidate is a hybrid photovoltaic PbTe CTD, similar to the PbSnTe device recommended for Channels 9 and 10. As mentioned above, PbTe might eventually be used as a monolithic CTD.

Lead sulfide elements could also be considered for Channels 6 and 7, and require less cooling than InSb or PbTe. Their response times, however, are longer than the SMSS dwell time, and they may require amplifying buffer stages for coupling to CCDs without a loss in sensitivity.

Figure 6-1 shows the detectivities required in the three longer-wavelength channels in order to meet the system-sensitivity guideline of $NE\Delta T = 0.1^{\circ}K$ with the baseline 75-cm optical aperture at $f/1.7$. The $280^{\circ}K$ values are all about a factor of 35 below those for background-limited photovoltaic detectors viewing a $280^{\circ}K$ background, with 50% quantum efficiency (η) and a 34° full-angle conical field of view ($f/1.7$ optics).

Table 6-3 identifies the baseline detector materials and types of CTDs recommended for the SMSS focal plane together with required detectivities. Figure 6-2 plots required versus available D^* . Monolithic silicon CTD technology for the visible spectrum offers a solution to the multiple-detector problem through low-cost batch fabrication, serial readout, high quantum efficiency, wide dynamic range, high reliability, low power requirements, high packing density, low-noise processing, and absence of solar-overload damage. Monolithic indium antimonide devices and hybrid combinations of IR arrays have a potential for extending CTD technology to the long-wavelength bands.

6.2 CTD SATURATION EFFECTS

The problem of saturation may be significant for Channels 9 and 10. Table 6-4 gives maximum photon-flux values for $f/1.7$ optics using a NASA specification for the maximum visible and infrared ($320^{\circ}K$) radiance. For Channels 9 and 10, the number of photons is an order of magnitude greater than for the shorter-wavelength channels.

The worst case is Channel 10 (the 10.4- to 12.5- μm band), in which a $320^{\circ}K$ scene will provide a background flux of 3.4×10^{16} photons/cm²-sec with an $f/1.7$ cold stop (as compared with 2.5×10^{16} in the 8.2- to 9.3- μm band and 2.4×10^{15} in the 3.5- to 5- μm band). The number of in-band photons incident on an 84x84- μm detector in 1.62 msec is as follows:

$$\begin{aligned} & (3.4 \times 10^{16} \text{ photons/cm}^2\text{-sec}) (7 \times 10^{-5} \text{ cm}^2) (1.6 \times 10^{-3} \text{ sec}) \\ & = 3.9 \times 10^9 \text{ photons} \end{aligned}$$

675-1687

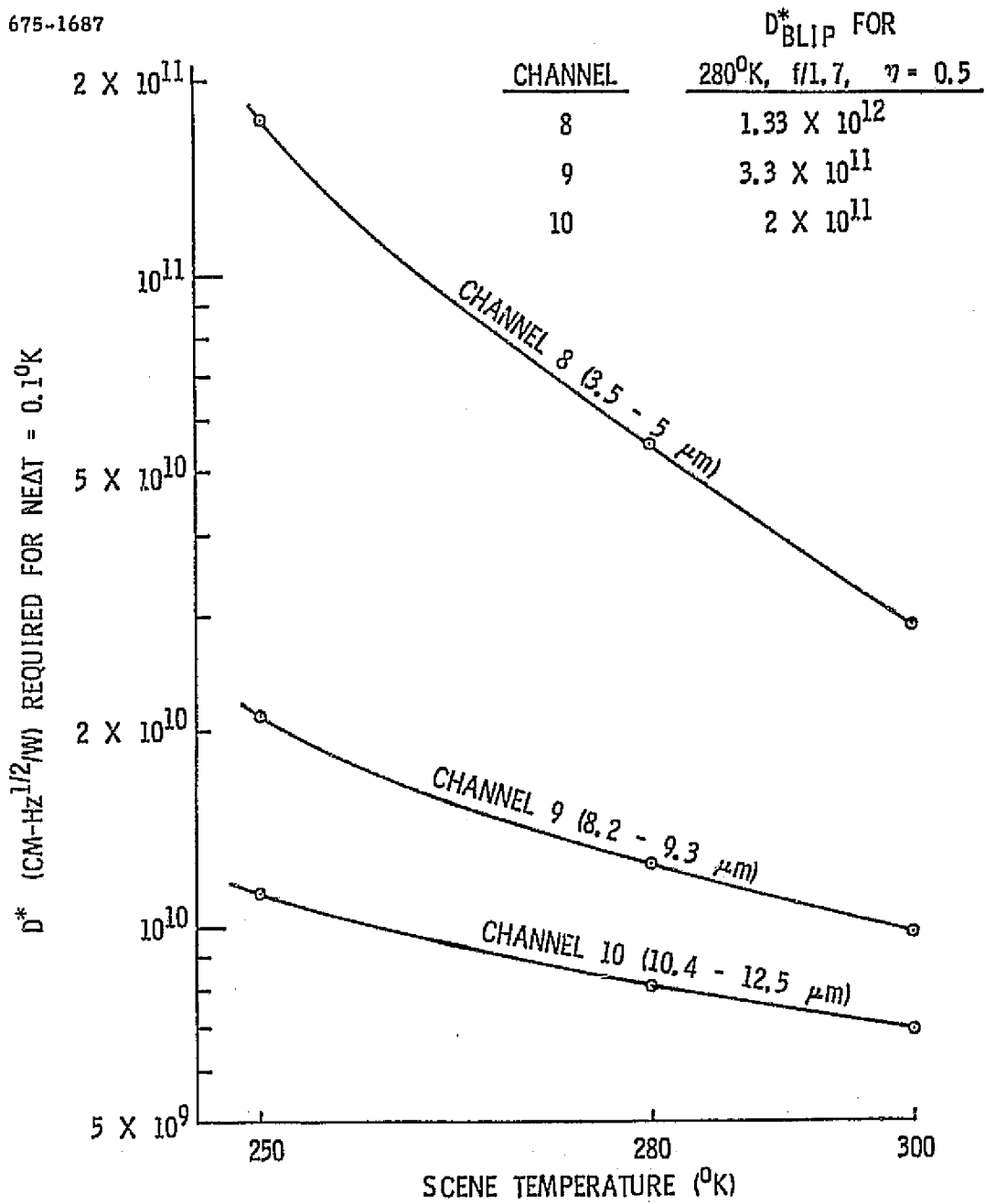


FIGURE 6-1 INFRARED-DETECTIVITY REQUIREMENTS FOR CHANNELS 8, 9, AND 10



TABLE 6-3 RECOMMENDED BASELINE SMSS MATERIALS AND DEVICES[†]

Channel No.	Spectral Pass Band (μm)	Detector Material	Type of CTD	Spectral Radiance Change ($\text{W}/\text{m}^2\text{-sr}$)	Required D^* ($\text{cm-Hz}^{1/2}/\text{W}$)
Short Wavelengths--Operating Temperature = 300°K					
1	0.45-0.52	Si	CID	0.010	1.9×10^{10}
2	0.52-0.6	Si	CID	0.022	8.7×10^9
3	0.63-0.69	Si	CID	0.024	8.0×10^9
4	0.69-0.75	Si	CID	0.025	7.7×10^9
5	0.8-0.95	Si	CID	0.06	3.2×10^9
Long Wavelengths--Operating Temperature = 80°K					
6	1.55-1.78	InSb	CID	0.014	1.4×10^{10}
7	2.05-2.35	InSb	CID	0.004	4.8×10^{11}
8	3.5-5	InSb	CID	0.00347 ^{††}	5.6×10^{10}
9	8.2-9.3	PbSnTe	Hybrid direct injection	0.0152 ^{††}	1.3×10^{10}
10	10.4-12.5	PbSnTe			
[†] Optical aperture = 75 cm. Focal ratio = f/1.7. Optical efficiency = 0.5. Electronic efficiency = 0.8. Instantaneous field of view, IFOV = 66 μr . Solar-irradiance values calculated for albedo = 30%, using minimum NASA Goddard Space Flight Center specifications for Earth Observation Satellite (EOS) radiance in Ref. 6-5.					
^{††} Values for $\Delta N/\Delta T$ [$\approx N_{\Delta\lambda} c_2/\lambda T^2$, where ΔN = radiance change, ΔT = temperature change, $c_2 = hc/k$ (where c = velocity of light in a vacuum, h = Planck's constant and k = Boltzmann's constant), λ = wavelength, and T = temperature (°K)] obtained by interpolation from tables in Ref. 6-6 for use in computing the radiance contrast of small temperature inhomogeneities.					

1175-1308

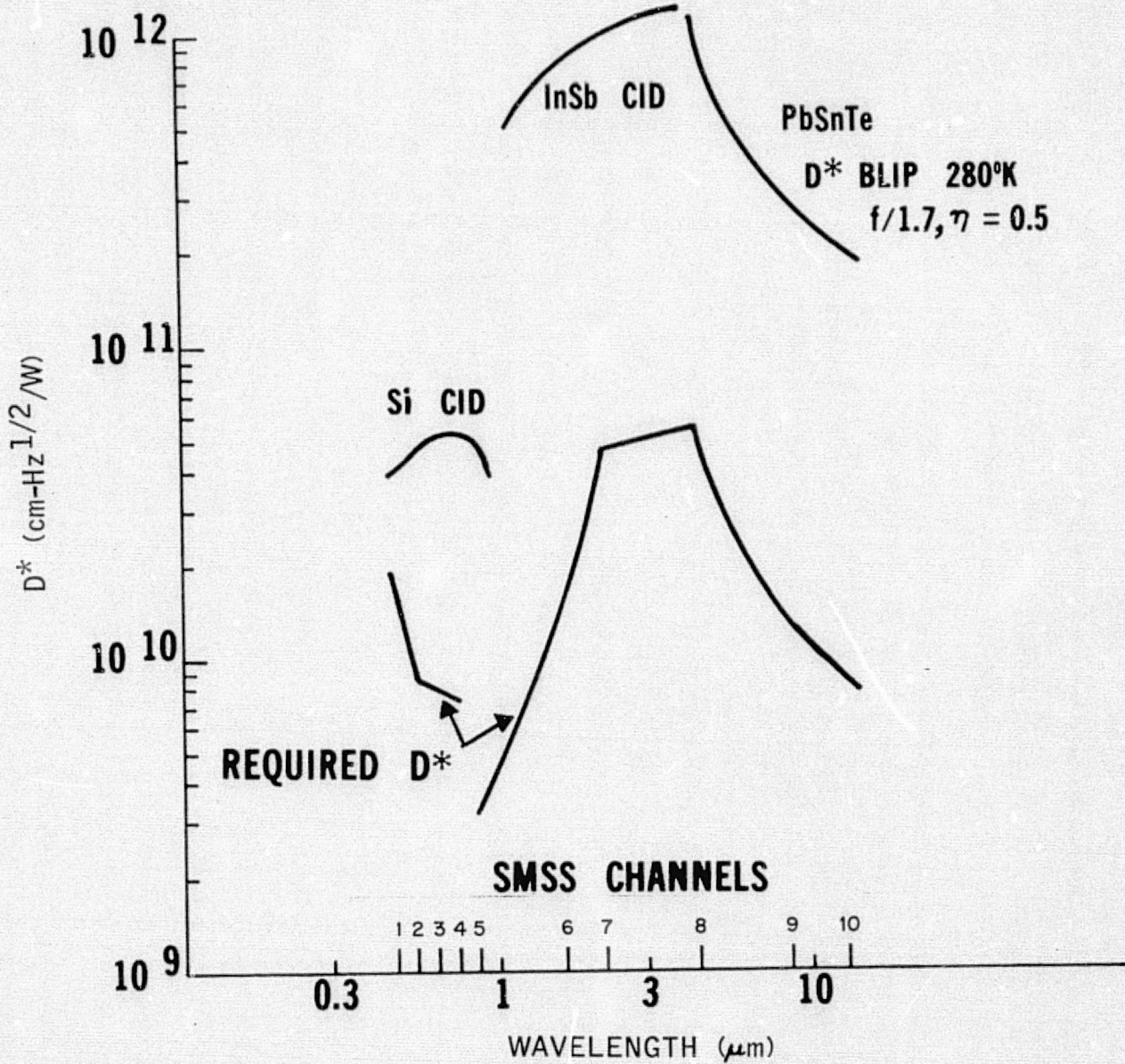


FIGURE 6-2 REQUIRED D^* VS AVAILABLE D^*



TABLE 6-4 MAXIMUM-RADIANCE, DYNAMIC-RANGE, AND PHOTON-FLUX DATA

Channel No.	Spectral Band (μm)	Radiance ($\text{W}/\text{m}^2\text{-sr}$)			Photon Flux (10^{15} photons/ $\text{cm}^2\text{-sec}$)
		Maximum	Minimum Change	Required Dynamic Range	
1	0.45 - 0.52	21	0.010	2100	1.3
2	0.52 - 0.60	24	0.022	1100	1.8
3	0.63 - 0.69	17	0.024	600	1.5
4	0.69 - 0.75	15	0.025	600	1.5
5	0.80 - 0.95	30	0.060	500	3.6
6	1.55 - 1.75	7	0.014	500	1.6
7	2.08 - 2.35	3	0.004	800	0.9
8	3.8 - 5.0	3.8	0.00347	1100	2.4
9	8.2 - 9.3	21.0	0.0152	1380	24.9
10	10.4 - 12.5	25.8	0.0235	1100	33.7

If the quantum efficiency is 50%, about 2×10^9 carriers will be generated by these photons. This is approximately 20 times the maximum number that can be handled without saturation by a conventional CTD having a gate area equal to the detector area, an oxide thickness of 1000 \AA , and an effective gate potential of 10 V. (The use of an oxide with a higher dielectric constant, such as titanium dioxide, TiO_2 , would increase this capacity by about 30 times.) The charge generated in each detector must therefore be reduced to about 1×10^8 carriers for conventional CTDs. Consequently, the sampling time must be reduced to about 0.08 msec.

If a background-subtraction circuit is used that effectively removes all d-c background below some threshold, say 1.5×10^{16} photons/ $\text{cm}^2\text{-sec}$ (scene temperature slightly below 260°K), this problem will be somewhat alleviated. The maximum number of carriers per detector per second is reduced by a factor of 2, permitting the sampling-time interval to be doubled. The dynamic range, however, is improved by an order of magnitude,

as shown in Table 6-5. For an NE Δ T of 0.1 $^{\circ}$ K, it should be possible to cover a range of about 60 $^{\circ}$ K in scene-temperature variation (260 to 320 $^{\circ}$ K), using 8-bit quantization or 256 amplitude levels separated by 0.16 $^{\circ}$ K. The contrast between levels is improved from 0.8 to 8%. The noise level of the device should be 100 carriers per sample or lower.

Potential digital and analog systems for the removal of high-background bias are covered in Section 8.

6.3 NONUNIFORMITIES IN RESPONSE OF DETECTOR ELEMENTS

A problem in the design of a multielement scanner is that of response nonuniformities in individual elements. A fixed-pattern type of noise is characteristic of such scanners, but it is possible to reduce the noise by one of a number of on-board compensation circuits or by means of accurate calibration of the response of all channels and ground data processing. NASA space imagery has been processed for nonuniform response, as well as to emphasize details, to modify tonal range, and to aid in picture interpretation (Ref. 6-7).

The compensating circuit shown in Figure 6-3 (based on Ref. 6-8) can be used with the CTD shift-register approach. The serial readout from several hundred detector elements is amplified by one integrating preamplifier and is then demultiplexed into parallel channels that are first processed through low-pass filters (LPFs) and are then matched to each other by varying the attenuation pads in each channel. The signals out of the variable pads are fed to signal-processing circuits. If the array ages, the pads must be reset. If the amplifier gain is sufficiently high, the parallel channels can be passive elements, resistors, and capacitors.

A possibly more-compact way to compensate for variations in response in either one- or two-dimensional arrays requires a read-only memory (ROM) and a variable-gain amplifier as shown in Figure 6-4 (also based on Ref. 6-8). The responsivity variations are measured by flooding the array

TABLE 6-5 IRCTD PARAMETERS FOR 10.4- TO 12.5- μm BAND*

Scene Temperature ($^{\circ}\text{K}$)	Without Background Subtraction**		With Background Subtraction at 1.5×10^{16} photons/cm ² -sec***	
	Flux (photons/cm ² -sec)	Carriers per Detector in 0.08 msec	Effective Flux (photons/cm ² -sec)	Carriers per Detector in 0.16 msec
320	3.4×10^{16}	1×10^8	1.9×10^{16}	1×10^8
260	1.7×10^{16}	5×10^7	0.1×10^{16}	5×10^6

* Operation at 80 $^{\circ}\text{K}$, quantum efficiency of 50%, f/1.7 cold stop.
** Dynamic range = 2 to 1. Contrast between levels = 0.8%.
*** Dynamic range = 20 to 1. Contrast between levels = 8%.

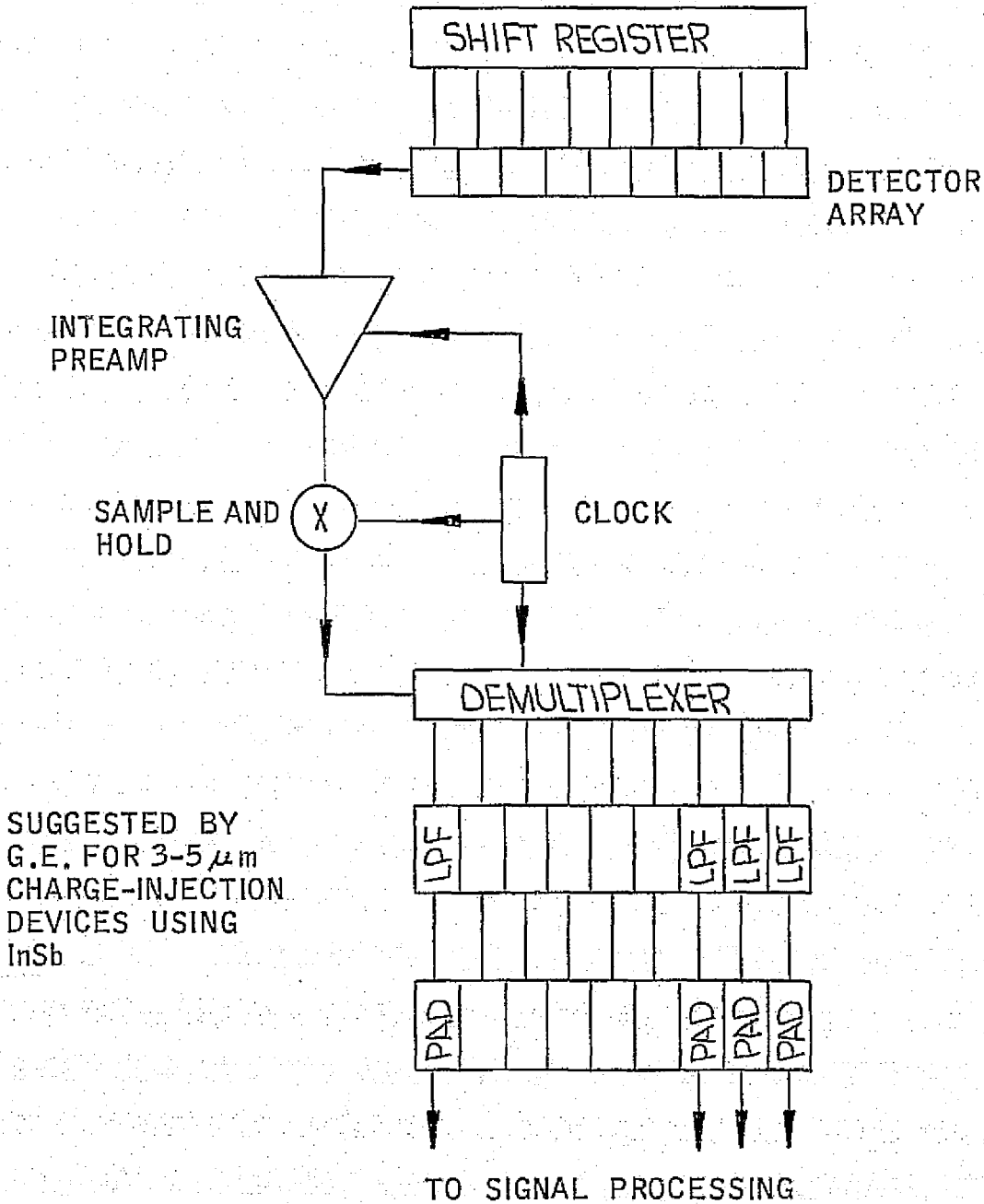
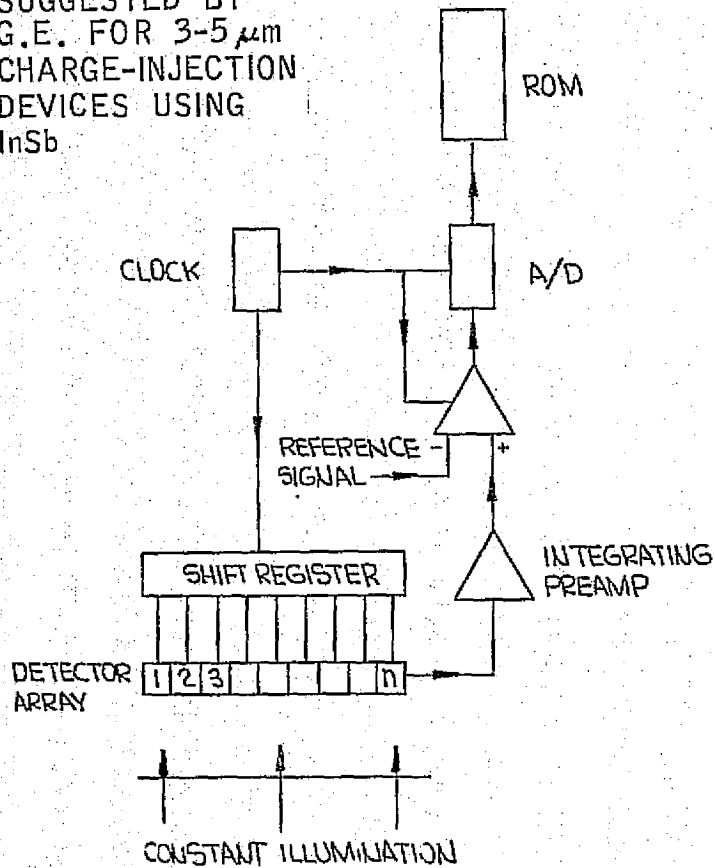
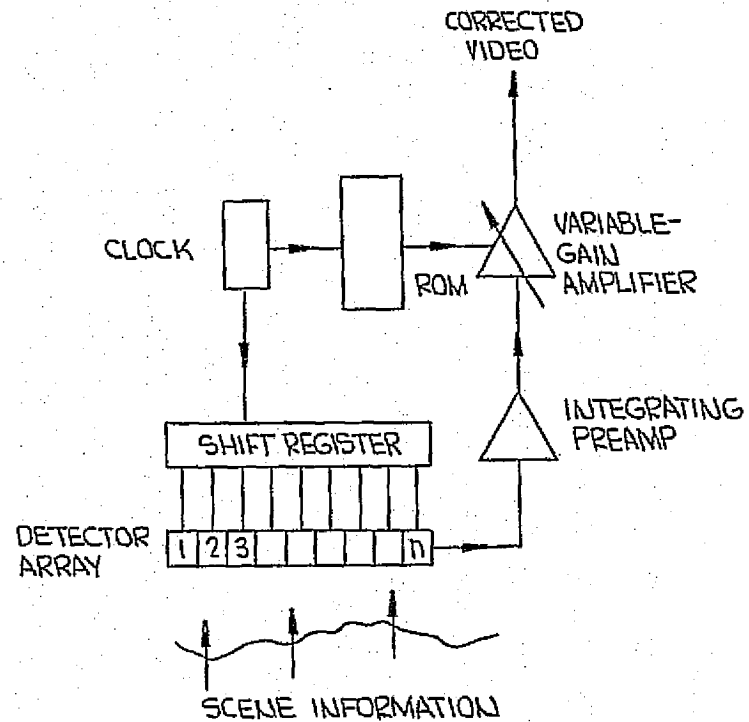


FIGURE 6-3 ONE-DIMENSIONAL CTD SYSTEM WITH PARALLEL PROCESSING, SCHEMATIC

SUGGESTED BY
G.E. FOR 3-5 μm
CHARGE-INJECTION
DEVICES USING
InSb



A. RESPONSIVITY MEASUREMENT



B. SYSTEM OPERATING

FIGURE 6-4 ELECTRONIC NONUNIFORMITY COMPENSATION

with uniform light. The serially read signals from the inhomogeneous array are amplified in the usual way and are compared with a reference signal, are A/D-converted, and are then stored permanently in an ROM device.

The uniformity data stored in the ROM can be used to compensate for the array when the system is in operation (Figure 6-4B). The stored information and the array are scanned synchronously, and the resulting signals are fed simultaneously to an amplifier whose gain is controlled by the ROM data. To simplify the system, the amplifier gain is controlled directly by the digital information from the memory. If the array ages non-uniformly, the ROM must be reset or replaced.

Fixed-pattern noise can also be effectively eliminated by means of overscanning or combining the outputs of a small subarray of detector elements in the scanning direction. The approach not only smooths out non-uniformities but also improves sensitivity by the square root of the number of subarray elements, when signals are added coherently or in phase by routing them through sections of a delay line corresponding to scan-time separations. This has been called a "delay and add" technique or "time-delay integration".

The need for removing fixed-pattern noise due to response non-uniformities can be appreciated by considering equivalent D^* or NEAT values for the conceptual scanner designs.

The signal-to-nonuniformity-noise ratio for a system with 1% non-uniformity (i.e., S/N_{nu}) would be

$$\frac{S}{N_{nu}} = \frac{N_{\Delta\lambda}}{gN_{\Delta\lambda}} = \frac{N_{\Delta\lambda}}{0.01N_{\Delta\lambda}} = \frac{100}{1}$$

where $N_{\Delta\lambda}$ = scene radiance in the $\Delta\lambda$ spectral band (1.4 mW/cm²-sr for the 11- μ m band, and 0.089 mW/cm²-sr for the 4- μ m band)

g = nonuniformity factor



The signal-to-background-noise ratio (S/N) is given by

$$\frac{S}{N} = \frac{\pi \sqrt{2t_d} N_{\Delta\lambda} \theta D K_o K_e D^*}{4 (f/\text{no.})}$$

where t_d is dwell time, D is aperture, θ is instantaneous field of view, K_o is optical efficiency, and K_e is electronic efficiency. Equating the foregoing relations, an equivalent nonuniformity D^* can be expressed (using original baseline values) as

$$D_{\text{nu}}^* = \frac{4 (f/\text{no.})}{\pi \theta D K_o K_e N_{\Delta\lambda} \sqrt{2t_d}} = \frac{1.85 \times 10^6}{N_{\Delta\lambda}}$$

when $g = 0.01$ for 1% nonuniformity. For the 4- μm band,

$$D_{\text{nu}}^* = 1.85 \times 10^6 = 2.08 \times 10^{10} \text{ cm-Hz}^{\frac{1}{2}}/\text{W}$$

as compared with a photon-noise-limited D^* of 10^{11} . For the 11- μm band,

$$D_{\text{nu}}^* = \frac{1.85 \times 10^6}{1.4 \times 10^{-2}} = 1.32 \times 10^9 \text{ cm-Hz}^{\frac{1}{2}}/\text{W}$$

as compared with a photon-noise-limited D^* of 10^{10} . Expressed in terms of NEAT, the equivalent nonuniformity values are 0.3°K for the 4- μm band and 0.66°K for the 11- μm band.

Consequently, if IR-detector-array nonuniformities cannot be reduced below 1% (to about 0.1%), their effect must be removed by data processing in order to maintain the desired sensitivity levels. This is accomplished by the automatic calibration technique described in Section 9.

6.4 FOCAL-PLANE DESIGN CONCEPT USING PRESENTLY AVAILABLE CTDs

As noted above, a number of commercial CTDs can be considered for use on the SMSS focal plane. Presently available CTDs are applicable to the short-wavelength channels (0.45 to 0.95 μm), and a number of firms including Aerojet are working on IRCTDs under both Government and independent research and development funding. Progress in their development is expected to be sufficiently rapid to permit their inclusion in the SMSS system design.

A conceptual design has been developed for the short-wavelength section of the SMSS focal plane (Channels 1 through 5) and is discussed below. The long-wavelength section (Channels 6 through 10) will probably be similar, but will require active detector cooling and a Dewar assembly.

Two types of CTD configurations are commercially available: linear-imaging arrays and area-imaging arrays, in sizes shown in Table 6-1. Because the SMSS has only five visible-spectrum channels, considerable redundancy can be built into the system with area arrays.

For minimum complexity and cost, it would be advantageous to minimize the total number of arrays. In all cases, the array-pixel size is less than the desired SMSS-pixel size, and some provision must also be made to sum signals from adjacent resolution elements prior to data output. This can be accomplished at the output-transfer gate or the reset circuit for most of the available configurations.

An output-transfer-gate summing sequence is illustrated in Figure 6-5 (where ϕ_1 through ϕ_3 are clock phases and S_1 through S_3 are signals from adjacent resolution elements). A similar procedure can be used with the reset gate to collect the charge in the floating diffusion for more than one clocking cycle. It can be followed for an arbitrary number of clocking cycles as long as the total signal charge does not exceed the transfer-gate storage capacity. Although three-phase clocking is illustrated, this scheme will work equally well for two- or four-phase clocking. The output data rate from

475-1786

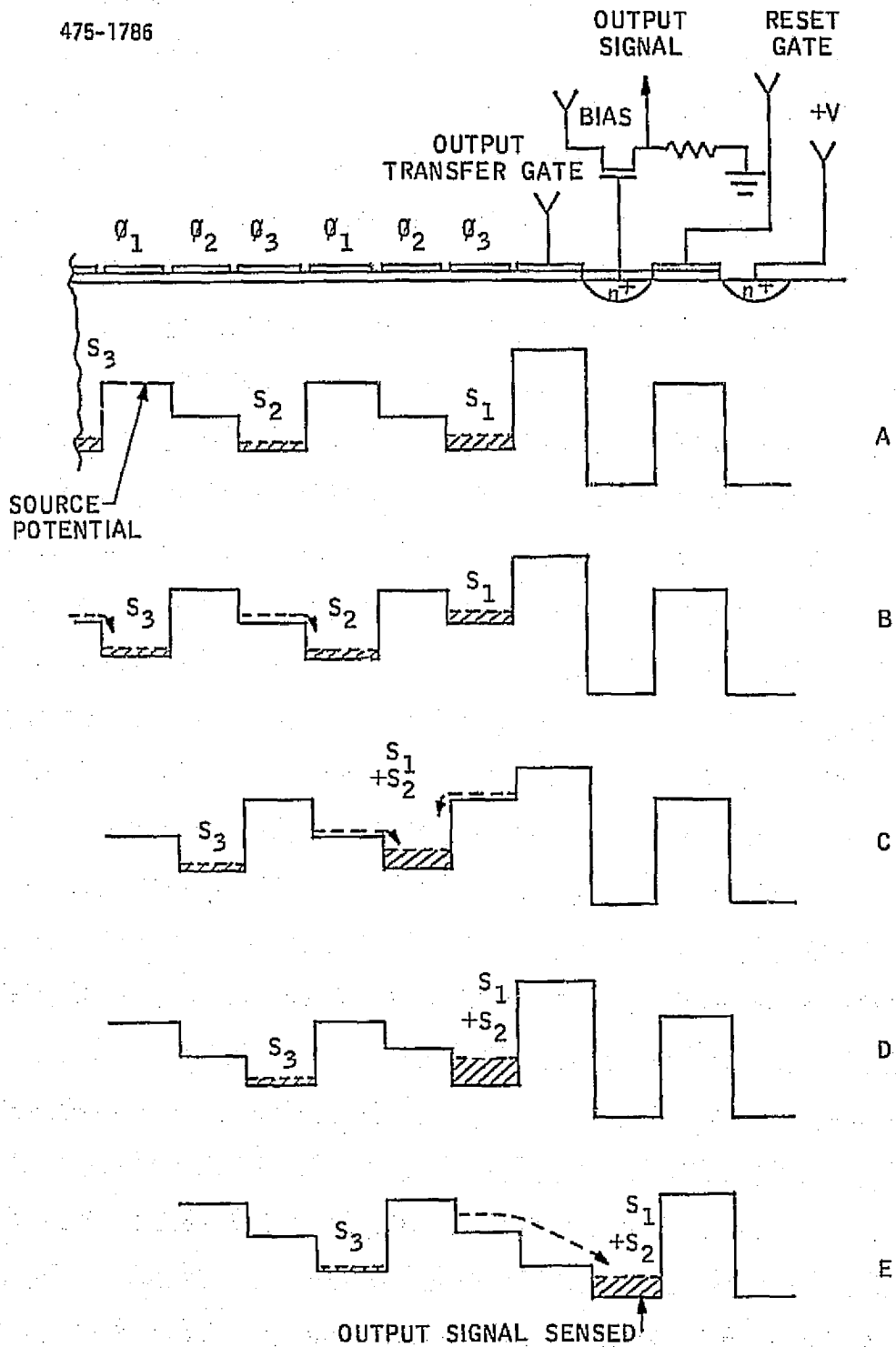


FIGURE 6-5 CLOCKING SEQUENCE FOR SUMMING SIGNALS FROM TWO RESOLUTION ELEMENTS



each array will be 617 Hz (75-cm-aperture system) times the number of SMSS pixels on that array.

Each linear array would be filtered for only one of the selected wavelength bands. Its output would therefore simply be data from that spectral channel. In contrast, if an area array is used, the output data will be a time-multiplexed combination of the five spectral channels, as shown in Figure 6-6. Reconstruction of each spectral channel will be required either (a) on the focal plane with CTD demultiplexing, (b) just before the data-storage step after digitizing, or (c) on the ground after data retrieval.

Most of the seven commercially available CTDs characterized in Table 6-1 are promising for SMSS use, but the General Electric (GE) 100x100-element CID array has a pixel size most nearly matching that of the SMSS. (This array makes it unnecessary to employ the signal-summing approach illustrated in Figure 6-5.) Because the sensitivity of this device is equal to or better than that of the others, it is the recommended choice, and a possible focal-plane layout based on its use is shown in Figure 6-7.

In that concept, forty 100x100-element arrays are used in a staggered pattern to obtain a 4000-pixel SMSS channel for a 75-cm-aperture system. Each array is divided into five columns of 100 elements each, with each column representing 1/40th of a single channel. Staggering is required to provide element-to-element coverage in the SMSS crosstrack direction. With this configuration it will be necessary to delay the readout of alternate arrays in order to reconstruct the ground scene. Of the 400,000 pixels on the 40 arrays, only 20,000 are required to cover Channels 1 through 5.

The focal plane for the reflective Schmidt optics will be slightly curved. It is believed that the depth of focus will be sufficient to permit the mounting of eight segments of five arrays each on an eight-faceted substrate that approximates the focal-plane curvature. Filters for the individual channels can be deposited on a large substrate for subsequent

475-1781

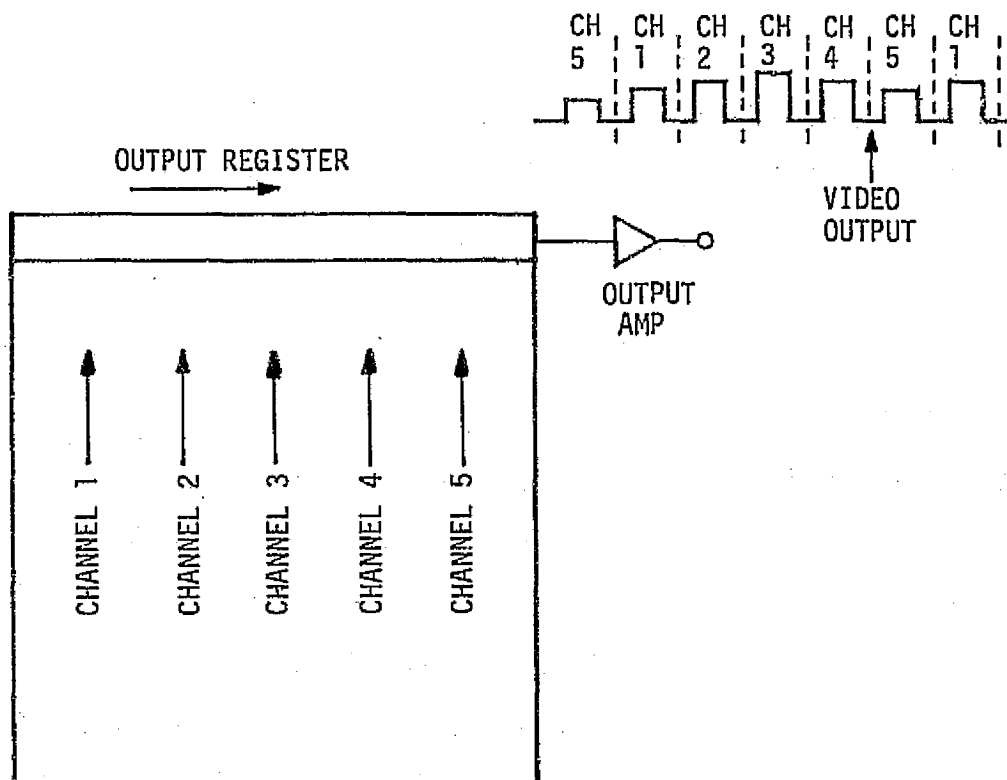


FIGURE 6-6 AREA-ARRAY DATA FORMAT



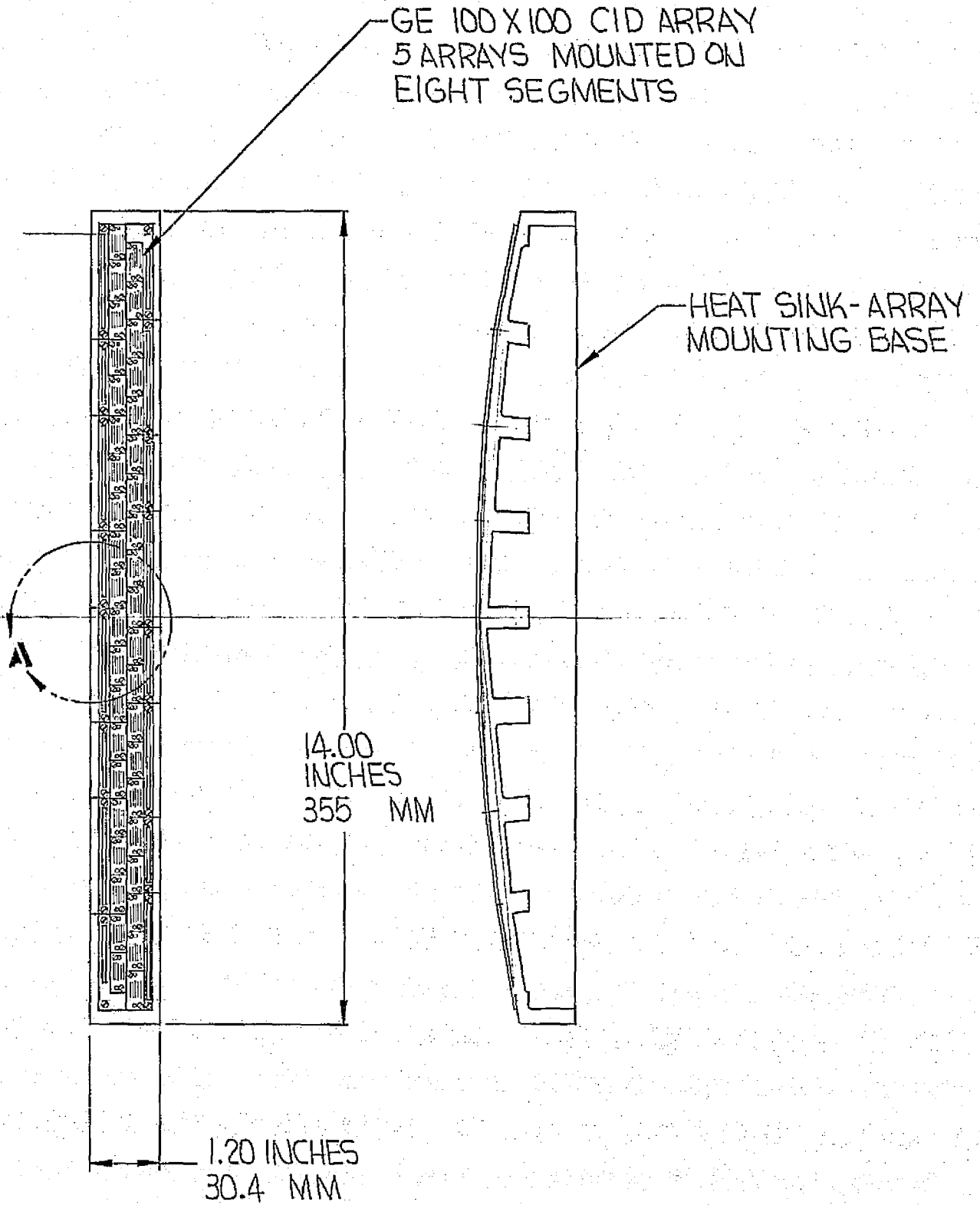


FIGURE 6-7 (Sheet 1) SHORT-WAVELENGTH FOCAL-PLANE CONCEPT





ORIGINAL PAGE IS
OF POOR QUALITY

6-24

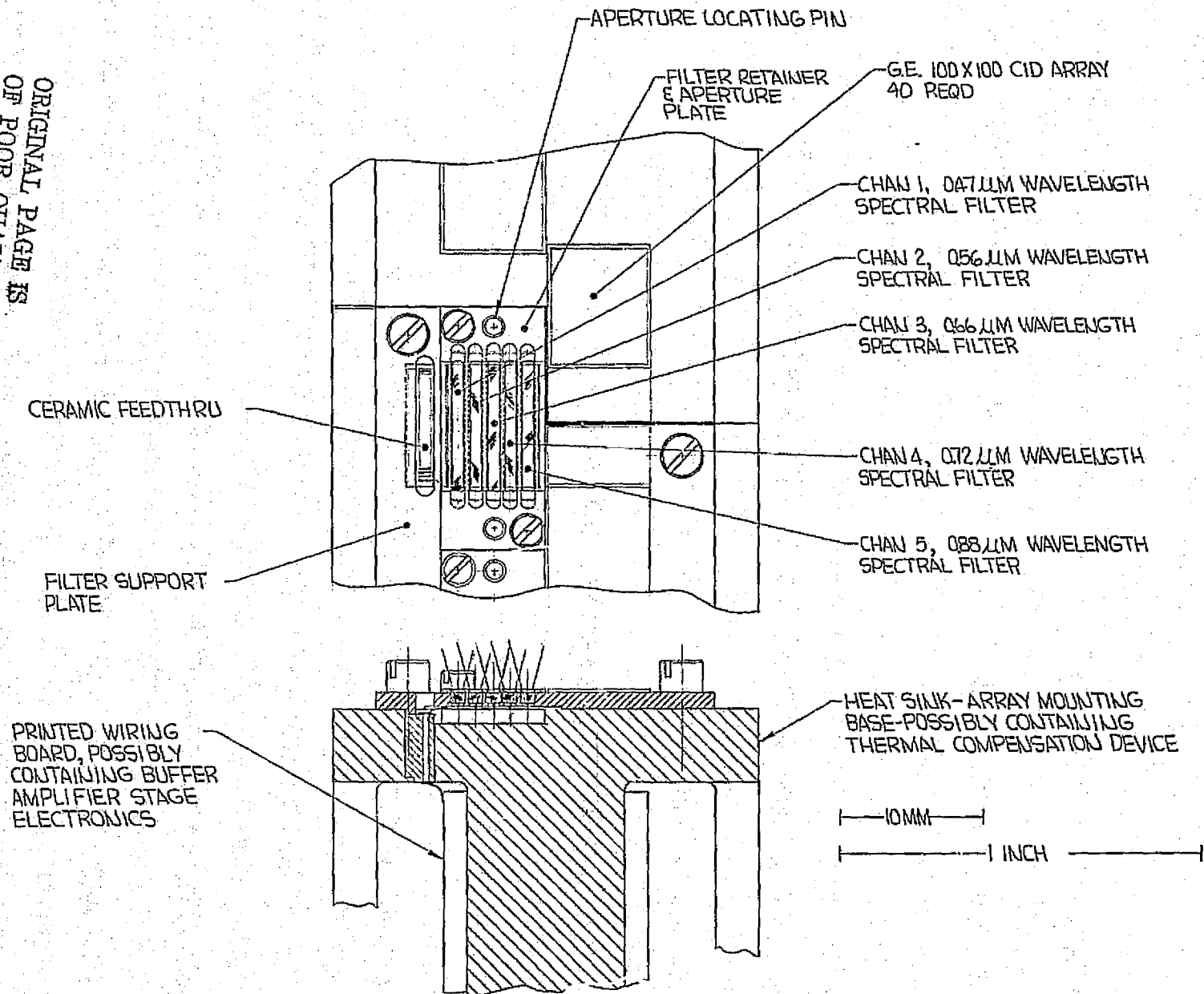


FIGURE 6-7 (Sheet 2) SHORT-WAVELENGTH FOCAL-PLANE CONCEPT

separation into strips. The strips can then be installed in filter frames that are mounted onto each eight-array segment. Figure 6-7 conceptually illustrates this approach.

Signal, bias, and clocking leads can be fed through the focal-plane-support structure via inlaid strips adjacent to each array, and further signal conditioning, buffering, etc. can be accommodated on the back of the array-support structure. In keeping with SMSS modularity, a focal-plane layout of this type could easily be adapted to change the spectral coverage by installing different filter-frame assemblies.

A concept for an IRCTD hybrid array is shown in Figure 6-8, and additional focal-plane considerations and design concepts are covered in Section 7.

1175-1328

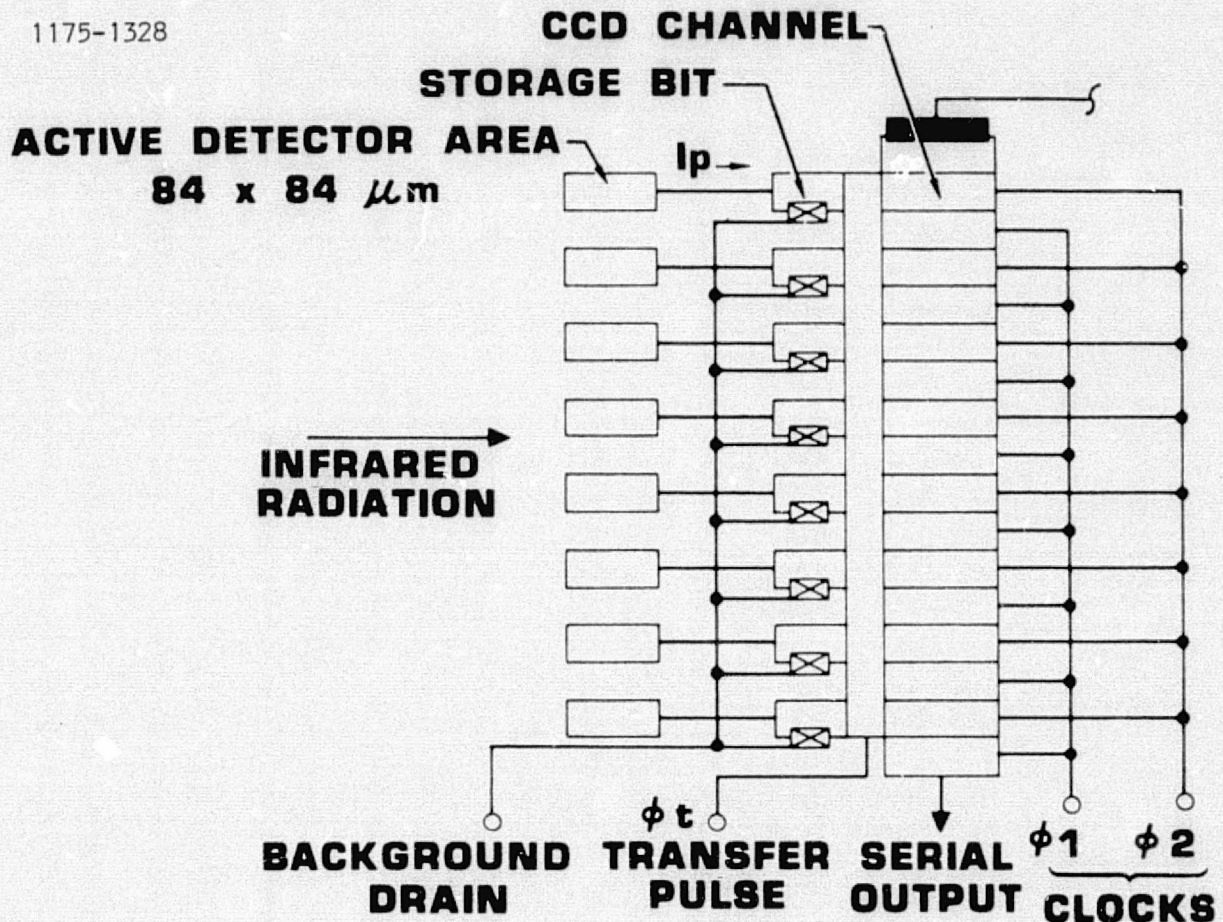


FIGURE 6-8 IRCTD HYBRID ARRAY CONCEPT



Section 7

FOCAL-PLANE/GIMBAL-MODULE CONSIDERATIONS AND DESIGN

7.1 FOCAL-PLANE COOLING AND CONFIGURATION

Potential cooling systems for the SMSS focal plane were compared and analyzed on the basis of an assumed operating temperature of 80°K (infrared channels). Also assumed were a data-gathering duty cycle (focal-plane power on) of 2 hours per day for a 10-day mission, and a focal-plane power dissipation of 9 W. Preliminary calculations indicated an average heat load of approximately 16 W, with 15 W during the off period and 24 W during the on period.

Three cryogenes were evaluated, as were closed-cycle mechanical refrigerators and Joule-Thomson open-cycle refrigerators. A suggested cooling-system design was generated, heat loads were calculated, and preliminary focal-plane/Dewar-assembly details were conceived. These investigations and their results are discussed below.

7.1.1 Cooling Evaluation

The three cryogenes evaluated were nitrogen, which can either be a liquid at 63 to 77°K or a solid below 63°K, and methane and argon, which will be solid at 80°K or lower. With the SMSS focal-plane heat loads, the cryogen-vent-vapor flow rate will be high and vapor-cooled shields are practical. As a result, the heat leak into Dewar vessels was neglected in this analysis. The resulting weight and volume of the cryogen would be 10 to 20% higher if a vent-vapor-cooled shield were not employed. The conventional heat-balance equation was used for the analysis:

$$W = \frac{Qt}{h}$$

where W = weight of cryogen
 Q = heat load
 t = time
 h = heat of vaporization or sublimation

The results were as follows:

Coolant	Heat of Sublimation or Vaporization		Weight		Volume	
	J/kg	cal/g	kg	lb	Liters	cu ft
N ₂	2×10^5	48	69	152	86	3.0
CH ₄	5.6×10^5	133	25	54	56	2.0
A	1.9×10^5	46	73	160	46	1.6

The calculations indicated that methane would add the least total weight (25 kg) and argon had the smallest volume (46 liters). Nitrogen could be a liquid or a solid, but the others must be solid to meet the 80°K requirement.

When closed-cycle mechanical refrigerators were considered, it was found that the necessary cooling might be provided by two devices with a weight of approximately 23 kg (50 lb) and a power requirement of approximately 1 kW; in addition, 1 kW of heat would have to be rejected at approximately 325°K. If a two-speed cooler were available, the power and heat-rejection requirements would be about half these values during the off period. Because the overall operating time for the SMSS is relatively short (240 hours maximum), a mechanical cooler could meet the lifetime requirement.

These closed-cycle types of refrigerators have been under development for use in spacecraft for several years, and one has operated in space for 500 hours. Such a cooler could be acceptable for the SMSS if power, vibration, and heat-rejection requirements were not overriding considerations.

Joule-Thomson (J-T) coolers were also examined for SMSS use. The most common open J-T system is the Air Products AC-1 unit rated at 7 W at 80°K. Two units would be needed during the off period and four during the on.

This cooler requires a nitrogen flow of 1.58 kg/hour. For two units operating for 10 days, more than 680 kg (1500 lb) of gas (plus the tank weight) would be necessary. The Hymatic MC-8 cooler is listed at 10 W at 80°K with a flow rate of 0.128 kg/hour. The related weight of gas and high-pressure tankage would be approximately 230 kg (500 lb). These values indicated that the J-T approach does not offer a practical method for focal-plane cooling.

The results of this investigation are summarized in Table 7-1. Solid nitrogen is recommended for SMSS focal-plane cooling because of its inherent safety, simplicity, and support logistics, notwithstanding the weight and volume penalties in comparison with methane or argon. Mechanical refrigerators are not recommended, because of their relatively large power consumption and increased system complexity. They would also require a large radiator panel to dissipate the refrigeration-system heat. Joule-Thomson open-cycle refrigerators weigh more than 680 kg (1500 lb) and therefore would not be practical.

7.1.2 Suggested Cooling Design

The suggested design (shown in Figure 7-1) provides sufficient volume for two separate solid-cryogen Dewar vessels, each of which is mounted at the end of a copper heat-conduction bar connecting it to the focal plane (which is housed in its own Dewar vessel). A flexible braid will be used for part of the length to allow focal-plane movement.

The operating heat load is conveyed to the external coolers through the two 61-cm-long bars. The temperature drop (ΔT) for a bar of 3.8x3.8-cm cross section will be 12.4°K, including a 5-cm-long flexible braid having a 2°K ΔT . Each bar would weigh approximately 6.8 kg (15 lb).



TABLE 7-1. COMPARISON OF FOCAL-PLANE COOLING SYSTEMS

Type	Advantages	Disadvantages
Mechanical refrigeration	Light weight [23 kg (50 lb)] Unrestricted duty cycle	Higher power consumption (1 kW) Vibration Large radiator required Limited life
Open-cycle liquid cryogen	Simplified servicing, abort-dump capability	Logistic ground support equipment (GSE) required Fluid transfer at zero gravity difficult Limited duty cycle
Open-cycle Joule-Thomson	--	Far too heavy [680 kg (1500 lb)]
Open-cycle solid cryogen	Canister-loading concept Lower temperature available for given cryogen, higher density	Requires conduction bar for heat transfer Abort jettison difficult GSE more complex

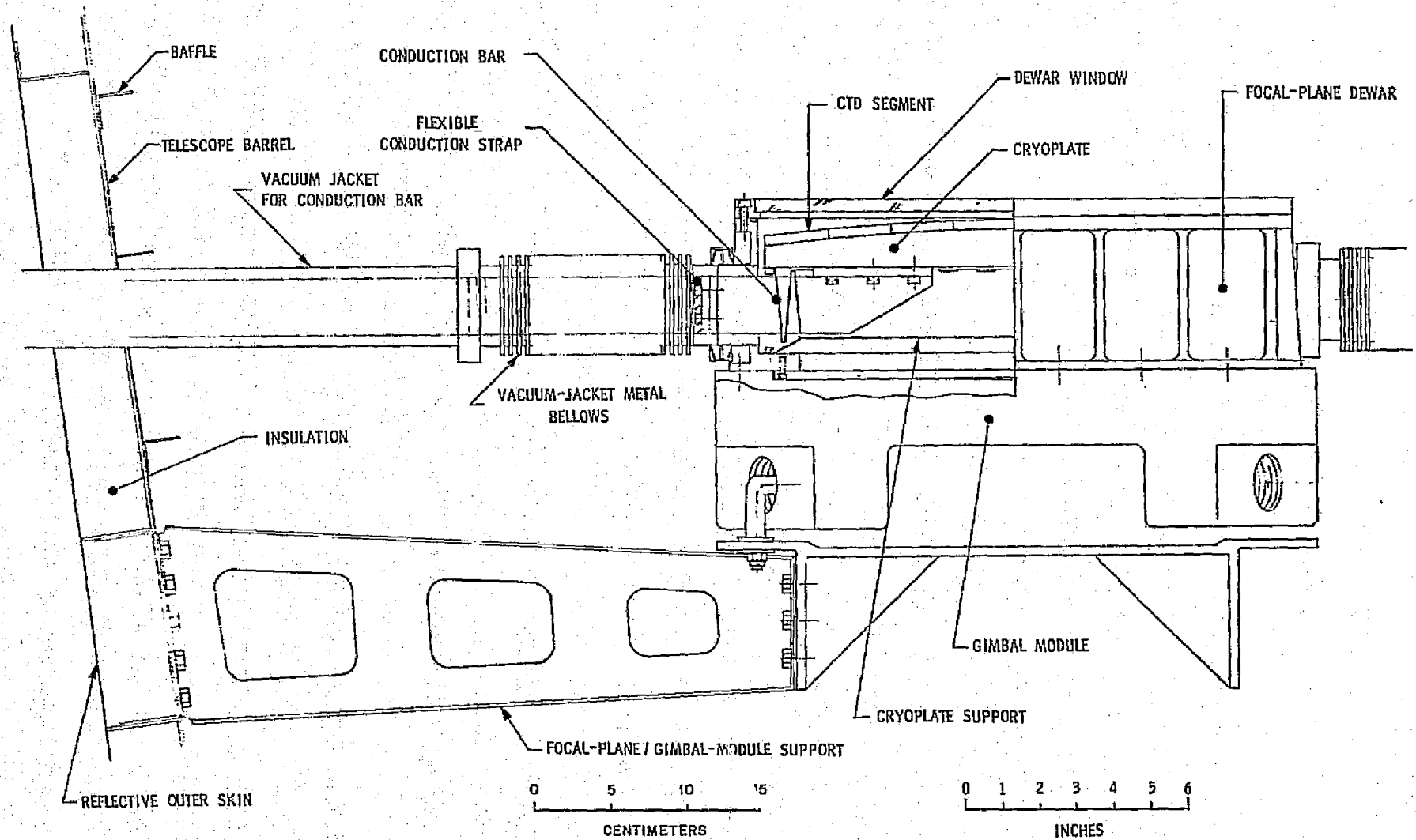


FIGURE 7-1 FOCAL-PLANE/GIMBAL-MODULE ASSEMBLY, COOLING AND SUPPORT DETAILS

The ΔT along the bars requires that the cryogen operate at about 68°K, which can readily be achieved by cryogen venting at lower than atmospheric pressure.

Figure 7-1 shows the focal-plane module mounted to the gimbal module, with the conduction-bar assemblies attached. The vacuum-jacketed bars are terminated outside the telescope barrel with a bayonet-type connection so that the Dewar assemblies are removable. This configuration is considered desirable because several different sizes of containers could be substituted, depending on the particular mission requirements. In addition, the cryogen could be loaded and solidified in a service location for subsequent installation at the launch site or payload-assembly area.

Although connecting each vacuum jacket to a Dewar vessel increases complexity, this approach is considered necessary to facilitate qualification, ground checkout, and system calibration. Elimination of the vacuum system would force all developmental, qualification, and prelaunch testing to be performed in a vacuum chamber.

The conduction bars will be equipped with flexible braids of thin copper wire to accommodate the focal-plane motions required for image-motion compensation and focusing. Because these excursions will be small, the braided-copper technique is feasible. Braided conductors have been used on smaller systems at Aerojet and have not presented special problems. Scaling up to the SMSS requirements should create no new difficulties.

7.1.3 Heat Loads

Heat-load calculations were made on the basis of the SMSS configuration described in the preliminary specification and the preliminary design shown in Figure 7-1. A value of 9 W was assumed for the electrical heat load, Q_1 (including the lead wires), and was considered conservative for this analysis. The focal-plane support employs pleated titanium for connection to the cold station.

The support uses 6Al-4V titanium with a thermal conductivity of 0.06 W/cm-°K at a mean temperature of 190°K for an ambient temperature of 300°K and an 80°K infrared focal plane. It has an area of 4.42 cm² and a length of 26.4 cm. The resulting heat leak, Q₂, is 2.23 W (from the conventional conductance equation).

Radiative heat leak to the focal plane was considered without radiation shields. The surface on which the detectors are mounted was assumed to have an emissivity of 0.8. The area is 315.74 cm², and the heat load for an assumed view factor of 1.0 is given by

$$Q_3 = (0.8)(1.0)(0.03157 \text{ m}^2)(5.67 \times 10^{-8} \text{ W/m}^2\text{-}^\circ\text{K}^4)[(300)^4 - (80)^4]$$

$$= 11.52 \text{ W}$$

The remaining area of the focal plane is 536.7 cm². It would be gold-plated to achieve an emissivity of 0.03. The heat load for the 1.0 view factor is given by

$$Q_4 = (0.03)(1.0)(0.05367 \text{ m}^2)(5.67 \times 10^{-8} \text{ W/m}^2\text{-}^\circ\text{K}^4)[(300)^4 - (80)^4]$$

$$= 0.74 \text{ W}$$

The total heat load on the focal plane is then

	Watts	
	Power Off	Power On
Electrical, Q ₁	0	9
Support, Q ₂	2.2	2.2
Radiation to focal-plane face, Q ₃	11.52	11.52
Radiation to focal plane, Q ₄	0.74	0.74
Total	14.46	23.46

7.1.4 Focal-Plane/Dewar Assembly

The focal-plane/Dewar assembly consists of ten staggered linear arrays of detectors (as discussed in Section 6) that are mounted in a Dewar vessel, which in turn mounts on the gimbal-module assembly. Focal-plane details are illustrated in Figure 7-2.

It was determined early in development of the SMSS conceptual design that the system should be operable under earth-ambient conditions. Space simulation will undoubtedly be used during developmental testing, but elimination of the space-simulation requirement for routine system checkout will significantly reduce test complexity, time, and cost. For this reason, the detectors are Dewar-housed to permit cooling to 70 to 80°K (for IR detection).

Accordingly, as shown in Figure 7-2, the detectors/CCD for IR channels are mounted on the cryoplate, which attaches to the conduction bar through flexible straps. The cryoplate is held on the Dewar housing by a thermal-isolation support. The latter provides a long conduction path with minimal cross section, and rigidly supports the focal plane to prevent movement or vibration.

The spectral filters are mounted in small assemblies. For the visible channels, these assemblies incorporate five strip filters mounted in a single frame. Forty such frames will be needed for the visible channels. For the IR channels, each frame will mount a single filter and 16 assemblies will be necessary for each channel (or a total of 80 frames). The filter elements will be cemented into the frames, which will then be attached to the main Dewar closure frame by means of special indium gaskets to provide hermetic sealing. In keeping with the system-flexibility criterion for the SMSS, the filter frames can be changed between missions to provide different spectral coverage or resolution as required by various experimenters.



1175-1348

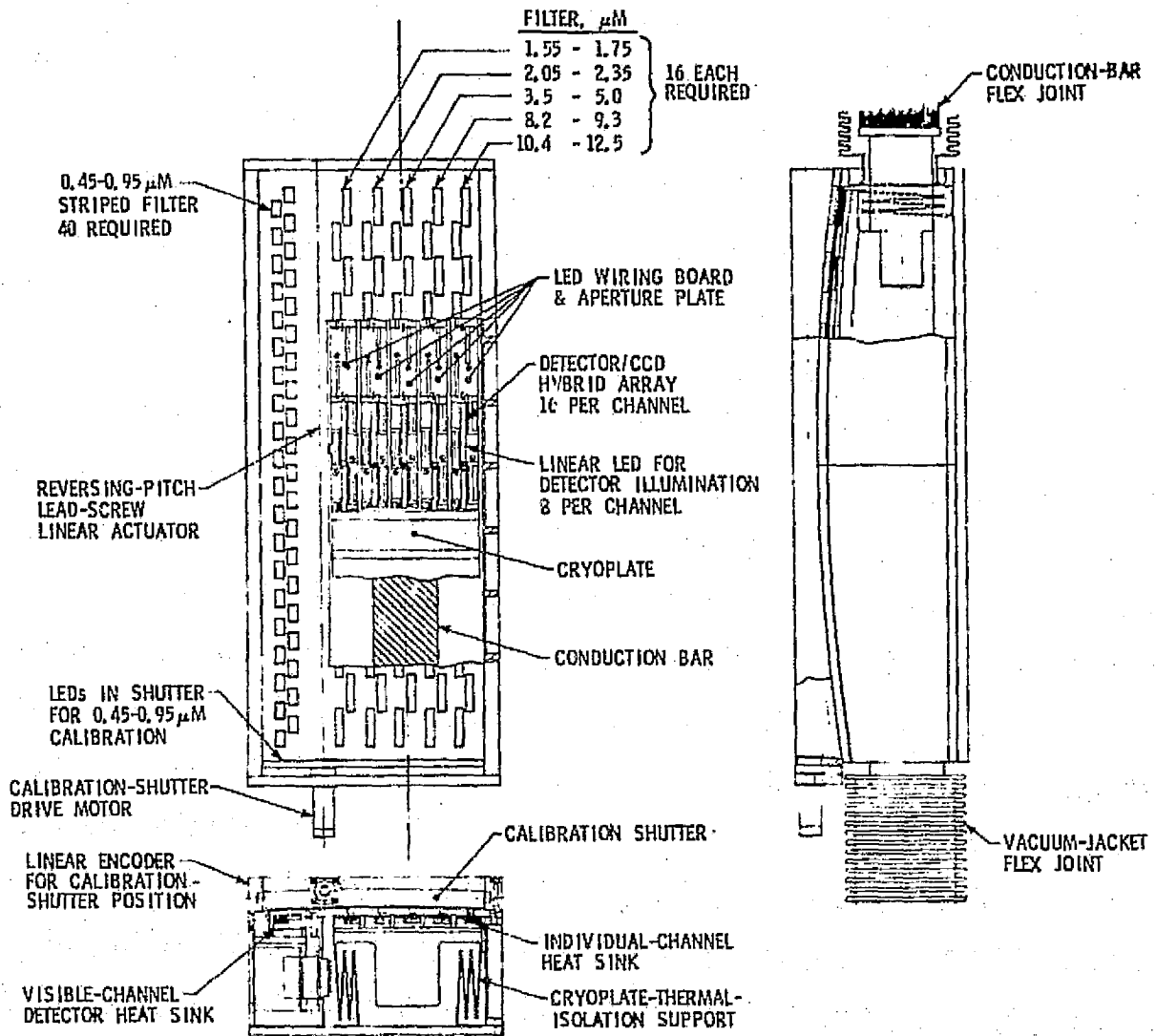


FIGURE 7-2 SMSS FOCAL-PLANE/DEWAR ASSEMBLY



ORIGINAL PAGE IS
OF POOR QUALITY

The assembly is also fitted with a shutter that traverses the length of the focal plane during calibration. The shutter consists of a small bar that blocks radiation from the earth scene during calibration and presents a background of known radiance by virtue of precise temperature monitors mounted in the bar. Bar motion is accomplished by means of a reversing lead screw, and bar position is provided by a linear encoder.

The assembly described above and illustrated in Figure 7-2 represents a potential design concept. It is not intended to accurately define the required focal plane, but rather to illustrate the feasibility of the basic SMSS focal-plane requirements:

- Modularity
- Operability under earth-ambient conditions
- Capability for changing spectral bands and spectral resolution.

7.2 ACTIVE FOCUSING

It is planned that beryllium will be used not only for the primary and secondary mirrors of the SMSS but also (to assure minimum distortion and misalignment due to thermal changes) for the telescope and the mirror mounts. Compensation would be required if dissimilar materials were used but this approach permits fixed-focus optics, a proven technique in many optical systems. However, an active-focusing mechanism appears desirable because

- a. Detailed thermal and structural design effort is reduced, since minor variations in alignment due to thermal stresses, launch and landing vibration and shock, and zero-gravity conditions can readily be corrected in orbit.
- b. Substitution of focal-plane or gimbal modules would not require complex realignment procedures, and such replacements could be accomplished in the field.
- c. The focal plane is gimballed for image-motion compensation and focus would add only one more degree of freedom, a minor impact on complexity.



The total depth of focus planned for the SMSS is 286 μm (0.0011 in.), as illustrated in Figure 5-33. Adjustment during operation will require a focus-monitoring system (e.g., Figure 7-3) that can translate the focal plane along the optical axis. The translation function can be accommodated in the gimbal module (see paragraph 7.3).

The system determines the SMSS focus condition by detecting the presence and phase of two, small, collimated, light-emitting-diode (LED) sources. The LEDs are attached to the telescope and are focused on detectors mounted on the focal plane. They are pulsed alternately; as noted in Figure 7-3, one pulse is designated as positive and the other as negative. The collimated beams are then focused onto the apex of a roof mirror mounted on the focal plane.

When the system is in focus, the detectors have minimum response. If the focal-plane position is too short, the plus and minus beams energize the corresponding plus and minus detectors. If the focus position is too long, the plus beam energizes the minus detector and the minus beam energizes the plus detector. The correct position is thus readily determined, as is the direction of motion required for best focus. With this system, focus can be monitored and adjusted by the payload specialist in the Orbiter cabin, or can be accomplished automatically with a logic circuit in the SMSS electronics.

7.3 GIMBAL MODULE

7.3.1 Description

The gimbal module is incorporated in the suggested design to provide a servoed focal-plane assembly for image-motion compensation. By introducing appropriate, small, compound motions of the detectors in the focal surface, the SMSS line of sight can be short-term-stabilized at the nominal pointing angle in space.



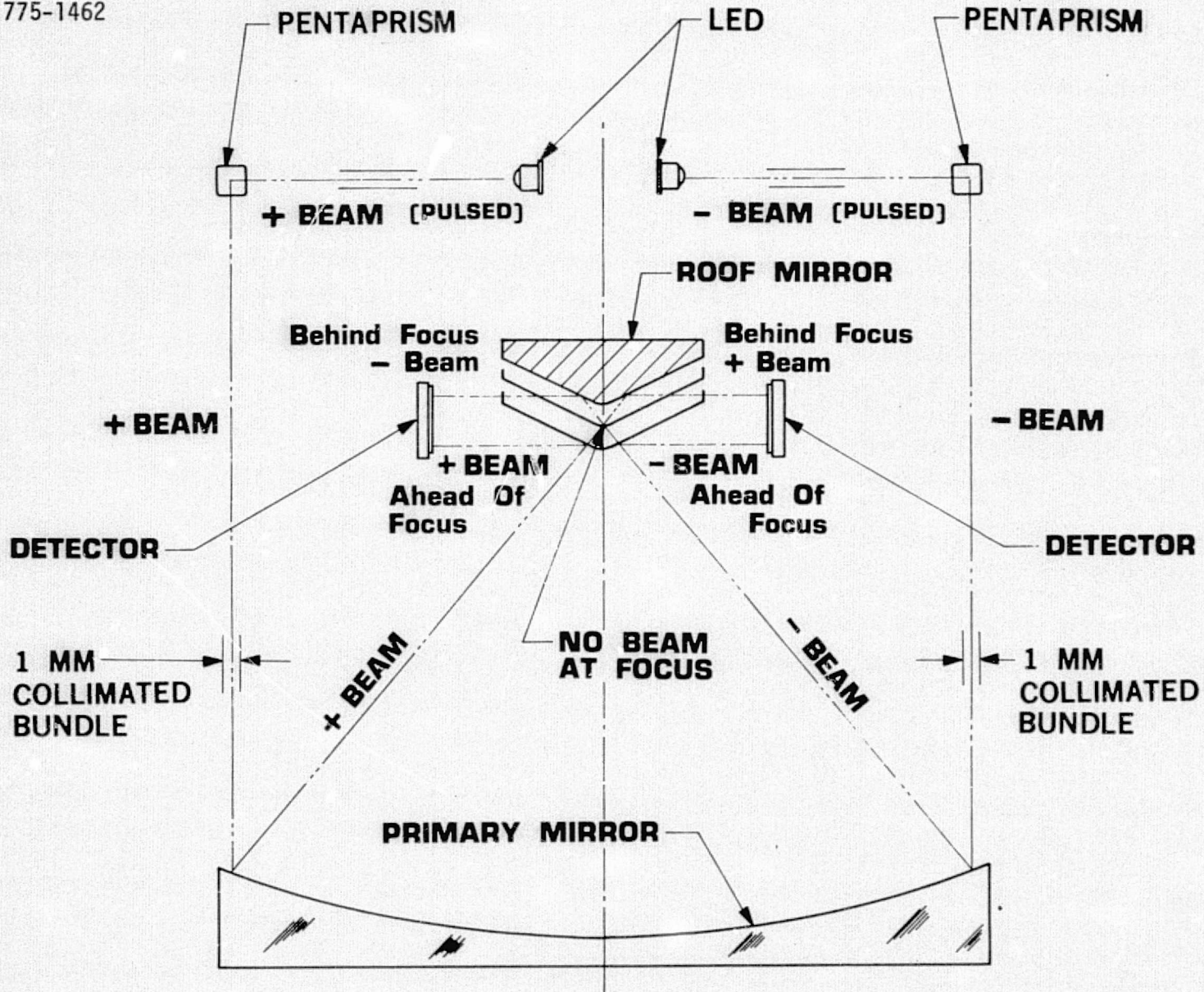


FIGURE 7-3 SMSS ACTIVE FOCUS, SCHEMATIC

As presently envisioned, the module will be 12.25 cm wide, 35.50 cm long, and 12.75 cm deep. It will provide for roll compensation with a translation in its long dimension (cross-track direction), for pitch with a translation along its width (track direction), for yaw with a rotation about the telescope axis, and for focus with a translation along that axis.

The entire mechanism is housed in an enclosure that can be maintained at a slightly positive pressure to circumvent the usual design problems associated with vacuum operation of mechanical systems and motors (cold welding, outgassing, optical-system contamination, arcing, etc.).

The module is supported by a "spider" that mounts on the telescope structure. Four bellows assemblies positioned to minimize unbalanced torques provide for connection to the support spider. The bundles of wires to the focal plane and the gimbal module will be positioned similarly, as will the cryogen supply and exhaust connections, so that the system is essentially balanced.

Figure 7-4 was developed for use in scoping the module. Position encoders are not shown but will be required, probably with momentum-compensation devices as well. The intent was to develop a preliminary layout for module analysis to verify feasibility. The layout employs commercially available stepper motors, gears, slides, etc. It is likely that specially tailored devices will be required in the actual design.

7.3.2 Gimbal-Servo Analysis

This analysis is based on the conceptual gimbal module described above. If a nominal downlooking sensor is assumed, Orbiter-yaw compensation requires that the detector assembly rotate in the focal surface, Orbiter pitch requires that the detectors translate fore and aft (parallel to the longitudinal dimension of the Orbiter), and Orbiter roll requires translation from side to side. Servos to produce motions in these coordinates are depicted in Figure 7-4.



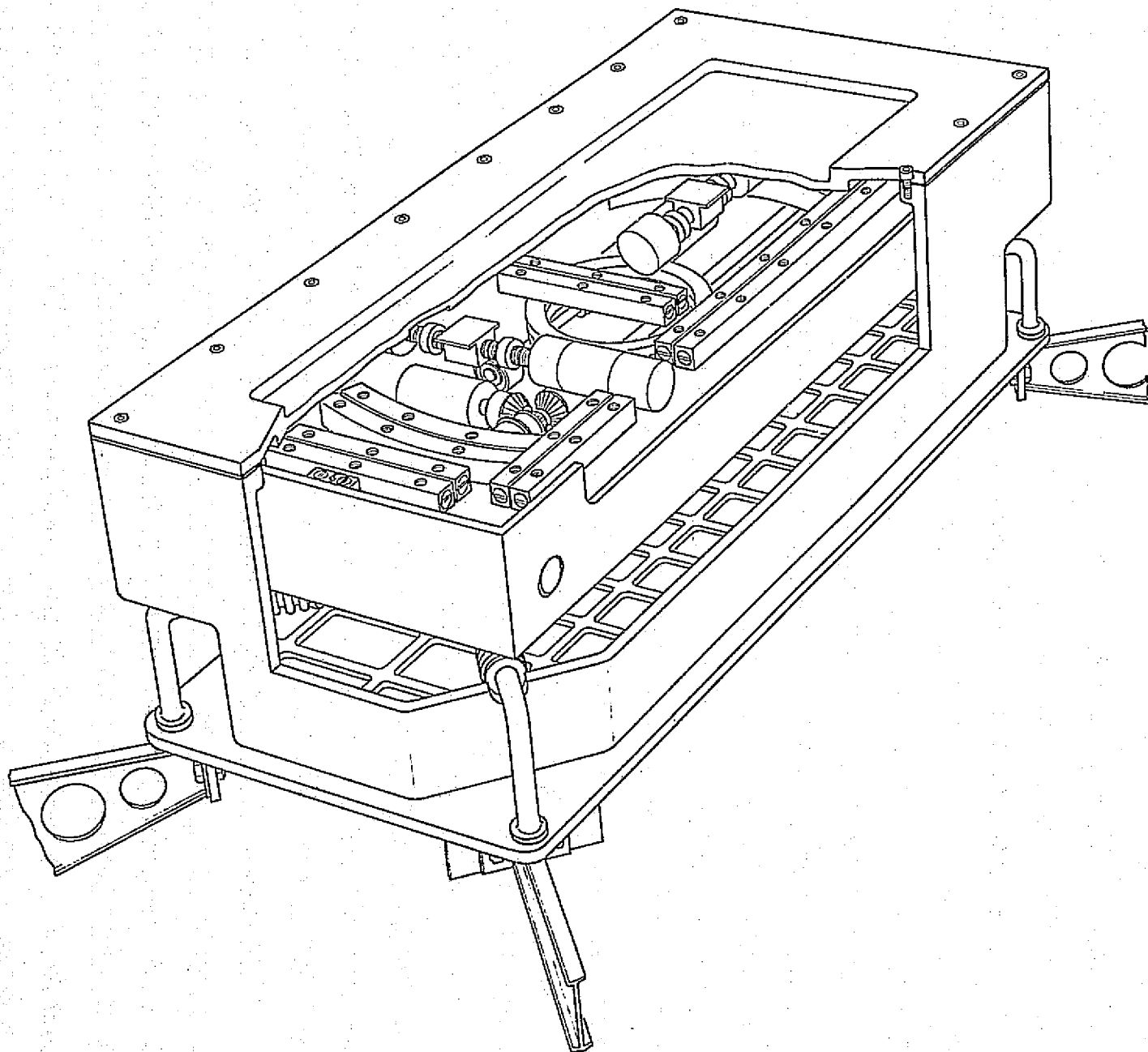


FIGURE 7-4 PRELIMINARY LAYOUT, GIMBAL MODULE WITH "SPIDER" SUPPORT

This concept requires that sufficiently accurate correction signals be available and that the servos can reproduce the commanded motions at the focal plane. The ensuing analysis assumes that a source of such correction signals is available, that the Orbiter is at a constant nominal attitude, and that it is undergoing an essentially triangular limit cycle within its $\pm 0.1^\circ$ attitude-control deadband.

The maximum drift velocity in normal operation is expected to be $\leq 0.01^\circ$ per second. In the most dynamic case, the frequency of the 0.2° -peak-to-peak-amplitude triangular-limit cycle will be $\frac{1}{40}$ Hz. This motion corresponds to 52.9 resolution elements for the $66\text{-}\mu\text{r}$ -resolution SMSS and requires a 4.5-mm peak-to-peak translation in the focal surface of the 75-cm-diameter, $f/1.7$ telescope. The maximum rate of correction for a drift rate of $0.01^\circ/\text{sec}$ will be 0.22 mm/sec.

The following maximum angular accelerations of the Orbiter are expected:

Axis	Predicted Maximum Angular Acceleration (deg/sec ²)	
	Primary Thrusters	Vernier Thrusters
Roll	± 1.46	$\pm 3.2 \times 10^{-2}$
Pitch	+1.64, -2.05	$+2.6 \times 10^{-2}$, -2.2×10^{-2}
Yaw	± 0.97	$\pm 2.3 \times 10^{-2}$

The maximum linear acceleration of the focal plane in the pitch-correction axis is then 4.562 cm/sec^2 , and the maximum in the roll-correction axis is 3.249 cm/sec^2 . The maximum acceleration in the yaw-correction axis is simply the yaw rate of $1.693 \times 10^{-2} \text{ rad/sec}^2$.

The masses of the loads in the pitch- and yaw-correction axes are conservatively estimated at 9 and 8 kg, respectively. The mass moment of inertia is estimated at $8.09 \times 10^5 \text{ g-cm}^2$. A peak accelerating force of



0.409 N (0.092 lb) is thus required in pitch. In roll, the peak force is 0.26 N (0.058 lb). The peak accelerating torque in the yaw-correction axis is calculated as 1.4×10^{-4} kg-m (1.01×10^{-3} lb-ft).

If the system were frictionless, the shaft power required to accomplish these motions would be 8.9×10^{-5} W (1.2×10^{-7} hp) in the pitch axis and 6.0×10^{-5} W (8×10^{-8} hp) in the roll axis. In the yaw axis, the shaft power required would be 2.3×10^{-5} W (3.1×10^{-8} hp). The system can obviously use very small prime movers, and much of the power will be dissipated in friction.

Another test of the effectiveness of this feed-forward image-stabilization system is its ability to follow the essentially triangular worst-case command (assuming that a perfectly accurate correction command is available). The correction signal will be identical to the limit cycle (with the proper scaling), and is assumed to be a perfect triangular wave. The actual limit cycle will have slightly rounded peaks. The period of acceleration for the Orbiter varies from about 0.625 sec for the roll axis to 0.91 sec for the negative-pitch axis.

In terms of the feed-forward correction, a perfect triangular wave is a worst case and was used to test the dynamic accuracy. The expression for the idealized command signal, scaled to units of sensor resolution elements $[C(t)]$, is as follows:

$$C(t) = 26.44 \left(\frac{4t}{T} - 1 \right) \text{ for } 0 < t < \frac{T}{2}$$

$$C(t) = 26.44 \left[1 - \frac{4 \left(t - \frac{T}{2} \right)}{T} \right] \text{ for } \frac{T}{2} < t < T$$

etc., where T , the period of the limit cycle, is 40 sec. The expression can be written in the following form:

$$C(t) = 26.44 \left[-1 + \frac{4t}{T} - \frac{8 \left(t - \frac{T}{2} \right)}{T} u \left(t - \frac{T}{2} \right) + \frac{8 \left(t - T \right)}{T} u \left(t - T \right) - \dots \right]$$

where $u \left(t - t_0 \right) \equiv 0$ for $0 < t < t_0$
 $\equiv 1$ for $t_0 < t < \infty$

This function transforms to

$$C(S) = 26.44 \left[\left(\frac{4}{T} \cdot \frac{1}{S^2} - \frac{1}{S} \right) + \frac{8}{TS^2} \sum_{n=1}^{\infty} (-1)^n e^{-n \frac{T}{2} S} \right]$$

where S is the Laplace operator.

It was assumed that the dominant closed-loop singularities of the servo response can be represented as a pair of complex poles with critical damping $\left(\zeta = \frac{1}{\sqrt{2}} \right)$. The servo transfer function is then given by

$$G(S) = \frac{\omega_n^2}{S^2 + 2 \zeta \omega_n S + \omega_n^2} \Big|_{\zeta=1/\sqrt{2}}$$

where ω_n is the natural frequency. Thus,

$$G(S) = \frac{\omega_n^2}{S^2 + \sqrt{2} \omega_n S + \omega_n^2}$$

Letting $\alpha = \frac{\omega_n}{\sqrt{2}}$,

$$G(S) = \frac{2 \alpha^2}{S^2 + 2 \alpha S + 2 \alpha^2}$$

$$= \frac{2 \alpha^2}{(S + \alpha)^2 + \alpha^2}$$

The transform of the output response is given by

$$R(S) = G(S) C(S)$$

Hence,

$$R(S) = \frac{2 \alpha^2}{(S+\alpha)^2 + \alpha^2} (26.44) \left[\frac{4}{TS^2} - \frac{1}{S} + \frac{8}{TS^2} \sum_{n=1}^{\infty} (-1)^n e^{-\frac{nT}{2S}} \right]$$

Partitioning for convenience,

$$R(S) = 26.44 \left[R_1(S) + R_2(S) + R_3(S) \sum_{n=1}^{\infty} (-1)^n e^{-\frac{nT}{2S}} \right]$$

$$R_1(S) = \frac{4}{T} \frac{2 \alpha^2}{S^2 [(S+\alpha)^2 + \alpha^2]} + \frac{4}{T} \left[\frac{1}{S^2} - \frac{1}{\alpha S} + \frac{1}{\alpha} \frac{(S+\alpha)}{(S+\alpha)^2 + \alpha^2} \right]$$

$$R_2(S) = \frac{-2 \alpha^2}{S [(S+\alpha)^2 + \alpha^2]} = \left[-\frac{1}{S} + \frac{S + 2\alpha}{(S+\alpha)^2 + \alpha^2} \right]$$

$$R_3(S) = \frac{8}{T} \frac{2 \alpha^2}{S^2 [(S+\alpha)^2 + \alpha^2]} = \frac{8}{T} \left[\frac{1}{S^2} - \frac{1}{\alpha S} + \frac{1}{\alpha} \frac{S + \alpha}{(S+\alpha)^2 + \alpha^2} \right]$$

Thus, the inverse transforms are

$$R_1(t) = \frac{4}{T} \left[t - \frac{1}{\alpha} (1 - e^{-\alpha t} \cos \alpha t) \right]$$

$$R_2(t) = e^{-\alpha t} (\sin \alpha t + \cos \alpha t) - 1$$

and

$$R_3(t) = \frac{8}{T} \left[t - \frac{1}{\alpha} (1 - e^{-\alpha t} \cos \alpha t) \right]$$

In the first interval ($0 < t < \frac{T}{2}$),

$$\begin{aligned} R(t) &= 26.44 [R_1(t) + R_2(t)] \\ &= 26.44 \left\{ \frac{4t}{T} - 1 - \frac{4}{\alpha T} + e^{-\alpha t} \left[\left(\frac{4}{\alpha T} + 1 \right) \cos \alpha t + \sin \alpha t \right] \right\} \end{aligned}$$

The difference between the desired and the actual response is given by

$$\begin{aligned} E(t) &= C(t) - R(t) \\ &= 26.44 \left\{ \frac{4}{\alpha T} - e^{-\alpha t} \left[\left(\frac{4}{\alpha T} + 1 \right) \cos \alpha t + \sin \alpha t \right] \right\} \end{aligned}$$

In the second interval ($\frac{T}{2} < t < T$),

$$\begin{aligned} R(t) &= 26.44 \left[R_1(t) + R_2(t) - R_3\left(t - \frac{T}{2}\right) u\left(t - \frac{T}{2}\right) \right] \\ &= 26.44 \left\{ 3 - \frac{4t}{T} + \frac{4}{\alpha T} + e^{-\alpha t} \left[\left(\frac{4}{\alpha T} + 1 \right) \cos \alpha t + \sin \alpha t \right] \right. \\ &\quad \left. + e^{-\alpha\left(t - \frac{T}{2}\right)} \cos \alpha\left(t - \frac{T}{2}\right) \right\} \end{aligned}$$

and

$$E(t) = - \left\{ \frac{4}{\alpha T} + e^{-\alpha t} \left[\left(\frac{4}{\alpha T} + 1 \right) \cos \alpha t + \sin \alpha t \right] \right. \\ \left. + e^{-\alpha \left(t - \frac{T}{2} \right)} \cos \alpha \left(t - \frac{T}{2} \right) \right\}$$

After the transients have died out, the steady-state error in the first interval is $26.44 \left(\frac{4}{\alpha T} \right)$ elements and in the second interval is $-26.44 \left(\frac{4}{\alpha T} \right)$ elements.

A typical instrument servo of this kind can have a time constant as short as 30 msec (or a natural frequency of about 33.3 rad/sec). With a 40-sec Orbiter limit cycle of motion (i.e., $T = 40$), the error is computed as follows:

$$\left| E(t) \right| = \frac{(26.44)(4)}{\alpha T} = \frac{(26.44)(4 \sqrt{2})}{\omega_n T} \\ = \frac{(26.44)(4 \sqrt{2})}{(33.3)(40)} = 0.112 \text{ element}$$

The transient errors will die to 1% of their initial values in

$$t = \frac{\sqrt{2}}{\omega_n} \ln 10^2 = \frac{6.513}{\omega_n} = 0.196 \text{ sec}$$

This implies that, for roughly 99% of the time, the steady-state ± 0.11 -element error will hold and the data will be valid.

The position limit cycle and idealized image-motion-compensation (IMC) command (C) and response (R) are shown in Figure 7-5. A block diagram for the IMC servo system is presented in Figure 7-6.



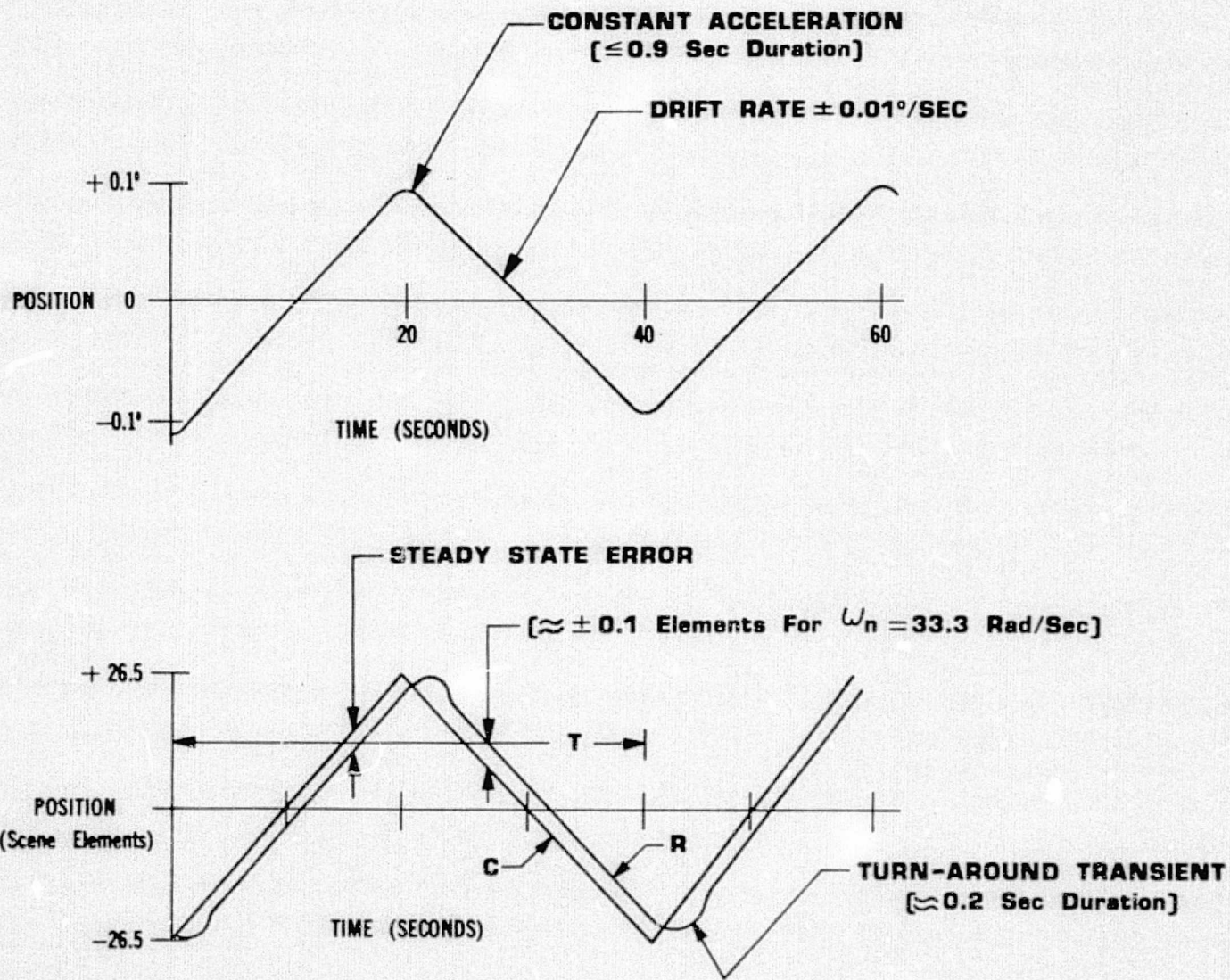
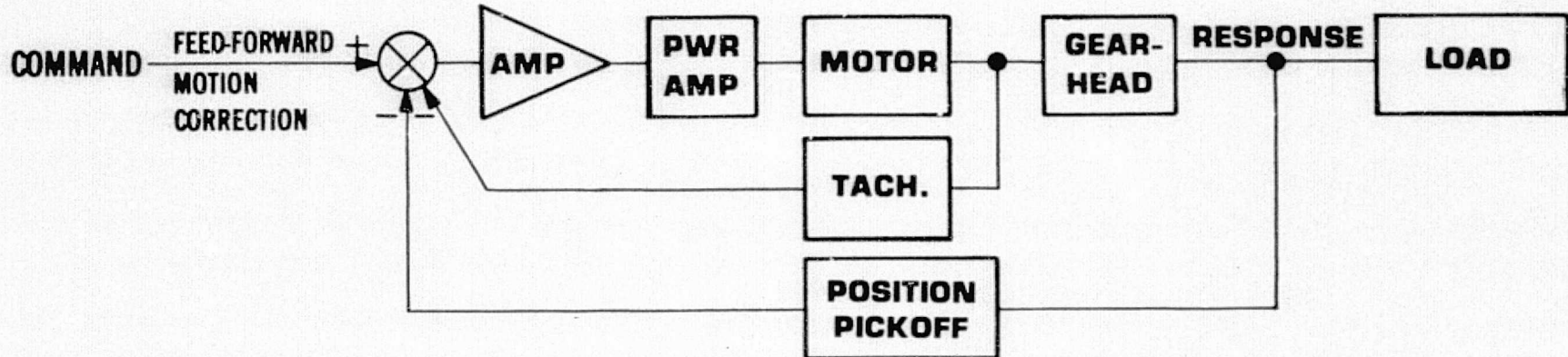


FIGURE 7-5 ACTUAL-POSITION LIMIT CYCLE (WORST CASE) AND IDEALIZED IMC COMMAND AND RESPONSE



CLOSED-LOOP TRANSFER FUNCTION, FOCAL-PLANE MOTION COMPENSATION SERVOS [EACH AXIS]

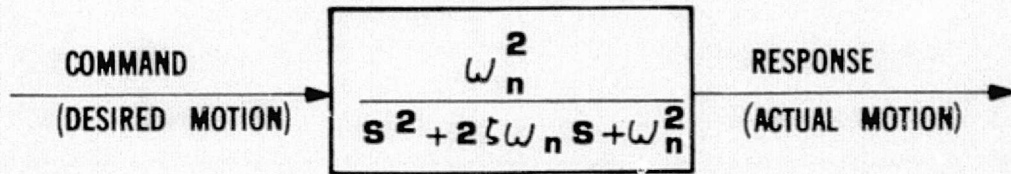


FIGURE 7-6 FOCAL-PLANE MOTION-COMPENSATION SERVOS (EACH AXIS), BLOCK DIAGRAM

Section 8

DATA PROCESSING AND DATA COMPRESSION

8.1 DATA-HANDLING CONCEPTS

A simplified diagram of sampling electronics for the SMSS is presented in Figure 8-1. The system incorporates visible-light and IR detector arrays that collect, in a CTD shift register, a charge proportional to the radiation incident on them for a dwell time that varies with the orbital altitude.

In the case of the visible-spectrum detectors, the dwell time for the 185-km orbit is 1.62 msec, and the CTD register is cleared at a TC_1 rate of 618 times per second. The charge packets stored in the CTD must then be shifted out and digitized for recording on a high-data-rate system. Because the N -length register must be cleared in 1.62 msec, and $N = 4000$, $NT_C = 2.475$ MHz, which is the shift rate and is also the rate at which A/D converters must operate.

One of several possible schemes for making gross corrections to cell variability is to change the gain of an amplifier feeding an A/D converter. If a series of words of r bits each is stored in a recirculating shift register and is shifted in synchronism with the data from detectors, these words can be used to modify the gain of the amplifier through which the data pass. If the r -bit words are made inversely proportional to the detector sensitivities (or gain), the output of the amplifier would correct for gross differences in sensitivities.

A possible way to implement this scheme is shown in Figure 8-1. The r -bit word is applied to a digital-to-analog (D/A) converter, whose output voltage is applied to the integrating amplifier. The amplifier gain is made proportional to this applied voltage.



The outputs of the A/D converters (one for each channel) are sampled in the right combination by the recorder formatter and input multiplexer to satisfy the input requirements of the data-recorder system. Because only six of the ten arrays are to be active at a time, the combined data rate for the assumed parameters at 8 bits/detector sample is 119 Mbps. The rate would be increased slightly by such ancillary data as frame-synchronization words.

An alert header would also be necessary in order to identify calibration data to the data-reduction system. A 20-bit, 1-sec clock is inserted that will present unique time (GMT) for as long as a week. A timing and control unit synchronizes all processes in the sampling system.

Although the simplified concept outlined above can function satisfactorily for the visible channels, the high background level presented to some of the IR arrays would cause the CTD shift registers to saturate long before the 1.62-msec ground-resolution sampling time has passed. Figures 8-2 and 8-3 illustrate two methods of processing IR data to overcome this problem; Figure 8-4 diagrams the timing for both.

The digital system shown in Figure 8-2 essentially unloads the IR array "m" times faster than the visible array. The value for m is chosen so that the charge does not saturate the CTD. The data are corrected as before and are digitized. They are then shifted through two adders, the first of which adds the complement of the background charge divided by m. The difference is then added to the contents of an 8-bit by N-bit recirculating shift register that sums the Δ samples (Δ = total charge minus background) of the N detectors of the IR array.

Once during every m cycles of the register, the output signal disables the recirculation and shifts the data out to the recorder system. Because this occurs at a much higher rate than for the visible channels, a buffer would probably be needed to reduce the output rate. Buffering could





SEE FIGURE 8-4 FOR
SIGNAL-TIMING RELATION. IPS

8-5

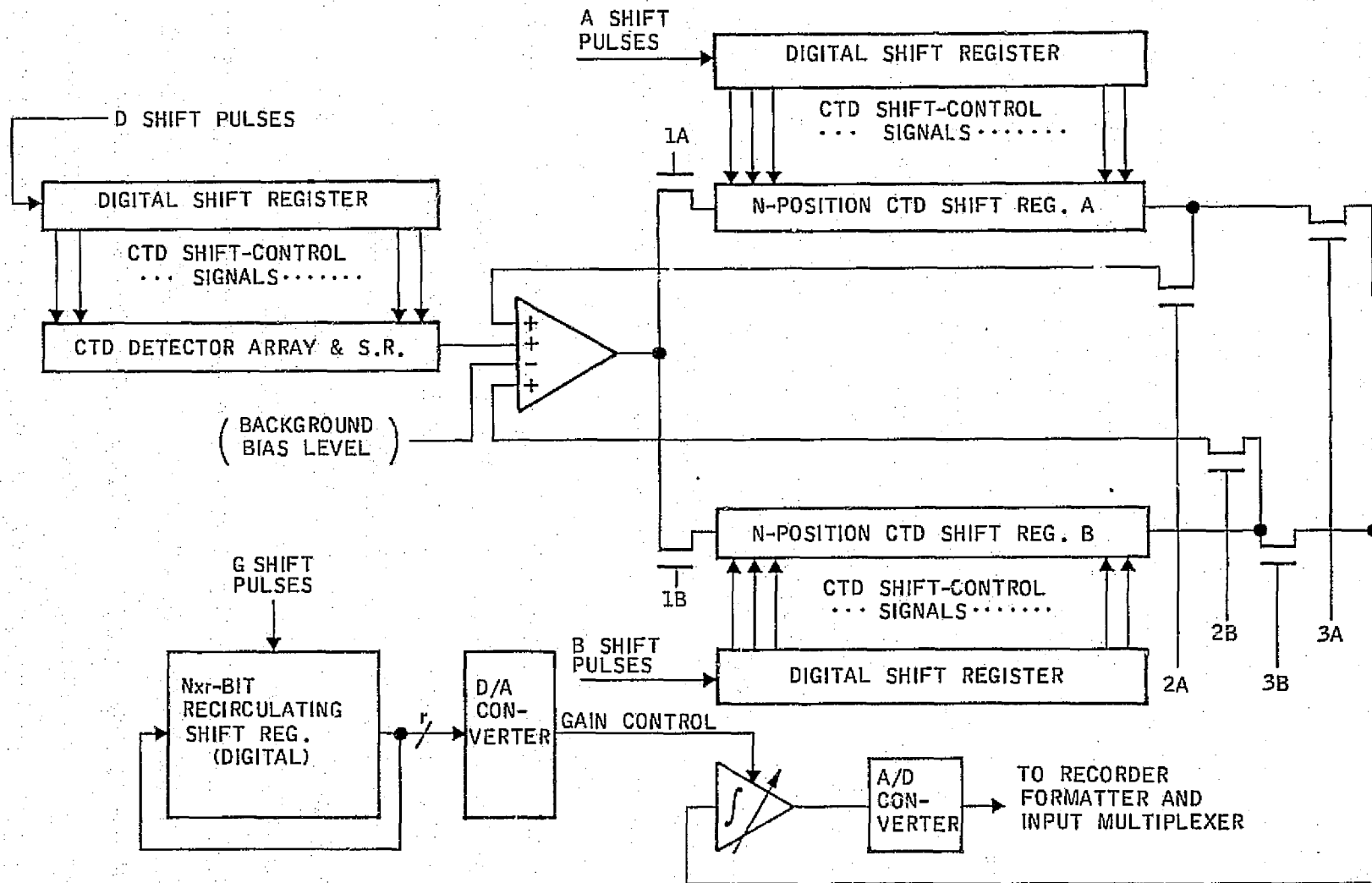


FIGURE 8-3 ANALOG MODIFICATION FOR REMOVAL OF HIGH-BACKGROUND BIAS

675-1143

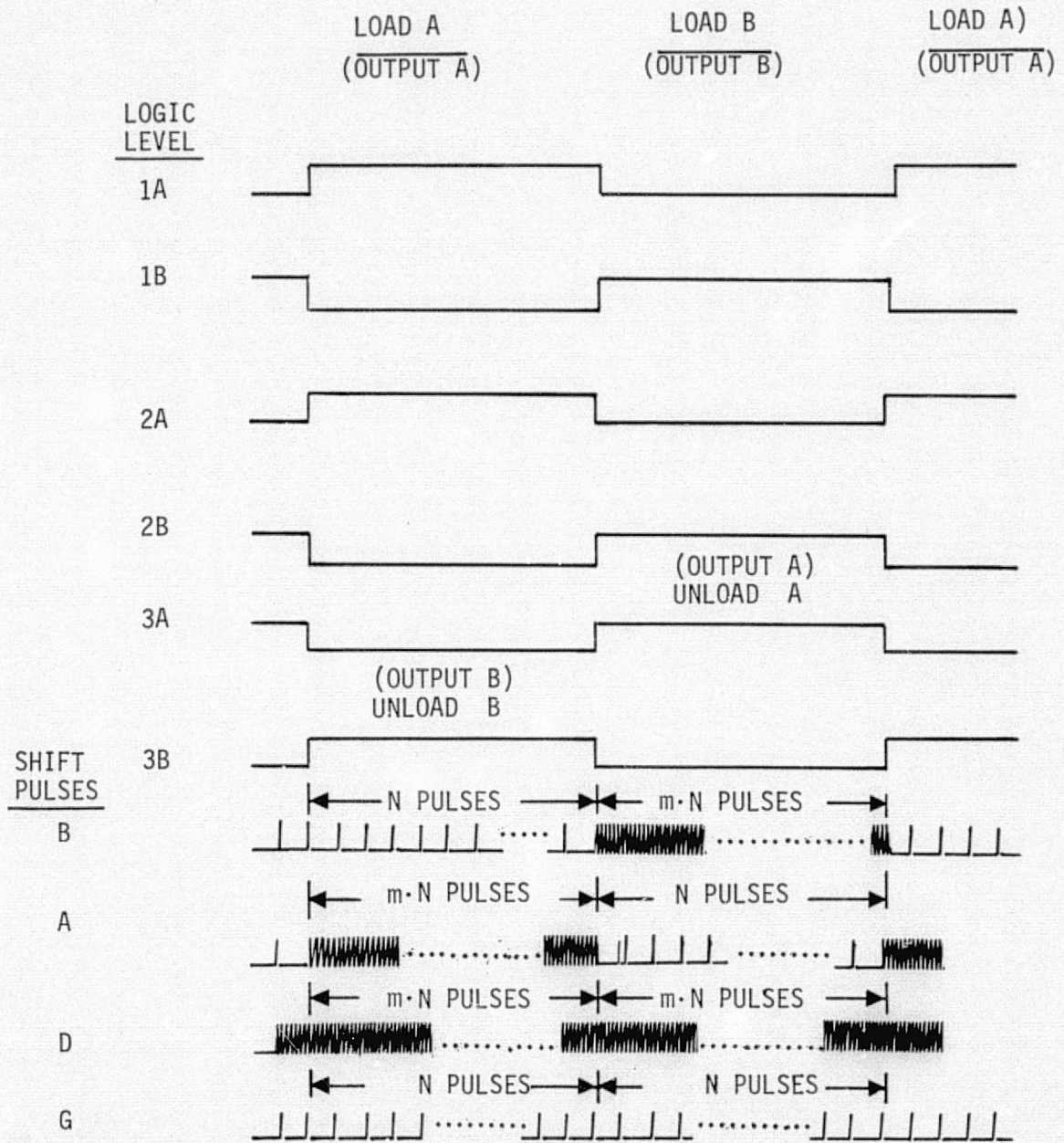


FIGURE 8-4 TIMING DIAGRAM



be accomplished with a second recirculating shift register that would accept the data at the higher rate and then clock it out at the nominal 2.5 megawords per second.

An analog concept for the handling of the high background level or bias is illustrated in Figure 8-3. The same principle as above is applied in that the detector CTD shift register is unloaded m times per scene-resolution element (1.62 msec). An analog signal proportional to the background-bias level is subtracted in the integrating amplifier, and the difference is added m times to the previous Δ signal. The resulting signal is switched to read out to the A/D and recording systems at a lower rate compatible with the real-time scene-resolution rate (2.5 megasamples per second). While one shift register is being emptied, the signals from the detector array are switched to a second shift register and the process is repeated, pingponging back and forth between the two arrays.

Two other possible methods of overcoming the IR-saturation problem have to do with the CTD itself. One involves detector-array design to make the CTD storage portion large as compared with the detector area. This approach increases the storage capacity relative to the detector efficiency; consequently, more time elapses before the storage elements are saturated. The second method involves an integrated configuration that in essence subtracts the background-bias level within the CTD and disperses this bias back into the substrate material m times per sampling period. These two techniques (which are under investigation but not yet developed) would be preferable to the two external methods previously discussed. This is because of insertion losses that could be accumulated in the analog approach each time the charges were recirculated, and because of the complexity and speed with which the digital-accumulation approach would have to operate. All these methods, however, are conceptually feasible and could be made to operate satisfactorily.



8.2 DATA COMPRESSION

Several methods of data compression can be considered for the SMSS system, whose data are to be recorded and brought down physically by the Space Shuttle rather than transmitted to the earth. The availability of high-data-rate recording systems during the applicable period (1980) has been established, and the need to compress data would stem only from the desire to reduce the amount of recording medium (reels of tape) used in a mission, or to prolong the period between tape changes.

Data compression has the disadvantage of introducing more-complicated data-handling logic and hence more components. Because it also increases the value of every piece of information, every bit drop becomes more critical. Because it alters the data from the basic form, raw data are not available.

The methods of data compression that can be considered range from very simple to very complex.

One approach involves data-rate reduction by recording only every other sample ("comb thinning") and assumes that the crosstrack ground resolution is higher than necessary. To accomplish this data compression (approximately 50%), it is necessary only to skip every other convert-and-transfer-to-recorder-system pulse.

A second method assumes that the intensity resolution is greater than required, and it is necessary therefore only to record returns from data areas exceeding some intensity threshold (average background). A threshold level is set and intensities are compared with it. Only the returns exceeding the threshold are converted and recorded. They must be identified as to their positional origin in the scene because there is a loss of "frame position" (or framing) in a thresholding scheme. All missing data samples are assumed to be background of no interest.

A third method assumes that, in an overall scene, the data from a neighboring pixel will be near the intensity of the pixel itself. Consequently, if a threshold is set on the difference or delta intensity and only the deltas that exceed the threshold are recorded, some data-rate reduction will occur. As in pure thresholding, identifiers must be applied to the data that exceed the threshold, because framing is lost in the process.

A method introduced by D. Huffman (described in Ref. 8-1) makes use of the fact that certain data values are more likely to occur than others. His scheme employs a variable-length code in which the values most likely to occur are given the shortest code words and the least likely the longest. A series of data points can thus be described in a minimum-length message. Although the code words are of variable length, data framing is maintained in the absence of errors.

An attractive approach would be to combine the delta approach (with a high probability of very small deltas) and the Huffman encoding technique. It has the advantages of (a) forcing a high probability of occurrence on a certain segment of the data (near-zero differences), and (b) the frame retention of Huffman encoding. The compression realized depends on the behavior of the data and therefore on the delta values. Implementation is expedited by the fact that the detectors are "scanned" by a CTD shift register that simultaneously makes data available from the Nth and the (N+1)th cells and therefore simplifies the delta differencing. This approach is sketched below (where ROM represents read-only memory).

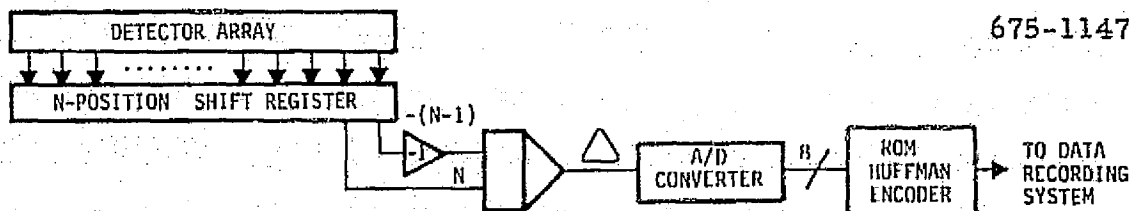


Table 8-1 summarizes applicable data-compression techniques.





TABLE 8-1 APPLICABLE DATA-COMPRESSON TECHNIQUES

Item	Type	Description	Remarks
1	Comb thinning	Removes data from every other detector in the arrays.	Reduction \approx 50%. Assumes cross-path resolution higher than necessary. Easy to accomplish.
2	Thresholding	Discards all data whose intensity is less than a threshold (T).	Assumes an intensity resolution greater than required. Amount of reduction depends on data content. Requires identifiers be appended to data because framing is lost in thresholding.
3	Pixel Δ + threshold	Differences adjacent-channel data and thresholds; discards all $\Delta < T$, where Δ = difference from last channel whose $\Delta > T$.	Assumes smooth intensity variations across a scene. Amount of reduction depends on data content. Requires that identifiers be appended to passed data because framing is lost in thresholding.
4	Huffman coding (minimum-path technique)	Assigns data intensities a variable-length code, with most-probable values given shortest code words.	Assumes <u>a priori</u> knowledge of data values. Amount of reduction depends on data distribution and ability to predict its probability. Maintains framing if errors are negligible.
5	Combination of pixel Δ + Huffman coding	Differences adjacent-channel data and performs Huffman coding on the resultant difference.	Has the advantages of Item 3 without thresholding and resultant loss of framing. Has advantages of Item 4 with a higher probability of accurate <u>a priori</u> data prediction and therefore is most likely to produce substantial data compression.

Section 9

REAL-TIME CALIBRATION

The method proposed for calibrating SMSS detector arrays in orbit is illustrated in Figure 9-1.

A sliding shutter masks out incident radiation during the injection of a known level of excitation from internally mounted LEDs. Two calibration levels are used: (a) a reference level, and (b) one that is near full-scale. The reference level is employed to remove offset differences between detectors.

Switch S1 is electronically connected to the calibrate (CAL) position for the sample period corresponding to the time when the sample from Cell N is shifted out. Cell N is under the shutter, and the known excitation level, L_0 , is impinging on it. The reference level, V_0 , is thus obtained and stored in the recirculating shift register for offset corrections. Switch S1 and the shutter are synchronized so that only the signal from the detector being calibrated is inserted in the register. The data remaining in the register recirculate unaltered (S1 in OPER position).

A second level of calibration, L_1 , is then injected onto the detectors by the LEDs under the shutter. The offset value obtained earlier is removed from the output voltage, and the value V_1 is stored in a second, synchronized, recirculating shift register by the action of S2. S2 is also synchronized with the shutter so that only the signal from the detector or detectors being illuminated by the calibration source is inserted into the register. The remaining data in the shift register that stores gain corrections are circulated without alteration.



BEST ORIGINAL PAGE IS OF POOR QUALITY

975-1600

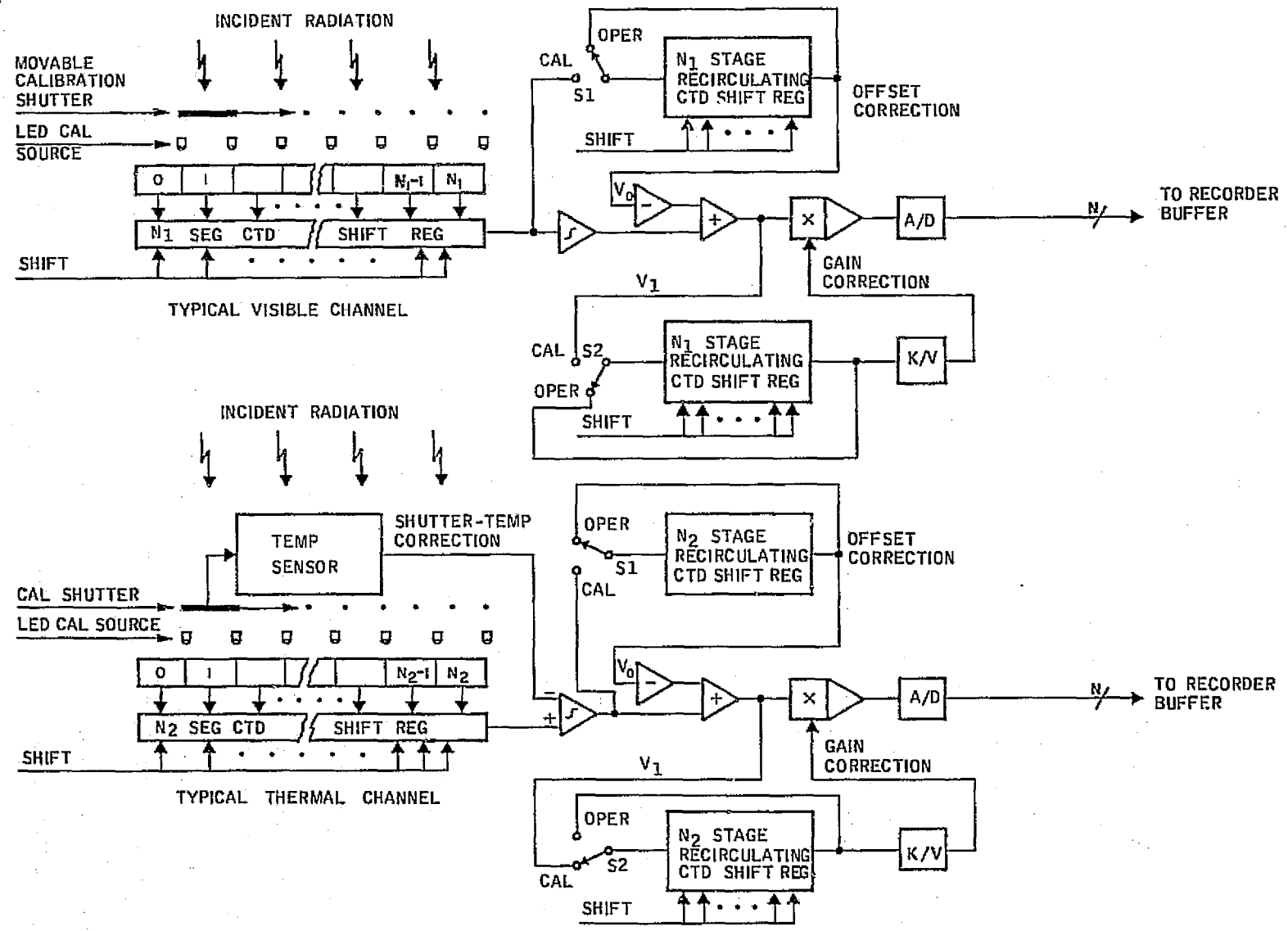


FIGURE 9-1 ONBOARD CALIBRATION, BLOCK DIAGRAM

Report 4 5231

The value V_1 , then, is the response of the detector to a known level of radiation. The detector output, corrected for offset, can be multiplied by a value K/V_1 , where K is the desired response at the L_1 calibration level. All detectors will therefore exhibit one identical response for inputs of L_1 radiation. If the response of all detectors is linear over the range of interest, all detectors will have been calibrated to respond identically to any level, L_N , of incident radiation within their linear operating region.

A refinement for the thermal (long-wavelength) channels includes the extraction of any input due to the temperature of the calibration shutter. This input is removed by subtracting a voltage proportional to the shutter temperature from the detector output signal. The voltage is obtained by instrumenting the shutter with a temperature sensor as illustrated by the second general channel (N_2).

An analog-calibration-correction method is used in this technique. The same method could be implemented with digital storage and arithmetic operations. This could be accomplished by sampling calibration data after conversion of the analog voltage to a digital value and by performing subtractions and multiplications with a digital arithmetic-logic unit (ALU).

Section 10

GROUND SUPPORT EQUIPMENT

Ground support equipment is required by the SMSS to confirm performance parameters, verify flight readiness and peak system performance, aid in ground calibration, and assist in troubleshooting during repair.

Figure 10-1 shows the SMSS and ground support equipment (GSE) required to perform these tasks. The equipment includes a target simulator, gimbal service, cryogenic service, a high-data-rate (HDR) recording (and playback) system, an Orbiter interface and power simulator, an electronic-checkout system, and a video processor and hard-copy recorder device.

10.1 TARGET SIMULATOR

The target simulator (Figure 10-2) will produce a scene for the SMSS front-end optics that can be used for an end-to-end check of the system with the aid of an HDR recording system identical in electrical characteristics to the one carried by the Orbiter. The data are then played back through the electronic checkout module, which is capable of selecting any channel for video processing through the associated digital-to-analog (D/A) conversion system so that the scene may be viewed on a high-resolution-television monitor or evaluated on hard copy.

The simulator was developed by Aerojet and can be made available for the SMSS development, qualification, and prelaunch testing and checkout. It was designed and fabricated for the Air Force Avionics Laboratory, Wright-Patterson Air Force Base during 1966-1968 at a cost of approximately \$1.1 million. Its primary use is with the Air Force Dynamic Analyzer for the evaluation of infrared-reconnaissance sensors. Although it presently interfaces with the analyzer, relatively minor modifications would be required

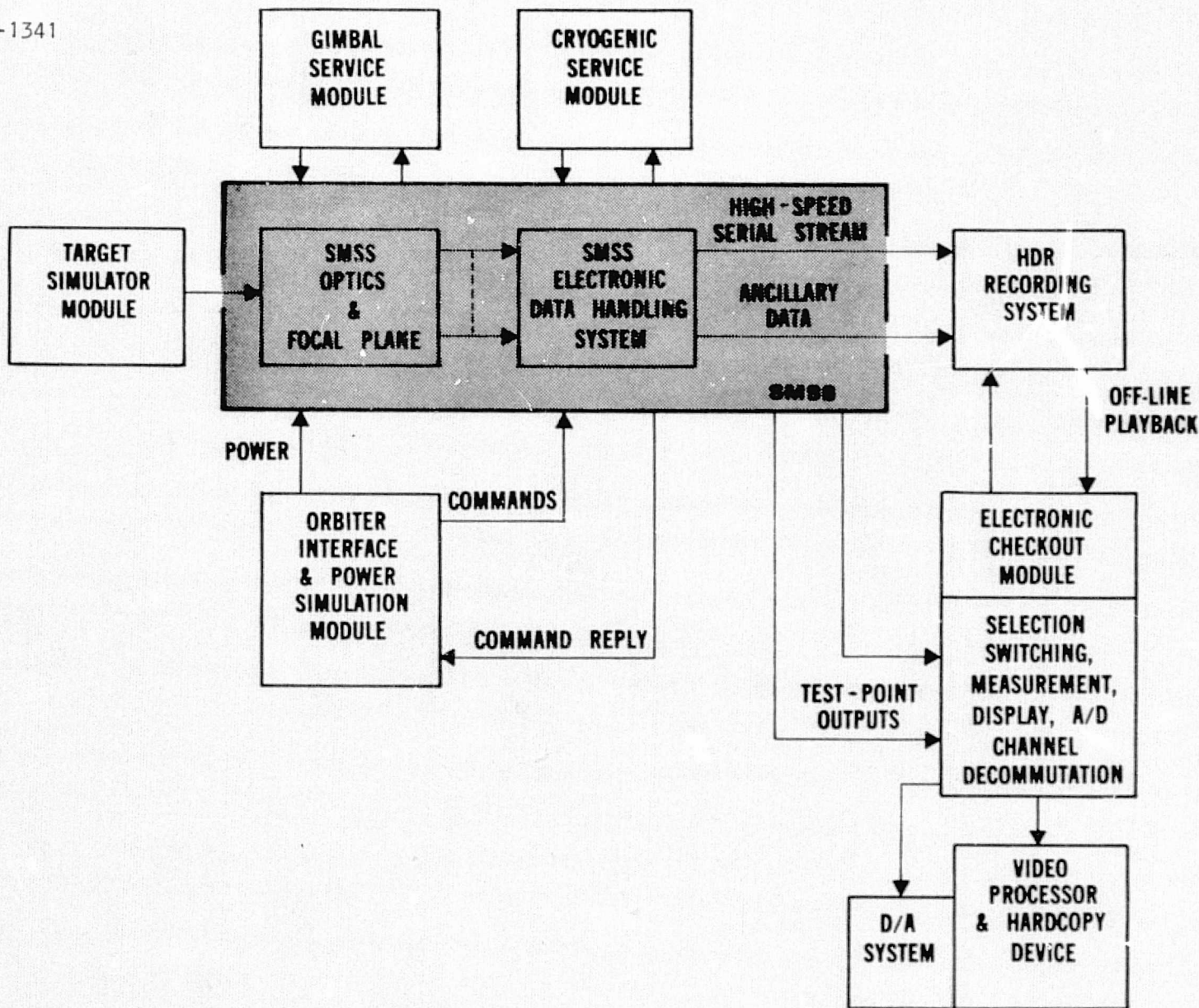
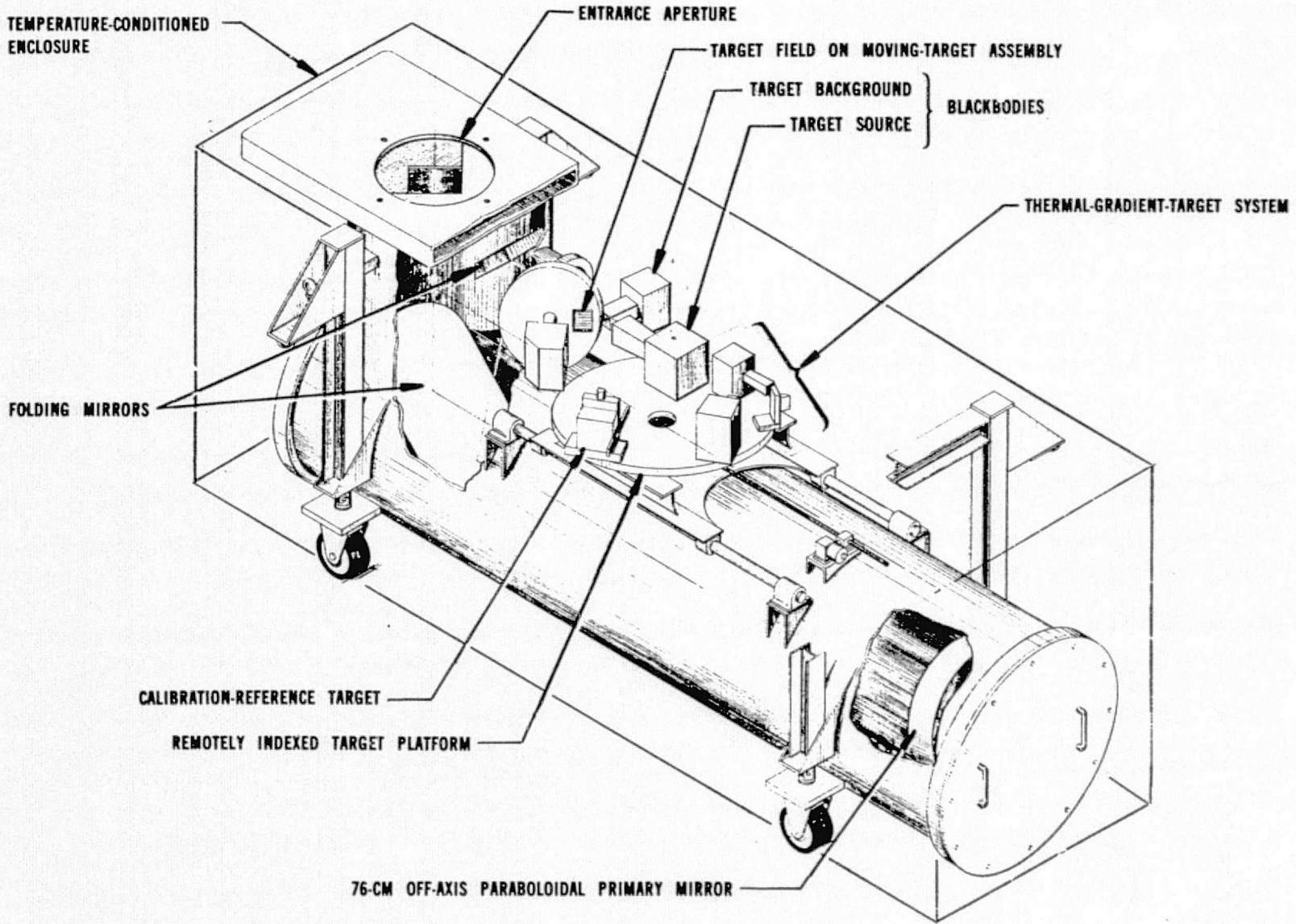


FIGURE 10-1 GROUND SUPPORT SYSTEM, SMSS SIGNAL PROCESSING

1275-1409



10-3

FIGURE 10-2 INFRARED TARGET SIMULATOR, ISOMETRIC VIEW

for use in SMSS checkout. Its capability to test the functioning of the SMSS infrared channels is inherent, because it was designed to test a variety of IR sensors. Although the simulator is presently incapable of checking out systems operating below $1\ \mu\text{m}$, the target subsystem is modular and modifications to include a visible-spectrum target capability would not be difficult.

The resolution of the simulator is approximately 10 seconds of arc, which will be adequate for SMSS operational checkout (but not quantitative evaluation), assuming that the SMSS final design retains the recommended $66\text{-}\mu\text{r}$ IFOV (approximately 14 seconds of arc). Absolute radiometric calibration and radiometric-gradient measurements (NEAT and NEAp) can be made quantitatively during SMSS development and qualification testing as well as during prelaunch checkout and calibration.

Table 10-1 summarizes the capabilities and characteristics of this key GSE item.

The simulator (see Figure 10-2) incorporates a reflective collimator with a remote-controlled movable-target-turret assembly providing the required target types and groundspeed-simulation mechanism. The auxiliary equipment consists of the operator's control console and an air-conditioning unit. The two beam-deviating plane mirrors reflect turret-generated patterns to a 76-cm (30-in.), aspheric, primary collimating mirror. The second plane mirror will reflect the primary-formed collimated beam to the SMSS installed on a platform above the simulator for testing. The collimating optical elements are housed in a cylindrical tank-type structure that provides a mounting for the target turret and thermal-enclosure panels.

Simplified selection of test targets is provided by a turntable sequencer that automatically performs the functions necessary for selection. Target-source temperatures are set by direct-reading dials that eliminate the need for applying calibration-curve corrections to the setting. Target temperatures are displayed on panel meters for coarse readings. The



TABLE 10-1 SIMULATION CAPABILITIES AND CHARACTERISTICS

Parameter	Simulator Capability
Viewing altitude	Simulates viewing altitude from 60 m (200 ft) to infinity.
Spectral range of targets	1 to 20 μm .
Target motion	Simulates target motion from 5.0 mr/sec to 7.0 rad/sec (SMSS requires 9 to 41 mr/sec).
Moving IR targets	Simulates targets to perform resolution and sensitivity tests, both along and across the simulated line of flight, with a temperature range from -20 to 500°C.
Calibration reference	Target temperature adjustable from -20 to 1000°C; eight operator-selected filters and nine operator-selected apertures in any combination; drive permits target positioning at any point in target field.
Thermal-gradient target	Adjacent extended sources with temperature differential adjustable from 0 to 15°C and average temperature adjustable between -20 and 500°C.
Modulation transfer function (MTF)	MTF method of image analysis with temperature range from -20 to 500°C, and background simulation from -25 to 500°C.
Background temperature	Simulates a constant background temperature adjustable from -25 to 500°C.
System size	594 cm long, 240 cm high, 168 cm wide (234 x 94.5 x 66 in.)
System weight	Approximately 6300 kg (14,000 lb)
Collimator subsystem	
Type of optics	Reflective, folded, off-axis, parabolic
Collimator-beam size	68.5 cm (25 in.)
Effective focal length	620 cm (244 in.)
System focal ratio	f/11.5
Spectral range	1 to 20 μm
Focus	60 m (200 ft) to infinity
Target field angle	0.8° by 0.8° (10 x 10 cm, or 4 x 4 in.)
Total resolution	9.54 seconds of arc (center of field)

(continued)



TABLE 10-1 SIMULATION CAPABILITIES AND CHARACTERISTICS (CONT.)

Parameter	Simulator Capability
Target subsystems	
Moving target	Rotating disk with optical reimaging: lateral distortion 0.0254 cm (0.010 in.), field curvature 0.0762 cm (0.030 in.), astigmatism 0.152 cm (0.060 in.), coma 0.0254 cm (0.10 in.), longitudinal distortion 15%
Target source	Blackbody
Background target	Blackbody, adjustable from -20 to 500°C
Thermal-gradient target	
IR sources	Two blackbodies
Source dimensions	2.5 x 5 cm (1 x 2 in.)
Temperature differential	Adjustable between 0 and 15°C
Differential-temperature readout accuracy	0.01°C
Average source temperature	Adjustable between -20 and 300°C
Calibration-reference target	
Aperture sizes	0.025, 0.051, 0.102, 0.127, 0.203, 0.254, 0.406, 0.508, and 0.813 cm (0.01, 0.02, 0.04, 0.05, 0.08, 0.10, 0.16, 0.20, and 0.32 in.)
Filters	Eight, in spectral range to match SMSS channels
Chopper	Variable over range from 5 to 1000 Hz
Drive	x- and y-position drive for location at any point in target field
Source	Blackbody
Aperture (collimator)	Adjustable from 0 to 63.5 cm (25 in.)
Auxiliary equipment	
Temperature conditioning	
Collimator	77 ± 1°F
Housing	77 ± 2°F
Target backgrounds	-40°C
Control console	Remote target control, temperature control, aperture, focus, window temperature, MTF recording

temperature analog is then switched to a digital meter that provides the test value directly in degrees for accurate data acquisition. A similar technique will be used for all system functions that specify test conditions for SMSS evaluation.

The large collimator mirrors are mounted permanently; after initial alignment, they do not require movement for a test. Focusing is accomplished by a remote-controlled target-carriage assembly. This method assures that system alignment is retained.

The simulator environment is maintained at precise temperature and humidity levels so that variations in the field-checkout environment will not affect the test data. Environmental control is provided by a self-contained, completely automatic system designed for continuous operation. A minimum of monitoring functions are included on the control console to assure proper operation.

Test-data reduction is simplified by positioning the various targets in an easily recognizable pattern in the field. In addition, the radial slots, bars, and holes used with the moving target are optically reimaged so that all targets are presented rectilinearly on the resulting display record. This attribute eliminates the necessity for special data-reduction skills and techniques for evaluating the test.

10.2 ELECTRONIC CHECKOUT MODULE AND AUXILIARY EQUIPMENT

The Orbiter interface and power simulator supplies the power required for the SMSS in a form and capacity equal to that furnished in orbit. Proper operation of the inverters and regulators is confirmed by monitoring the voltage test points available to the electronic checkout module (ECM). The ECM also contains circuits to generate all commands to the SMSS and to monitor command verification. The ECM is used in conjunction with the interface and power simulator to assure that the commanded operation is performed as well as properly verified.

The ECM contains the electronic circuitry required to switch any of the available test points to appropriate standard test equipment in the module. It also contains a single channel for converting, to digital form, any selected channel output from the focal plane. The ECM may utilize the HDR unit to record this output, or may switch the output directly to the video processor for viewing or for hard-copy production.

The ECM also contains equipment required to synchronize and decommutate channel data from the HDR recording system. This allows the finished product to be viewed either for end-to-end test purposes or for postflight processing of real data.

The standard test equipment in the ECM encompasses a high-speed counter, a time-code translator capable of displaying GMT or MET, a digital multifunction meter, a high-speed oscilloscope, a general-purpose bit synchronizer, and a frame-synchronizer decommutator. Also included are test instruments needed to align and check out the HDR recording system.

The video processor and hard-copy device constitute a TV monitor with a resolution approximating that of the SMSS and an associated hard-copy unit to produce permanent images for detailed analysis. They can be used to view scenes as input from the target simulator through the ECM as either analog or digital data.

A gimbal service module will be used during prelaunch system checkout to verify the operational status of the gimbal module, IMC, automatic focus, and calibration systems.

The preliminary investigation of SMSS focal-plane cooling requirements indicated the desirability of open-cycle solid (or liquid) cryogen cooling. A cryogenic service module will therefore be necessary for solidification of the liquid cryogen (LN₂) and for transferring the cryogen to the SMSS.



Appendix A

CONSIDERATIONS RELATED TO EARTH-OBSERVATION MISSIONS

Typical missions related to SMSS requirements were analyzed in a survey of Refs. A-1 through A-8 covering investigations conducted by or for NASA (the Goddard Space Flight Center, the Lyndon B. Johnson Space Center, and the NASA/Scientific and Technical Office). The analyses indicated the applicability of the conceptual SMSS for research experiments, data-acquisition measurements, and proof tests of components.

Research experiments can be conducted with the SMSS to determine the feasibility of making particular measurements from a space platform. Although a multipurpose, modular, SMSS sensor may in some cases provide more channels and a higher signal-to-noise ratio (S/N) than necessary, the data obtained will define the optimum number of detector channels, the required resolution (spatial and spectral), and the necessary S/N value. Missions need not be on optimal orbits to satisfy these objectives.

In addition, data-acquisition measurements can be cost-effectively performed from the Shuttle Orbiter if they are not required too frequently, or if the sensor weight, volume, and support requirements (e.g., cryogenics and data rate) are not compatible with an unmanned satellite. Routine, frequent, measurements with a more readily integrated sensor can probably be most-cost-effectively performed by an unmanned vehicle such as the Earth Observatory Satellite (EOS).

The SMSS could also be used for proof tests of components selected for other unmanned satellites or deep-space platforms. A focal plane for a deep-space sensor could be checked out before it is deployed on a costly, extended mission in which inadequate performance could negate the mission effectiveness and perhaps cause a delay of several years before the desired measurements can be obtained.



Several earth-observation missions that can be cost-effectively performed with the SMSS are discussed below.

1 AGRONOMY

The Shuttle Orbiter offers an ideal platform for earth-signature measurements to assist analysts in the study of field-crop production and soil management within the United States and elsewhere. Needs for greater food production are growing with increasing world population, the inability of many low-production nations to purchase food from others, and recognition that underprivileged peoples must be fed.

U.S. farmers, with the support of the Department of Agriculture, have developed the most efficient land-use program of any nation, and U.S. agricultural methods have created exportable produce that enhances the U.S. trade balance. Timely observations of crop status from a space platform will assist in the prediction of food production for U.S. consumption as well as for export, in evaluation of land usage, and in detection of infestations that degrade production. Given an alert, farmers can take preventative measures before serious damage results. Space surveys of snow cover and rainfall can be used to determine if an adequate water supply can be developed. The type of vegetation in remote areas will indicate whether the land can be used for efficient farm production.

It is planned that the EOS-A satellite will employ a thematic mapper for agronomy applications. A resolution of 30 m will be adequate for use in surveying individual farm plots of the order of 16 hectares (40 acres) or less. However, the four wavebands selected for the spectral regions of plant-reflected radiations, a minimum S/N of 5 or 10, and the combination of several plant species in a single resolution element will make it extremely difficult for EOS-A to distinguish plant types or evaluate plant health. Unmanned-satellite sensor parameters are severely limited by payload weight, volume, and telemetry requirements. It is true that an aircraft-based sensor, using more detectors in more wavebands, could achieve spatial and spectral



resolution better than the thematic mappers, and the telescope design could provide an adequate S/N value. However, cost-effective aircraft coverage is limited to relatively small areas by aircraft velocity, altitude, and in-flight time constraints.

The SMSS concept is ideally suited for agronomy applications. The additional wavebands and increased S/N will be beneficial in distinguishing crop types. Such improved performance will also be useful in measuring signature differences due to crop health or the influx of weeds. Orbiter flights could also determine snow-coverage areas and evaluate the developable water resources.

Figures A-1 and A-2 (derived from Ref. A-4) illustrate the spectral signatures of several types of crops. Some are very similar (e.g., corn and soybeans) and it is necessary to measure the signatures precisely in multiple wavebands to distinguish between them. Lesser differences must be detected to assess crop health.

Crop types and health can be most effectively discriminated by means of multiple spectral bands in the peaks and valleys of the crop signatures. On the basis of crop signatures as in Figures A-1 and A-2, candidate bands may be as listed in Table A-1 (which was adapted from Ref. A-7 prepared by the LANDSAT-D Thematic Mapper Technical Working Group). Figures A-3 and A-4, respectively, show the range of visible-scene radiance and the required visible-region dynamic range.

The Infrared and long-wavelength infrared (LWIR) portions of the spectrum may provide additional information to distinguish crop species and plant health. The band between 0.69 and 0.75 μm will offer measurements of reflectance rise; however, the crossover in the crop irradiances in this spectral region may reduce the value of these data in the identification of plant types. Measurements in several spectral bands in the LWIR region will provide data for use in deriving plant spectral-emissivity variations.

874-1141

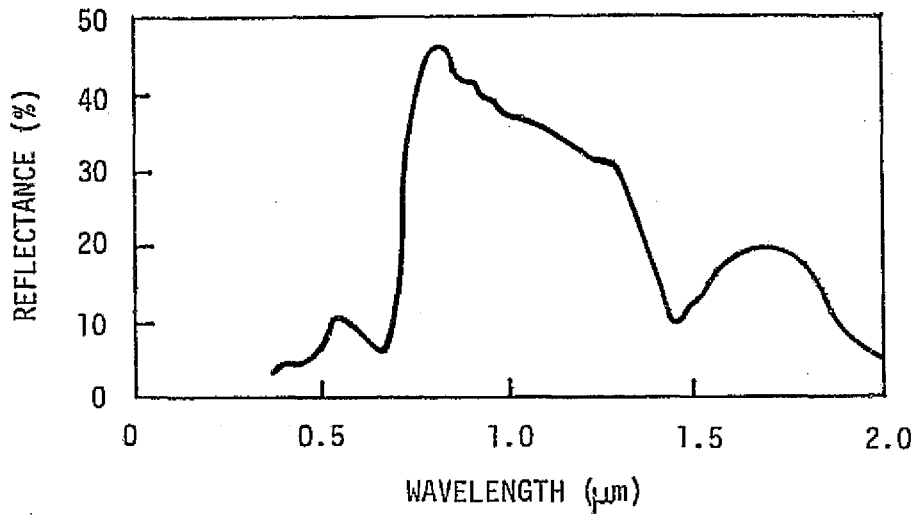


FIGURE A-1 TYPICAL SPECTRAL RESPONSE OF VEGETATION

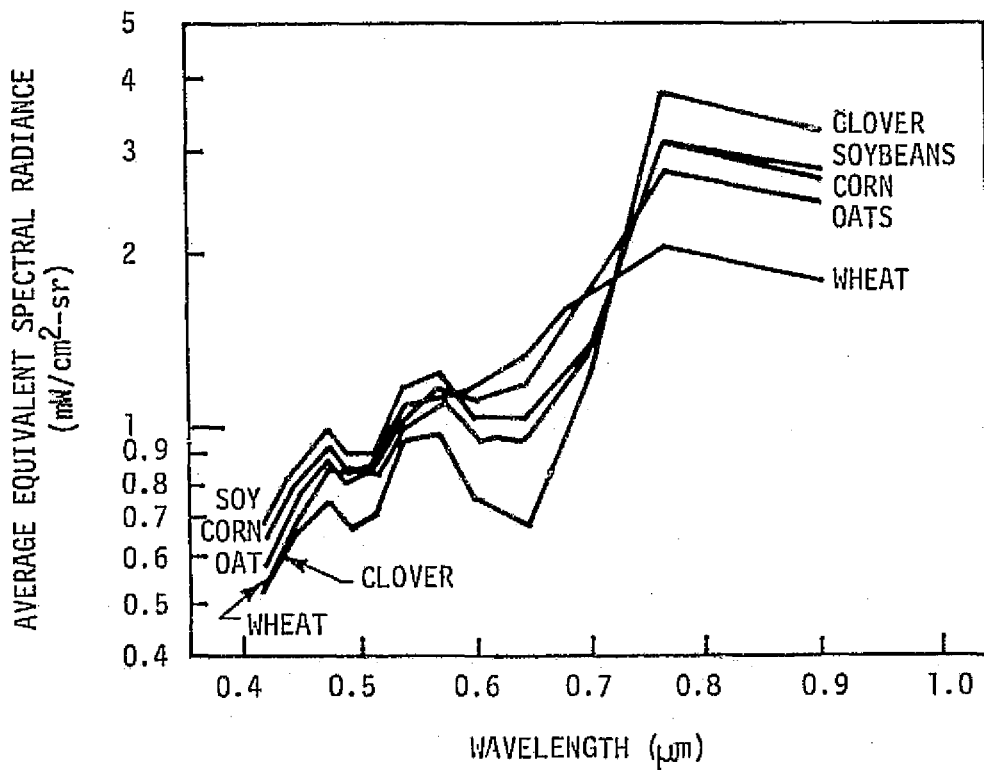


FIGURE A-2 COMBINED SIGNATURES FOR FIVE CROPS



TABLE A-1 CANDIDATE SPECTRAL BANDS FOR AGONOMY APPLICATIONS*

Recommended Wavelength Band (µm)		Priority	Value or Purpose	Comments
For Thematic Mapper (Ref. A-7)**	For SMSS (Tentative)			
0.45-0.52	0.45-0.52	Desirable, but not vital	Land-use mapping, soil/vegetation differences, deciduous/coniferous differentiation	Believe this band would be useful but probably cannot effectively document impact of its absence. (Possible research needed.) Would be willing to sacrifice this band in favor of 0.72-0.80 µm band if further research offers no conclusive evidence to the contrary, and if seven bands are not possible.
0.52-0.58	0.52-0.60	Necessary	Green reflectance, which is controlled by pigmentation (type and quantify)	Keep it centered in as narrow a band as possible around peak of green reflectance.
0.63-0.69	0.62-0.69	Absolutely necessary	Chlorophyll absorption band	Keep it centered in as narrow a band as possible, centered around maximum chlorophyll absorption band.
0.72-0.80	0.69-0.75	Highly desirable	Vegetation-stress detection	Highly desirable for vegetation-stress detection, but band should be as narrow as possible, right on the shoulder of the vegetation curve.
0.80-0.91 or 0.98-1.08	0.80-0.95	Absolutely necessary	High vegetative reflectance, species identification, water-body delineation	Bandwidth not critical, good S/N vital, desirable to stay away from water-absorption band at 0.925 µm. This band critical for effective species differentiation and identification. Approximately 0.98-1.08 µm is better from standpoint of vegetative condition and atmosphere attenuation, but approximately 0.80-0.91 µm may be required because of energy and instrumentation difficulties in 0.98-1.08 µm band.
1.55-1.75	1.55-1.75	Absolutely necessary	Snow/cloud differentiation, vegetative-moisture condition	Essential for snow/cloud differentiation (the only wavelength band where this can be done reliably on basis of spectral response). Best single channel for discrimination of vegetation, water, and soil features.
(-) (-) (-)	2.05-2.35 3.5 -5.0 8.2 -9.3	(-)	(-)	(Additional thermal bands in SMSS; no thematic-mapper counterparts.)
10.4-12.5	10.4-12.5	Necessary	Temperature variation and characteristics, vegetative density, cover-type identification, vegetative-stress conditions	Bandwidth not critical, but stay above O ₃ absorption band at 9.6 µm.

* Derived from Ref. A-7 except for column 2.

** See Table A-2 for comments on bandwidth. These recommendations are based on ~10% (rather than ~50%) filter-transmission cutoff points.

ORIGINAL PAGE IS
OF POOR QUALITY

A-5

Report 5231

TABLE A-2 THEMATIC-MAPPER WAVELENGTH-BANDWIDTH COMMENTS*

Comments Related to Increasing Bandwidth on Lower Side	Recommended Wavelength Band (μm)**	Comments Related to Increasing Bandwidth on Upper Side
Not critical, other than from atmospheric-attenuation and path-radiance standpoint.	0.45-0.52	Undesirable because of overlap (and therefore higher correlation) with 0.52-0.58 μm band.
Not recommended (too short of green reflectance peak).	0.52-0.58	Desirable to keep band as narrow as possible around green peak, but could be broadened in this direction if necessary, up to 0.59-0.60 μm .
Undesirable because band must be kept as narrow as possible around chlorophyll absorption band, but if it must be widened, increased width to 0.62 or possibly 0.61 μm would not be disastrous from a vegetative-reflectance standpoint.	0.63-0.69	Not recommended (sharp increases of vegetation reflectance occur above 0.69 μm).
Definitely not recommended (because of sharp decrease in reflectance short of 0.72 μm). 0.73 μm or maybe even 0.74 μm would possibly be better than 0.72 μm .	0.72-0.80	Undesirable, in order to keep band as narrow as possible around vegetation-reflectance shoulder, but could be increased if necessary from instrumentation standpoint.
Not recommended, because of overlap with 0.72-0.80 μm band	0.80-0.91 or	Not critical other than from standpoint of water-absorption band at 0.925 μm .
Not critical, other than from standpoint of absorption band centered at 0.925 μm .	0.90-1.08	Not critical.
Avoid water-absorption band.	1.55-1.75	Avoid water-absorption band.
Avoid ozone-absorption band.	10.4-12.5	Avoid carbon-dioxide-absorption band.
<p>* Derived from Ref. A-7.</p> <p>** It is suggested that these bandwidth recommendations be evaluated in terms of filter characteristics involved and the other system parameters, and that possible or necessary changes be reviewed in conjunction with a few life scientists who are knowledgeable about vegetative reflectance.</p>		





A-7

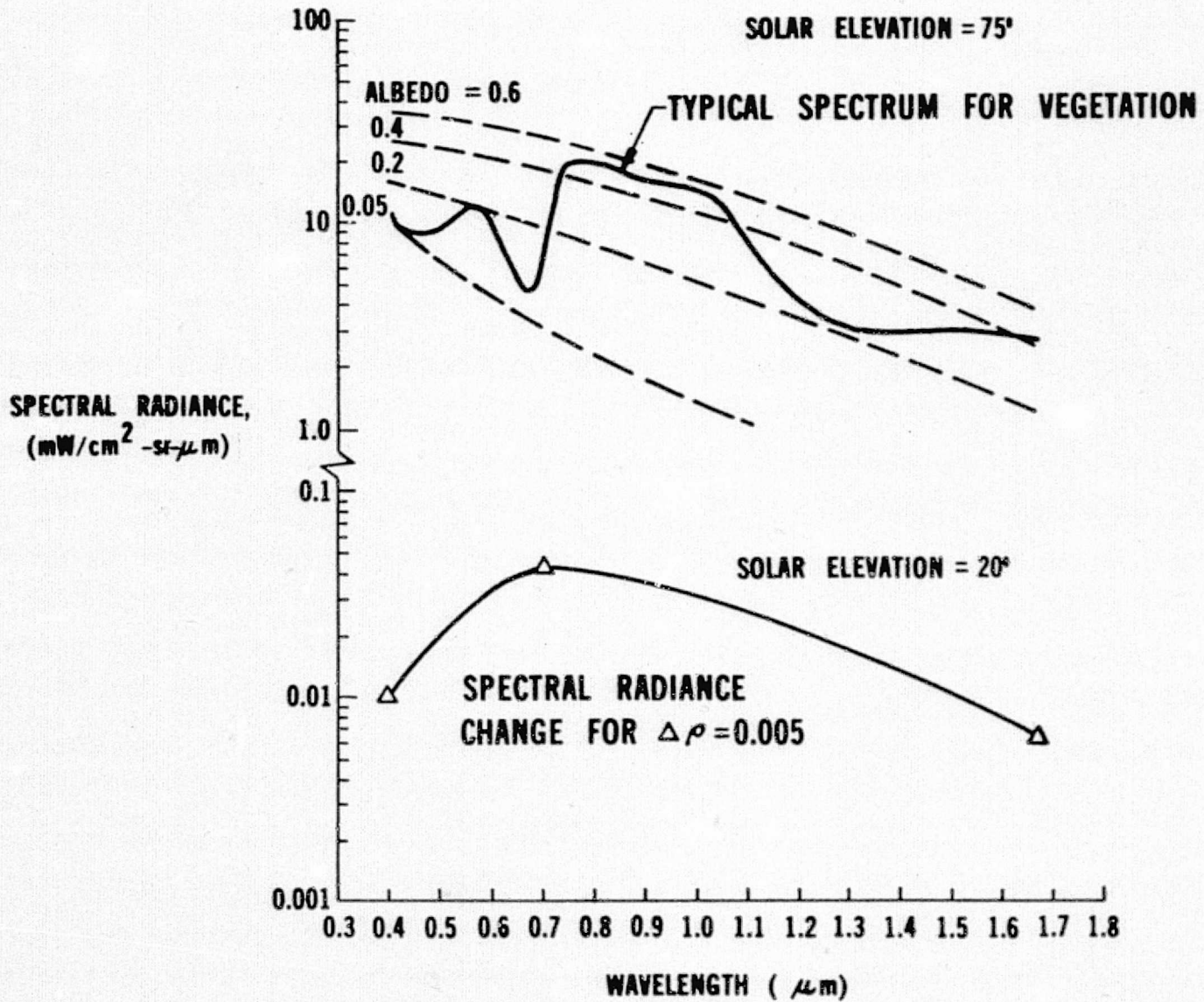


FIGURE A-3 RANGE OF VISIBLE-SCENE RADIANCE



A-8

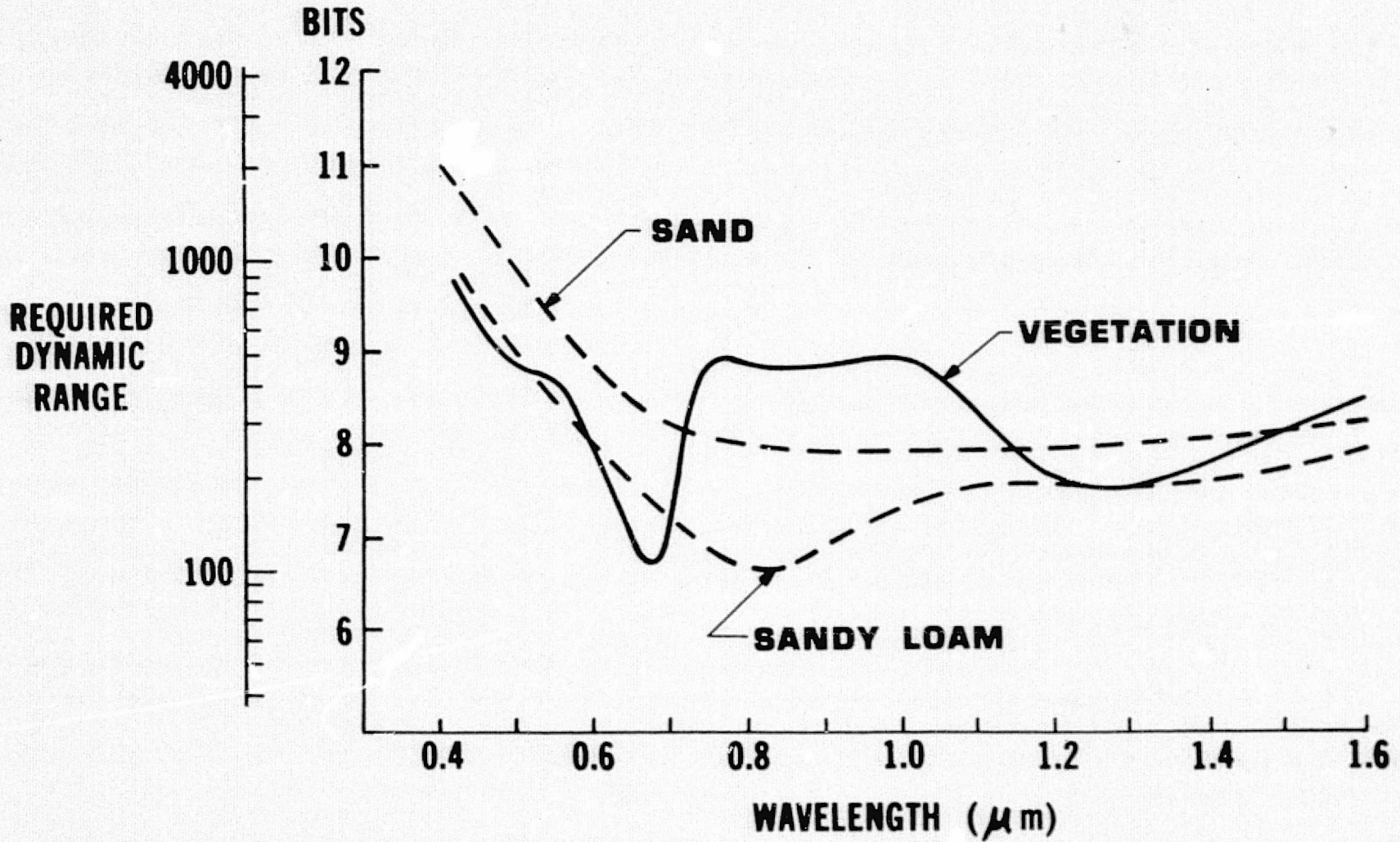


FIGURE A-4 REQUIRED VISIBLE-REGION DYNAMIC RANGE

Emissivity data on plant life of interest may yield long-wavelength signature variations comparable to those in the visible and IR spectra to permit plant species to be distinguished and their health to be determined.

The most-cost-effective SMSS sensor design should have an S/N error comparable to the sensor-calibration error against low-reflectance earth scenes that present a minimum radiance. As an example, for a 5% calibration accuracy (relative), an S/N much in excess of 20 will not significantly reduce the total measurement errors but will incur design requirements for a larger sensor aperture or a more sensitive detector element. Hence, for a facility that will provide useful data for field-crop-production and soil-management studies, a sensor with the following requirements is indicated:

Instantaneous field of view (IFOV)	Less than 20 x 20 meters
Sensitivity	S/N = 20 at 5% absolute calibration accuracy
Spectral bands (8 or more)	Given in Table 3-2

2 ATMOSPHERIC PHYSICS

As described in Ref. A-4, future EOS missions may use separate sensors for investigations of cloud physics and atmospheric-temperature profiles. A cloud-physics radiometer would employ five IR wavebands to estimate cloud pressure, altitude, thickness, water or ice content, water-droplet size, and condensed-water density. An upper-atmosphere sounder may use four LWIR bands to estimate atmospheric-temperature profiles.

A modular optical sensor designed for the Shuttle program could incorporate detector arrays to perform both types of experiments (i.e., cloud physics and LWIR upper-atmosphere sounding). Correlation of the measurement results could provide additional value. With a modular SMSS, the experiments could be conducted on selected flights with detector arrays designed for the specific experiment.



Measurements of cloud characteristics are essential for weather forecasting. An international cooperative effort is underway in the Global Atmospheric Research Program (GARP) to achieve increased understanding of the general circulation of the atmosphere and to develop the physical and mathematical basis for extended weather predictions. The World Weather Watch (WWW) is sponsored by the World Meteorological Organization (WMO) to expand the observing network, improve global telecommunications, and facilitate data collection through the establishment of world meteorological criteria. GARP is the research arm and WWW is the operational arm. As stated in Ref. A-4:

Detailed knowledge of the altitude distribution and composition of clouds is required for these programs because of the importance of clouds to radiative transfer and the thermodynamic and dynamic interaction of clouds and the environment. Calculations indicate an extreme sensitivity of the atmospheric state to the amount and distribution of clouds. Their determination thus represents one of the important links in a complete theory of the general circulation. Accurate global observations of cloud distributions will be important in developing comprehensive theories and again, later in checking the accuracy of numerical calculations. It is also possible to calculate albedo and the solar and thermal flux divergences of the atmosphere.

The Shuttle Orbiter is an ideal platform, and the SMSS an ideal instrument, for use in demonstrating the feasibility of a space-platform-based sensor to determine cloud characteristics, and for demonstrating the optimum sensor wavebands and measurement-accuracy requirements. The Shuttle/SMSS could satisfy the GARP research-measurement goals. After the design requirements are established from a space platform for a sensor to measure cloud characteristics, routine coverage on a daily basis can be more readily achieved from an unmanned weather satellite.

Measurements of atmospheric-temperature profiles and the composition of the upper air are needed for an understanding of atmospheric processes (e.g., dynamics and photochemistry). Quoting again from Ref. A-4:



For example, recent investigations of the ozone content of the atmosphere, inferred from Nimbus 3 spectra in the 9.6- μm ozone absorption band, indicate a high correlation between ozone in the upper air and tropospheric weather systems. The sensing of ozone profiles on a global scale and to higher altitudes will be of increased importance as similar studies progress. The measurement of airglow and scattering in the ultraviolet, visible, and near infrared can reveal information regarding the constituents of the high atmosphere and the atomic and molecular transitions resulting in the observed emissions. The spatial and temporal monitoring of water vapor in the upper atmosphere would be applicable to studies of transport mechanisms such as the possibility that large quantities of water vapor are injected into the stratosphere by cumulus towers, especially in the tropics. Similarly, the detection and monitoring of other trace constituents such as the oxides of nitrogen, sulfur dioxide, methane, and ammonia would be applicable to studies of transport mechanisms as well as having obvious implications with respect to environmental quality and atmospheric pollution...

Measurements of temperature profiles at low as well as high altitudes will contribute to an understanding of weather phenomena, cloud physics, and other characteristics of the atmosphere. Storm-front motions and cloud concentrations will be correlated with the spatial distributions of atmospheric-temperature profiles. Temperature inversions can produce smog concentrations in metropolitan areas. Simultaneous measurements of cloud patterns, cloud physics, atmospheric-temperature profiles, and atmosphere composition can contribute greatly to an understanding of atmospheric phenomena.

The SMSS can incorporate a number of the atmospheric-physics measurements. The large sensor aperture required for other experiments can achieve the high signal level required for precise measurements of cloud and atmosphere signatures. The Orbiter therefore offers a highly desirable platform for simultaneous measurements of atmospheric phenomena, and the experiments could be conducted on selected missions. With increased understanding of atmospheric phenomena, sensor configurations can be selected and design requirements can be established for sensor deployment on unmanned satellites to acquire data on a more routine, daily, scheduled basis.



Discussions in Ref. A-4 indicate that five spectral bands would be desirable for use in determining cloud altitude, thickness, and particle characteristics:

<u>Channel</u>	<u>Center Wavelength (μm)</u>	<u>Bandwidth (μm)</u>
1	0.754 ± 0.001	0.005
2	0.763 ± 0.0005	0.005
3	1.61 ± 0.002	0.072
4	2.06 ± 0.02	0.050
5	2.125 ± 0.02	0.032

These bands would make it possible to infer the cloud-top pressure level, the density and phase of condensed water in the cloud, a drop-size parameter, and the cloud thickness, both optical and geometrical. One is the oxygen "A" band at $0.763 \mu\text{m}$, and another is the carbon dioxide band at $2.06 \mu\text{m}$. Two others just outside them are used for reference to determine the atmospheric attenuation of the absorption-band signals and indicate cloud-top height and thickness. The fifth channel at $1.61 \mu\text{m}$ gives an indication of cloud-particle size, because cloud scattering is a strong function of the particle size at $1.6 \mu\text{m}$ and $2.1 \mu\text{m}$.

Although such narrow spectral bands are not presently planned for the SMSS, the high sensitivity and the modular character of the SMSS focal plane would permit economical modification. The data obtained could be used to assess the feasibility of including an atmospheric-sounding experiment on a satellite-borne sensor.

Wavelengths for upper-atmosphere-composition and temperature-profile sensors were selected in Ref. A-4 to correspond to the wavebands of the Nimbus-F limb radiance inversion radiometer (LRIR). This sensor scans the atmospheric limb in four spectral intervals to make the following vertical-profile measurements:

Temperature, $\pm 6^{\circ}\text{K}$, 2 km vertical resolution, 15 to 70 km
 Water vapor, ± 2 ppm, 5 km vertical resolution, 15 to 42 km
 Ozone, ± 0.001 cm NTP/km, 2 km vertical resolution, 15 to 50 km.

The spectral bands useful for these measurements are as follows:

<u>Spectral Band (μm)</u>	<u>Purpose of Measurement</u>
9.4-10	Ozone concentration
20-40	Water-vapor concentration
14.0-16.3 and 14.5-16.7	Temperature profile

Additional bands could be selected to determine the concentration and altitude distribution of other atmospheric trace constituents.

The weather is in a constant state of flux, and the daily or even hourly atmospheric measurements required for forecasting or updating should be performed from an unmanned satellite. The atmospheric-physics sensors should be considered as research tools. The spatial resolution for downward-looking sensors as characterized by the cloud-physics radiometer should approximate the lateral dimensions of clouds:

<u>Cloud Type</u>	<u>Median Lateral Dimensions</u>	
	<u>nmi</u>	<u>km</u>
Cumulus	0.5 x 0.5	0.9 x 0.9
Stratocumulus	1.0 x 0.8	1.9 x 1.5
Stratus	5.0 x 0.5	9.0 x 0.9
Cumulonimbus	3.0 x 3.0	5.5 x 5.5
Altostratus	1.0 x 1.0	1.9 x 1.9
Alto cumulus	2.0 x 1.5	3.7 x 2.8
Cirrus	0.5 x 0.1	1.0 x 0.2
Cirrostratus	1.0 x 0.1	1.9 x 0.2
Nimbostratus	5.0 x 1.0	9.0 x 1.9

These dimensions indicate that an IFOV of 0.1 km (~ 0.05 nmi) could accurately determine cloud characteristics. This value is well within the planned SMSS capability. If a cloud subtends only a portion of the IFOV, it may be difficult to detect and distinguish its characteristics from background radiation. Many clouds that were observed by ground sensors have not been detected by spacecraft. Less-severe resolution requirements are imposed on atmosphere-composition and temperature-profile measurements because less-severe lateral gradients will occur. An IFOV of several kilometers (~ 3 km or 1.5 nmi) should suffice.

A preliminary set of sensor design requirements was derived on the basis of the foregoing considerations and of analyses reported in Ref. A-4. The spectral bands are discussed above, and other parameters are as follows:

<u>Sensor</u>	<u>No. of Wavebands</u>	<u>IFOV (mr)</u>	<u>Calibration Accuracy</u>
Cloud physics	5	2	2% absolute, 0.1% relative
Optical sounder	~ 6 (TBD)	6	Temp $\pm 1^\circ\text{K}$, water vapor ± 0.5 ppm, ozone ± 0.0007 cm NTP/km

3 ATMOSPHERIC POLLUTION

The effectiveness of using a spacecraft to obtain an understanding of the depositions, reactions, and global effects of atmospheric pollutants has not yet been demonstrated. As discussed below, the SMSS is a highly suitable instrument for determining the measurement requirements of an atmospheric-pollution sensor. If frequent spaceborne measurements become necessary, the requirements can be incorporated in a dedicated sensor deployed on an unmanned satellite.

The experiments would be conducted to determine the causes and conditions of critical smog concentrations, and the interaction of pollutants with the atmosphere. They are most effectively performed in conjunction with



atmospheric-physics experiments (see paragraph 2, above). High smog concentrations are frequently associated with temperature-inversion layers that trap polluting gases in urban basins when normal circulation effects would dissipate them.

The measurements should be undertaken to determine the spatial and the vertical (if possible) distributions of CO, CO₂, and selected trace gases in relation to atmospheric temperature and water-content profiles. The information would provide data needed to determine atmospheric interactions of pollutants, the locations of sinks, and other phenomena that reduce the global concentrations of polluting gases.

Measurements could be made on different Orbiter passes at different times of the day to evaluate the sun's photochemical effect on pollutants. After the feasibility of useful measurements has been demonstrated, the requirements derived for routine, daily measurements may be incorporated in a sensor deployed on an unmanned satellite. If infrequent measurements are called for, the Shuttle system may be more cost effectively used for them.

The spectral bands that are used should be in the absorption regions of the pollutants to be detected. They may range from 0.3 μm for ozone to 20 μm for the trace elements. A region from 2 to 20 μm is suggested for the remote gas filter correlation analyzer investigated by General Dynamics Convair Division and described in Ref. A-4. Other suggested sensors can have narrow-bandpass filters in the absorption bands of the selected constituents.

Because the atmospheric interactions of such pollutants as CO are not well understood, global coverage is desirable to locate possible sinks where they can form harmless components of the atmosphere. Global coverage is also desirable to determine regions where CO₂ or particulate matter can cause heating or cooling of the earth's surface.

Insufficient information is available to define the required spatial resolution. For downward viewing, the resolution may amount to several degrees in order to determine the horizontal distribution of pollutants. For the derivation of vertical distributions by scanning the earth limb from an altitude of 470 km (250 nmi), a viewing range of approximately 2400 km (1300 nmi) and a sensor resolution of 1 m result in a vertical resolution of 2.4 km (1.3 nmi). Global coverage may also be achieved by viewing the earth limb from different directions relative to the satellite flight path.

4 HYDROLOGY

Hydrology is taken here to include the surface and near-surface properties of oceans, seas, lakes, and rivers. Previous space measurements have been confined to larger bodies of water, but the spatial resolution achievable with the SMSS will permit studies of rivers and local coastal conditions.

Two ocean- and lake-surface experiments are defined in Ref. A-4: one to survey the surface temperature and the other to determine the spectral signature of water. A sea-surface-temperature imaging radiometer uses five wavebands to derive thermal emission and temperature from the total irradiance. The total irradiance includes cloud and atmospheric self-radiation and reflected solar radiations, and the total signal is attenuated by the atmosphere. An ocean-scanning spectrophotometer uses about 20 spectral bands over the 0.4 to 0.7- μ m region to measure the near-surface (\sim 10 to 100 m in depth) spectral signature. Reflected solar radiations from beneath the surface can reveal the presence of chlorophyll, which is indicative of plant life and sediment. Each sensor has an IFOV of approximately 2 x 2 km (\sim 1 mile square). Their coverage is therefore restricted to large bodies of water, and the resolution is inadequate to detect variations near coastlines.

It would be highly desirable for an Orbiter-based sensor to obtain thermal and spectral signatures with a spatial resolution adequate to measure the water-surface and near-surface properties of rivers and coastal

regions. Only a large-aperture sensor such as the SMSS can provide both high spatial and high spectral resolution.

There will be a large degree of correlation between water-surface temperature and plant life. A spatial resolution of about 10 to 20 m would also permit monitoring of the characteristics of rivers and coastal regions where man-made thermal disturbances, sewage, and other factors disturb the environment. The discharge of eroded soil at deltas where rivers enter the sea could also be observed by changes in water color.

With 10 to 20-m spatial resolution, the mission objectives of the SMSS could be broadened well beyond those of satellite-based sensors described in Ref. A-4. The SMSS could monitor the thermal pollution caused by nuclear powerplants and then determine the effects of the thermal environment on plant life in the water. The chemical pollution of rivers by industrial facilities could be detected and the downstream persistence of pollutants could be determined. Many other measurements, including those of ocean properties favorable to fish life, could be postulated to assist in the most efficient use of the ocean and inland-water environment.

The interchangeable focal plane planned for the SMSS makes it suited for the measurements discussed above. The data could be obtained on selected flights to determine sensor effectiveness with regard to ocean, river, and other water-surface characteristics. A limited number of missions could also provide sufficient data for analysis to determine the required sensor performance and the desired measurement frequency. If such measurements are deemed sufficiently valuable to be made frequently, the required sensor could be incorporated in the EOS or another unmanned satellite. If they are required less frequently, they may be made more cost effectively on Orbiter missions.

A theoretical study by Anding, et al. in Ref. A-5 and reported in Ref. A-4 indicated that five spectral bands are required for accurate measurements of sea-surface temperature from space:



<u>Spectral Band (μm)</u>	<u>Parameter</u>	<u>Measurement</u>
10.5-11.5	IR window	Thermal emission from surface
8.85-9.35	Water-vapor continuum	Water-vapor correction
6.5-7.0	Water-vapor absorption	Thin cirrus tag and correction
3.6-4.1	IR window	Cloud tag (night) and correction
0.2-4.0	Solar radiation	Cloud tag (day) and correction

A sensor resolution of approximately 10 to 20 m will be required to measure river pollution and to accurately resolve human perturbations of ocean water near coastlines. This resolution over extended ocean areas may result in excessive data-storage requirements. For ocean areas, the detector outputs could be smoothed over multiple resolution elements prior to storage, or the outputs of only selected detectors could be retained, for ground processing.

5 GEOLOGY

In the visible wavelengths the SMSS will be able to chart geological features that are of interest to scientists and also may indicate the presence of oil or mineral formations. Compositional mapping is truly a multispectral-scanner application because minerals, rocks, and soils exhibit characteristic reflectance and emittance features throughout the 0.45 to 12.5- μm range. A Space-Shuttle-borne large-aperture scanner with many thermal channels has been described (Ref. A-8) as the ultimate means of providing geologists with unique information that cannot be detected by cameras or the human eye.

The SMSS can survey large, extended areas in remote regions that are not readily explored by ground- or aircraft-based sensors. Geological faults may be detected by changes in types of vegetation on the two sides of the fault, local depressions producing ponds along the fault, the disruption of river paths by the fault, and possible differences in exposed rock types at the fault through measurement of color variations.

High-resolution measurements may be able to determine earth contours from shadowed regions and the varying surface-reflected solar energy for different sun angles relative to the earth and sensor at different times of day. Large-scale anticlines (increases in local surface height due to folding or arches in stratified rock and substrata) may indicate oil deposits trapped in sandstone between rock layers. Anticlines in Saudi Arabia containing large oil deposits were about 90 km (~50 nmi) across and would be difficult to detect from near ground level. Evaporative basins can contain soluble minerals and may be detected by the absence of, or the type of, vegetation. River-bed surveys and accurate determinations of current and previous paths may aid in defining boundaries between private properties, local governments, states, or nations.

Geological formations are best derived from multispectral, high-spatial-resolution measurements at different times of day, but are required infrequently because changes occur over many years. The requirements are best satisfied by a multipurpose sensor in the Space Shuttle System. The desired high-resolution, multispectral-detector, focal plane could be used on three Orbiter passes at three different times of day (e.g., 0900, 1200, and 1500 hours). The multipurpose SMSS would be far more cost-effective for these measurements than an unmanned satellite.

The 0.45 to 2.5- μm region contains useful reflectance data. The 8.2 to 12.5- μm region contains even more compositional information, especially for silicate rocks, in the form of emittance minima. There is a requirement for spectral resolution of at least 0.5 μm to map these minima. Some data can be obtained from a single broadband thermal channel (e.g., 10.4 to 12.5 μm) recorded at different times of day and depending on thermal inertia. Such mapping, however, exhibits less systematic variation with rock type than do emittance minima (Ref. A-8).

Appendix B

BACKGROUND AND CONSIDERATIONS FOR OPTICAL-DESIGN SELECTION

1 FOCAL RATIO

A relationship similar to the diffraction-limit expression footnote in paragraph 5.1 of the main text exists for the linear image size (B), or the detector size related to the system resolution: $B = \beta f = 2.44 \lambda (f/\text{no.})$, where f is the effective focal length and $f/\text{no.} = f/D$. Figure B-1 shows that an image size of $\sim 60 \mu\text{m}$ (0.0025 in.) for a diffraction-limited system at $10 \mu\text{m}$ requires about $f/2.5$.

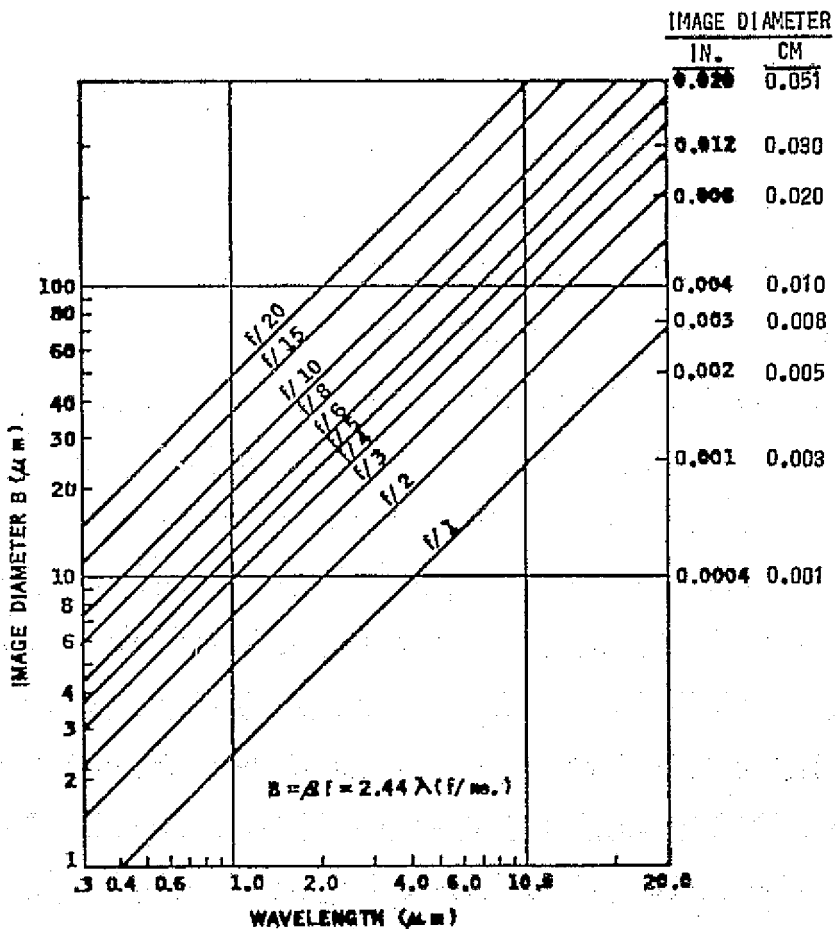
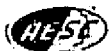


FIGURE B-1 LINEAR DIAMETER OF DIFFRACTION IMAGE OF A CIRCULAR UNOBSTRUCTED OPTICAL SYSTEM AS A FUNCTION OF FOCAL RATIO AND WAVELENGTH



The focal ratio is an important trade parameter that cannot be established simply from image considerations, because it also determines the sensitivity of the sensor system. A low-f/no. (or "fast") system is desirable (under certain conditions) for sensitivity, but high image quality is progressively more difficult with decreasing f/no. For diffraction-limited operation at $10\ \mu\text{m}$, an f/2.5 system is near the limit of attainment.

Figures B-2 and B-3 relate the mirror diameter, focal ratio, and relative fabrication time. They were useful in consideration of relative fabrication difficulties and limits. The curves were empirically obtained by a major large-optics fabricator and were adapted from Ref. B-1.

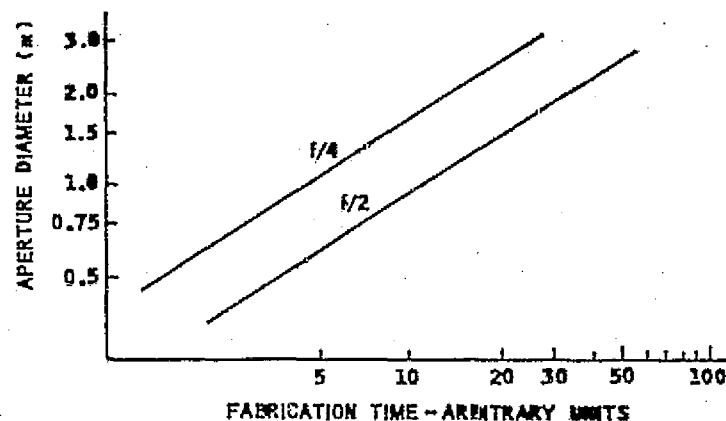


FIGURE B-2 APERTURE VS FABRICATION TIME FOR $\lambda/40$ RMS SURFACE

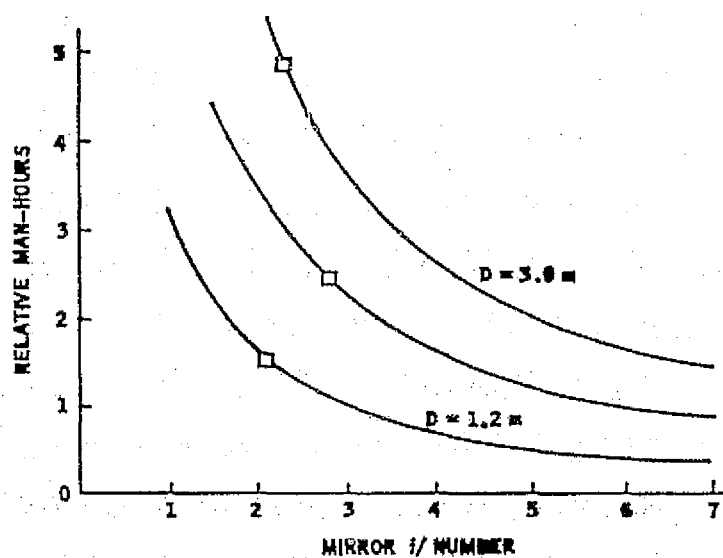


FIGURE B-3 MIRROR FABRICATION VS SIZE AND FOCAL RATIO



2 OPTICAL MATERIALS, PRELIMINARY CONSIDERATIONS

2.1 REFRACTIVE MATERIALS

The large wavelength region of interest and the large aperture diameter indicated that at least the main telescope should be reflective.

No refractive materials (a) transmit adequately from 0.3 to 14 μm , (b) have physical properties acceptable for field use, and (c) are obtainable in sizes large enough for full-aperture elements. Figure B-4 plots transmission vs wavelength for several representative materials that have suitable physical properties (such as hardness, solubility, and melting point).

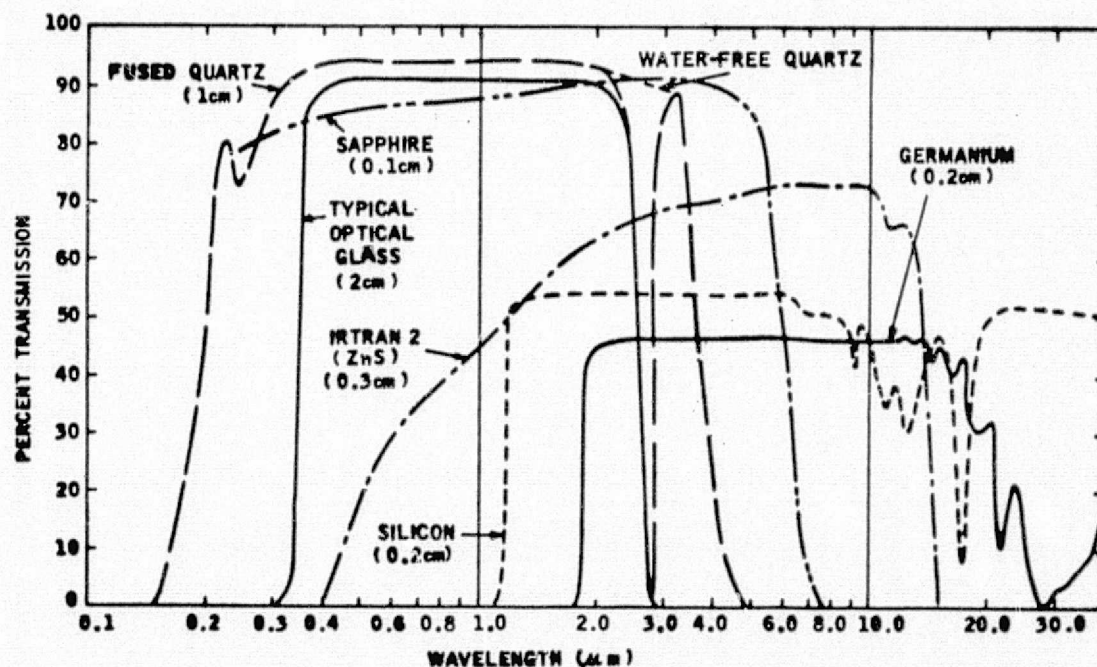


FIGURE B-4 REPRESENTATIVE TRANSMISSION (INCLUDING REFLECTION LOSSES)

Transmission curves for several other materials that cover the entire wavelength region are given in Figure B-5. However, these materials (most being of the alkaline-halide-salt family) are soft, highly soluble, and of small size. Consequently, the popular high-performance optical systems, such as Schmidt and Bouwers configurations that require full-aperture refractive correctors, cannot be used in their simple forms for the SMSS.

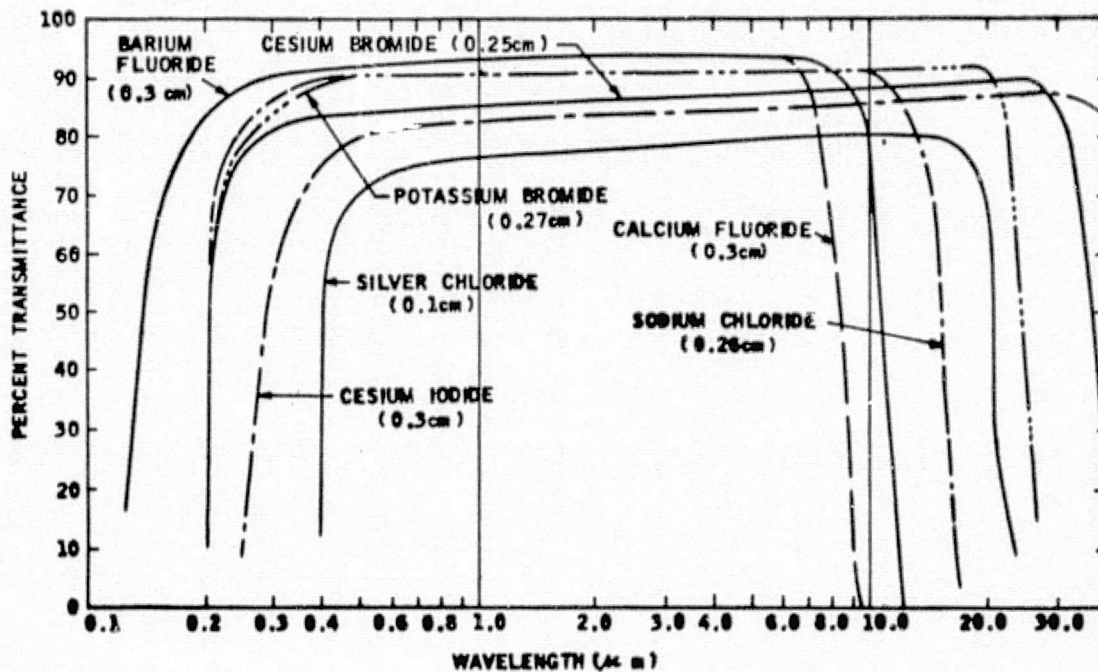


FIGURE B-5 REPRESENTATIVE TRANSMISSION (INCLUDING SURFACE REFLECTION)

The foregoing considerations did not positively rule out the possibility of refractive elements somewhere in the system. The use of several small-aperture systems following a large-aperture telescope, for the different wavelength bands within the total region, was possible, and this concept has been employed in previous applications. For the SMSS, however, a catadioptric-type system was considered unnecessarily complicated in comparison with an all-reflective Schmidt.

2.2 MIRROR-SUBSTRATE MATERIALS AND COATINGS

Five physical properties are most important for large reflective systems subjected to wide temperature variations: density, modulus of elasticity, thermal conductivity, specific heat, and coefficient of expansion. The first two influence the structural design, with the ratio of density to modulus of elasticity being the important relationship.

Significant advances in mirror-material design and fabrication have occurred recently because of the great interest in large, spaceborne,

optical systems. Two basic design approaches have been developed. One allows only small variations with temperature changes by using low-expansion materials (such as CER-VIT and ULE). However, these materials have low thermal conductivity and require long "soak" periods to attain stabilized temperatures.

The other approach is the use of metals to permit rapid attainment or restoration of the desired operating temperature and mirror shape. Several optical fabricators have had good success with this approach. Beryllium has recently been chosen for several systems, especially because methods have been developed to overcome the inhomogeneity and surface scatter evident in its earlier application. With proper design and fabrication of the mirrors and the entire optical structure from beryllium, there are no focus shifts as the telescope temperature changes.

Material considerations for the SMSS are discussed in more detail in Section 8, below.

The reflectivities of several typical mirror coatings as a function of wavelength are given in Figure B-6. Silver and aluminum would both be acceptable for the region from 0.35 to 14 μm , but the durability of aluminum would be superior and Al is therefore recommended as the SMSS coating material.

3 SCANNING SYSTEMS

The impacts of various types of potentially applicable scanning approaches on selection of the SMSS optical system are briefly discussed below. As discussed in Section 4.3 of the main text, the pushbroom type is recommended.

3.1 VEHICLE-MOTION SCAN

The pushbroom system (see Figure 4-3 of the main text) is attractive because scanning is provided by orbiting-vehicle motion and requires no moving parts. The optics, however, must have a field of view (perpendicular



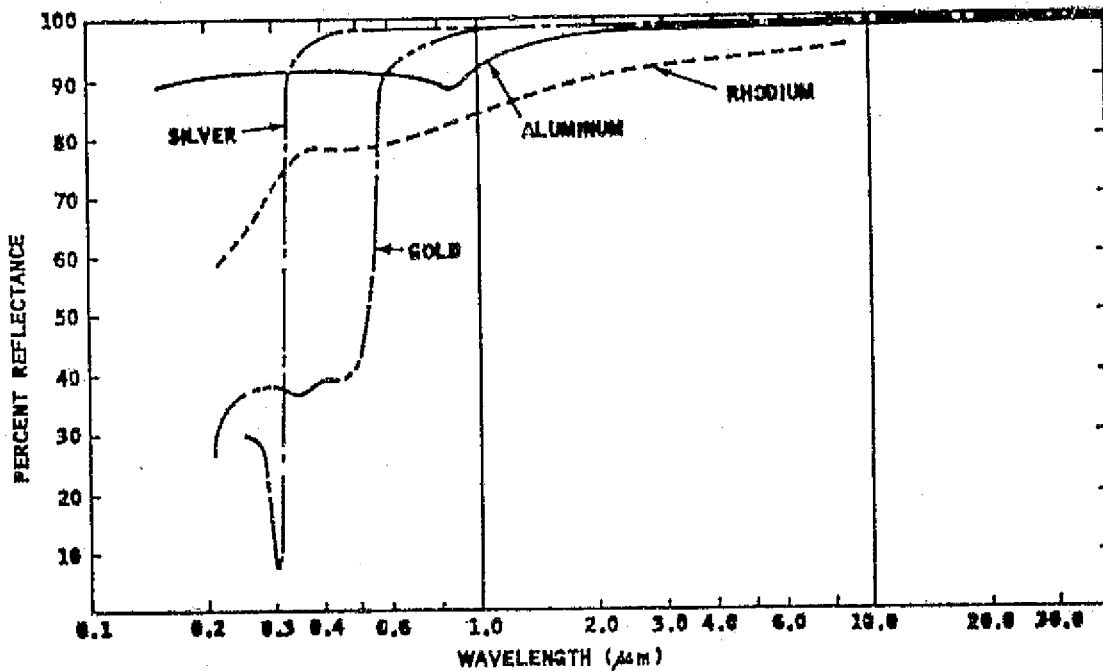


FIGURE B-6 REPRESENTATIVE REFLECTANCE OF SELECTED MIRROR COATINGS

to the satellite motion) equal to the swath width. For the SMSS application, a swath width of 15° is desired, which is difficult to obtain with an all-reflective system. Consequently, the optical system for this method must be one of the more sophisticated designs, such as an all-reflective Schmidt configuration or a confocal paraboloid.

3.2 OBJECT-PLANE SCAN

Object-plane scanning has the attractive property that the telescope field of view (FOV) is the small instantaneous field and not the total scanned field. For the SMSS, therefore, a telescope with excellent image quality over only 1° or less would be needed. This would permit selection from more candidate systems than would be possible with the pushbroom approach.

There are certain disadvantages, however. An example, an oscillating-mirror object-plane scanner must be larger than the desired system aperture and yet maintain a precise optical surface during the rapid start-and-stop operation necessitated by the rapid scan rate. Improvements

in mirror materials, structural design, drive mechanisms, optical-fabrication techniques, and other areas have overcome these obstacles to some extent on several large-aperture systems during the past several years but, for a system as large as the SMSS, the very large oscillating or rotating mirror system would introduce momentum-compensation and reaction problems as well as increased weight and power consumption.

3.3 IMAGE-PLANE SCAN

Image-plane scanning exhibits generally opposite properties to those of object-plane scanning. The scanners are usually small, being in the converging beam or small-diameter afocal region, but the optics must perform over the entire scanned field, just as with pushbroom systems.

Image-plane scanners can take either an oscillating or a rotating configuration. An oscillating flat mirror, with its simplicity and size, offers a very attractive approach, especially when the mirror movement is small (i.e., for small scan fields).

The advantages of a rotary scanner become evident as the desired scan field increases (e.g., beyond about 15°). For example, the advantages of a rotating drum, with its small-aperture relay optics, begin to overcome its undesirable properties, such as size.

4 BASIC SURVEY OF OPTICAL SYSTEMS

Figures B-7 through B-9 illustrate several types of optical system that were considered for the SMSS. Their characteristics and merits are discussed below.

4.1 SINGLE-MIRROR-SYSTEM CHARACTERISTICS

A spherical mirror (Figure B-7A) is especially interesting when the aperture is located at the center of curvature: The aberrations of coma and astigmatism are zero, the image is located on a curved focal surface centered about the mirror's center of curvature, and the image quality is

Type	Schematic	Size	Additional Comments
<p>A</p> <p>Single Mirror System</p> <p>Sphere or Paraboloid</p>		<p>Sphere:</p> <p>Long:</p> $L = 2f$ For $D = 1\lambda$, $f/5.4 \rightarrow 50 \mu m$ <p>Paraboloid:</p> $L = f$ $\theta < 1^\circ$	<p>Sphere: Axial image size limited by spherical aberration; coma and astigmatism are zero when stop is at center of curvature; backward curving image plane. Large mirrors.</p> <p>Paraboloid: Spherical aberration = 0. With stop at focus, astigmatism = 0 and image size limited by coma. Small field-of-view. Backward curving field.</p>
<p>B</p> <p>Two-Mirror System</p> <p>Cassegrain Dall-Kirkham Ritchey-Chretien</p>	<p>Primary: Concave Secondary: Convex</p>	<p>Short:</p> $L/D \leq 1$ $d/D \approx 1$ $L \ll f$	<p>Cassegrain: Primary-Paraboloid; Secondary-Hyperboloid. Coma same as paraboloid of same f/l; astigmatism greater than paraboloid.</p> <p>Dall-Kirkham: Primary-Ellipsoid; Secondary-Sphere.</p> <p>Easier to fabricate the Cassegrain, but image larger.</p> <p>Ritchey-Chretien: Both mirrors aspheric. Excellent image quality possible over a moderate field.</p>
<p>C</p> <p>Gregorian</p>	<p>Primary: Concave Secondary: Concave</p>	<p>Moderate:</p> $L/D \approx 2$ $d/D \approx 1$ $L < f$ $\theta < 1^\circ$	<p>Gregorian: Primary-Paraboloid; Secondary-Ellipsoid. Performance same as Cassegrain. Field stop at intermediate image provides good off-axis rejection.</p>

FIGURE B-7 BASIC MIRROR SYSTEMS -- I

Type	Schematic	Size	Additional Comments
<p>A</p> <p>Schwarzschild</p>	<p>Primary: Concave Secondary: Concave</p>	<p>Moderate:</p> $L/D \approx 1.5$ $d/D \approx 1$ $L < f$ $1^\circ < \theta < 5^\circ$	<p>Schwarzschild: Both mirrors aspheric. Excellent image quality over moderate field. Image plane between mirrors.</p>
<p>B</p> <p>Catadioptric</p> <p>Bouwers or Maksutov</p>	<p>Stop for Bouwers Stop for Maksutov Primary: Sphere</p>	<p>Bouwers:</p> <p>Long:</p> $L = 2f$ $d \approx \theta$ <p>Heavy:</p> <p>Thick Meniscus</p> <p>Maksutov:</p> $L \approx f$ $d \approx \theta$	<p>Bouwers: All surfaces concentric about C. Excellent image quality over large fields. Alignment easy. Large, heavy corrector and very large mirror. Backward curving image plane.</p> <p>Maksutov: All surfaces not concentric. For better color correction than Bouwers. Full aperture corrector, but corrector and mirror smaller than Bouwers.</p>
<p>C</p> <p>Schmidt</p>	<p>Stop for Schmidt</p>	<p>Long:</p> $L = 2f$ $d = \theta$ <p>Moderate Weight;</p> <p>Plate Thin</p> $10^\circ < \theta < 25^\circ$	<p>Schmidt: Aspheric plate at center of curvature provides excellent image performance over large field-of-view. Very large mirror for large FOV. Backward curving image plane.</p>

FIGURE B-8 BASIC MIRROR SYSTEMS -- II



ORIGINAL PAGE IS OF POOR QUALITY

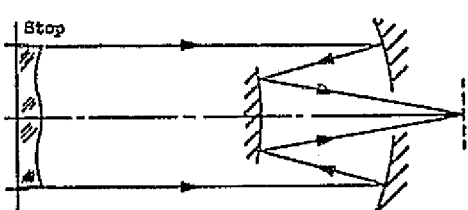
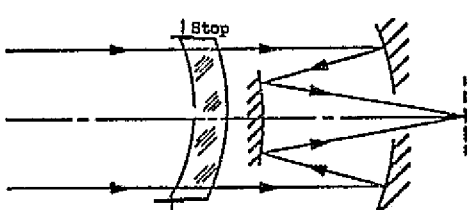
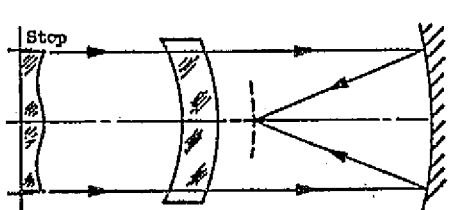
Type	Schematic	Size	Additional Comments
A Schmidt-Cassegrain		$f < L < 2f$ Moderate Weight $1^\circ < \theta < 10^\circ$	<u>Schmidt-Cassegrain</u> : Image quality and field-of-view better than Cassegrain, but less than Schmidt. Focal surface flat or inward curving and accessible.
B Makautov-Cassegrain		$L < f$ Heavy $1^\circ < \theta < 10^\circ$	<u>Makautov-Cassegrain</u> : Performance similar to Schmidt-Cassegrain above, but system heavier due to large meniscus.
C Schmidt-Bowers		$L \approx 2f$ Heavy $\theta > 10^\circ$	<u>Schmidt-Bowers</u> : Also called "Corrected Concentric". Extremely high performance over large field.

FIGURE B-9 BASIC MIRROR SYSTEMS -- III

limited only by spherical aberration. The change of image quality with focal ratio for this stop position is shown in Figure B-10. To obtain a 50- μ r image, a focal ratio of about $f/5.4$ is required. With an aperture 1 m in diameter, and thus a 5.4-m focal length, the stop must be 10.8 m (35.6 ft) from the mirror for the zero coma and astigmatism condition. The mirror size is determined by the field of view.

The paraboloidal mirror has an attractive feature in that there is no spherical aberration. It does have coma and astigmatism, given by $\beta_c = \theta/16(f/\text{no.})^2$ and $\beta_a = \theta^2/2(f/\text{no.})$, respectively, when the stop is at the mirror, where θ is the semifield angle. These values, which also are valid for a spherical mirror with the stop at the mirror, are plotted in Figure B-11 for several focal ratios. The astigmatism is a function of the stop position and is zero with the stop located at the focal plane. This case, in which only coma (and field curvature) remains, is shown in Figure B-12.



B-10

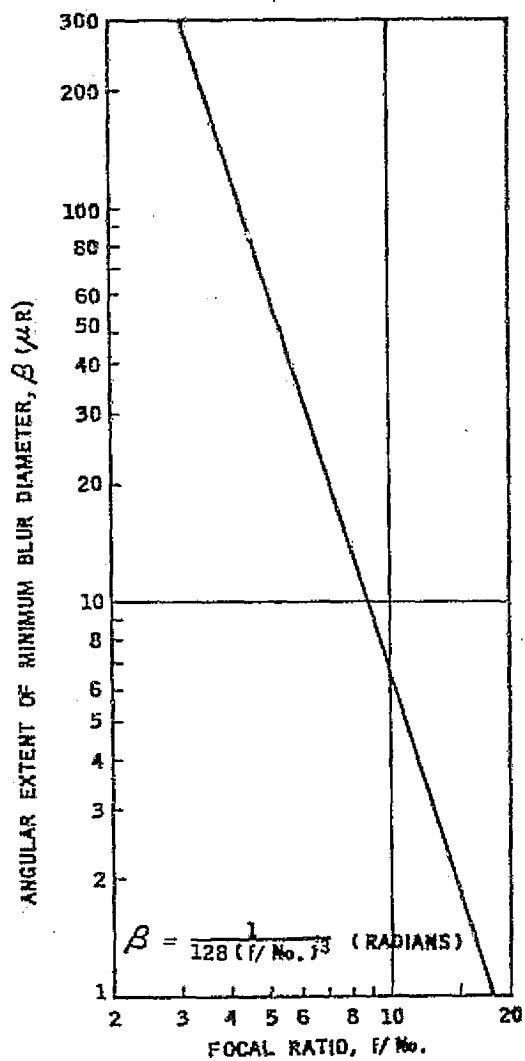


FIGURE B-10 ANGULAR-BLUR DIAMETER FOR SPHERICAL MIRROR

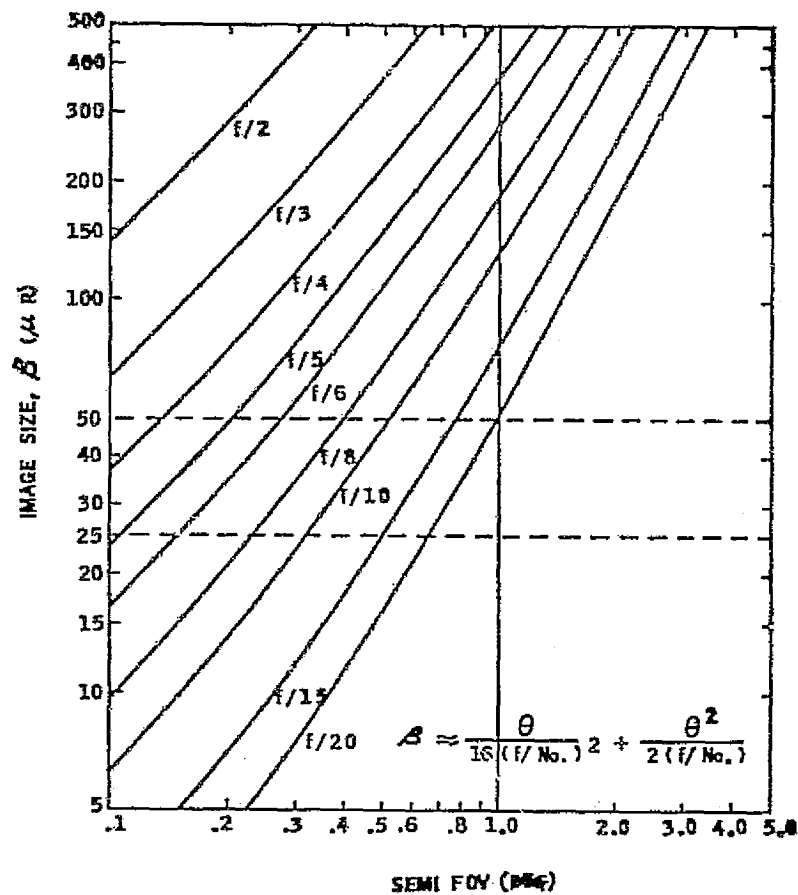


FIGURE B-11 PARABOLOID: STOP AT MIRROR

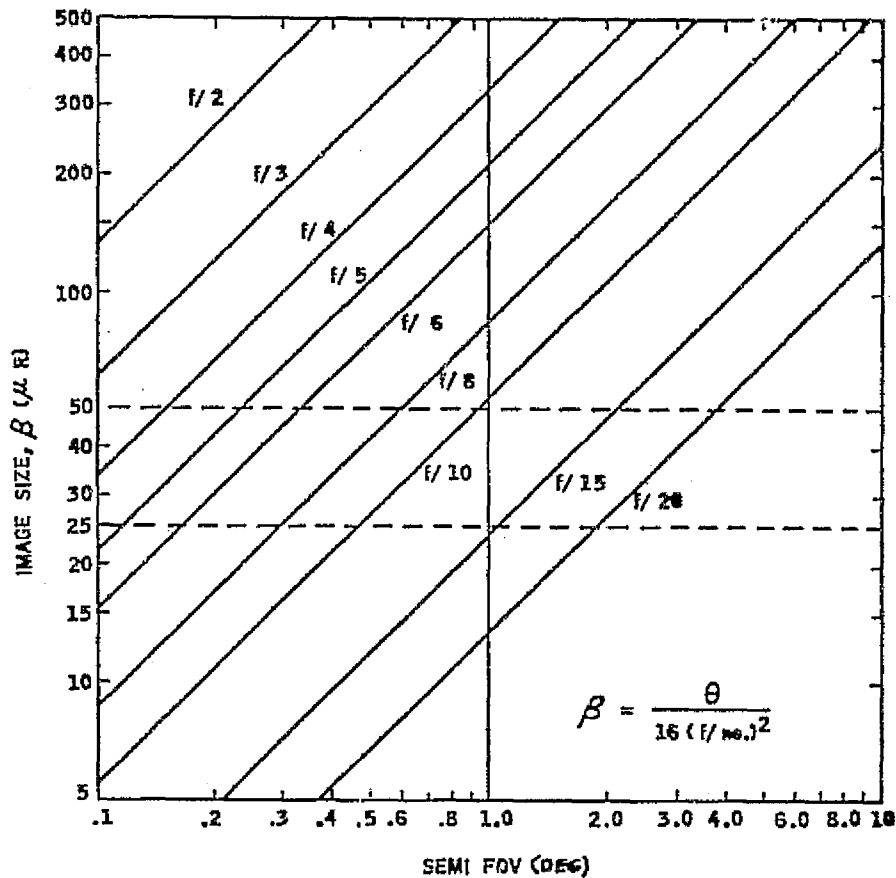


FIGURE B-12 PARABOLOID: STOP AT FOCAL PLANE

These curves indicate that the use of a paraboloid is limited to small fields of view and high focal ratios to obtain an image size of 25 to 50 μ r.

4.2 TWO-MIRROR-SYSTEM CHARACTERISTICS

Many forms of two-mirror systems have been devised. Three general configurations are shown in Figures B-7B, B-7C, and B-8A. Each form was derived to provide certain advantages, but each also has limitations. The classical Cassegrainian (concave paraboloid and convex hyperboloid, Figure B-7B) and the Gregorian (concave paraboloid and concave ellipsoid, Figure B-7C) have performance characteristics similar to those of a paraboloid (Figure B-7A) of equivalent focal length and aperture with the stop at

the mirror. Thus, Figure B-11 can also be used to determine the approximate performance and field limitations for these two-mirror forms.

A two-mirror system that is free of both spherical aberration and coma can be obtained in two forms by allowing the mirror surface to depart from conical shape. The concave-convex form (Figure B-7B) is termed a Ritchey-Chrétien configuration and the concave-concave (Figure B-8A) the Schwarzschild, after their developers. Although performance is greatly improved, the field coverage is still rather limited, due both to image quality and secondary-mirror obscuration.

4.3 CATADIOPTRIC-SYSTEM CHARACTERISTICS

The performance of a single- or two-mirror system can be greatly improved by the use of a full-aperture refractive corrector. In a catadioptric system, which combines refractive and reflective elements, the refractive corrector can take the form of a thick meniscus lens, as in the Bouwers or Maksutov (Figure B-8B), or an aspheric plate such as the Schmidt in Figure B-8C. Figures B-9A and B-9B illustrate the use of the correctors with a two-mirror system. The Schmidt-Bouwers [or "corrected concentric" (Figure B-9C)] form provides excellent performance.

As noted in Section 2, above, however, the SMSS application does not permit the use of full-aperture refractive correctors.

Small lens or aspheric-plate correctors in the converging beam near the image plane are helpful in extending the field coverage and performance of mirror systems, although not to the extent of the large correctors. Another alternative is the use of several small objective systems for different spectral regions following a large collecting system.

5 OPTICAL SYSTEMS CONSIDERED FOR SMSS TELESCOPE

Systems that were considered candidates for the SMSS are discussed below. They are illustrated in optical schematics, which in most cases present both azimuth-plane and elevation-plane views. All are based on a 1-m aperture.



The systems usable in the pushbroom mode include an all-reflective Schmidt telescope, an off-axis reflective Schmidt, and the spherical mirror. An oscillating-mirror object-plane scanner can be employed with either of the two reflective Schmidts that are discussed, an on-axis Cassegrain-type telescope, or an off-axis Cassegrain. Also considered were (a) a multiple-mirror configuration, (b) an image-plane scanner with a large spherical mirror and a series of small "inverse-Cassegrain" relays, and (c) a confocal-paraboloid system suitable for either pushbroom or oscillating-mirror scanning.

Figure B-13 shows the aperture-obscuration configurations (cross-hatched, with source of obscuration identified) for various systems for the axial and extreme-field positions, and system characteristics are summarized in Table B-1.

5.1 ALL-REFLECTIVE SCHMIDT SYSTEM

The refractive aspheric plate of the classical Schmidt telescope is replaced with an aspheric (almost-flat) mirror or mirrors in the configurations shown in Figures B-14 and B-15. In the example of Figure B-14, the corrector mirror is tilted slightly to allow the incoming beam to clear the primary, and the aspheric zones are elliptical instead of circular.

The dominant aberration of the classical Schmidt (spherochromatism) is eliminated because no refractive element is used. As a result, performance better than that indicated by the classical equations can be obtained for a specified focal ratio, although the mirror tilt introduces some additional degradation.

A general set of equations relating performance, focal ratio, plate tilt, and FOV was not found in the literature. Information in the few references to some recently designed or constructed reflective Schmidt telescopes seems to indicate that the desired SMSS optical performance can be obtained with an $f/1.5$ to $f/2.0$ system over a 10 to 20° FOV. Figure B-14 shows an $f/1.5$ configuration.



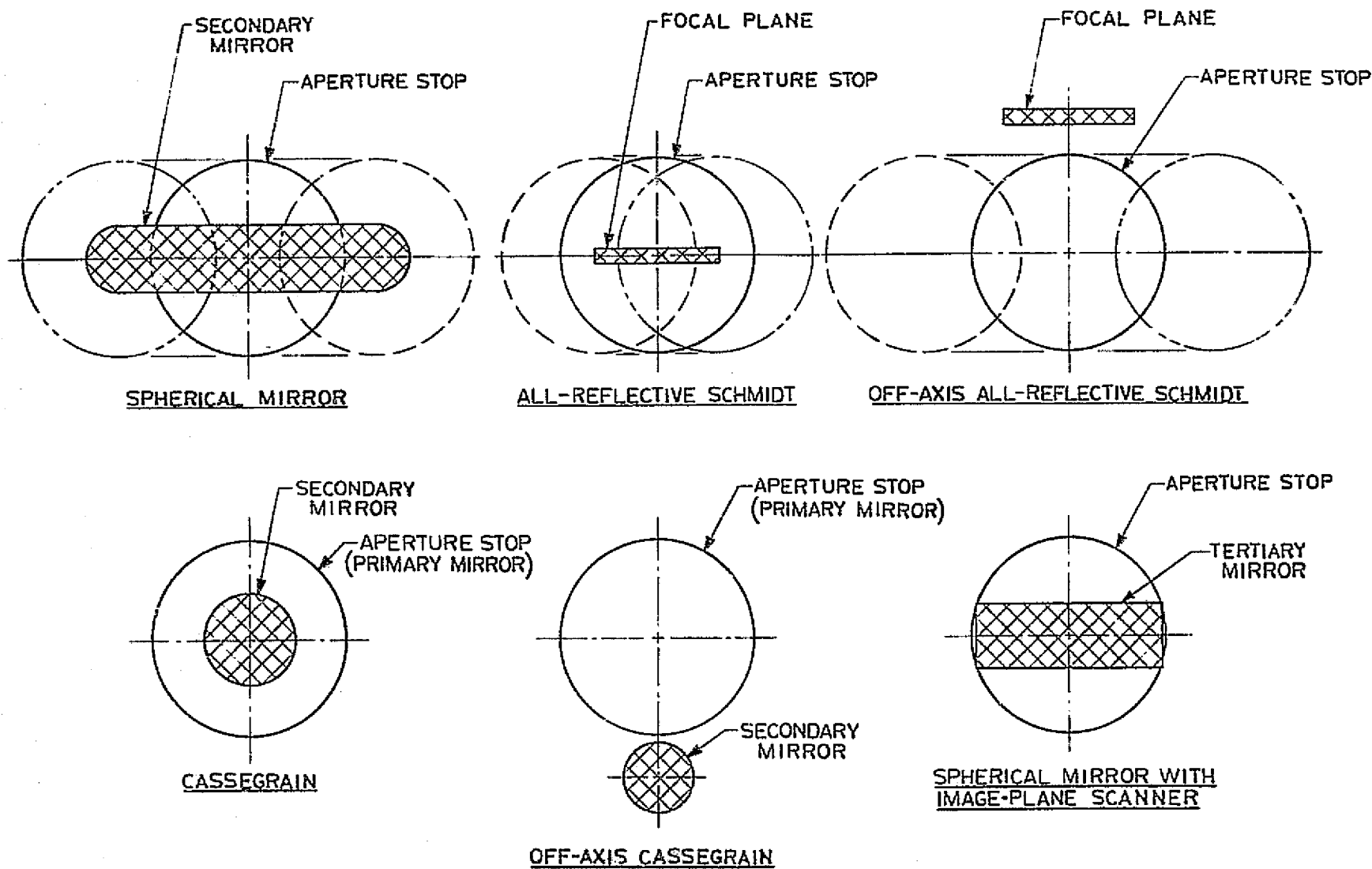


FIGURE B-13 APERTURE CONFIGURATIONS FOR VARIOUS OPTICAL SYSTEMS

TABLE B-1 CHARACTERISTICS OF VARIOUS CANDIDATE OPTICAL SYSTEMS

Type	Scan Method	f/No.	FOV	Mirror Size	No. of Mirrors	Obscuration	Advantages	Disadvantages
All-reflective Schmidt	Pushbroom	f/1.5 to f/2.0	10 to 20° linear	Large (oval)	2	Small	Relatively simple design and alignment.	Fabrication of aspheric corrector. Focal plane relatively inaccessible.
	Mechanical	Same	1 x 22°	Minimum (round)	2	Very Small		
Off-axis reflective Schmidt	Pushbroom	f/1.5 to f/2.0	10 to 20° linear	Large (oval)	2-3	None	Focal plane accessible. No obscuration.	Fabrication and alignment difficult.
	Mechanical	Same	1 x 22°	Minimum (round)	2-3	None		
Spherical mirror	Pushbroom	f/5.5 or slower	10° linear	Large (oval)	2	Large	Simple system.	Large primary mirror. Large central obscuration. Deployable aperture required. Large (linear) image size.
Cassegrain (Ritchey-Chretien)	Mechanical, object-plane scan	f/2.5	1 x 22°	Minimum	3	Moderate	Well-known system. Small instantaneous FOV.	Baffling difficult. Large scan mirror. Fabrication of aspheric mirrors.
Off-axis Cassegrain	Mechanical, object-plane scan	f/2.5	1 x 22°	Minimum	3 or 4	None	Well-known system. Focal plane accessible.	Large scan mirror. Fabrication of aspheric mirrors. Alignment.
Spherical with relay optics	Rotating, image-plane scan	f/1.2 to f/2.0	1 x 22°	Minimum	Many	Large	High scan efficiency. Slow rotation of relay assembly.	Large rotating drum and obscuration. Inaccessible focal plane.



ORIGINAL PAGE IS
OF POOR QUALITY

B-15

ORIGINAL PAGE IS
OF POOR QUALITY

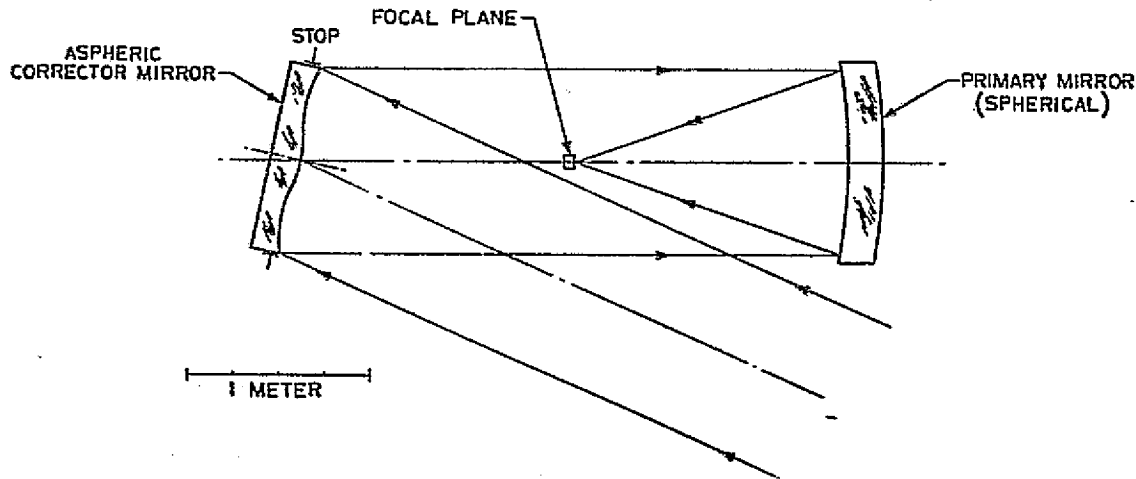
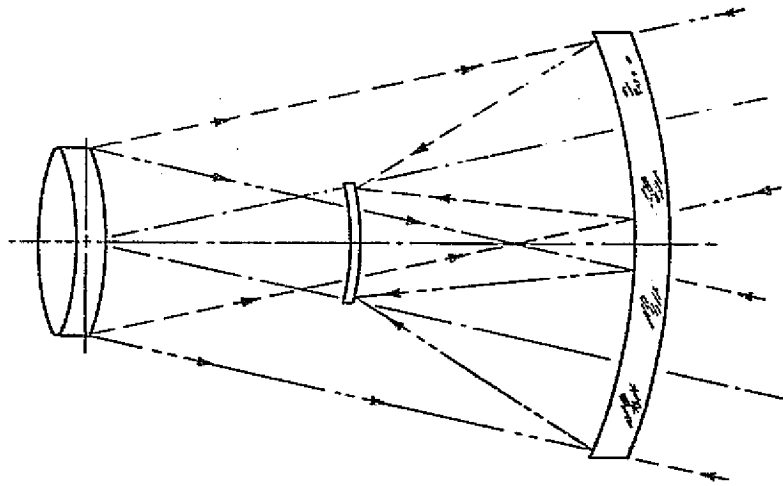


FIGURE B-14 ALL-REFLECTIVE SCHMIDT TELESCOPE WITH STOP AT CORRECTOR

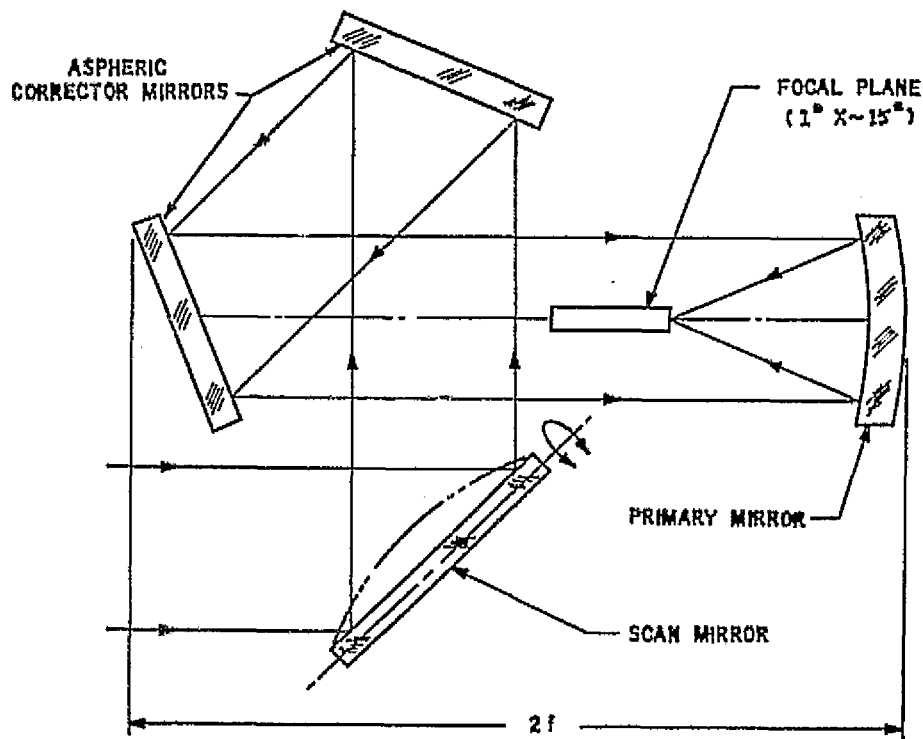


FIGURE B-15 ALL-REFLECTIVE SCHMIDT TELESCOPE: TWO CORRECTORS WITH OBJECT-PLANE SCANNING

This type of system could be used in either scanning mode. A linear-detector array for a 10 to 20° swath width (as in Figure B-14) would introduce very little obscuration for a pushbroom system, although the oval primary mirror would be moderately large.

For the mechanical, object-plane scanner, the corrector mirror could be oscillated to provide 22.5°-FOV coverage. The obscuration and primary-mirror size would be minimal, because the system would need only to cover the 1° field height. Mechanical stability, drive power, and induced momentum to the Orbiter, however, would introduce serious design problems with such a large oscillating mirror (more than 1 m in diameter), as it would with any system using this scan approach.

The all-reflective Schmidt system was selected as a prime candidate for further investigation.

5.2 OFF-AXIS REFLECTIVE SCHMIDT SYSTEM

An off-axis version of the all-reflective Schmidt is illustrated in Figure B-16. It has two advantages over the on-axis configuration: (a) no central obscuration, and (b) an easily accessible focal-surface region.

To provide a more compact package, the aspheric corrector plate has been moved toward the primary mirror, but this results in a greater tilt for the mirror. In addition, the location may require deeper aspheric zones in the corrector and departure from a spherical shape for the primary mirror, with attendant image degradation. These ramifications eliminated the off-axis variation from further investigation.

5.3 SPHERICAL MIRROR

A spherical mirror with the aperture stop at its center of curvature was considered attractive because it has only spherical aberration (on a curved focal surface) and no coma or astigmatism. In addition, the lateral spherical aberration is below a 54- μ r image size when the focal ratio is $f/5.25$ or larger.

Figure B-17 schematically shows an $f/5.5$ spherical mirror folded to fit within the Orbiter bay (4.57 m in diameter). A lightweight, deployable, aperture stop (with outside barrel and baffles) would be necessary to put the stop at the center of curvature of the mirror. If a compartment of about 3.0 m is allowed, a total FOV of approximately 10° could be achieved with a pushbroom sensor.

A reasonable FOV could thus be obtained with a simple optical system. The configuration was not recommended, however, because of the size of the primary mirror, the large central obscuration (see Figure B-13), and the large (linear) image size.



C. 3

ORIGINAL PAGE IS
OF POOR QUALITY

B-19

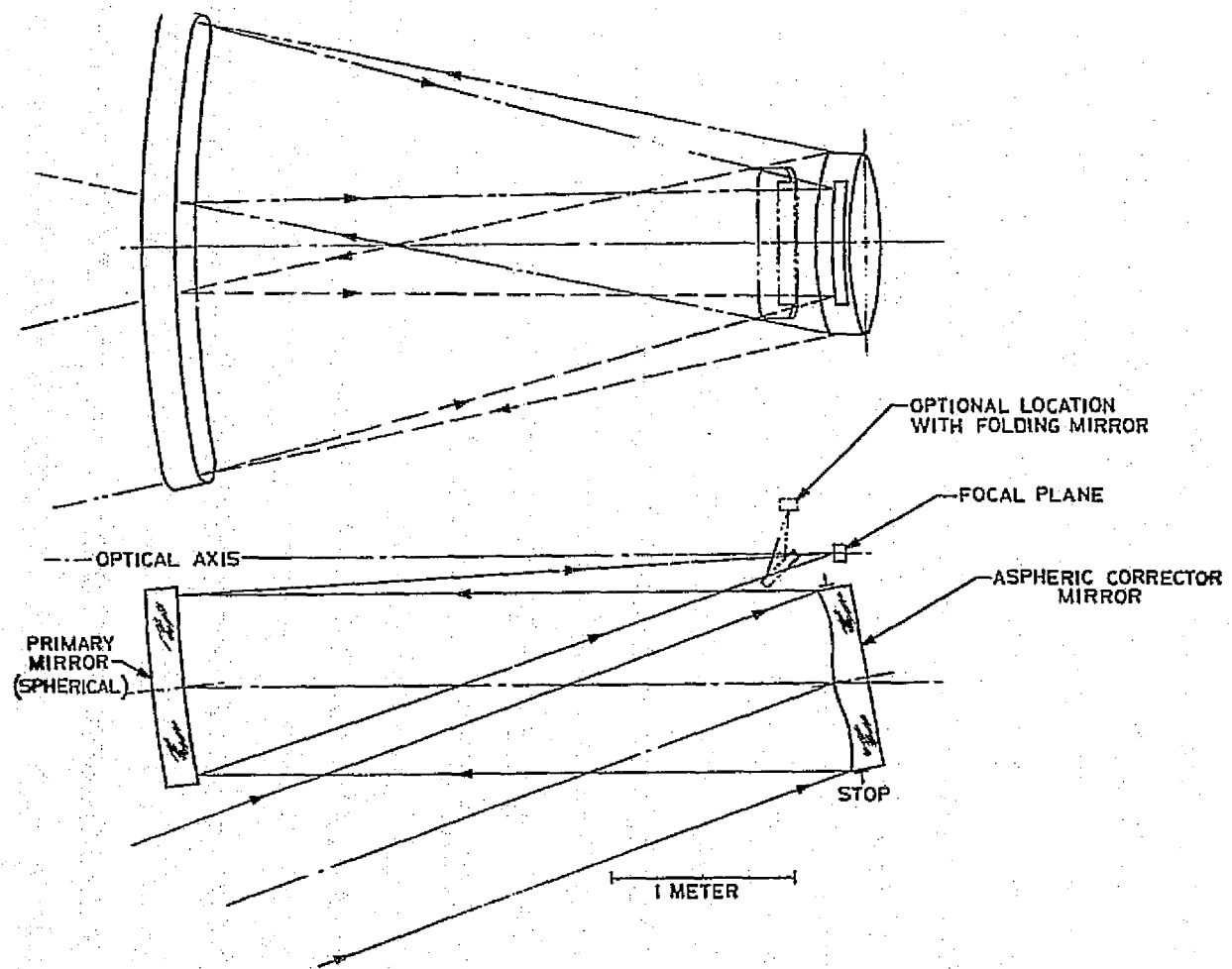


FIGURE B-16 OFF-AXIS ALL-REFLECTIVE SCHMIDT TELESCOPE WITH STOP AT CORRECTOR



B-210

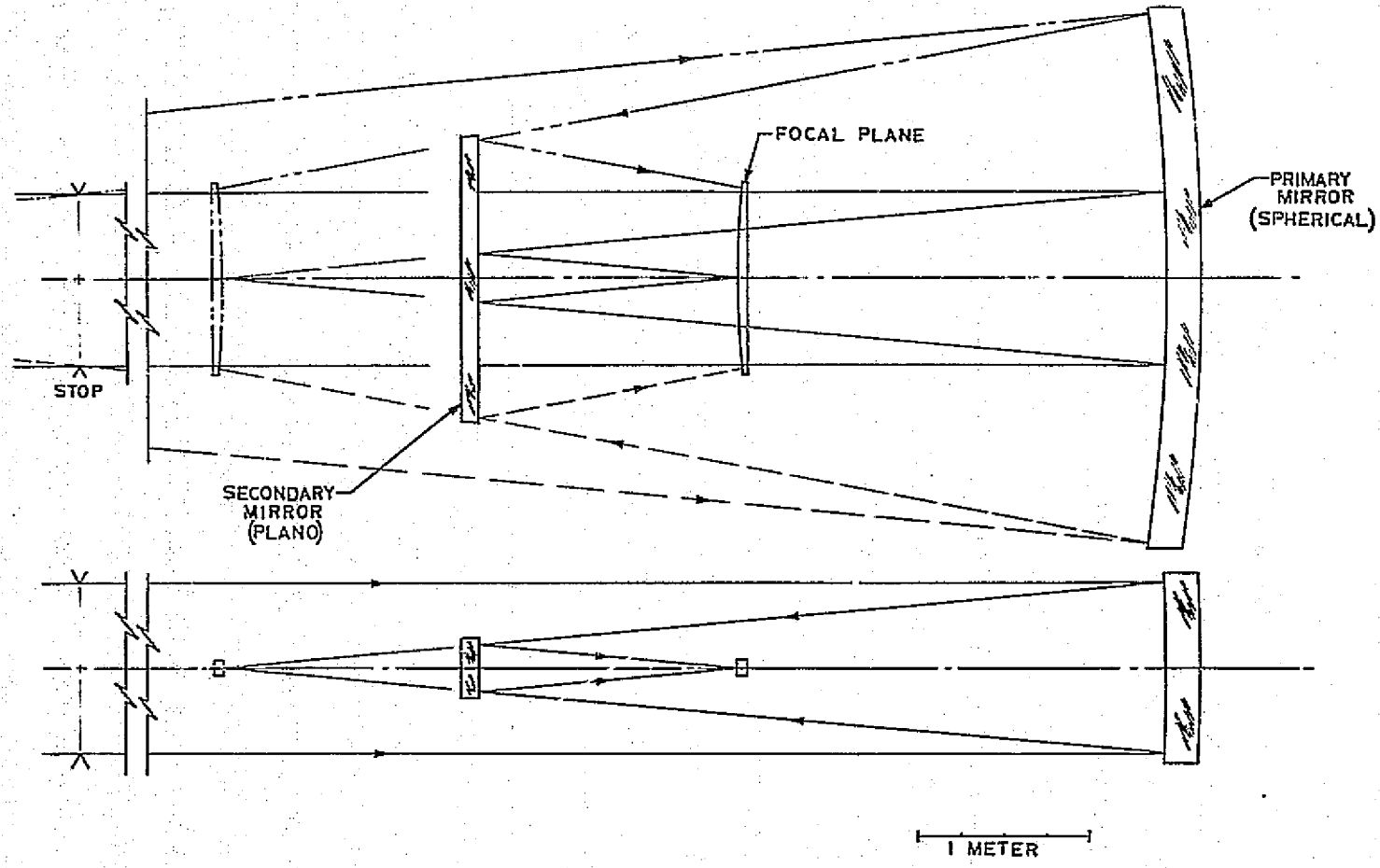


FIGURE B-17 SPHERICAL MIRROR, $f/5.5$ STOP AT CENTER OF CURVATURE

5.4 CASSEGRAIN SYSTEM

Figure B-18 depicts a Cassegrain-type two-mirror telescope with an oscillating-mirror object-plane scanner. The required field coverage is 1° . The mirror surfaces must depart from the paraboloid-hyperboloid combination of the classical Cassegrain configuration, possibly to the Ritchey-Chrétien form.

Cassegrain-system performance can be predicted from that of a paraboloid with equivalent focal length and aperture. Figure B-11 shows that an image size of about $50 \mu r$ over a $\pm 0.5^\circ$ FOV requires at least an $f/8$ system. The obscuration from the secondary mirror is shown in Figure B-13.

The relatively large obscuration, the necessity for two aspheric mirrors, and the large focal ratio made this configuration less attractive for a mechanical-scan system than the reflective Schmidt telescope.

5.5 OFF-AXIS CASSEGRAIN SYSTEM

An off-axis version of the Cassegrain system is shown in Figure B-19. It has the advantages of no central obscuration and an easily accessible focal region. The focal length, however, is about 3 times that of the on-axis version for the same entrance-aperture size and focal ratio, and the linear size of the detectors must increase correspondingly.

Although this configuration was more attractive than the on-axis version, it had the same disadvantages of requiring two aspheric mirrors and a larger focal ratio than the reflective Schmidt.

5.6 MULTIPLE-MIRROR CONFIGURATION

Multiple mirrors offered another approach, employed by several designers during the past few years, to increase the resolution and field of the system. One such design by Meinel and Shack at the University of Arizona is shown in Figure B-20 to depict the approach and possibilities. It yielded diffraction-limited performance at $f/1.75$ over a field exceeding 5° , although

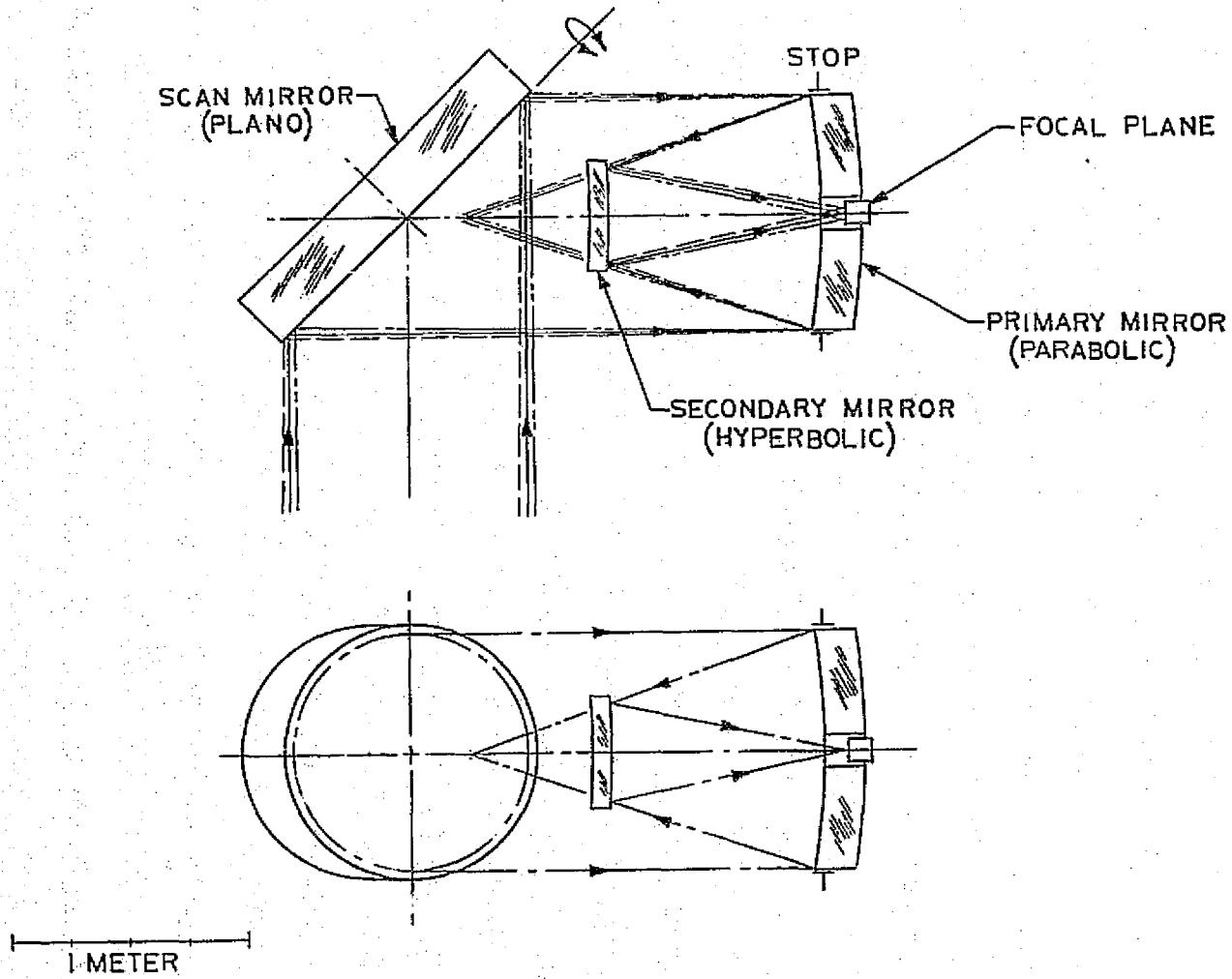
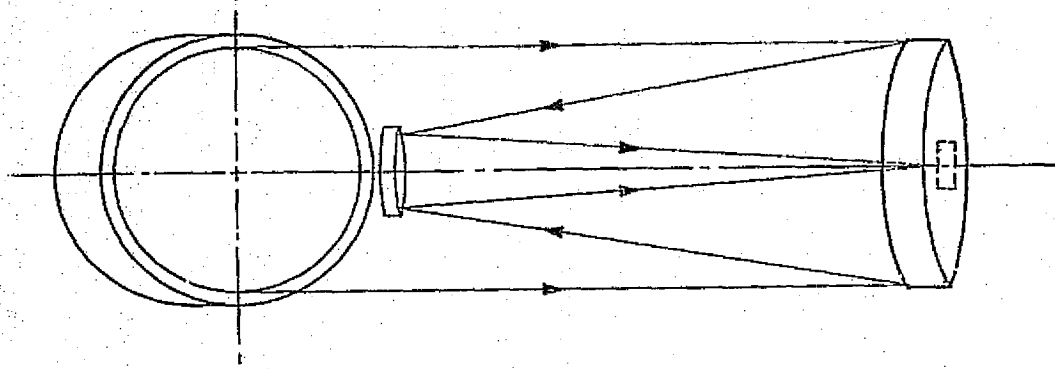


FIGURE B-18 CASSEGRAIN TELESCOPE WITH SCANNING MIRROR, $f/2.5$ STOP AT PRIMARY MIRROR



B-23

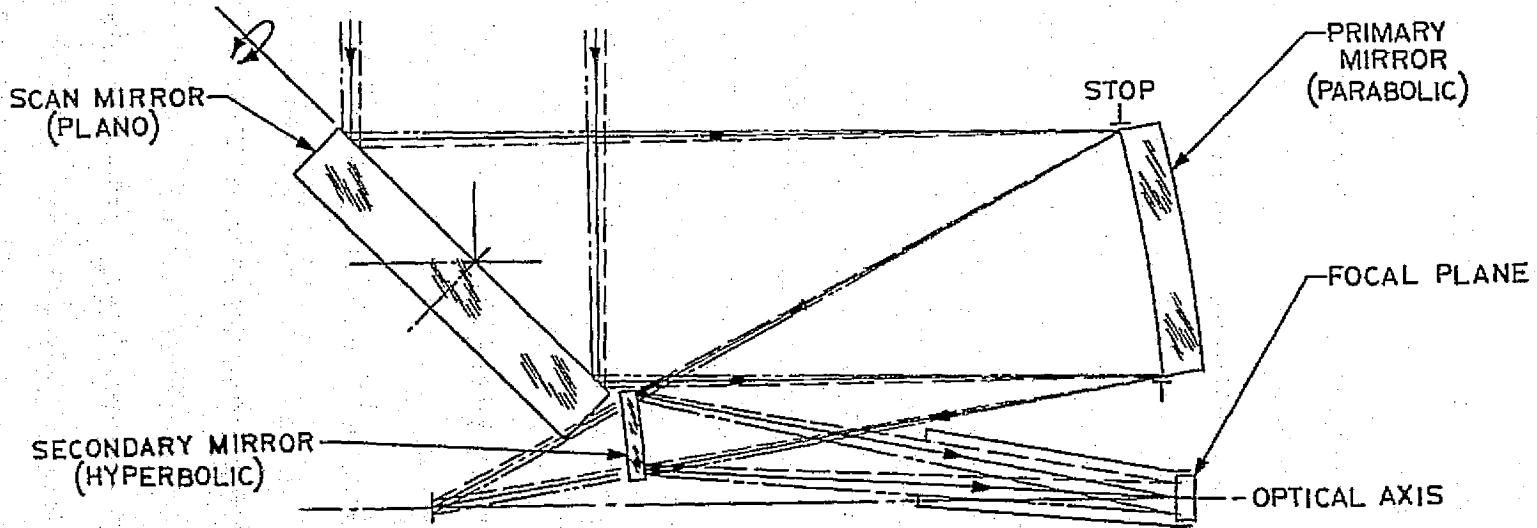


FIGURE B-19 OFF-AXIS CASSEGRAIN TELESCOPE WITH SCANNING MIRROR, $f/2.5$ STOP AT PRIMARY MIRROR

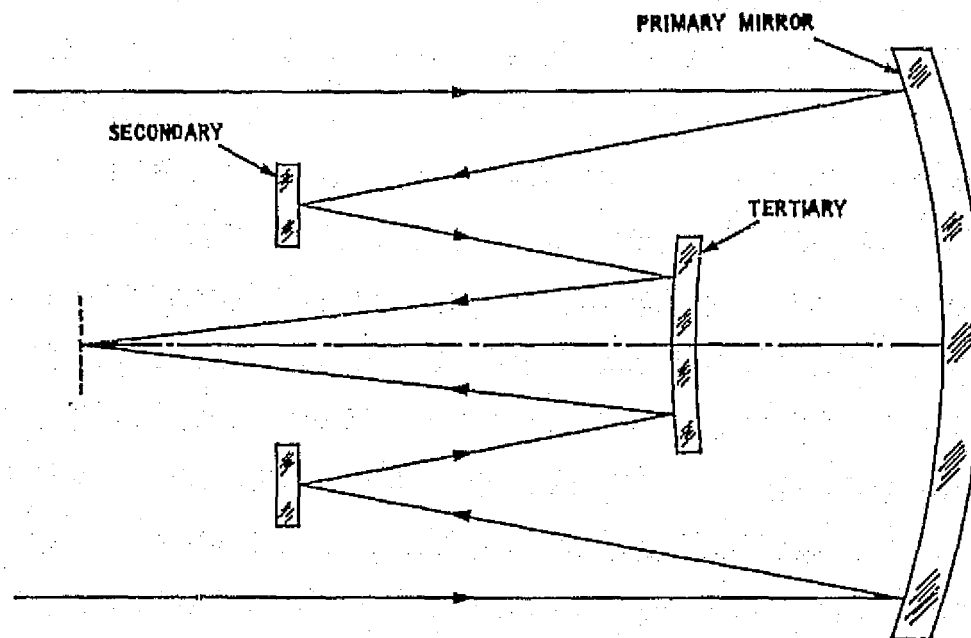


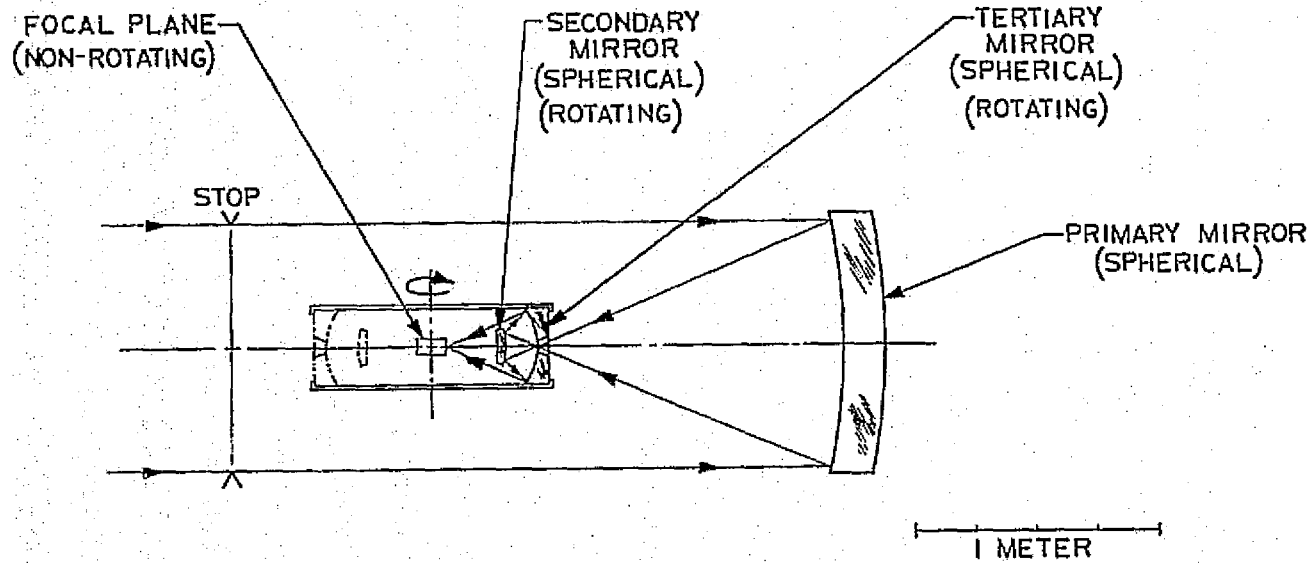
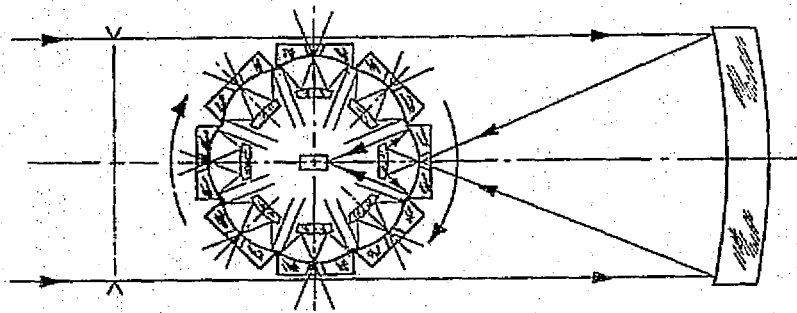
FIGURE B-20 THREE-MIRROR OPTICAL SYSTEM

the obscuration ratio was rather high and it required that all the mirrors be aspheric. Many other forms have been devised and reported, but are in general more complex than the all-reflective Schmidt.

5.7 SPHERICAL MIRROR WITH RELAY OPTICS (IMAGE-PLANE SCANNER)

Figure B-21 depicts a spherical mirror with an aperture stop at the center of curvature and a large number of small inverse-Cassegrain relays in a rotating relay drum. It is intended only to illustrate a possible configuration. No attempt was made to match the drum and primary-mirror-image-surface radii, to minimize relay-mirror sizes, or to balance the spherical aberration of the primary mirror with that introduced by the relays.

As the relay units rotate, they send the image (formed by the spherical primary on a backward-curved prime focus) to the fixed detector arrays in the center of the drum. With eight relays as shown, a swath width up to 45° could be obtained. The 1° FOV perpendicular to the swath direction would be parallel to the axis of drum rotation.



B-25

FIGURE B-21 SPHERICAL MIRROR WITH IMAGE-PLANE SCANNER

5.8 CONFOCAL PARABOLOID SYSTEM

Figure B-22 illustrates an arrangement that has become popular for applications requiring a large-aperture, wide-spectral-region system. This concept uses two paraboloids with a common axis and focus. It is shown in an off-axis form that eliminates the usual central obscuration and allows for excellent stray-energy rejection. In the afocal beam after the second paraboloid, small telescopes covering individual spectral bands can be inserted, using either reflective or refractive elements (as shown).

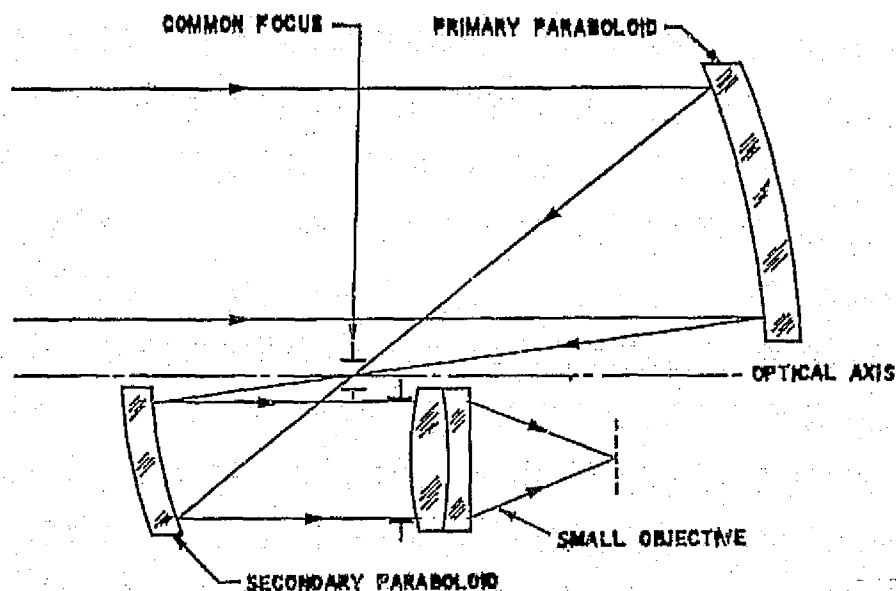


FIGURE B-22 OFF-AXIS CONFOCAL PARABOLOIDS WITH SMALL OBJECTIVES

Scanning can be provided either by vehicle motion or by an oscillating scan mirror. With this configuration it is also possible to place the scanning mirror in the afocal beam after the secondary, thus considerably reducing scan-mirror size. The degree of complexity of this system, however, made it unattractive for further investigation.

6 OPTIMIZATION OF ALL-REFLECTIVE SCHMIDT SYSTEM

The all-reflective on-axis Schmidt configuration (Figure B-14) was selected as having significant potential for meeting SMSS requirements and as warranting concentrated investigation because it offers

- a. Relative simplicity, having only two mirrors, with one of them spherical
- b. Adaptability to the self-scan or the mechanical-scan approach
- c. Acceptable obscuration
- d. Excellent image quality at low focal ratios
- e. Large field of view
- f. Lack of spectral limitations.

The optimization of this system is discussed below.

6.1 GENERAL CONSIDERATIONS

As noted in paragraph 4.1, a spherical mirror with an aperture stop at its center of curvature (e.g., the Schmidt primary) is limited in optical performance only by spherical aberration; coma and astigmatism are eliminated. Complete correction of the spherical aberration can be achieved (for a given field position) by "redirecting" the incident rays with an appropriately shaped aspheric plate at the primary center of curvature. The configuration also greatly increases the usable field size and yields excellent image quality for a given size of primary.

Many authors have reported on theoretical developments of the Schmidt concept, but in most instances discuss only the catadioptric version. Several recent papers, however, describe Schmidt systems using a reflective corrector (Refs. B-2 through B-7). Ref. B-2 is particularly pertinent, describing a system that essentially satisfies the SMSS requirements. Optical performance as a function of field angle at specific focal ratios is tabulated below for several of these systems.

<u>Source</u>	<u>Semi-FOV (degrees)</u>	<u>Image Size (μr)</u>	<u>Focal Ratio (f/no.)</u>
Ref. B-4, L. C. Epstein, Chrysler Space Systems	3	5	4
Ref. B-6, J. A. Decker, Spectral Imaging, Inc.	3	11	3.1
Itek Corporation, telephone conversation	11	20	2.6
Ref. B-2, D. E. Oinen, Eastman Kodak Company*	5	50	1.5
Ref. B-2, as above	9	84	1.5

Telescope layouts were prepared to determine the suitability of the all-reflective Schmidt for interfacing with the Orbiter vehicle. They are shown in Figures B-23 and B-24, which are based on the following parameters: an f/1.5 system, with a 100-cm primary mirror and with the optical axis of the reflective corrector plate tilted 20° from the primary optical axis. Although these parameters were altered as the optimization effort progressed, the layouts illustrated the feasibility of mounting a telescope of this size in the Orbiter. The Orbiter dimensions were taken from Ref. B-8 ("Space Shuttle System Payload Accommodations").

Figure B-23, a cross-sectional view of the telescope mounted in the Orbiter payload compartment, was prepared to demonstrate satisfactory interfacing rather than to illustrate a suggested structural design. The structure is rigidly attached to the payload-retention points, because telescope gimbals will not be required for image-motion compensation or pointing. Figure B-24, another schematic representation, presents a side view of the SMSS in the payload compartment.

* Approximates SMSS characteristics.





ORIGINAL PAGE IS
OF POOR QUALITY

B-29

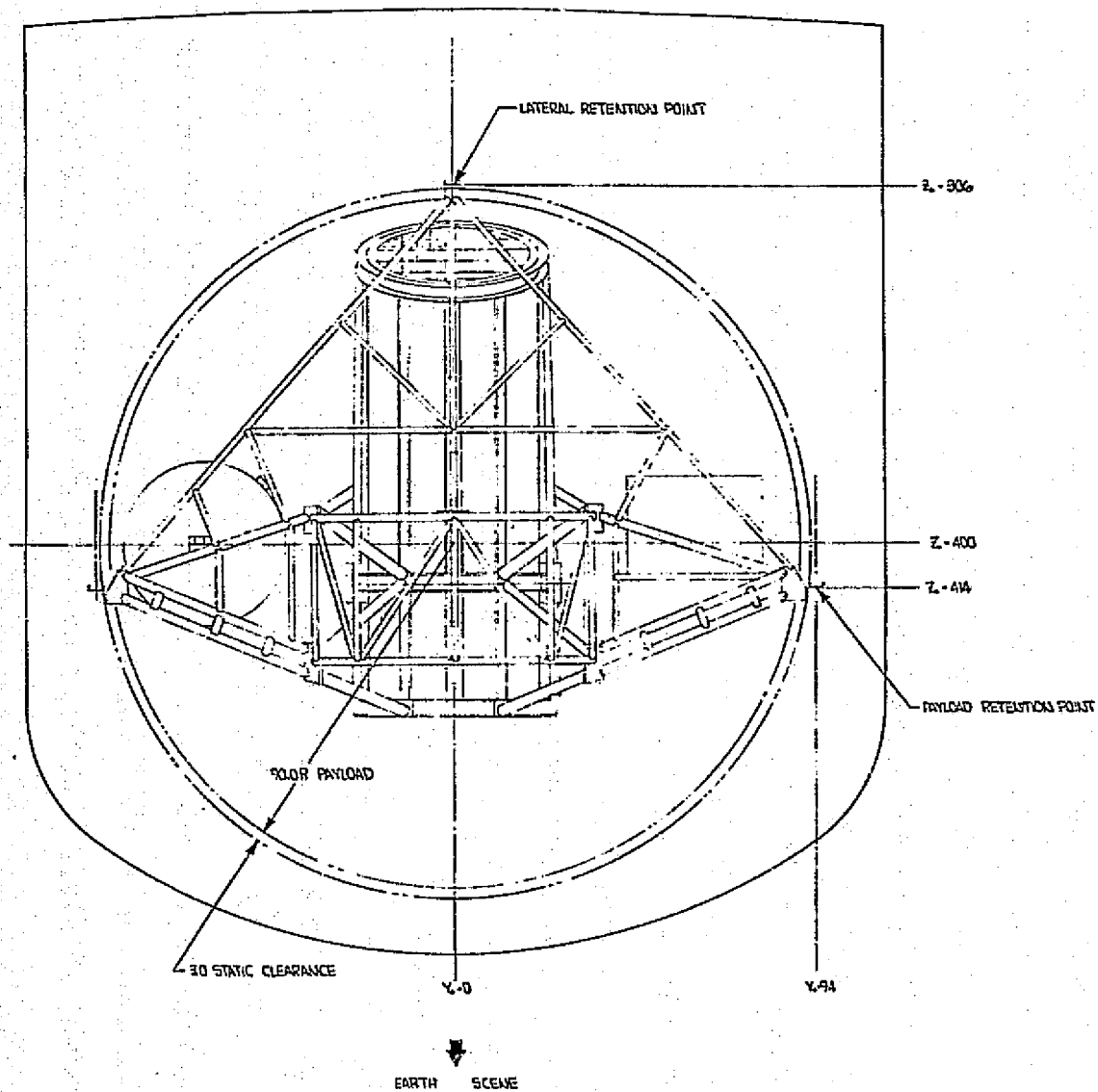
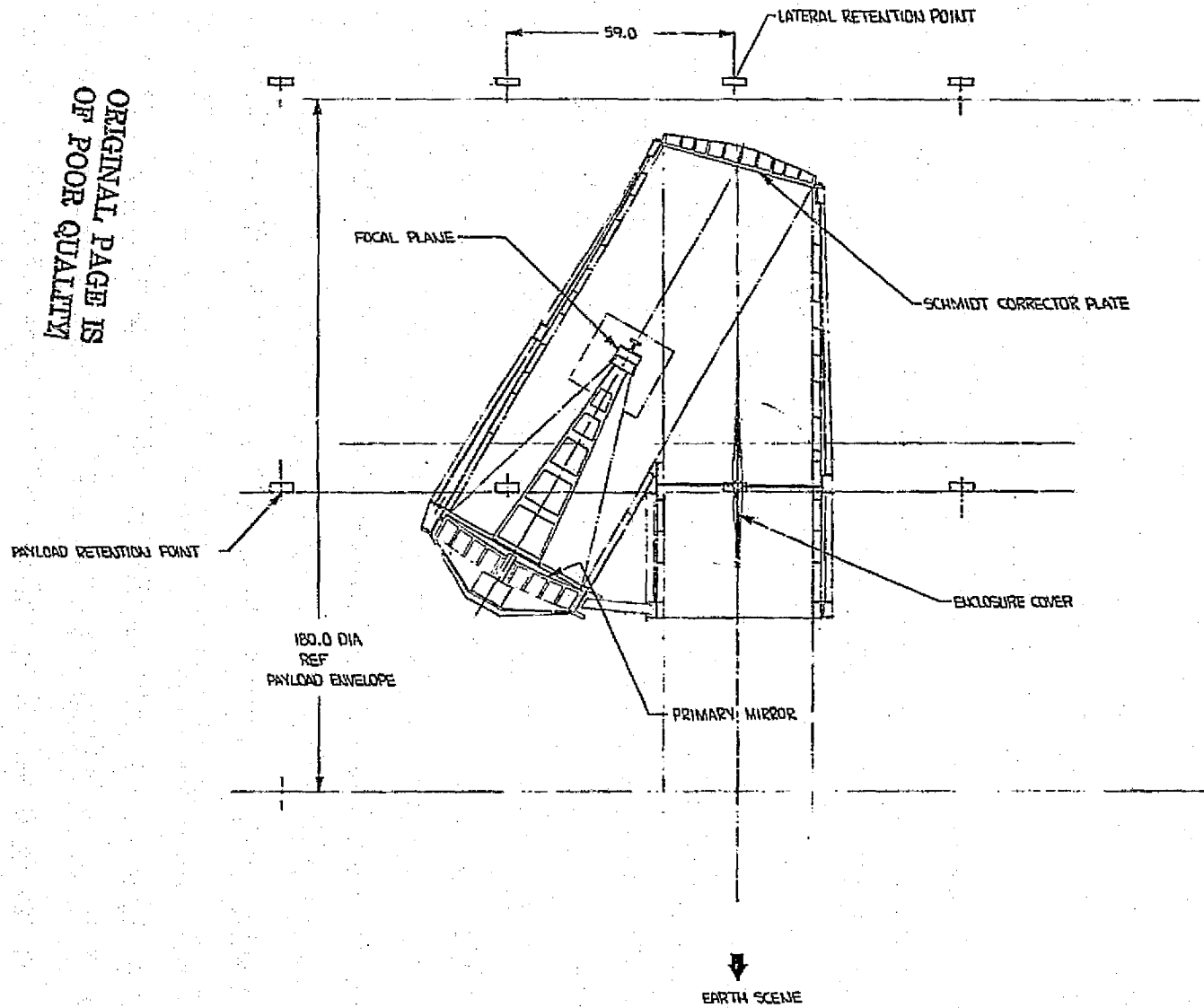


FIGURE B-23 INTERFACE-FEASIBILITY LAYOUT, SMSS MOUNTED IN ORBITER (CROSS-SECTIONAL VIEW)



ORIGINAL PAGE IS
OF POOR QUALITY



B-30

FIGURE B-24 INTERFACE-FEASIBILITY LAYOUT, SMSS MOUNTED IN ORBITER (SIDE VIEW)

6.2 ANALYTICAL AND COMPUTER OPTIMIZATION

Although the all-reflective Schmidt configuration was suggested as long ago as 1939, it has seldom been considered because the required corrector-mirror tilt and the resulting elliptical zones formerly cast doubt on the performance capabilities and the possibility of fabrication.

The fabrication impact has been reduced greatly by advancements in the generation of aspheric optical surfaces, and the performance implications of mirror tilt and elliptical zones are considered below. Because little design information was available in the literature, two courses were pursued: (a) a review of the theory of Schmidt-telescope aberrations, considering the use of a mirror for the corrector element, in preparation for (b) computer optimization with different focal ratios ($f/nos.$) and fields of view.

Bowen's excellent, simplified treatment of the theoretical basis of the original Schmidt telescope (refractive corrector) in Ref. B-9 was used for this study. The performance of the all-reflective version, unlike the classical Schmidt, is limited only by off-axis aberrations because it has no chromatic aberration. Following Bowen's development, the off-axis aberrations can be treated by calculating the changes (Δa and Δb) in displacements by the rays at the focal plane. For a refractive Schmidt, they are approximately

$$\Delta a \cong \frac{K_2 f (\sin \phi)^2}{128 n (f/nos.)^3}$$

and

$$\Delta b \cong \frac{K_1 f (\sin \phi)^2}{128 n (f/nos.)^3}$$



where f = system focal length
 ϕ = semifield angle
 n = corrector-plate index of refraction
 $f/\text{no.}$ = focal ratio = focal length/aperture diameter

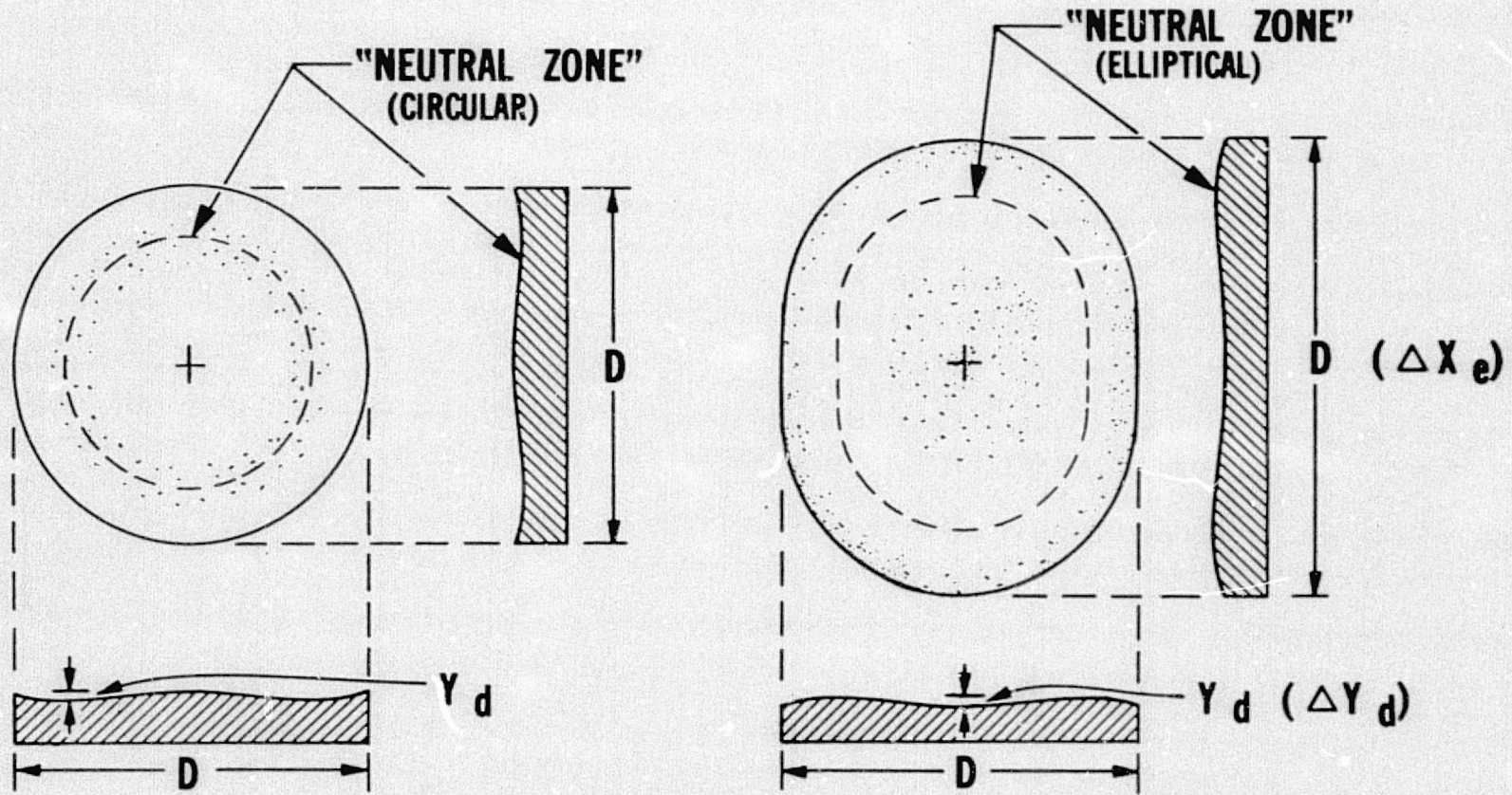
and the K_1 and K_2 coefficients are functions of the index of refraction, the ray location on the plate, and the location of the "neutral zone" (i.e., the region parallel to the plano surface of the plate). Inserting the factor $128 n$ into the coefficients and combining these equations yields the following approximation:

$$\begin{aligned} r &\cong \sqrt{(\Delta b)^2 + (\Delta a)^2} \\ &\cong \sqrt{(K_1')^2 + (K_2')^2} \left[f (\sin \phi)^2 / (f/\text{no.})^3 \right] \\ &\cong \frac{K_r f (\sin \phi)^2}{(f/\text{no.})^3} \end{aligned}$$

where r is the average image radius. As noted by Bowen, these equations are based on the first term of an expansion and are not exact for low focal ratios. In addition, they do not take into account the image effects caused by mirror tilt in the all-reflective configuration.

Figure B-25, which highly exaggerates profiles in the interest of clarity, demonstrates two differences between the refractive and reflective Schmidt systems.

As shown, the zones of the refractive type are circular and axially symmetric, whereas the reflective-corrector zones are nonrotationally symmetric. (The terms ΔX_e and ΔY_d used in Figure B-25 are defined in Figure B-26.)



● CLASSICAL REFRACTIVE SCHMIDT PLATE WITH CIRCULAR ZONES

● REFLECTIVE SCHMIDT MIRROR WITH ELLIPTICAL ZONES

FIGURE B-25 COMPARISON OF SURFACE PROFILES FOR REFRACTIVE AND REFLECTIVE SCHMIDT CORRECTORS

275-1839

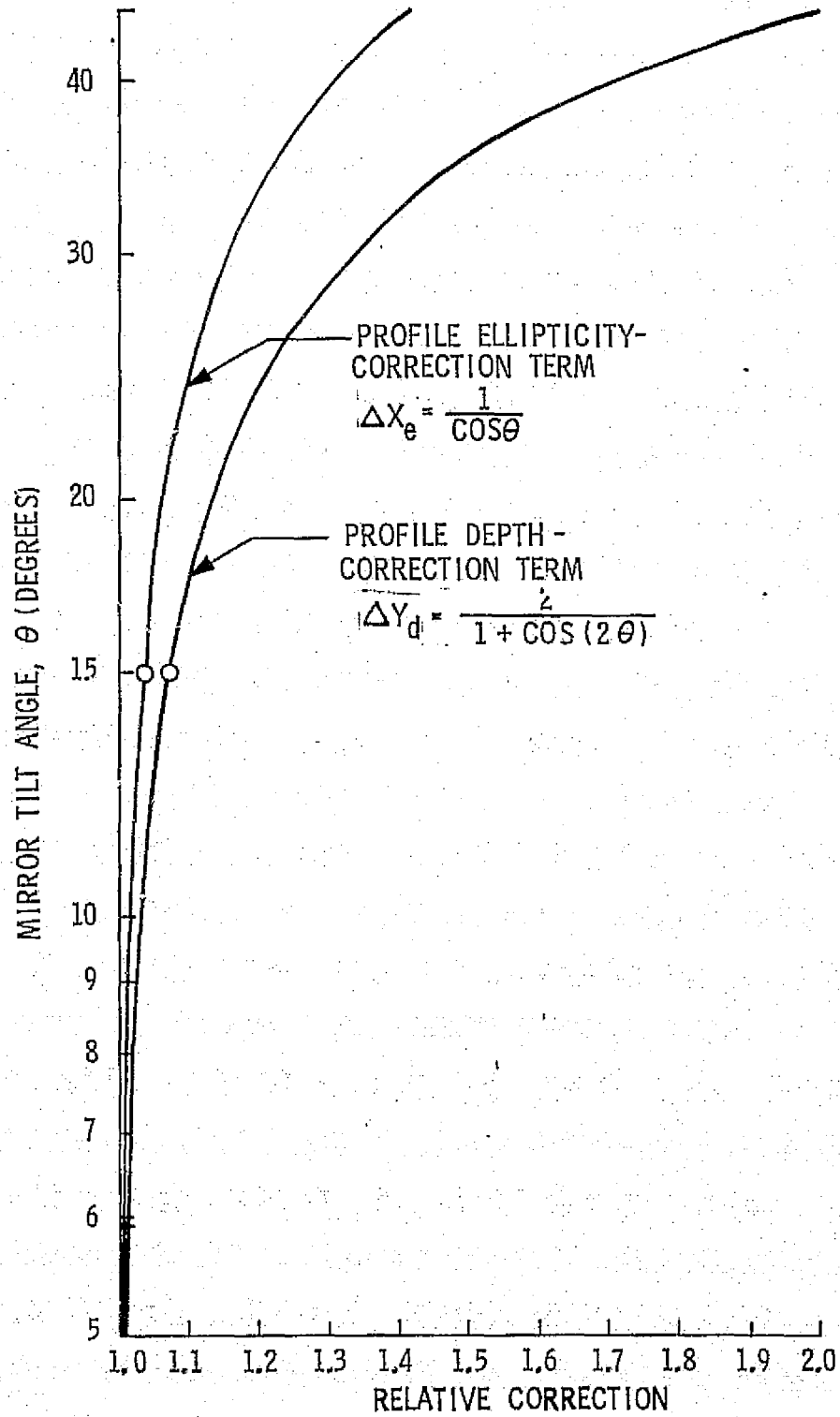


FIGURE B-26 CORRECTION TERMS FOR CORRECTOR MIRROR OF REFLECTIVE SCHMIDT

The other difference arises from the fact that the ray deviation necessary for the required optical correction is produced by two different mechanisms (refraction and reflection) that involve exactly converse curved surfaces. The classical refractive plate is convex in the center and has a neutral zone that is usually located at 0.707 of the plate radius (for minimum chromatic aberration) or 0.866 (for optimum off-axis correction) and falls at the thinnest portion of the corrector. The reflective corrector requires a concave surface at the center. Because chromatic aberration is no concern with a mirror, the neutral zone can be located wherever required (even off the actual surface) for the best performance over the field. For the corrector mirror, this zone is the position of maximum mirror thickness.

The deviations from the circularly symmetric profile are very small for small mirror-tilt angles. This fact is indicated in the two curves of Figure B-26.

One of the curves ($\Delta X_e = 1/\cos \theta$) gives the required "ellipticity correction", which is the ratio of corrector-mirror length to width. For the 15° mirror-tilt angle considered for an $f/1.5$ system, this factor is 1.0353--i.e., the corrector mirror is 1.0353 m long for a 1.000-m width. The amount of ellipticity is thus only 3.53%.

The second curve in Figure B-26 is for the term $\Delta Y_d = 2/[1 + \cos(2\theta)]$, which Oinen (Ref. B-2) cited as providing a correction to the magnitude of the surface contours to account for non-normal incidence of rays on the corrector surface. For a 15° tilt, this correction term is 1.072. Consequently, the depth or height of a given location on a mirror tilted at 15° must be only 7.2% greater than for a mirror perpendicular to the optical axis.

After the relationship of reflective-Schmidt performance to the fundamental design parameters of FOV and focal ratio was investigated in reviewing the theory of Schmidt-telescope aberrations, computer optimization was used to obtain the desired information.



An available program (COP)* was used for the optimization. The intent was to provide data on which to base the selection of a suitable focal ratio and FOV, although this application of COP did not simulate corrector-mirror tilt.

The optimization covered various focal ratios (from f/1.2 to f/2.0) and semi-FOV angles from 5 to 10° (see Figure B-27). Additional optimization runs were made for f/1.5, 1.7, and 1.8 with different fields and "weightings" on the relative field position (Figures B-28 and B-29). The plots give the image quality in microradians as a function of semifield angle for the various focal ratios. All systems were assumed to have a 100-cm aperture. The distance from the primary mirror to the focal plane is approximately equal to the focal length, and the corrector mirror is placed at the primary-mirror center of curvature.

These plots showed that the desired image size of 50 μ r (later modified to 66 μ r) could be obtained over a total FOV of 10° with an f/1.5 system. To achieve the same performance for the requested 15° FOV, the focal ratio must be increased to at least f/1.7.

The optimization runs indicated that the exact image quality depends not only on focal ratios but also on the number of parameters varied, the field angles, and the weights used. Because windows and filters near the focal plane might be used to improve the image quality, it is suggested that this approach be considered during the detailed-design phase of the SMSS program.

The runs tended to illustrate a beneficial aspect of the all-reflective Schmidt: that the FOV can be large without significant loss of image quality at the edges of the field. This attribute results, in part, because there is no chromatic aberration and the plate contour can be

* David Grey's COP program, written by David Grey Associates, 60 Hickory Drive, Waltham, Massachusetts.

275-1146

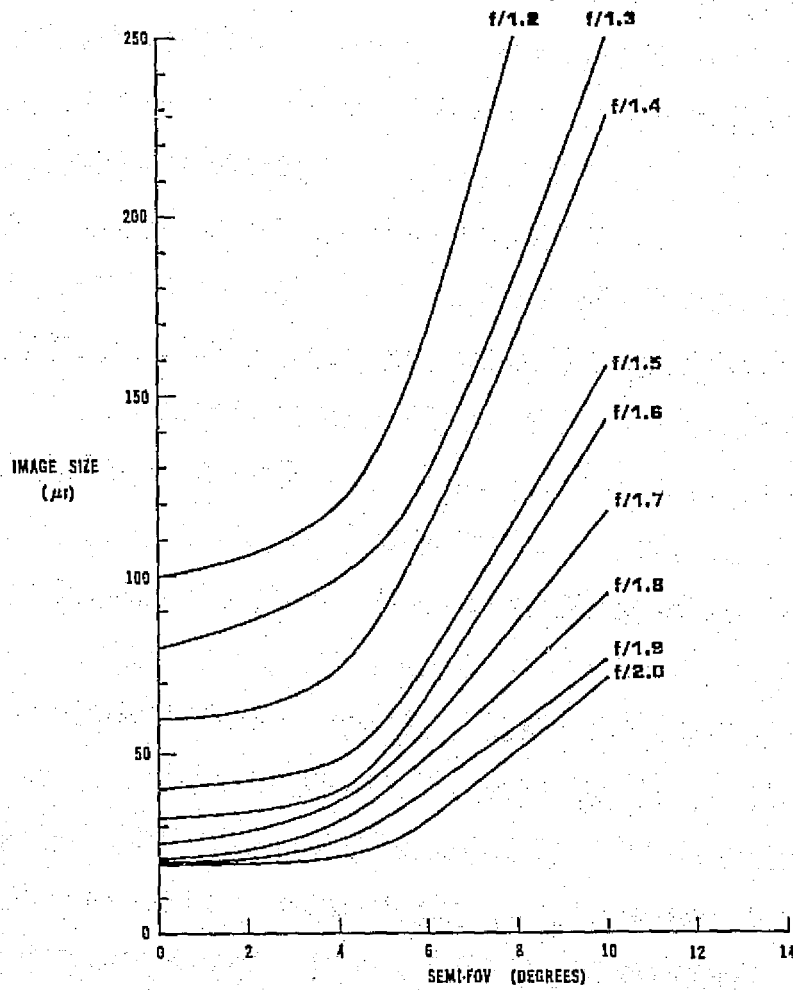


FIGURE B-27 INITIAL OPTIMIZATION, ALL-REFLECTIVE SCHMIDT TELESCOPE



275-1838

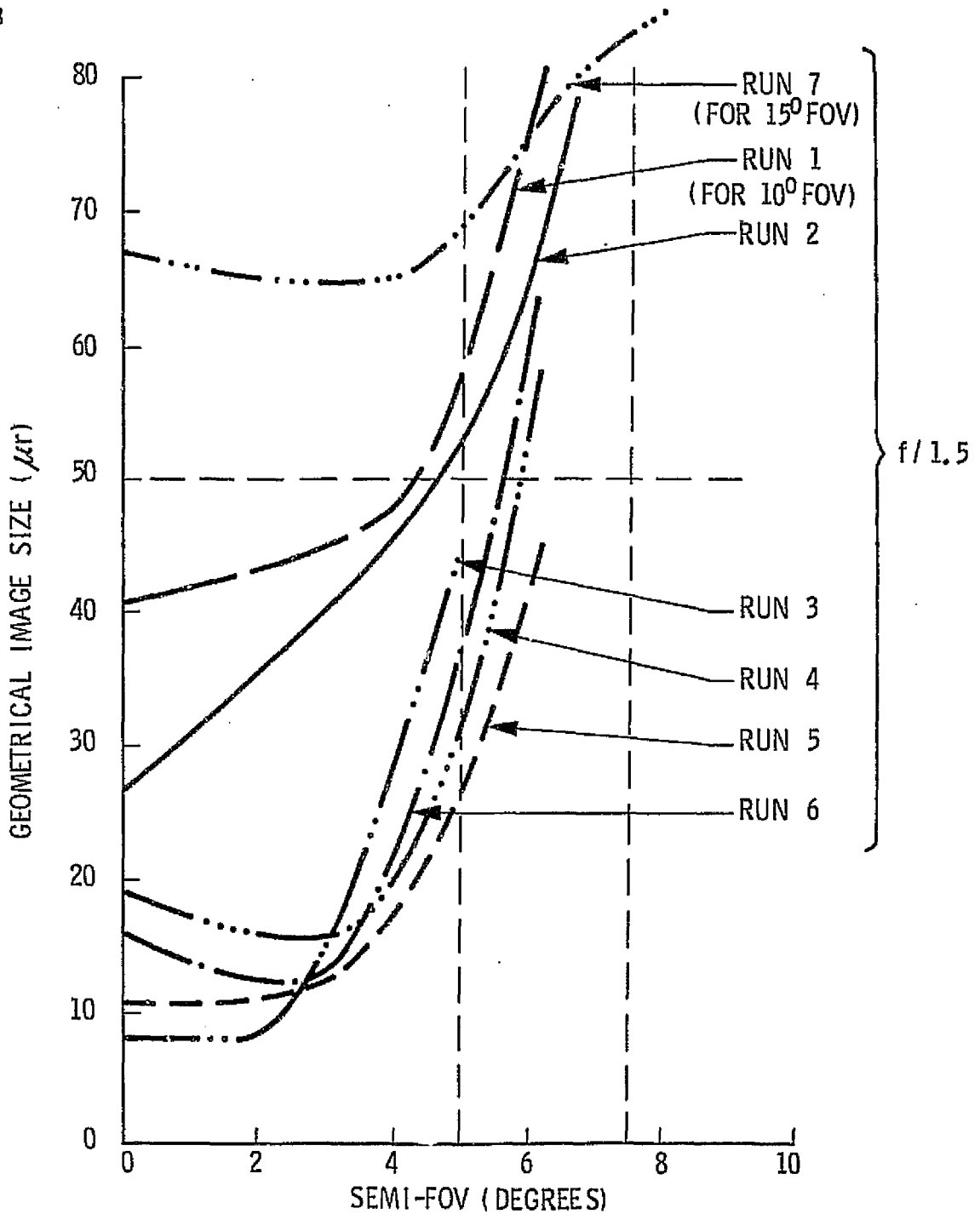


FIGURE B-28 RESULTS OF INITIAL DESIGN STUDY FOR f/1.5 REFLECTIVE SCHMIDT



275-1837

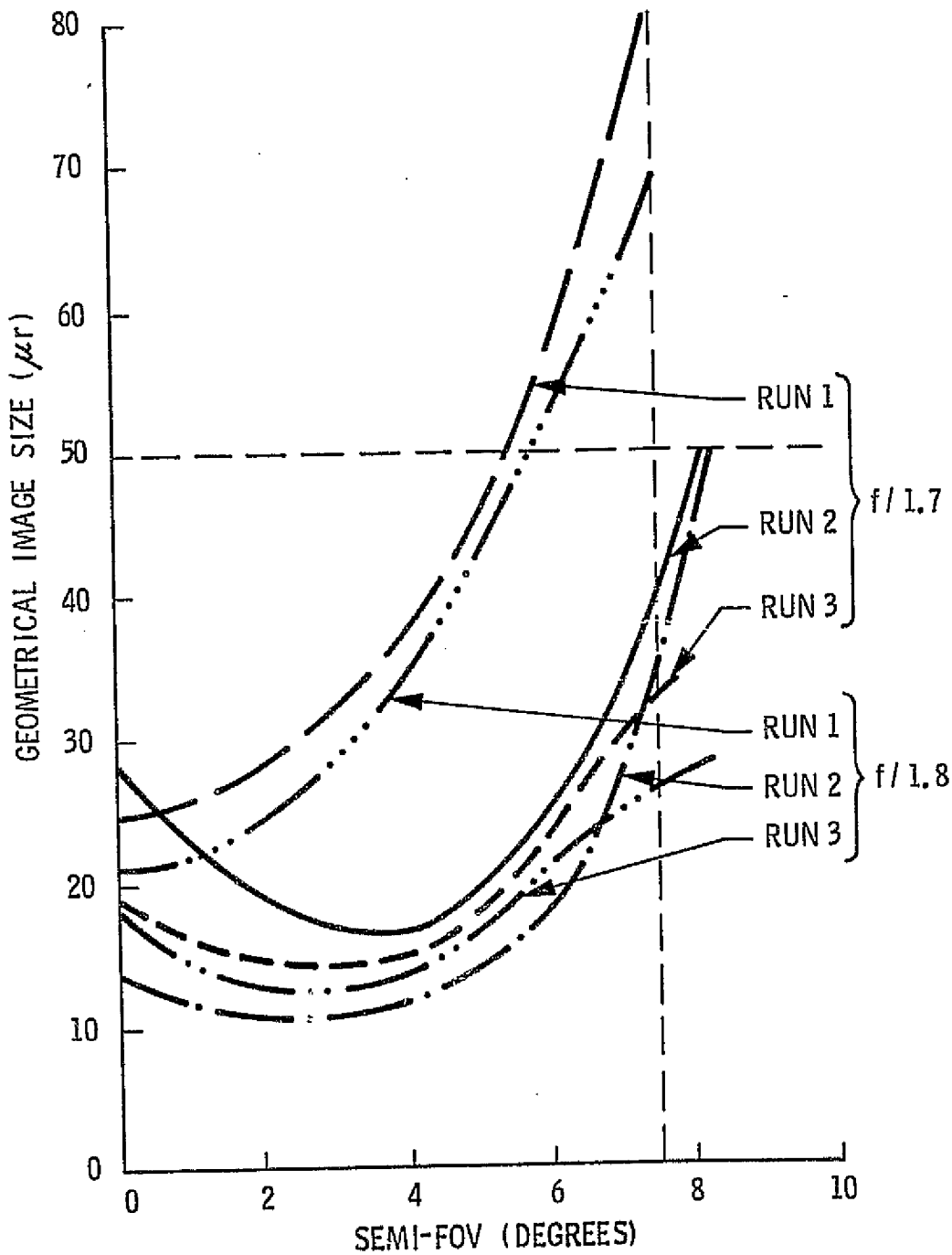


FIGURE B-29 RESULTS OF INITIAL DESIGN STUDY FOR $f/1.7$ and $f/1.8$ REFLECTIVE SCHMIDT



optimized to correct the residual coma and astigmatism. It is thus possible to correct for aberrations over a relatively wide FOV without the accompanying increase in chromatic aberrations associated with the catadioptric type of Schmidt system.

An additional computer run was made in which the spacing between the primary and corrector mirrors was shifted slightly as compared with previous runs. The purpose was to emphasize improved resolution at the edge of the field at the expense of on-axis performance. The results are plotted in Figure B-30. Extensive optimization will be required during the detailed-design phase, but the analyses and simulations described here have indicated that the all-reflective Schmidt system can readily satisfy SMSS requirements.

7 PHYSICAL CHARACTERISTICS OF SCHMIDT OPTICS

Figure B-31 shows the range of Schmidt-system primary-mirror lengths required to avoid vignetting, as a function of focal ratio and FOV. Figure B-32 presents examples of the depth-of-focus variation with focal ratio for a 75-cm aperture.

Table B-2 gives approximate mirror weights and sizes, using quartz and beryllium for selected apertures and focal ratios considered for the SMSS.



575-1243

GEOMETRICAL
IMAGE SIZE (μr)

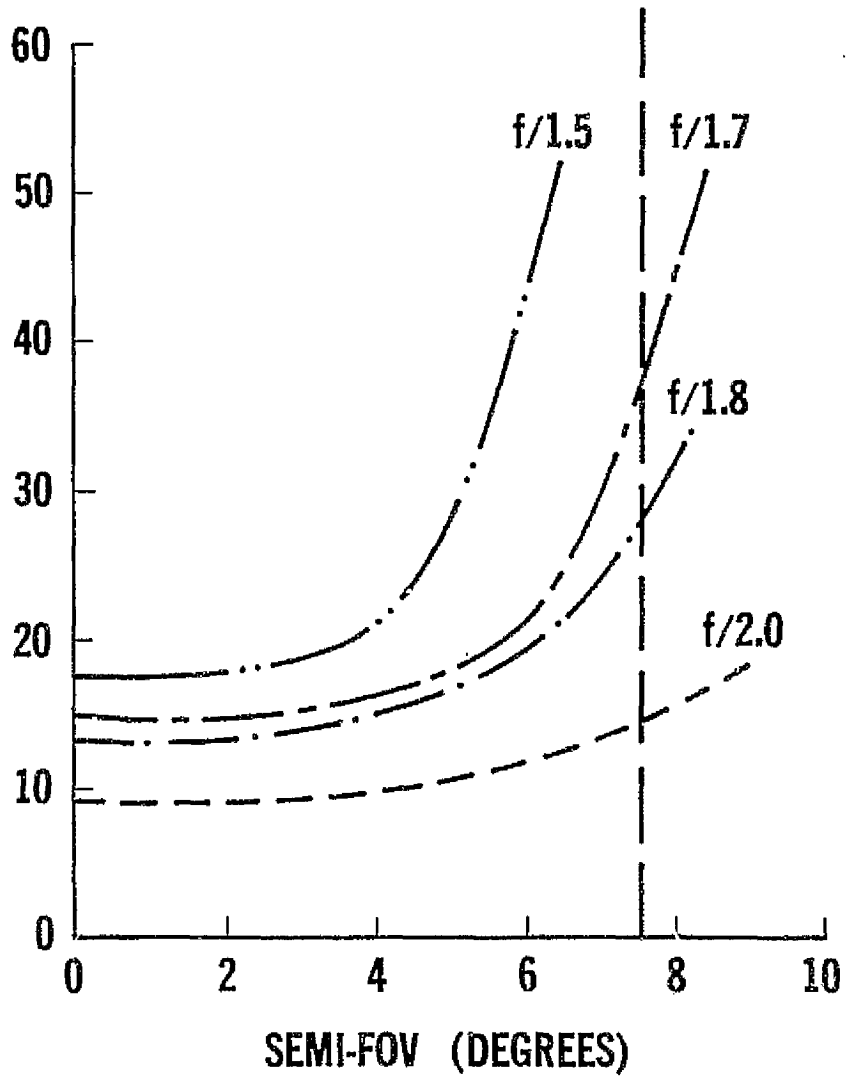


FIGURE B-30 REFLECTIVE-SCHMIDT COMPUTER OPTIMIZATION FOR WIDE FIELD





B-42

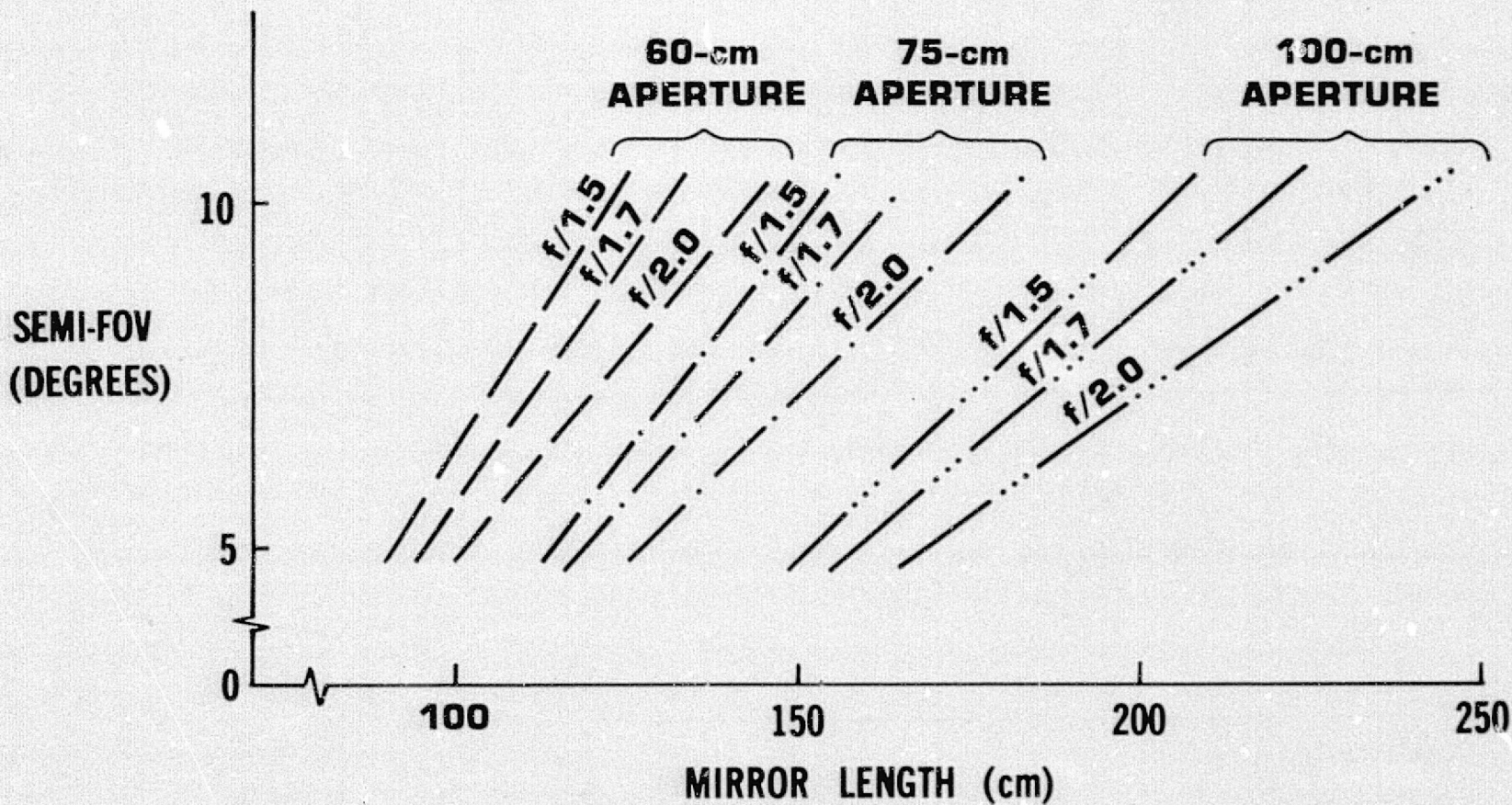
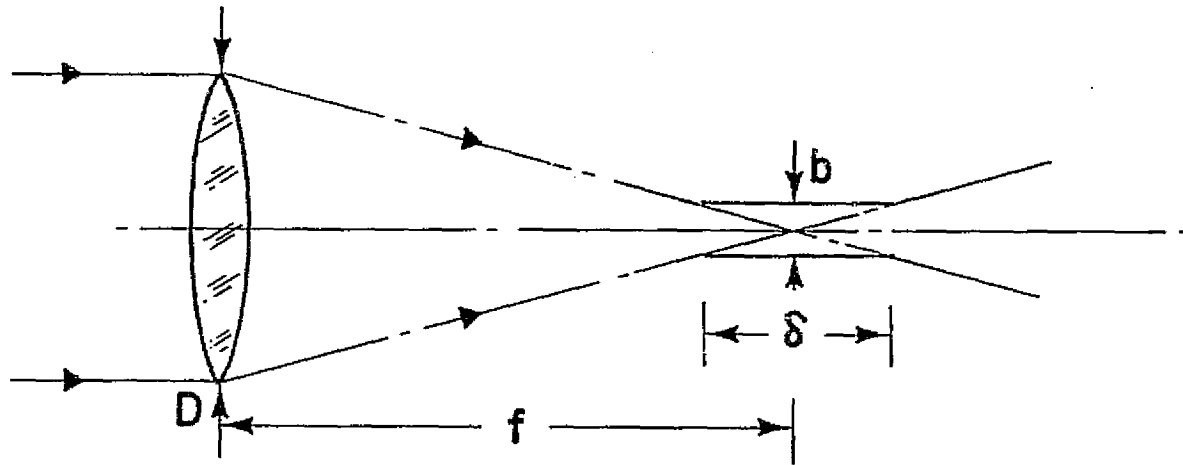


FIGURE B-31 MIRROR SIZE (APERTURE AT CENTER OF CURVATURE)



$\delta = 2(f/\text{no.})b$, where $b = \text{LINEAR IMAGE SIZE}$

EXAMPLES: FOR $f/1.7$, 75-cm-APERTURE SMSS, $b = 84 \mu\text{m}$ AND

$\delta = 286 \mu\text{m}$ (or 0.0011 in.)

FOR $f/2.0$, 75-cm-APERTURE SMSS, $b = 84 \mu\text{m}$ AND

$\delta = 336 \mu\text{m}$ (or 0.0013 in.)

FIGURE B-32 DEPTH OF FOCUS



TABLE B-2 APPROXIMATE WEIGHT AND SIZE OF MIRRORS*

Aperture D (cm)	Focal Ratio	Mirror Element	Size	Weight			
				Quartz		Beryllium	
				kg	lb	kg	lb
60	f/2	Primary	64.3 x 122.7 x 11.7 cm (25.3 x 48.3 x 4.6 in.)	61		14	
		Corrector	59.9 x 62.0 x 7.6 cm (23.6 x 24.4 x 3 in.)	15	135	3	31
		Total		<u>76</u>	<u>33</u>	<u>17</u>	<u>7</u>
75	f/1.7	Primary	79.5 x 141.5 x 14.0 cm (31.3 x 55.7 x 5.5 in.)	101		20	
		Corrector	74.9 x 77.7 x 9.52 cm (29.5 x 30.6 x 3.75 in.)	29	225	6	45
		Total		<u>130</u>	<u>65</u>	<u>26</u>	<u>13</u>
100	f/1.5	Primary	105.4 x 178.3 x 17.8 cm (41.5 x 70.2 x 7 in.)	218		45	
		Corrector	100.1 x 103.6 x 12.7 cm (39.4 x 40.8 x 5 in.)	68	485	14	100
		Total		<u>286</u>	<u>150</u>	<u>59</u>	<u>30</u>

* Based on 70% lightweighting, thickness/average diameter = 1/8 for quartz. An equivalent mirror fabricated of beryllium typically weighs only one-fifth as much as the quartz mirror.

8 APERTURE SIZE

The size of the primary mirror needed to cover a 15° swath without vignetting losses led to reexamination of the original resolution guidelines and to tradeoffs inherent in aperture-size reduction as discussed below.

An aperture of 75 cm was selected instead of the 100 cm originally considered as the SMSS baseline. The maximum diameter of the elliptical primary mirror is then reduced from 193 cm to 145 cm. The weight of the optical elements can be as low as 26.4 kg (58 lb) for beryllium (selected as discussed in Section 9). The mirror weight can be scaled approximately with the cube of the diameter. The mounting structure scales approximately as the diameter squared. Thus, the mirror weight would be reduced by more than 50% and the mounting-structure weight by more than 40%.

If the detector-element size remains the original $85\ \mu\text{m}$ [or, as a refinement, is adjusted to the $84\text{-}\mu\text{m}$ picture-element (pixel) size of commercially available charge-injection devices (CIDs)], the angular resolution of the detectors at $f/1.7$ is changed from $\sim 50\ \mu\text{r}$ to $66\ \mu\text{r}$ (or from 9.25 to 12.2 m of surface resolution at an orbital altitude of 185 km).

The diffraction limit at $12.5\ \mu\text{m}$ is $40.7\ \mu\text{r}$ for the 75-cm aperture (see Figure B-33). The number of channels (ten, with six in operation at any time) remains the same, but the number of detectors per channel for a 15° swath is reduced from 5250 elements to 4000 elements. These can be provided, for the five visible-spectrum channels at least, by a staggered array of forty 100×100 -element CIDs as discussed in paragraph 6.5.

The data rate is reduced from 207 Mbps to 119 Mbps, because there are fewer detector elements and the dwell time is increased to 1.62 msec. The sensitivity is improved by about 15% because of the increased dwell time. [The influences of aperture diameter (D) and resolution (θ) on sensitivity can be neglected because $D\theta$ remains essentially constant.]



$$S = \theta h = \frac{2.44 \lambda h}{D}$$

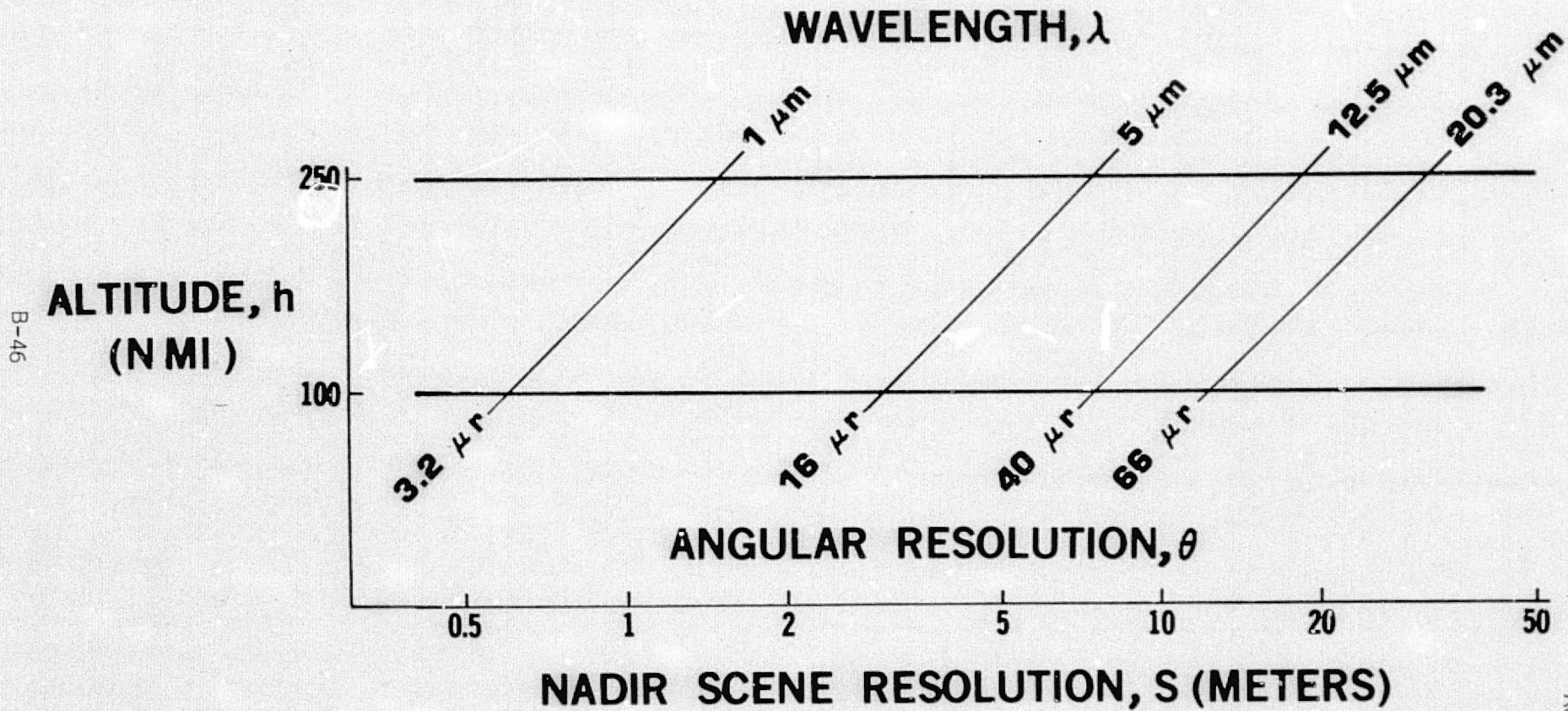


FIGURE B-33 DIFFRACTION-LIMITED RESOLUTION FOR 75-cm APERTURE

The system parameters discussed above are summarized in Table B-3, which also characterizes two other aperture/focal ratios (75/2.0 and 60/2.0) for comparison.

TABLE B-3 COMPARISON OF SMSS SYSTEM PARAMETERS WITH APERTURE REDUCTION*

Parameter	Values for Indicated Apertures (cm)/ Focal Ratios (f/no.)			
	100/1.7	75/1.7**	75/2.0	60/2.0
Total detector elements	52,500	40,000	56,100	44,625
Element IFOV (μ r)	~50	66	40/80***	50/100***
Element size (μ m)	85	84	60/120***	60/120***
Dwell time (msec)	1.22	1.62	0.98/1.96***	1.22/2.44***
NEAT ($^{\circ}$ K)	0.115	0.10	0.090	0.064
Data rate (Mbps)	207	119	{ 324 max 202 min	207 max 130 min
Surface resolution (m) at 185 km	9.25	12.2	7.4/14.8***	9.25/18.5***
* 15° swath, ten channels (0.45-12.5 μ m), 8-bit encoding. ** Revised baseline. *** Channels 1-7/Channels 8-10.				

Figures B-34 and B-35 schematically illustrate the impact on overall dimensions. Their shaded portions represent the optical-bundle size for the 75-cm-aperture system, which is superimposed on the original 100-cm system. The two telescopes are depicted cross sectionally in Figure B-34 and in a side view in Figure B-35.



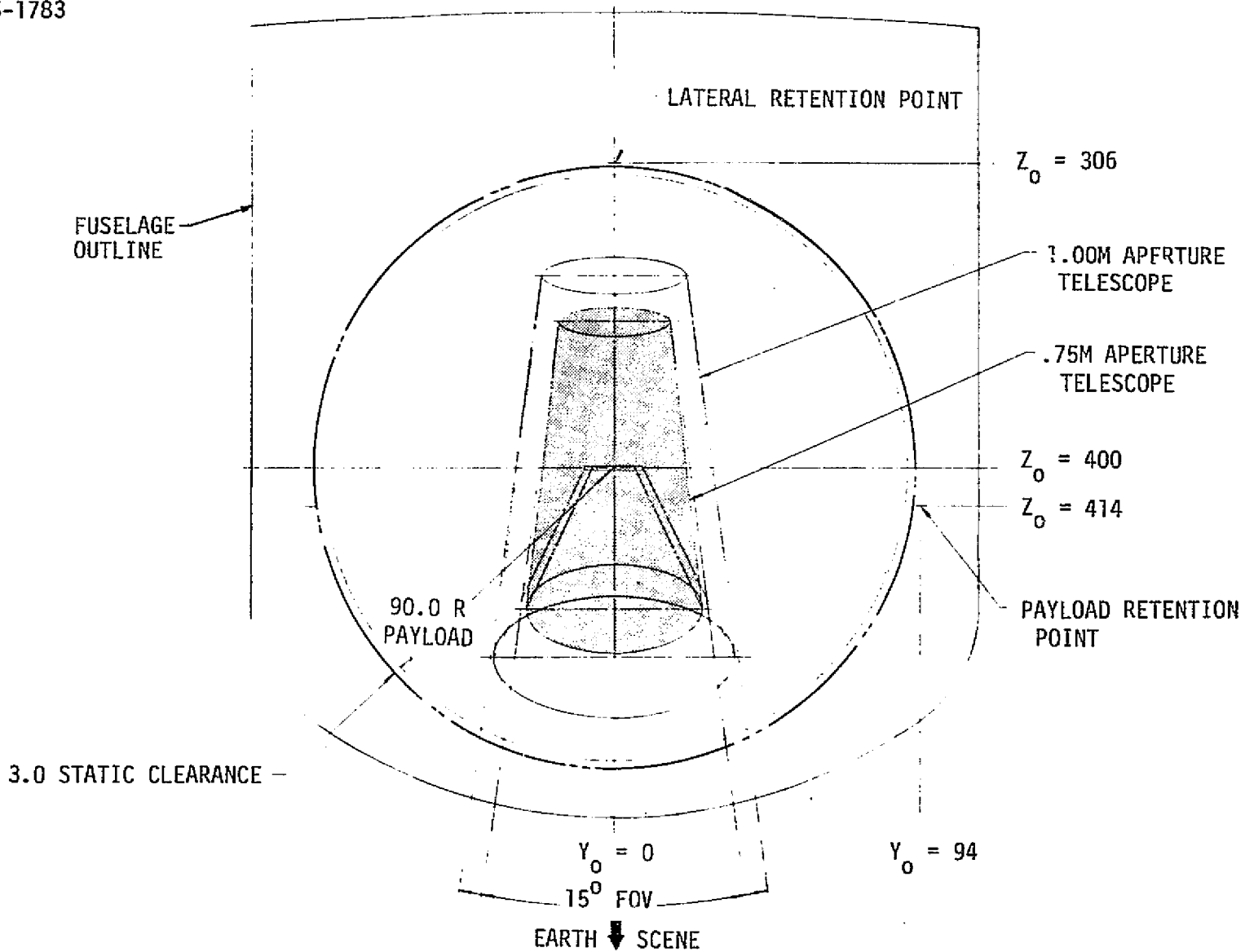


FIGURE B-34 TELESCOPE IN ORBITER, CROSS SECTION (TWO SIZES)

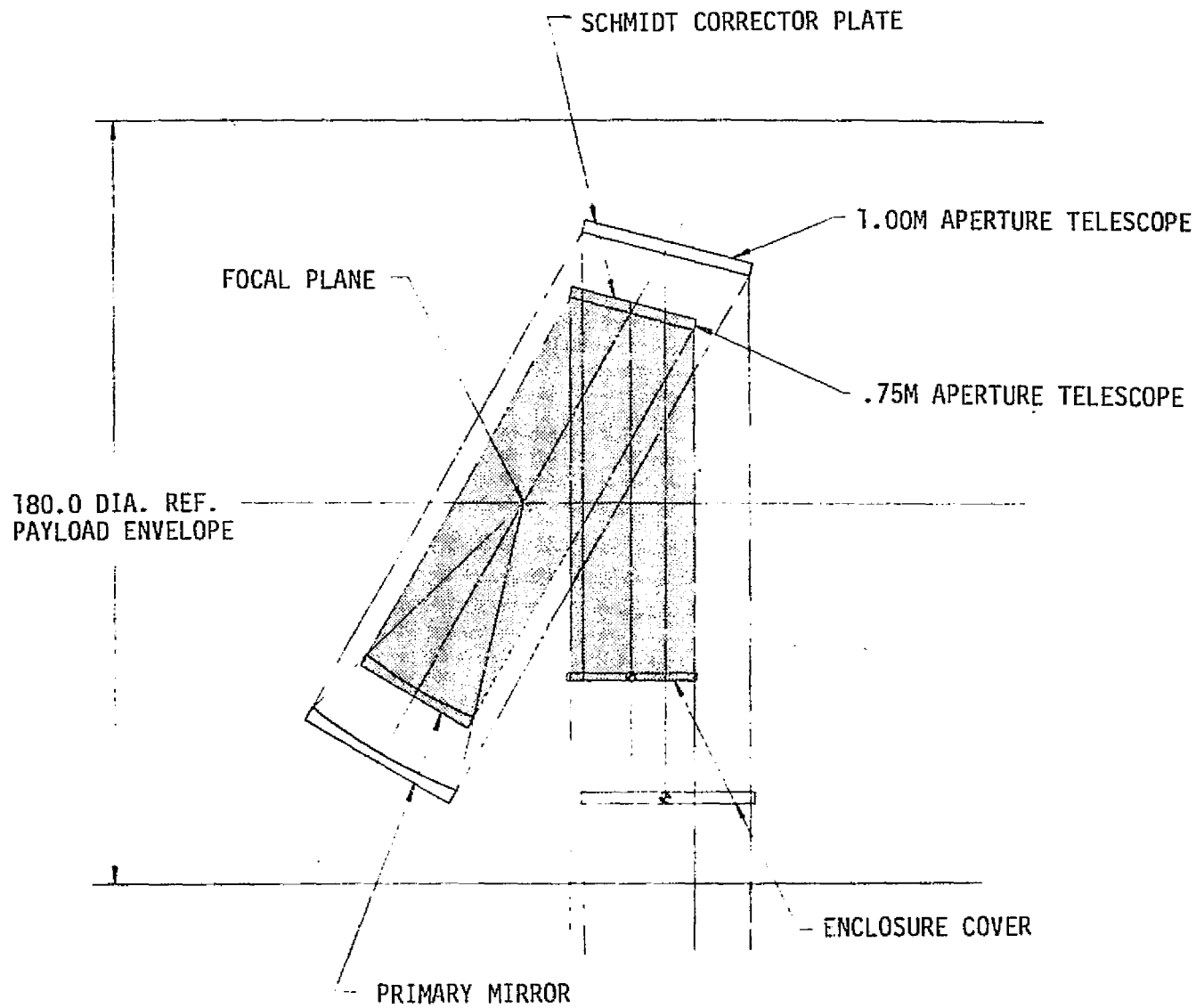


FIGURE B-35 TELESCOPE, SIDE VIEW (TWO SIZES)

B-49

Although a 75-cm system reduces the instantaneous field of view (IFOV) to $66 \mu\text{r}$ and the surface resolution to 12.2 m for a 185-km orbit, considerable improvement is achieved for other important parameters: e.g., reduction in mission-data rate, improved system sensitivity, reduction in number of detectors, increased simplification, and reduced system cost and weight. In addition, the larger size would have created more difficulty in integrating the telescope into the Orbiter payload bay. The reduced volume enhances the optimization of SMSS utility, and together with the other advantages appears to outweigh the spatial-resolution penalty.

9 MIRROR AND STRUCTURAL MATERIAL TRADEOFFS

The primary and corrector mirrors on the all-reflective Schmidt telescope for the SMSS must perform sufficiently well to ensure that the reflected wavefront has the required shape to a high degree of accuracy. Because the recommended system operates at $66 \mu\text{r}$ (as determined in Section 8), and the diffraction limit is $40 \mu\text{r}$ at the longer wavelengths for a 75-cm aperture, each surface must have an rms accuracy of approximately 1/20th wavelength.

The mirror material must be sufficiently stable to accept and retain this quality for long periods under adverse conditions of external forces, thermal effects, and long-term creep.

Materials are available with low thermal-expansion coefficients that make them attractive, from the standpoint of reduced mirror-surface deformation, for applications involving small thermal gradients throughout their volume. For larger and more rapid overall-temperature variations, however, they may lack the required uniform expansion characteristics or thermal conductivity.

In addition, materials exist that have excellent thermal conductivity, high stiffness-to-weight ratio, and isotropic expansion coefficients, thus providing high creep stability.



Weight has a high priority in the selection of mirror-substrate materials for space use; mirror reductions also permit weight savings in the mounting and telescope structures. Fabrication methods are well advanced for most suitable materials, and computer-aided techniques are available whereby deflection can be compensated while the structures are being worked and tested, so that suitable performance can be achieved in the space environment as well as in the laboratory.

A mirror can be considered as a thin reflecting surface whose optical figure is maintained by a supporting structure. The reflector is a thin layer of metal or a dielectric applied by vacuum deposition. The performance depends on the optical properties of the reflector and on substrate design and material. The substrate must maintain the desired figure throughout the mirror lifetime in a changing environment of temperature, mechanical loads, and thermal gradients.

Weight, size, and other restrictions on the SMSS application required that tradeoffs be made in material selection and in the substrate design and optical performance to arrive at the optimum form. For highly precise space applications, traditional glasses have given way in recent years to high-quality grades of low-expansion fused silica and ultra-low-expansion dielectrics--e.g., ULE titanium silicate glass (Corning Glass Works) and CER-VIT glass-ceramic (Owens-Illinois, Inc.). Advanced metal-mirror fabrication techniques have also been developed for substrates such as aluminum, beryllium, and copper. Beryllium has received the most attention.

The choice of materials was governed by the following considerations:

- a. Optical--Reflectivity, surface roughness, figure, diffuse scatter, scratch/dig
- b. Structural--Density, dimensional stability, stiffness, creep, microyield strength



- c. Thermal environment--Thermal-expansion coefficient, thermal conductivity, thermal shock, thermodynamic conditions
- d. Environmental--Corrosion, radiation damage, bimetallic effects
- e. Manufacturing and processing--Cost, size, weight constraints, efficient lightweight designs, commercial availability, workability with high figure and low scatter, testing constraints, optical figure.

Generally, candidate materials can be screened on the basis of thermal and mechanical properties, of which the most important are shown in Table B-4. Materials having small and uniform thermal-expansion coefficients are desirable because the substrates, which will be fabricated at one temperature, must perform throughout a range of temperatures without introducing irregularities and complex changes in the surface figure. To quickly dissipate the effects of front-surface thermal loads, a high thermal conductivity is also required.

Changes in expansion coefficient with temperature for several promising mirror materials are illustrated in Figure B-36, which was adapted from Ref. B-10. As shown there, ULE and CER-VIT provide good dimensional stability, exhibiting low expansion coefficients around 300°K and varying little within $\pm 100^\circ\text{K}$ from this temperature. Figure B-36 also shows that the glasses have lower conductivity values from 300°K to the lower temperatures than do the metals.

Combinations of thermal properties can result in useful tradeoff criteria. The ability of a material to remain dimensionally stable with thermal changes varies directly as the ratio $K/\alpha\rho$, where K is the thermal conductivity, α is the thermal-expansion coefficient, and ρ is the density. The $K/\alpha\rho$ column in Table B-4 indicates that beryllium and CER-VIT are about equally stable but are less stable than ULE. This ratio is generally valid for the slowly varying thermal conditions expected during SMSS-telescope operation with the door open and a constant thermal input from the earth.

TABLE B-4 ROOM-TEMPERATURE PROPERTIES OF MIRROR-SUBSTRATE MATERIALS*

Material	ρ Density (g/cm ³)	E Modulus of Elas- ticity (10 ⁹ N/cm ²)	K Thermal Con- ductivity (cal/cm-sec-°K)	C Specific Heat (cal/g-°K)	α Coeff of Expansion (10 ⁻⁶ /°K)	E/ ρ (10 ⁶ cm)	K/ ρC $\times 10^3$	D = K/ ρC	α/D $\times 10^{-6}$	Microyield Strength	
										MPa	psi
Fused silica	2.20	7.0	0.0033	0.188	0.55	3.18	2.7	0.008	69	10.3	1500
ULE	2.21	6.74	0.0031	0.183	0.03	3.05	47.0	0.008	4	10.3	1500
CER-VIT	2.5	9.23	0.004	0.217	0.1	3.7	16.0	0.008	14	10.3	1500
Aluminum	2.70	6.9	0.53	0.215	23.9	2.56	8.2	0.92	26	0.014-55.2	2-8000
Beryllium	1.82	28.0	0.38	0.45	12.4	15.4	16.5	0.46	27	0.014-69.0	2-10000

* The most significant parameters are α , ρ , the microyield strength, and

D = K/ ρC = thermal diffusivity

α/D = thermal-distortion index

E/ ρ = modulus-to-density ratio.

B-53

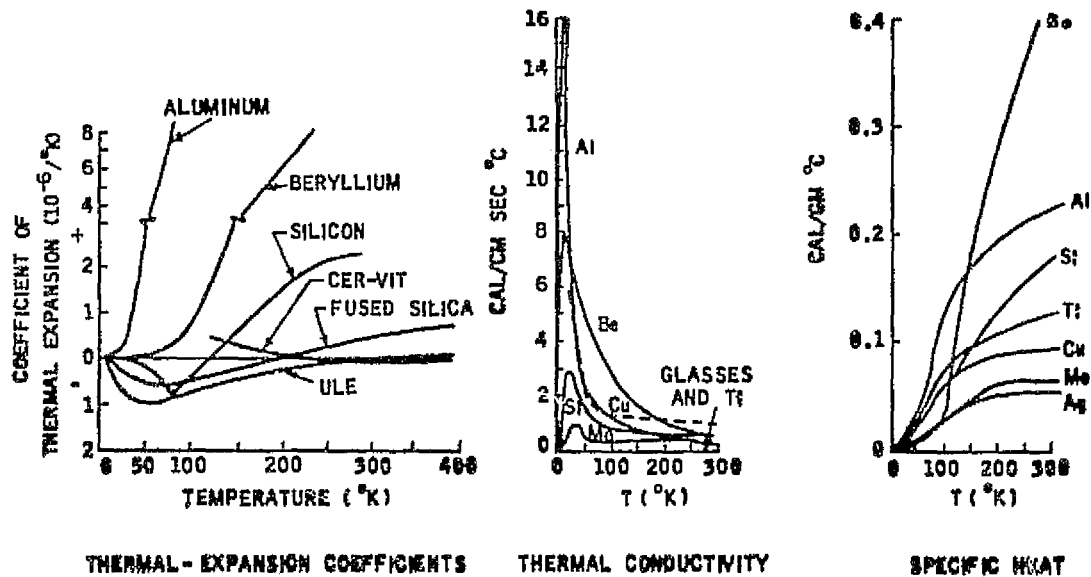


FIGURE B-36 THERMAL PROPERTIES OF MIRROR MATERIALS

Another figure of merit is the thermal diffusivity ($D = K/\rho C$, where C is the specific heat). A high diffusivity is desirable when there are thermal transients. The diffusivities in Table B-4 indicate that the metal mirrors are the most resistant to distortion due to thermal gradients. For the SMSS, diffusivity must be rated as a more important characteristic than $K/\alpha\rho$.

The two ultra-low dielectrics (ULE glass and CER-VIT glass-ceramic) have thermal-expansion coefficients 1/400th that of beryllium and consequently have higher $K/\alpha\rho$ and α/D values but much lower thermal diffusivities. They are used in large telescopes when the thermal environment can be closely controlled, whereas metals are being employed increasingly when that environment is less easily controlled (e.g., SMSS). The reason is that metals can attain thermal equilibrium in less than 1% of the time required by the dielectric materials (which, on the other hand, are less sensitive to thermal effects).

Other substrate characteristics important for successful space operation are material density (ρ) and elastic modulus (E). A high modulus-to-density ratio (E/ρ) indicates a lightweight, very stiff structure.

As shown in Table B-4, the ratio for beryllium is 5 times greater than for the glasses. Also desirable is a high microyield strength, which signifies the stress level below which plastic deformation will not occur.

In addition to the foregoing parameters, manufacturing, mechanical, and optical-processing considerations are important in SMSS design. These and other factors are discussed below for three of the more promising materials.

The fabrication and optical finishing of ULE titanium silicate are in accordance with generally accepted techniques. The substance is made in boules that can be shaped and fused together to provide monolithic, light-weight optics. It has the same general, random, molecular structure as glass and fused silica; hence, its dimensional stability is generally comparable to that of fused silica. This structural similarity, coupled with very low thermal expansion, makes ULE an attractive candidate material. Because it can be fused with a flame or in a furnace without altering its expansion properties, the size and configuration can be varied to accommodate most applications.

Fused-silica mirrors of astronomical quality are traditionally in the shape of right circular cylinders. For spaceborne high-performance systems, this form is disadvantageous because the self-weight deflection (proportional to d^4/h^2 , where d is the diameter and h the thickness) requires a thick and hence a heavy mirror. In recent years, techniques have been developed for the economical fabrication of mirrors with a mechanical stiffness approaching that of solid substrates at weight reductions up to 70%. The simplest approach has been the removal of cores from the rear surface in a predetermined pattern; the limiting factor here is the required thickness of the remaining webs, and weight reductions of 50% have been achieved. Weight can be reduced further with a rear-surface plate, and still further by means of egg-crate construction or the use of round quartz tubes as separators between the front and rear plates.

Beryllium has been employed extensively in high-efficiency space applications because of its low density, its high modulus, and the resultant high stiffness-to-weight ratio. Some of its advantages and disadvantages are as follows:

<u>Advantages</u>	<u>Disadvantages</u>
Low density	High cost
High elastic modulus	Relatively high thermal-expansion coefficient
Microyield and micro-creep strength	Anisotropy in thermal expansion
Good oxidation resistance	Toxicity
Low vapor pressure	Poor corrosion resistance in chloride environments
Good thermal conductivity	Residual porosity
High heat capacity	
Directly polishable	
High reflectivity at infrared wavelengths	

Solely on the basis of modulus-to-density ratio (E/ρ), a beryllium mirror weighs about one-third as much as a glass mirror of the same aperture, provided that the materials are stressed to 6.9-13.8 MPa (1000-2000 psi, a typical value for glass) in order to prevent plastic deformation. Most beryllium mirrors have a higher microyield strength [up to 690 MPa (100,000 psi)], resulting in further weight saving.

An optical surface can now be generated directly onto bare beryllium substrates, eliminating the need for the thick metal coatings that were formerly applied to obtain a hard "polishable" surface. In the IR band, a well-polished surface is generally sufficiently reflective, but the reflectivity in the visible spectrum is about 50% and a thin optical coating will be needed for SMSS use.

Although beryllium components are usually more costly than other materials, beryllium mirrors can cost less, in the large size required by the SMSS, than mirrors made of some of the low-expansion glasses and glass-ceramics.

The dimensional stability of beryllium is related to the method of mirror manufacture and subsequent processing. Temporal stability has been greatly improved in recent years by means of special stress-relieving and machining techniques. Thermal stability is directly related to a crystallographic anisotropy induced during manufacture. Beryllium parts are usually fabricated by powder-metallurgical methods to develop the required isotropic structure and to increase the strength. The isotropy of micro-properties is approached statistically by using a large number of grains having a random orientation.

Most beryllium components are made by vacuum hot pressing of powder in a die to achieve up to 99% of bulk density. Cylindrical billets are formed that are then machined to the desired shape.

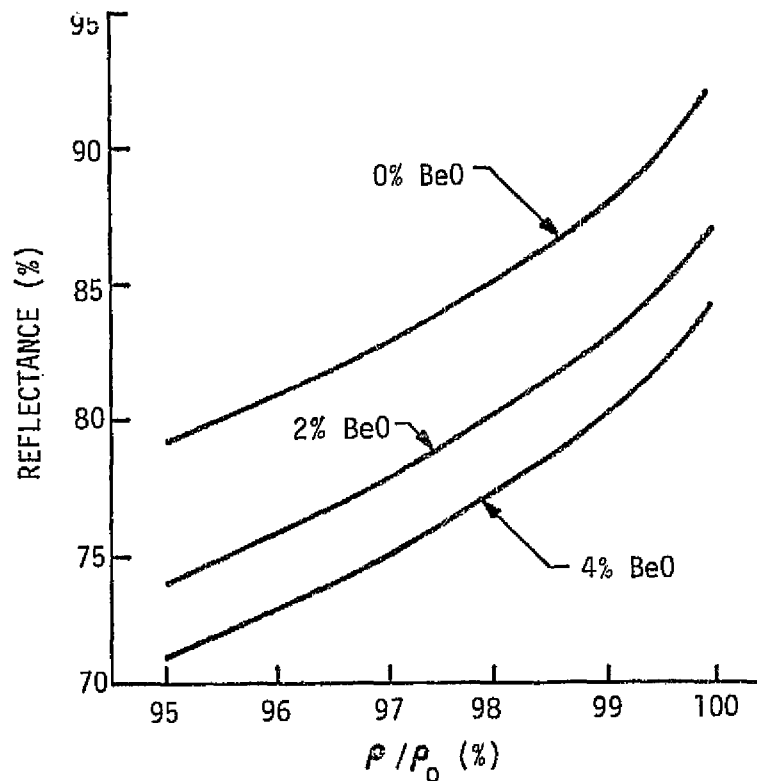
For large mirrors, undesired effects can be produced by non-uniform crystal orientation, which is generally attributed to plastic flow during the pressing operation. New techniques have been developed recently for close control of pressure/temperature parameters to achieve a high level of optical-mirror stability.

In the final processing, electroless nickel coatings have been applied to provide a hard, readily polishable, reflective surface and a high reflectance across the wavelength spectrum of interest. Because the thermal-expansion coefficients of known coatings do not match that of beryllium, thermal stresses can be developed even though the component has been symmetrically and uniformly coated. Therefore, a controlled operating temperature is required.



Bloxson and Schroeder (Ref. 5-11) have shown that high-quality optical surfaces can be directly prepared on bare beryllium substrates. Surface reflectance on bare polished beryllium is shown in Figure 5-38 as a function of oxide concentration and the ratio of material density to bulk density (ρ/ρ_0). The figure indicates that maximum reflectance occurs with minimum surface porosity and minimum oxide content. A tradeoff is necessary between high strength (high oxide) and high purity (low strength), because the oxide distribution affects both the reflectance and the scatter of the base substrate. If low scatter is a critical consideration and the mirror temperature can be closely controlled, an electroless nickel coating would provide an effective surface.

475-1785

FIGURE B-37 REFLECTANCE OF ALUMINUM-COATED BERYLLIUM AT 0.6 μm

Spectral reflectance from bare polished beryllium is affected by surface quality, and for high-purity material is degraded primarily by scattering at surface defects. Figure B-38 shows the reflectance of bare and coated beryllium. In the visible spectrum, bare beryllium requires thin, vapor-deposited high-reflectance coatings.

475-1782

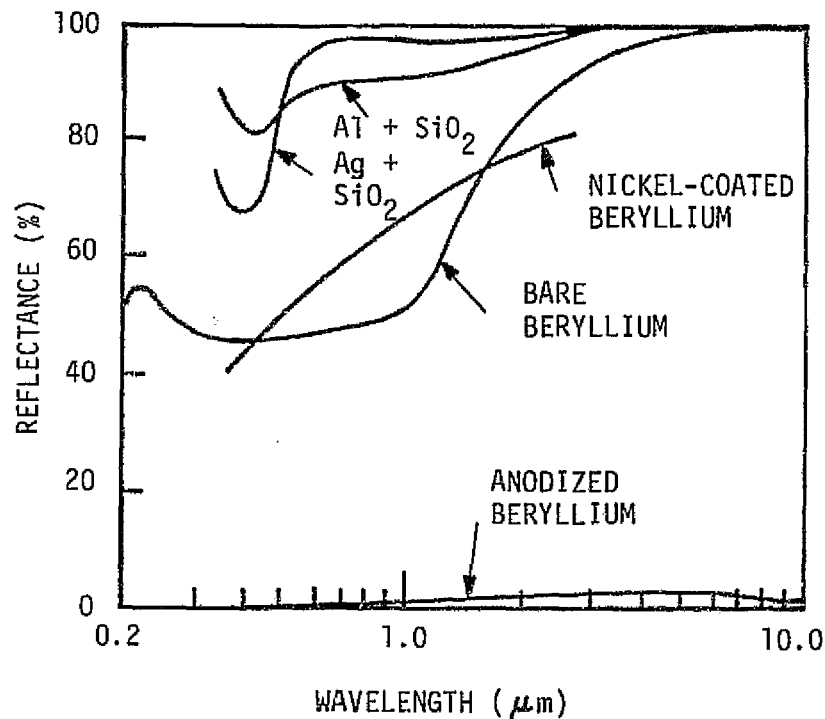


FIGURE B-38 REFLECTANCE OF OPTICAL COATINGS AND MIRROR SUBSTRATES

Diffuse reflectance or scatter is a direct measure of surface smoothness or quality. A very low scatter is not a necessity for the SMSS because the scene is fairly uniform and no high-intensity sources are known that might cause an unexpected loss of system sensitivity. Scatter is important, however, because it directly affects reflectance; it can be expressed as the total integrated hemispherical scatter (TIS), which is generally obtained by numerical integration from angle-dependent measurements. For comparison purposes, TIS values for beryllium and other candidate mirror substrates, all with aluminized polished surfaces, are as follows:

<u>Material</u>	<u>TIS at $\lambda = 0.63 \mu\text{m}$ (decimal fraction)</u>
Nickel-coated beryllium	15 to 50×10^{-5}
Bare beryllium	40 to 100×10^{-5}
Beryllium with sputtered beryllium coating	12 to 50×10^{-5}
Fused silica	13 to 50×10^{-5}
CF ⁺ -VIT C-101	20 to 60×10^{-5}
ULE titanium silicate	14 to 60×10^{-5}

Because scatter intensity is dependent upon surface reflectivity, the fact that all these mirrors have the same reflective coating of aluminum ensures that scattering is a function of surface defects.

The scatter intensity for bare beryllium at small angles from a specular beam is about 3 times that for fused silica, while at larger angles the TIS is significantly greater. This is shown for various materials at a wavelength of $10.6 \mu\text{m}$ in Figure B-39, where the bidirectional reflectance distribution function (BRDF) is plotted as a function of angle. At the higher incident angles, sputtered beryllium shows significant improvement over bare polished beryllium.

In summary, it was found that a mirror material suitable for the SMSS telescope must have the following main characteristics:

- a. Demonstrated short- and long-term optical-surface stability required by the thermal and dynamic environment of repeated launch and recovery
- b. Minimum weight consistent with dimensional stability so that the telescope will be sufficiently light to permit mounting on a stabilized pointing platform
- c. Sufficiently advanced fabrication state of the art to provide a mirror of the necessary dimensions.

On the basis of these criteria, beryllium is recommended for the mirror substrates (aluminum-coated) as well as for the telescope components that will provide thermal compensation for boresight alignment and focus.



475-1784

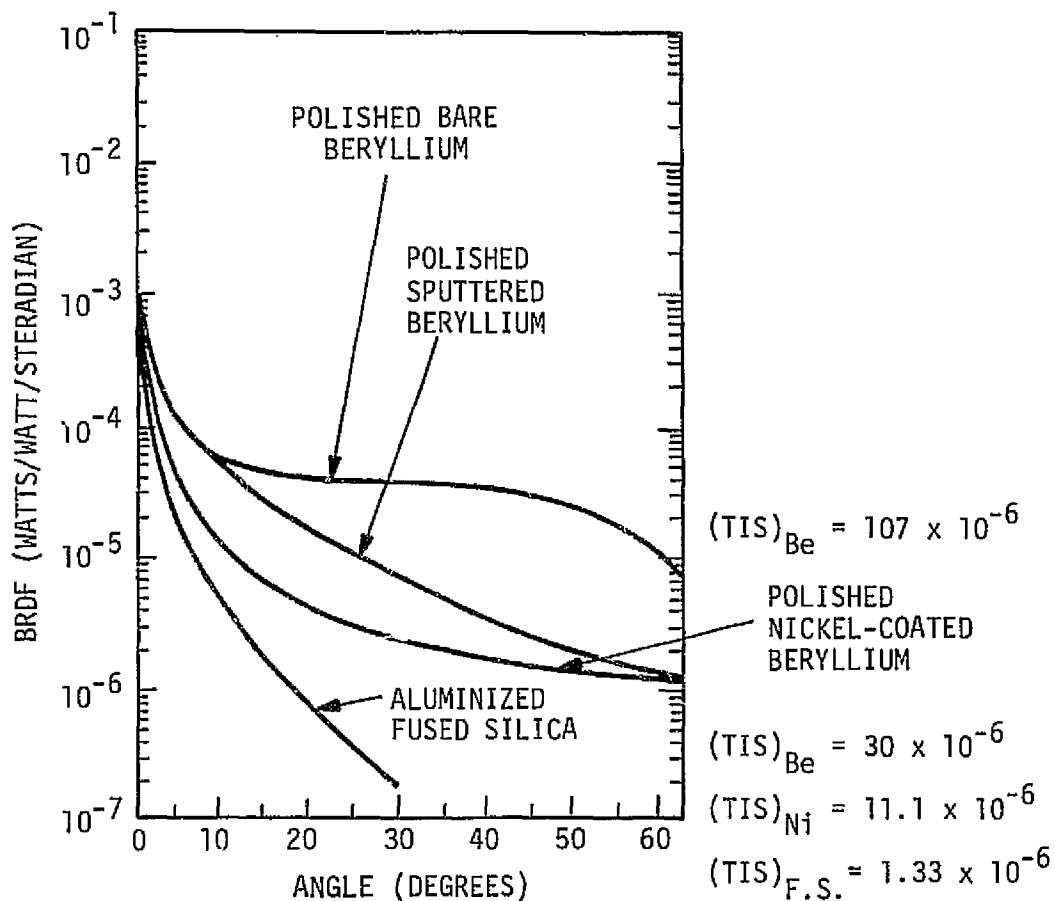


FIGURE B-39 SCATTER FUNCTION OF STATE-OF-ART MIRROR SURFACES, $\lambda = 10.6 \mu\text{m}$



REFERENCES

- 2-1 Development Specification, Shuttle Modular Scanning Spectro-radiometer, Aerojet ElectroSystems Company Specification AE-23331 (prepared under NASA Contract NAS 9-14243), 26 November 1975.
- 2-2 LANDSAT-D Thematic Mapper Technical Working Group Final Report, NASA Lyndon B. Johnson Space Center Report JSC 09797, June 1975.
- 3-1 Definition of the Total Earth Resources System for the Shuttle Era, Volume 1, Total Earth Resources Program Scope and Information Needs, Preliminary, General Electric Company report under NASA Contract NAS 9-13401, 31 October 1973.
- 3-2 Advanced Scanners and Imaging Systems for Earth Observations, NASA Scientific and Technical Office (Washington) Special Report NASA SP-335, 1973.
- 3-3 Earth Albedo and Emitted Radiation [NASA Space Vehicle Design Criteria (Environment)], NASA Special Publication SP-8067, July 1971.
- 4-1 M. J. Duggin, "On the Natural Limitations of Target Differentiation by Means of Spectral Discrimination Technique", Ninth Symposium on Remote Sensing of the Environment, Ann Arbor, Michigan, 1974.
- 4-2 LANDSAT-D Thematic Mapper Technical Working Group Final Report, NASA JSC-09797, June 1975.
- 4-3 W. S. Kovach, "Energy Distribution in the PSF for an Arbitrary Passband", Applied Optics, Vol. 13, No. 8, pp. 1769-1771 (1974).
- 4-4 K. Seyrafi, Electro-Optical Systems Analysis, Los Angeles, Electro-Optical Research Company, 1973, pp. 209-213.
- 4-5 M. Vicars-Harris, "Slow Scan Operation of Long Linear CCD Arrays", presented at Symposium on Charge-Coupled Device Technology for Scientific Imaging Applications, sponsored by NASA Office of Aeronautics and Space Technology and Jet Propulsion Laboratory, Pasadena, California, 6-7 March 1975.



REFERENCES (CONT.)

- 4-6 F. C. Eliot, "Geometric Design of Linear Array Detectors", IEEE Transactions on Electron Devices, Vol. ED-21, No. 10, pp. 613-616 (1974).
- 4-7 D. F. Barbe, "Imaging Devices Using the Charge-Coupled Concept", Proceedings of the IEEE, Vol. 63, No. 1, pp. 38-67 (1975).
- 4-8 European Space Research Organization Spacelab Payload Accommodation Handbook, ESTEC Ref. No. SLP/2104, October 1974.
- 4-9 Space Shuttle System Payload Accommodations, Space Shuttle Program Document JSC 07700, Volume XIV.
- 4-10 Advanced Scanners and Imaging Systems for Earth Observations, National Aeronautics and Space Administration Special Publication NASA SP-335, Washington, NASA Scientific and Technical Office, 1973.
- 4-11 J. R. Hickey and A. R. Karoli, "Radiometric Calibrations for the Earth Radiation Budget Experiment", Applied Optics, Vol. 13, pp. 523-533 (March 1974).
- 4-12 Appendix C of Earth Observatory Satellite System Definition Study, Report No. 6, Space Shuttle Interfaces/Utilization, General Electric Space Division Document 74SD4250 under Contract NAS 5-20518, 16 September 1974.
- 6-1 T. F. Tao et al., "Feasibility Study of PbTe and $Pb_{0.76}Sn_{0.24}Te$ Infrared Charge Coupled Imager", Proceedings of CCD Applications Conference, Naval Electronics Laboratory Center, San Diego, September 1973, pp. 259-268.
- 6-2 D. E. French, et al., "Readout of PbSnTe Heterostructure Detectors Using Charge Coupled Devices" (Unclassified paper), Proc. IRIS, Vol. 19, pp. 201-221 (1974) (Secret document).
- 6-3 J. C. Kim, et al., "InSb Surface Charge-Injection Imaging Devices" (Unclassified paper), ibid, p. 243.
- 6-4 H. R. Hess, et al., "The MOSART (Monolithic Signal Processor and Detector Array Integration Technology) Program" (U) (Confidential paper), ibid, p. 171.



REFERENCES (CONT.)

- 6-5 GSFC Specification for Earth Observation Scanning Spectro-radiometer Experiment, NASA Goddard Space Flight Center Specification GSFC 73-15012, revised 20 September 1973.
- 6-6 M. A. Bramson, Infrared Radiation: A Handbook for Applications, New York, Plenum Press, 1968.
- 6-7 F. C. Billingsley, "Considerations for Digital Image Processing", in National Aeronautics and Space Administration Special Publication NASA SP-233, May 1969.
- 6-8 Evaluation of Background Suppression Techniques for 3-5 Micrometer Solid State Imagers, General Electric Company Tube Products Department Imaging Devices Operation final report to U.S. Army Night Vision Laboratory, February 1974.
- 8-1 D. E. Knuth, The Art of Computer Programming, Vol. 1, Fundamental Algorithms, Reading, Mass., Addison-Wesley, 1969, p. 402.
- A-1 Definition of the Total Earth Resources System for the Shuttle Era, Volume 1, Total Earth Resources Program Scope and Information Needs, Preliminary, General Electric Company report under NASA Contract NAS 9-13401, 31 October 1973.
- A-2 Advanced Scanners and Imaging Systems for Earth Observations, NASA Scientific and Technical Office (Washington) Special Report NASA SP-335, 1973.
- A-3 Earth Albedo and Emitted Radiation [NASA Space Vehicle Design Criteria (Environment)], NASA Special Publication SP-8067, July 1971.
- A-4 Earth Observatory Satellite Definition Phase Report, Volume 1, NASA Goddard Space Flight Center Report X-481-72-332, August 1971.
- A-5 D. Anding, R. Kauth, and R. Turner, Atmospheric Effects on Infrared Multispectral Sensing of Sea Surface Temperature from Space, University of Michigan Willow Run Laboratories report under Contract NAS 12-2117, 1970.



REFERENCES (CONT.)

- A-6 Space Shuttle Program, Space Shuttle System Payload Accommodations, Level 11 Program Definition and Requirements Volume XIV, NASA Lyndon B. Johnson Space Center Report JSC 07700, Volume XIV, Revision B, 21 December 1973.
- A-7 LANDSAT-D Thematic Mapper Technical Working Group Final Report, NASA JSC 09797, June 1975.
- A-8 R. K. Vincent, "The Potential Role of Thermal Infrared Multi-spectral Scanners in Geological Remote Sensing, Proc. IEEE, Vol. 63, pp. 137-147 (1975).
- B-1 R. M. Scott, "Optical Engineering", Applied Optics, Vol. 1, No. 4, pp. 387-397 (1962).
- B-2 D. E. Oinen, "Correcting Surface for a Two-Surface All-Reflecting Schmidt Lens", presented at 1973 Annual Meeting, Optical Society of America.
- B-3 L. C. Epstein, "An All-Reflection Schmidt Telescope for Space Research", Sky and Telescope, pp. 204-207, April 1967.
- B-4 L. C. Epstein, "Improved Geometry for the All-Reflecting Schmidt Telescope", Applied Optics, Vol. 12, No. 4, p. 926 (1973).
- B-5 D. Korsch, "Reflective Schmidt Corrector", Applied Optics, Vol. 13, No. 9, pp. 2005-2006 (1974).
- B-6 J. A. Decker, Jr., "Hadamard-Transform Instrumentation for Infrared Space Optics", Space Optics, Proceedings of Ninth Congress of International Commission for Optics, pp. 405-418, 9-13 October 1972.
- B-7 D. L. Fried, "Aspheric Correctors Without Rotational Symmetry", Applications of Geometrical Optics, Proceedings of 17th Annual Meeting, S.P.I.E., pp. 173-192, 27-29 August 1973.
- B-8 Space Shuttle System Payload Accommodations, Space Shuttle Program Document JSC 07700, Volume XIV.
- B-9 I. S. Bowen, "Schmidt Cameras", Chap. 4 (pp. 43-61) of Stars and Stellar Systems 1: Telescopes, G. P. Kuiper and B. M. Middlehurst, eds., University of Chicago Press, 1960.



REFERENCES (CONT.)

- B-10 R. A. Paquin and W. R. Goggin, Beryllium Mirror Technology, Perkin-Elmer Optical Group (Norwalk, Conn.) State of the Art Report, December 1972.
- B-11 J. T. Bloxson and J. B. Schroeder, "Preparation of Optical Surface on Beryllium," Applied Optics, Vol. 9, p. 539 (March 1970).

